

Computational Homogenisation and Multiscale Modelling Employing an Image-based Approach for the Structural Analysis of Shells

Von der Fakultät für Bauingenieurwesen
der Rheinisch-Westfälischen Technischen Hochschule Aachen
zur Erlangung des akademischen Grades einer Doktorin der Ingenieurwissenschaften
genehmigte Dissertation

vorgelegt von

Leonie Charlotte Josefine Mester
aus Bergisch Gladbach

Berichter: Universitätsprofessor Dr.-Ing. habil. Sven Klinkel
Universitätsprofessor Dr.-Ing. Stefan Löhnert
Tag der mündlichen Prüfung: 01. März 2024

Diese Dissertation ist auf den Internetseiten der Universitätsbibliothek online verfügbar.

Veröffentlicht als Heft 20 (2024) in der Schriftenreihe
des Lehrstuhls für Baustatik und Baudynamik
der RWTH Aachen

Herausgeber:

Universitätsprofessor Dr.-Ing. habil. Sven Klinkel

Organisation und Verwaltung:

Rheinisch-Westfälische Technische Hochschule Aachen
Fakultät für Bauingenieurwesen
Lehrstuhl für Baustatik und Baudynamik
Mies-van-der-Rohe-Str. 1
52074 Aachen

Telefon: +49 241 80 25088

Telefax: +49 241 80 22303

E-Mail: sekretariat@lbb.rwth-aachen.de

© 2024 Leonie Charlotte Josefine Mester

D 82 (Diss. RWTH Aachen University, 2024)

Alle Rechte, insbesondere das der Übersetzung in fremde Sprachen, vorbehalten.
Ohne Genehmigung des Autors ist es nicht gestattet, dieses Heft ganz oder teilweise auf fotomechanischem Wege (Fotokopie, Mikrokopie) zu vervielfältigen oder in elektronischen Medien zu speichern.

ISSN 1437-0840

ISBN 978-3-946090-19-9

Vorwort

Die vorliegende Arbeit entstand während meiner Tätigkeit als wissenschaftliche Mitarbeiterin am Lehrstuhl für Baustatik und Baudynamik der Rheinisch-Westfälischen Technischen Hochschule Aachen im Rahmen des Sonderforschungsbereichs Transregio 280 zum Thema "Konstruktionsstrategien für materialminimierte Carbonbetonstrukturen - Grundlagen für eine neue Art zu bauen" (Projektnummer: 417002380).

Mein besonderer Dank gilt Herrn Professor Dr.-Ing. Sven Klinkel, der mir die Anfertigung dieser Arbeit an seinem Lehrstuhl ermöglicht und mich die letzten Jahre stets unterstützt hat. Ich durfte viele Freiheiten genießen und war immer gerne Teil seines Teams.

Weiterhin möchte ich mich bei Herrn Professor Dr.-Ing. Stefan Löhnert für die Übernahme des Koreferates und bei Herrn Professor Dr.-Ing. Rostislav Chudoba für die Übernahme des Prüfungsvorsitzes bedanken. Beide haben die vorliegende Arbeit nicht nur abschließend begutachtet, sondern bereits während ihrer Entstehung durch konstruktive Diskussionen bei etwaigen Frühjahrs-, Herbst- oder iAG-Treffen im Rahmen des SFB/TRR 280 immer wieder bereichert.

Im Rahmen meiner Tätigkeit am Lehrstuhl durfte ich eine positive und freundschaftliche Arbeitsatmosphäre erleben. Dank meiner wunderbaren Kollegen und Kolleginnen bin ich stets gerne ins Büro gekommen. Für die vielseitige Unterstützung, sowohl in fachlicher als auch organisatorischer Hinsicht, möchte ich mich bei euch allen bedanken. Dazu zählen auch die Hiwis, Bacheloranden und Masteranden, welche diese Arbeit tatkräftig unterstützt haben. Durch meine Mitarbeit im SFB/TRR280 durfte ich zudem viele Wissenschaftlerinnen und Wissenschaftler aus Aachen und Dresden zu meinen Kolleginnen und Kollegen zählen. Der fachliche Austausch über verschiedene Disziplinen hinweg hat mir große Freude bereitet.

Abschließend möchte ich mich bei meinen Freundinnen und Freunden, meiner Familie und meinem langjährigen Partner für ihre moralische Unterstützung, ihr Verständnis und die nötige Ablenkung danken. Ein dreifaches BÄM! BÄM! BÄM! gilt den Shadow Fightern. Auf meine Eltern, Jutta und Rudolf, sowie meine drei großartigen Schwestern, Anni, Miri und Rieke, auf die ich immer zählen kann, ein dreimal kräftiges "Heu Pi".

Aachen, im März 2024

Leonie Charlotte Josefine Mester

Abstract

Shell structures represent efficient structural systems. Integrating materials with distinct properties, such as composites, can further enhance the structural performance of shells. These composite shell structures find application in various engineering fields, ranging from aerospace to civil engineering, providing a balance between strength and material consumption. Identifying the optimum designs, particularly in terms of load-bearing capacity and suitability, drives the need for accurate and efficient analysis methods accounting for the intricate material behaviour of composites.

In the scope of this work, a first-order homogenisation method for the analysis of shell structures, taking into account a detailed description of the microstructure, is proposed. The method allows the simulation of the structural behaviour at different length scales within a single framework. Thus, providing an approach able to capture the microscopic morphology while being computationally efficient. Although homogenisation methods are widely used and thoroughly investigated for three-dimensional problems, their application to structural elements, such as shells, still poses challenges. Specifically, assessing the homogenised shear stiffness often yields inaccurate results.

The main focus is on the coupling of the microscopic representative volume element (RVE) to the macroscopic shell formulation. For this purpose, three different boundary conditions for the RVE are presented. These differ mainly in the treatment of the macroscopic shear strain and impose different symmetry requirements on the RVE. Introducing an additional constraint at the microscopic scale corrects the homogenised shear stiffness components. Using linear-elastic benchmark examples, the approach is validated at the microscopic scale and further evaluated using multiscale examples, including geometrical and physical nonlinearities.

In the context of civil engineering, the proposed method is applied to examine carbon reinforced concrete shell structures. Image-based methods are used to capture the microscopic structure with high accuracy. The aim of this work is to combine a numerical analysis method with an accurate internal description to allow for the evaluation of novel production techniques and structural designs of, but not limited to, carbon-reinforced concrete shell structures.

Kurzfassung

Schalenstrukturen stellen effiziente Tragstrukturen dar. In Kombination mit Verbundwerkstoffen können die Struktureigenschaften weiter verbessert werden. Schalenstrukturen aus Verbundwerkstoff finden in verschiedenen technischen Bereichen, von der Luft- und Raumfahrt bis hin zum Bauwesen, Anwendung und zeichnen sich durch ihre hohe Tragfähigkeit bei gleichzeitig geringem Materialverbrauch aus. Um optimale Designs, insbesondere im Hinblick auf Tragfähigkeit und Brauchbarkeit, zu identifizieren, sind präzise und effiziente Analysemethoden, die das komplexe Materialverhalten von Verbundwerkstoffen berücksichtigen, unerlässlich.

Im Rahmen dieser Arbeit wird eine Homogenisierungsmethode erster Ordnung für die Analyse von Schalenstrukturen vorgeschlagen, welche eine detaillierte Beschreibung der Mikrostruktur berücksichtigt. Die Methode ermöglicht die Simulation des Strukturverhaltens auf verschiedenen Längenskalen. Auf diese Weise kann die mikroskopische Morphologie erfasst und zusätzlich eine effiziente Berechnung ermöglicht werden. Obwohl Homogenisierungsmethoden für dreidimensionale Probleme weit verbreitet und eingehend erforscht sind, stellt ihre Anwendung auf Strukturelemente, wie Schalen, nach wie vor eine Herausforderung dar. Insbesondere die homogenisierten Schubsteifigkeiten werden oft nur ungenau erfasst.

Der Schwerpunkt liegt auf der Kopplung eines mikroskopischen repräsentativen Volumenelements (RVE) mit der makroskopischen Schalenformulierung. Dazu werden drei verschiedene Randbedingungen für das RVE vorgestellt. Diese unterscheiden sich hauptsächlich in der Berücksichtigung der makroskopischen Schubverzerrung und stellen unterschiedliche Symmetrieanforderungen an das RVE. Durch die Einführung einer zusätzlichen Randbedingung auf mikroskopischer Skala werden die homogenisierten Schubsteifigkeiten korrigiert. Anhand von linear-elastischen Referenzbeispielen wird die Methode auf mikroskopischer Skala validiert und anhand von Multiskalenbeispielen, welche geometrische und physikalische Nichtlinearitäten berücksichtigen, evaluiert.

Im Bauwesen wird die Methode zur Analyse von Schalenstrukturen aus Carbonbeton eingesetzt. Dabei werden bildgebende Verfahren angewendet, um die mikroskopische Struktur möglichst präzise zu erfassen. Ziel der Arbeit ist die Kombination einer numerischen Analysemethode mit einer detaillierten Beschreibung der inneren Struktur, um die Bewertung von neuartigen Fertigungsmethoden und Strukturdesigns zu ermöglichen. Zu den möglichen Anwendungen gehören Schalenstrukturen aus Carbonbeton.

Contents

1	Introduction	1
1.1	Motivation	1
1.2	State of the art	3
1.3	Aim	11
1.4	Outline	11
2	Basic principles of continuum mechanics	13
2.1	Kinematics	13
2.2	Strains, stresses and constitutive relations	15
2.3	Weak form of equilibrium and linearisation	17
3	Nonlinear shell theory	19
3.1	Assumptions	19
3.2	Kinematics	20
3.3	Strains	23
3.4	Stresses and stress resultants	24
3.5	Constitutive relation	25
3.6	Weak form of equilibrium and linearisation	26
4	Fundamentals of computational homogenisation	29
4.1	Basic principles	29
4.2	Representative volume element (RVE)	31
4.3	HILL-MANDEL condition	34

5	Homogenisation of shear deformable shells	37
5.1	Macro-Meso transition	38
5.2	HILL-MANDEL condition	41
5.3	Peculiarities arising from the transverse shear deformation	44
5.3.1	Rigid body rotation of the RVE	44
5.3.2	RVE size dependence of shear stiffness components	44
6	Finite Element Formulation	49
6.1	Geometric Nonlinear Shell Element	51
6.2	Scaled Boundary Isogeometric Analysis	52
6.3	Transition element	57
6.4	Moment reduction constraint	61
6.5	Homogenisation algorithm	64
6.6	Boundary conditions for the RVE	66
6.6.1	Traction Boundary Conditions	68
6.6.2	Shell Boundary Conditions	70
6.6.3	Periodic Boundary Conditions	70
7	Numerical Examples	73
7.1	Preliminary Examples	74
7.1.1	Necessity of the moment reduction constraint (MRC)	74
7.1.2	Adaption of Shell Boundary Conditions	76
7.1.3	Comparison of boundary conditions	77
7.2	Mesoscopic Scale	83
7.2.1	Homogeneous, linear-elastic RVE	83
7.2.2	Layered, linear-elastic RVE	84
7.2.3	Findings from the mesoscopic scale	87
7.3	Multiscale	89
7.3.1	Beam	89
7.3.2	Layered cylindrical shell	94
7.3.3	Plate - elasto-plastic material	96
7.3.4	Plate - longitudinally reinforced	98
7.4	Discussion	104

8	Image-based modelling	107
8.1	Microtomography and Roving Extraction	108
8.1.1	Specimen	108
8.1.2	Microtomography	109
8.1.3	Segmentation	109
8.2	Parameterised RVE and determination of characteristic properties	111
8.2.1	Assumptions	112
8.2.2	Roving dimensions	113
8.2.3	In-Plane Dimensions	115
8.2.4	Shell Thickness	115
8.2.5	Concrete Cover	115
8.3	Examples	116
8.3.1	Tensile Test - linear-elastic	117
8.3.2	Tensile Test - microplane damage model	121
8.4	Discussion	123
9	Conclusion and Outlook	127
	Nomenclature	131
	Appendix A Boundary Conditions for the RVE	139
	Appendix B Derivation of differential operator	143
	Appendix C Deformation modes	145
C.1	Traction boundary conditions	146
C.2	Shell boundary conditions	147
C.3	Periodic boundary conditions	148
	Bibliography	149

Chapter 1

Introduction

1.1 Motivation

Resource efficiency is defined as the correlation between a particular benefit or outcome and the utilization of the necessary resources to attain it. In civil engineering, resource-efficient construction methods are increasingly essential due to the construction sector's critical role in reducing global CO₂ emissions. This challenge can be approached from two different perspectives.

On the one hand, the structural system can be designed to improve the resource efficiency. One example is the use of shell structures, which are able to carry high loads with minimal material consumption, thus being resource efficient. Shell structures are characterised as thin and often curved, with in-plane dimensions significantly larger than the thickness. Inspired by natural structures, such as leaves or nacre, shell structures have been widely adopted in various engineering applications.

On the other hand, the systematic use of composite materials can improve the resource efficiency of a structure. Composites combine two or more materials to achieve a specific overall material behaviour, which can be tailored to meet specific needs, including stiffness, strength, damping, and isolation. The combination of specific material properties is exploited in many engineering fields such that composites are now well established in various applications. In civil engineering, for example, a prevalent application is reinforced concrete, where the high compressive strength of concrete is combined with the high tensile strength of steel or e.g. carbon textile.

To maximise the load-bearing behaviour while being resource efficient, both concepts must be considered simultaneously. The combination of shell structures with composite materials has been adopted from nature and is currently being applied in many engineering fields. One example from nature is the microscopic brick and mortar structure of nacre (Fig. 1.1 (a)). In engineering, carbon fibre reinforced polymers (CFRP), which possess a layered microstructure (Fig. 1.1 (b)), are used in the aerospace and automotive industries, as well as in sports equipment. In contrast, the microstructure of carbon-

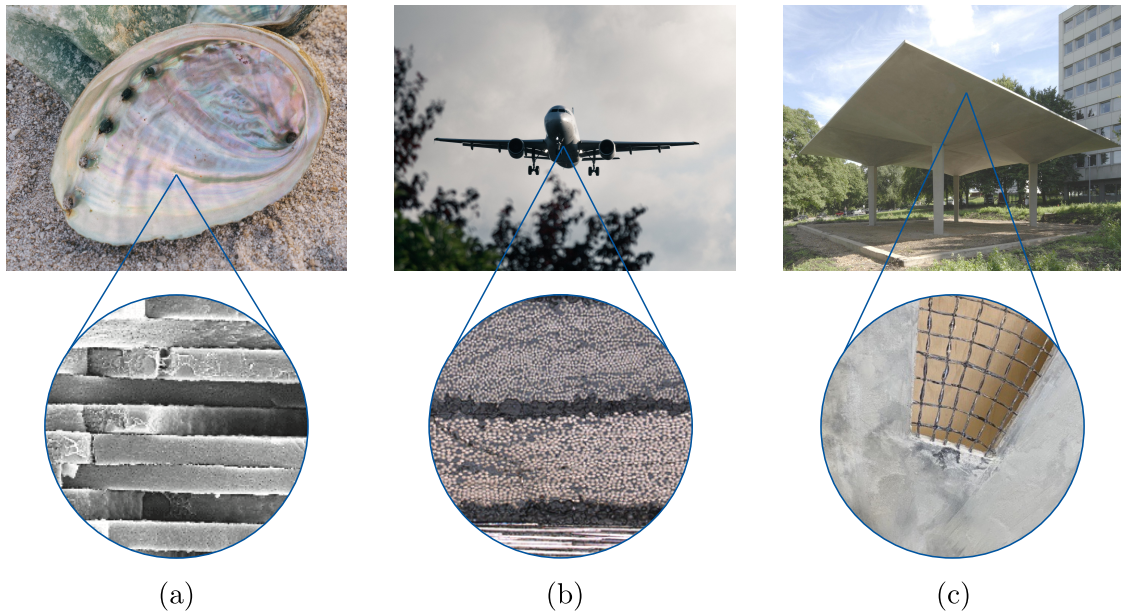


Figure 1.1: (a) Brick-and-mortar structure of nacre (b) Laminate structure of carbon fibre-reinforced plastic (CFRP) used in aeroplanes (c) Carbon-reinforced concrete ((a) - top: © A. Tarazevich - bottom: © ESA - E. Poloni; (b) - top: © N. Jeromin - bottom: [160]; (c) - top: © IMB, RWTH Aachen)

reinforced concrete is characterised by the grid-like structure of the reinforcing textile, see Fig. 1.1 (c).

To optimise the design process and to gain an in-depth understanding of the interdependence of the different materials, the development of sophisticated analysis methods is necessary. Identification of a suitable constitutive law, which characterises the composite material would require extensive material tests. To circumvent this drawback and together with the fact, that the structural scale and the material scale do not coincide in general, this gives rise to the development of a numerical multiscale method.

Multiscale methods typically consider structural problems on two scales. The micro- or mesoscopic scale takes the morphology and physical properties of the constituents into account. Whereas the macroscopic scale considers the structural dimensions and is treated as homogeneous. Therefore, multiscale methods are often referred to as homogenisation methods. This approach circumvents the necessity of extensive material tests on composites as well as the need for complex constitutive models for each composite material. Thus, the development of a homogenisation method is highly desirable, especially for shell structures.

Due to their reduced thickness, shell structures are particularly sensitive to imperfections. Non-destructive image-based methods, like computed tomography, allow insights into the shell structures. In this way, the influence of material imperfections on the load-bearing behaviour can be evaluated. In a civil engineering framework, for example, the position of the textile reinforcement within the concrete shell can be assessed and conclusions

regarding the production process can be drawn. These aspects necessitate the integration of image-based methods into multiscale approaches.

1.2 State of the art

In the following, the current state of the art is briefly summarised, covering all relevant research areas treated in this work. First, the discretisation technique used at the microscopic scale, the scaled boundary isogeometric analysis, is introduced. Secondly, an overview of possible shell formulations for the analysis of the macroscopic scale is given, including their advantages and disadvantages, leading to the formulation employed in this work. Regardless of the macroscopic and microscopic formulation, the state of the art of homogenisation methods in general is given. Subsequently, the focus lies on the homogenisation of structural elements, which includes the transition from volumetric to structural description. The problems arising from the coupling of a structural element with a volumetric description of the microscale are discussed and possible solutions proposed in the literature are presented. Finally, a brief overview of the possibilities of combining imaging techniques and homogenisation methods is given.

Scaled boundary isogeometric analysis Since the microscopic structures often take complex shapes, the use of scaled boundary isogeometric analysis (SBIGA) is an attractive option. It avoids the geometric approximation error of the finite element method (FEM) and is therefore well suited for the analysis of complex microstructures.

SBIGA uses the concepts of isogeometric analysis (IGA), which was first introduced by Hughes et al. [76] and is based on the idea of combining design and analysis. Geometries are often designed using Computer Aided Design (CAD) software. When using FEM for the analysis, the finite element mesh approximates the CAD geometry. This geometric approximation error may affect the quality of the solution [41]. Instead of using the standard LAGRANGE basis functions from FEM, IGA typically uses non-uniform rational B-Spline (NURBS) functions for the interpolation of the solution field. Exchanging the approximation functions allows to directly use the CAD geometry for analysis, this is one of the main advantages of IGA, because the meshing cost can be reduced. For more comprehensive information on NURBS, the reader is kindly referred to the standard literature [134, 144]. Although NURBS are the most widely used type of interpolation functions, other computational geometry technologies are possible, such as T-Splines [12, 43] or subdivision surfaces [36].

When adopting three-dimensional models from CAD, one faces the challenge that solids in CAD are usually described only by their boundary surfaces. This modelling technique is referred to as boundary representation (B-rep) of a solid. To use these surface descriptions for analysis, they need to be transformed into a volumetric description. Several different techniques have been proposed in the literature. For example, swept volume

parameterisation [2], the solution of an optimisation problem [131], NURBS-enhanced FEM [153] or the construction of tri-variate Bézier elements from volumetric T-splines [104]. In the scope of this work, IGA is combined with the concepts of the semi-analytical scaled boundary finite element method (SBFEM) [157, 158, 159] to obtain a volumetric description. In SBFEM, a scaling centre C can be defined for any star-convex domain, i.e. a straight line between the scaling centre and any point on the boundary is not allowed to be intersected. If this condition is satisfied, the interior of the domain can be described by a scaling parameter that runs from the scaling centre to the boundary. If the domain is not star-shaped, subdivision can be applied, in order to obtain multiple star-shaped geometries [127, 158]. However, subdivision can be quite tedious depending on the geometry. To overcome this issue, Bauer et al. [10] discuss various decomposition methods, such as quadtree decomposition and the art gallery problem. Nevertheless, these approaches are limited to two dimensions.

The required star-convexity of the geometries is a restrictive requirement. Therefore, different efforts have been made to relax this restriction. On the one hand, nonlinear scaling lines, such as curved scaling rays [7], circular arcs [80] or parabolic parameter lines [166], have been introduced to provide more flexibility. On the other hand, it has been proposed to place the scaling centre outside of the domain [32, 140, 148]. Unfortunately, all of these approaches are currently restricted to two dimensions. Here, star-shaped geometries are obtained through subdivision, linear scaling lines are employed, and the scaling centre is positioned within the structure.

Once the position of the scaling centre is defined, the problem can be described by means of one scaling parameter and two parameters describing the boundary. In classical SBFEM, the displacement field in the interior is solved analytically. To allow the investigation of nonlinear problems, a fully numerical scheme was proposed [27, 28, 30]. The displacement field in the interior is approximated by uni-variate B-Splines. Thus, instead of the tri-variate tensor-product commonly used in IGA for the description of solids, the formulation combines a bi-variate NURBS surface description with a uni-variate B-Spline description. Therefore, the combination of the NURBS surface representation of the boundaries with the scaling concept of SBFEM yields the scaled boundary isogeometric analysis (SBIGA) [27, 96, 127].

Shell formulation In the scope of this work, shell structures are examined at the macroscopic level. Irrespective of the volumetric discretisation technique used at microscopic scale, the macroscopic scale is discretised using a shell formulation. A lot of research has been conducted in the field, such that an extensive overview is beyond the scope of this work. Instead, a brief summary – without any claim to completeness – is given. For more comprehensive reviews on the subject of shell formulations, the interested reader is referred to e.g. [4, 5, 16, 86, 182].

In general, the use of structural shell elements implies that the three-dimensional kinematics used in a continuum mechanics context are modified a priori. For thin-walled

shell structures, this modification refers to the dimensional reduction from three to two dimensions [16].

These shell formulations typically distinguish between the KIRCHHOFF-LOVE and the REISSNER-MINDLIN kinematics and are referred to by the number of degrees of freedom they possess. The former theory is based on the works of Kirchhoff [88] and Love [107]. They assumed that the cross-section of the plate remains plane, implying that the cross-sectional axis remains perpendicular to the centre plane even after deformation. Therefore, the deformation behaviour due to transverse shear is described as rigid. Consequently, the KIRCHHOFF-LOVE theory is not able to account for transverse shear and is therefore only suited for thin shells. The theory describes the behaviour using three translational degrees of freedom, while the rotation is obtained as the derivative of the out-of-plane displacement. Hence, it is referred to as 3-parameter shell formulation.

In contrast, the theory of Reissner [141] and Mindlin [122] is an extension of the KIRCHHOFF-LOVE theory, as it allows for deformations due to transverse shear. The cross-section of the shell is thus allowed to rotate relative to the centre plane. It is referred to as a shear deformable shell formulation. In addition, REISSNER-MINDLIN theory offers the advantage that C^0 -continuous interpolation functions can be utilized, since two rotational degrees of freedom are introduced in addition to the displacement. For this reason, REISSNER-MINDLIN shells are often referred to as 5-parameter shells. In contrast, KIRCHHOFF-LOVE shells require C^1 -continuous interpolation functions due to the incorporation of the displacement derivative.

Within the 5-parameter shell, a plane stress state is assumed that requires a modification of the three-dimensional constitutive laws. These necessary modifications usually motivate the introduction of 6- and 7-parameter shell models, which introduce one or two additional degrees of freedom to account for thickness change and thus allow for the incorporation of three-dimensional constitutive laws, see e.g. [15, 22, 63]. However, for classical shell problems a 5-parameter shell is computationally more efficient since it necessitates less degrees of freedom.

The REISSNER-MINDLIN kinematics assume a constant transverse shear strain across the thickness of the shell, which implies a constant shear stress distribution over the thickness, or a constant shear stress for each layer in layered materials. However, this constant distribution is unphysical and does not coincide with the real shear stress distribution. It also violates the boundary conditions at the top and bottom surfaces. In shell theory, this problem can be addressed by an extension of the kinematic relationships, for example in multi-director shell formulations [101, 126, 139]. Alternatively, solid shell elements [74, 93, 94] can be used.

Overall, these methods are computationally expensive and therefore not well suited for the use within a homogenisation framework, which is why a 5-parameter shell is used. Nevertheless, the correct shear stress distribution must also be achieved during homogenisation within the RVE.

Shell formulations are known to suffer from locking phenomena. Locking leads to an

artificial stiffening of the system and therefore the results obtained are too stiff. For REISSNER-MINDLIN shells, membrane and shear locking are the most commonly observed [61]. Various methods have been proposed to avoid the different types of locking. The most well-known techniques to circumvent locking are selective reduced integration [185], the discrete shear gap method [17, 98], the assumed natural strain (ANS) method [48, 75] or the enhanced assumed strain (EAS) method [24, 155]. An overview can be found in [97].

In the scope of this work a shell formulation based on [61, 95, 174] with REISSNER-MINDLIN kinematics is employed. It offers the advantage of being computationally efficient, compared to other shell formulations. The material behaviour will be covered by the microscopic scale within the homogenisation approach. As discussed, a key point is the correct shear stress distribution. Locking effects of the shell formulation are cured by an assumed shear strain interpolation according to Dvorkin and Bathe [48] and the use of a mixed element formulation following the HU-WASHIZU principle. However, locking phenomena are not investigated throughout the scope of this work.

Multiscale methods At the microscopic scale, materials often exhibit heterogeneities, such as fibres, pores or phases of different materials. The definition of continuum material models is often complex. Thus, multiscale methods aim to substitute the complex microscopic material behaviour. The multiscale methods discussed in the following consider materials on two different length scales, referred to as macroscale and meso- or microscale. Alternatively, they can be referred to as coarse and fine scale in the literature.

One can distinguish between concurrent multiscale methods, which consider a strong coupling between the scales, and homogenisation methods, which assume a scale separation and aim to determine an equivalent overall material model. For the definition of effective material properties the microscopic heterogeneities are modelled discretely. In general, multiscale methods can be classified in analytical and computational approaches [59].

One intuitive analytical approach is the rule of mixtures, which predicts the effective properties as a weighted mean value. Voigt [168] assumed a constant strain across the microstructure, while Reuss [142] proposed, opposing to VOIGT, a constant stress distribution within the microstructure. It can be shown that the approaches of VOIGT and REUSS yield an upper and lower bound for the effective material properties, respectively. However, the bounding property of the VOIGT and REUSS approach applies only for linear-elastic materials. To incorporate nonlinear material behaviour, the approaches were advanced by Taylor [162] and Sachs [146] and build the counterparts to the theories of VOIGT and REUSS, respectively.

The bounds proposed by VOIGT/TAYLOR and REUSS/SACHS provide an initial estimate for the definition of effective material properties. However, they only account for the volume ratio of the heterogeneities and neglect the morphology of the constituents and their distribution. Eshelby [49] proposed a method, which considers ellipsoidal inclusions. The inhomogeneities were assumed to be dilutely distributed, such that their interaction

could be neglected. Since this assumption is unrealistic, the approach has been further developed and various models have emerged [102, 123]. These are generally referred to as dilute family methods.

Alternatively, a class of methods based on a variational approach was first proposed by Hashin and Shtrikman [64] and was later generalized, for example, by Hori and Nemat-Nasser [72] and Milton and Kohn [121].

Based on the analytical approaches, in the past decades various computational multiscale methods for the analysis of heterogeneous materials have been developed. Extensive overviews can be found for example in [56, 128, 130, 138, 147].

The class of direct micro-macro methods, also referred to as coupled multiscale methods, are based on the definition of a representative section of the microstructure, known as representative volume element (RVE). The RVE captures the relevant microscopic effects. However, the size of the RVE has to be chosen carefully. It needs to be large enough to be statistically representative [45] and at the same time as small as possible to reduce computational effort [84]. Many studies have been published on the choice of the correct RVE size, an overview can be found in [147].

To obtain the effective material response, the macroscopic strains are applied on the RVE. After the solution of a boundary value problem the effective material response can be derived. Feyel [51] introduced the so-called FE² method, which employs the finite element method (FEM) at both scales for the solution of the boundary value problem. The algorithmic treatment was further discussed e.g. in [52, 119, 120, 156]. Alternatively to using the FEM at microscopic level, other numerical methods may be employed, such as the fast Fourier Transform (FFT) [124] or the extended finite element method (XFEM) [20]. Here, the scaled boundary isogeometric analysis (SBIGA) [30] is used.

The macroscopic and microscopic scale are typically coupled in a point-wise manner, meaning that for each macroscopic point (each integration point in the finite element context) the stress-strain relationship is determined by the evaluation of a microscopic boundary value problem. This point-wise coupling requires a clear separation of scales. Because these methods consistently pass information between the scales, they are classified as synergistic [1].

The coupling between the scales is typically governed by the HILL-MANDEL condition [70, 110], which requires the energies on the two scales to be equal. The boundary conditions for the microscopic boundary value problem can be chosen, such that the HILL-MANDEL condition is a priori satisfied [99, 120]. Alternatively, a wider set of boundary conditions [109, 113] can be defined based on the IRVING-KIRKWOOD theory [78]. In contrast to the HILL-MANDEL condition the scale transition is achieved by a global constraint linking the macroscopic and the microscopic strains.

The assumption of scale separation is only valid if localisation does not occur [56]. For cases where these limitations cannot be met and moderate localisation occurs, the second-order homogenisation scheme can be used [54, 99, 100]. In first-order homogenisation

schemes only the deformation gradient is used for scale transition, whereas the second-order homogenisation schemes extend this approach by additionally accounting for the strain gradient. The latter allows for capturing size effects on the microscopic scale. An extensive overview on second-order homogenisation methods can be found in [143].

Furthermore, a challenging topic is the incorporation of material failure or softening, i.e. intense localisation, into multiscale methods. Gitman et al. [57] showed that in the softening regime, when strain localisation occurs at the microscopic scale, the RVE loses its representativeness. To overcome this problem, multiple special homogenisation schemes have been proposed, such as the multiscale aggregating discontinuities method [13] or the failure-zone averaging technique [128]. Alternatively, the multiscale projection method proposed by Loehnert and Belytschko [105] can be used for the detailed analysis of spatially limited areas which are prone to localisation. A brief comparison of the coupled multiscale method proposed in this work, which couples a macroscopic structural shell with a microscopic continuum representation, with a multiscale projection method has been presented in [118].

Homogenisation of structural elements In the scope of this work, the microscopic scale will be discretised using the scaled boundary isogeometric analysis (SBIGA), while shell elements are employed at the macroscopic scale. The use of SBIGA at the microscopic scale does not result in any distinctive features for the homogenisation algorithm. In contrast, the use of structural elements at the macroscopic scale is not straightforward. Many multiscale methods have been proposed for the analysis of beams and shells. See for example [26, 183] for beams with BERNOULLI kinematic, while [85, 91, 129, 181] consider shear deformable TIMOSHENKO beams.

The homogenisation approaches for structural shell elements can be classified into first-order [38, 39, 62, 65, 187], second-order [55, 69] and variationally consistent homogenisation approaches [19]. These can be further distinguished by the shell theory considered. First, Coenen et al. [38] proposed a homogenisation approach for thin shells (KIRCHHOFF-LOVE kinematics), which has been applied to masonry structures by Mercatoris and Masart [112]. As discussed above, these shell theories neglect the transverse shear and the through-thickness stress; therefore, efforts have been made to develop homogenisation techniques for thick shells.

Homogenisation approaches for 7-parameter plate [65] and shell models have been proposed [39, 53, 103], to account for the through-thickness normal strains. These models are not susceptible to Poisson thickness locking [65]. However, due to the extended kinematics they are computationally expensive and encounter convergence problems related to the plate theory [66].

The present work focuses on a homogenisation approach for shear deformable shells with REISSNER-MINDLIN kinematics and is based on the works of Gruttmann and Wagner [62] as well as Wagner and Gruttmann [175]. This approach was further developed by [68, 187] and applied for the analysis of sandwich structures with thin-walled cores. However, the

REISSNER-MINDLIN kinematics also assume a zero through-thickness normal stress. Rigorous consideration of the HILL-MANDEL condition lead to boundary conditions violating this assumption. Therefore, the choice of the correct boundary conditions is a key point. In the scope of this work, three types of boundary conditions are proposed. Their main difference is the application of the macroscopic shear strain on the RVE. All three boundary conditions will be compared to each other with regard to their suitability within the proposed homogenisation framework.

In order to evaluate the suitability, early publications on the topic [38, 39, 55] directly validate the homogenisation approach by multiscale examples, more recently the focus has shifted to validating the individual homogenised stiffness components [68, 69, 164] before analysing more complex multiscale examples. It can be observed that the membrane and bending contributions are homogenised with sufficient accuracy. However, the transverse shear stiffnesses are erroneous and cause two characteristic phenomena. On the one hand, the RVE is subject to rigid body rotations when shear strains are applied. To prevent this rotation, various measures have been proposed in the literature, such as applying specific boundary conditions [62], imposing a weak constraint on the lateral RVE surfaces [55], constraining the in-plane displacement [164] or restricting the average rotation of the RVE cross-section [89, 187].

On the other hand, a dependence of the shear stiffness on the in-plane RVE size is observed [19, 69, 116]. This has also been noticed by Klarmann et al. [91] for beam structures. Various measures have been proposed in the literature to overcome the dependence on the in-plane RVE size. Heller and Gruttmann [68] proposed the use of length-dependent shear correction factors to account for the size of the RVE. Klarmann [89] showed that the dependence of the shear stiffness components on the in-plane RVE size can be related to an unbalanced linear moment distribution. It develops when the macroscopic transverse shear strain is applied to the lateral RVE surfaces. Hence, Klarmann [89] proposed an additional constraint that reduces the linear moment distribution within the RVE. This approach was successfully adopted for shells by [117, 187]. Alternatively, [69] propose a volumetric constraint on the fluctuation moment within a second-order homogenisation framework to properly apply the transverse shear strains on the RVE.

In addition, the recent works of Müller et al. [125] and Börjesson et al. [19] should be mentioned. The former propose a homogenisation approach for shear deformable plates based on the IRVING-KIRKWOOD theory, which implies that the strains of the macroscale and the microscale are linked by a global constraint. No length dependence of the transverse shear stiffness on the in-plane RVE size is observed. In the work of Börjesson et al. [19] a framework based on the Variationally Consistent Homogenisation for shear deformable plates has been proposed. The membrane, bending and shear stiffnesses were correctly obtained; however, the torsional stiffnesses showed an RVE size dependence which was overcome by introducing an anti-periodic fluctuation field.

The present work deploys the idea of Klarmann et al. [91], where the linear bending moment distribution is reduced by an additional constraint. The approach is adapted for

shear deformable macroscopic shell structures and SBIGA at the microscopic scale.

Incorporation of image-based methods The detailed knowledge of the composition, size and shape of the heterogeneities can enhance the simulation of materials. It is therefore beneficial to include knowledge of the microscopic structure into the RVE. Image-based methods aim to provide a detailed reconstruction of the microstructure of a sample. Imaging methods such as computed tomography (CT) scans are used for this purpose. The image data obtained allows an examination of the microstructure.

In the past, image-based simulations have been used, for example, to investigate the material properties of concrete [21, 46] or paper [47]. An overview of the various applications of image-based simulation can be found in [50] and with application to concrete in [165].

In the context of numerical homogenisation, image-based methods can accurately determine the RVE morphology. Multiscale models have been successfully combined with computed tomography data for concrete [137, 161, 179], Titanium foams [33], fibre reinforced polymer [152], textile composites [133] as well as bone tissue [135]. Matouš et al. [111] present a comprehensive overview over image-based multiscale modelling.

The data from computed tomography has to be preprocessed to generate analysis-suitable representations. Using boundary detection techniques or voxel methods, hexahedral meshes can be generated. Alternatively, point clouds can be transformed into surface descriptions [14, 73]. However, a disadvantage of these methods is that the mesh size needs to be small in order to represent the heterogeneities with sufficient accuracy. Unfortunately, this requires high computational effort, which is particularly disadvantageous in the context of coupled multiscale approaches, as the microscopic boundary value problem is solved at every macroscopic integration point. A further drawback is that the representation with hexahedral elements does not allow for a smooth surface description; hence, unphysical stress concentrations and singularities may occur at reentrant corners associated with the voxel-based meshing strategy.

To overcome these drawbacks, the use of NURBS surfaces seems advantageous for the representation of the microscopic morphology, since NURBS surfaces promise a smooth surface description and increased accuracy at lower computational effort compared to standard hexahedral discretisations. Algorithms for the 3D reconstruction of NURBS surfaces from digital images are presented for example in [60, 169, 176]. To date, the literature has mainly reported the reproduction of individual objects rather than entire mesostructures. Furthermore, the reconstruction of mesostructural geometries based on CT data is very time-consuming. Thus, an efficient modelling strategy is highly desirable.

In the scope of this work, a parameterised model for the analysis of carbon-reinforced concrete is proposed. A balance between accuracy and computational efficiency is provided, while allowing a high degree of automation, making it easy to model a wide range of mesostructures. Furthermore, the proposed parameterised model is implicitly star-shaped, allowing analyses based on SBIGA.

1.3 Aim

The aim of this work is to develop a homogenisation approach for shear deformable shell structures based on the HILL-MANDEL condition. In particular, three different sets of boundary conditions are proposed to allow for a consistent scale transition between the macroscopic structural element and the microscopic continuum element. Particular attention is paid to the homogenised shear stiffnesses. The length dependence of the shear stiffness on the in-plane RVE size is reduced through adapting the approach of Klarmann [89] to shells. Generally, the approach can be used for the analysis of any composite shell structure. However, the work focuses on textile reinforced concrete shell structures. To achieve a high degree of accuracy in the microscopic representation, a parameterised RVE is introduced to incorporate computed tomography data into the homogenisation framework.

The main focus of this work can be summarised as

- Introduction and comparison of three different types of boundary conditions for the RVE to allow for a consistent scale transition between the microscopic continuum representation and the macroscopic structural shell.
- The constraint presented by Klarmann [89] for beams to reduce the length dependent behaviour of the homogenised shear stiffness components is adapted for shear deformable shell structures.
- A parameterised RVE for the multiscale analysis of textile reinforced concrete shell structures incorporating image-based methods is presented.

1.4 Outline

Following this introductory chapter, the theoretical foundations on which the developed homogenisation approach for shear deformable shells is based are presented.

In *Chapter 2*, the basic equations from continuum mechanics are recapitulated, since the microscopic scale is described by a three-dimensional continuum formulation.

The description of the microscale is followed by the description of the macroscopic scale. Thus, *Chapter 3* discusses the shell formulation with REISSNER-MINDLIN kinematics, which is employed throughout the work.

Chapter 4 presents the basic principles of numerical homogenisation. The choice of a representative volume element is discussed and the HILL-MANDEL condition, which enforces the energetic equivalence between the scales, is presented.

The microscopic and macroscopic descriptions are coupled within a homogenisation formulation for shear deformable shells in *Chapter 5*. The scale transition and the fulfilment

of the HILL-MANDEL condition are discussed. The peculiarities arising from the coupling of a structural element with a three-dimensional continuum element are also presented.

In *Chapter 6*, the finite element formulations are introduced. These include a shell element for the macroscopic scale and the approximation and discretisation technique used at the microscopic scale, which is the scaled boundary isogeometric analysis. Furthermore, the numerical treatment of the additional constraints that enables a consistent scale transition is presented. Finally, the three types of boundary conditions investigated in this work are derived.

After describing the theoretical foundations, the homogenisation algorithm is validated using several numerical examples, which are presented in *Chapter 7*. First, the assumptions made throughout the derivation of the homogenisation algorithm are validated using preliminary examples. Then, the homogenisation approach is verified using linear-elastic benchmarks for homogeneous and layered RVEs. Finally, four multiscale examples involving physical and geometrical nonlinearities are presented.

Chapter 8 deals with the integration of image-based methods into the homogenisation procedure. First, the fundamentals of microtomography and segmentation are explained, before a parameterised RVE for the analysis of carbon-reinforced concrete shell structures is introduced. An algorithm to determine the characteristic geometric properties of the carbon textile is presented.

To conclude, *Chapter 9* summarises the work and presents an outlook on prospective research topics.

Chapter 2

Basic principles of continuum mechanics

In the following, the fundamentals of continuum mechanics are briefly summarised. They form the basis for the derivation of the formulations describing the macroscopic and microscopic scale, as well as for the homogenisation approach. More extensive overviews on continuum mechanics can be found e.g. in [3, 71, 178].

2.1 Kinematics

A body \mathcal{B} , which is defined as a set of continuously distributed material points $\mathcal{P} \in \mathcal{B}$, is examined. The body is mapped to the Euclidean space \mathbb{E}^3 in which it occupies the region Ω , refer to Fig. 2.1. For time $t = 0$, this region is referred to as *reference configuration*. For different points in time the body \mathcal{B} occupies different regions Ω, \dots, Ω_t . For $t > 0$ the region Ω_t is referred to as *current configuration*.

An orthogonal basis system $\mathbf{e}_i = \{\mathbf{e}_1, \mathbf{e}_2, \mathbf{e}_3\}$ is introduced. With respect to this basis

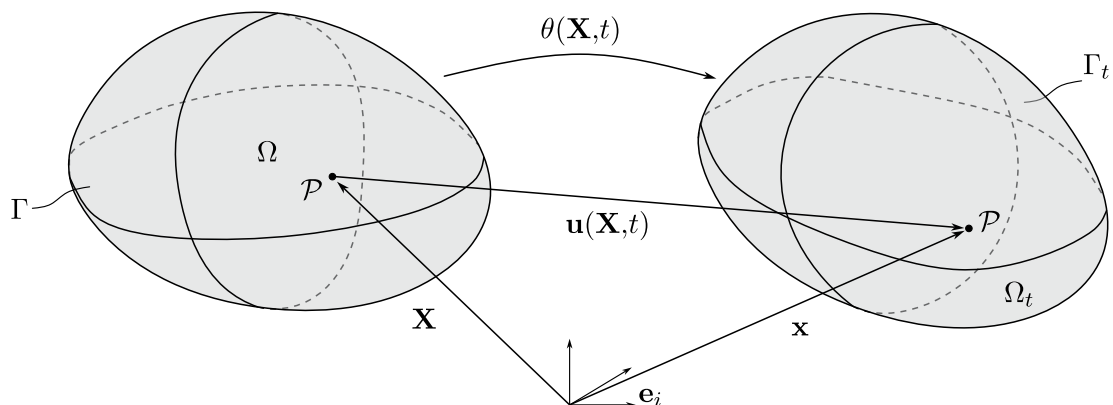


Figure 2.1: Continuum body in reference and current configuration

system, any material point \mathcal{P} can be described using the position vector \mathbf{X} in the reference configuration and \mathbf{x} in the current configuration.

The bijective mapping from the reference to the current configuration is introduced as

$$\mathbf{x} = \theta(\mathbf{X}, t), \quad (2.1)$$

where $\theta(\mathbf{X}, t)$ is defined as the motion of the body and is assumed to be invertible.

The displacement field \mathbf{u} describes the relation of a point in the reference configuration \mathbf{X} to the point in the current configuration \mathbf{x} . It is defined as

$$\mathbf{u}(\mathbf{X}, t) = \mathbf{x}(\mathbf{X}, t) - \mathbf{X}. \quad (2.2)$$

To describe the deformation of a body, the deformation gradient \mathbf{F} is introduced. It characterises the local deformation process by relating the infinitesimal tangent vectors $d\mathbf{X}$ and $d\mathbf{x}$ to each other.

$$d\mathbf{x} = \mathbf{F} d\mathbf{X} \quad (2.3)$$

$$\mathbf{F} = \frac{\partial \mathbf{x}}{\partial \mathbf{X}} = \text{Grad } \mathbf{x} = \mathbf{I} + \text{Grad } \mathbf{u} = \mathbf{I} + \mathbf{H} \quad (2.4)$$

\mathbf{I} denotes the identity tensor and \mathbf{H} is the second-order displacement gradient tensor which vanishes for rigid-body translations. In VOIGT notation the deformation gradient reads

$$\hat{\mathbf{F}} = [F_{11} \ F_{22} \ F_{33} \ F_{12} \ F_{21} \ F_{13} \ F_{31} \ F_{23} \ F_{32}]^T = \mathcal{D} \mathbf{x} = \mathbf{I} + \mathcal{D} \mathbf{u} \quad (2.5)$$

and can be expressed by means of the differential operator \mathcal{D} , which can be written as

$$\mathcal{D}^T = \begin{bmatrix} \frac{\partial}{\partial X_1} & 0 & 0 & \frac{\partial}{\partial X_2} & 0 & \frac{\partial}{\partial X_3} & 0 & 0 & 0 \\ 0 & \frac{\partial}{\partial X_2} & 0 & 0 & \frac{\partial}{\partial X_1} & 0 & \frac{\partial}{\partial X_3} & 0 & 0 \\ 0 & 0 & \frac{\partial}{\partial X_3} & 0 & 0 & 0 & \frac{\partial}{\partial X_1} & 0 & \frac{\partial}{\partial X_2} \end{bmatrix}. \quad (2.6)$$

To ensure the one-to-one mapping of the body \mathcal{B} during deformation, the inverse of \mathbf{F} must exist, such that

$$\mathbf{F}^{-1} = \frac{\partial \mathbf{X}}{\partial \mathbf{x}} = \text{grad } \mathbf{X}. \quad (2.7)$$

Consequently, the determinant of the deformation gradient cannot be zero, which implies that \mathbf{F} is nonsingular. The determinant of the deformation gradient is introduced as the JACOBI determinant

$$J = \det \mathbf{F} \neq 0. \quad (2.8)$$

To avoid a self-penetration of a body, it is further required that $J > 0$.

2.2 Strains, stresses and constitutive relations

The relevant strain and stress measures as well as the constitutive relationships are briefly summarised in the following. However, this is only a short overview and is not intended to be exhaustive. For a more detailed description on continuum mechanics, and alternative stress and strain measures, the reader is again referred to [3, 71, 178].

The GREEN-LAGRANGE strain tensor can be formally derived from the difference between the squared length of a line element in current and reference configuration. It reads

$$\mathbf{E} = \frac{1}{2} (\mathbf{F}^T \mathbf{F} - \mathbf{I}) \quad (2.9)$$

and can be expressed in VOIGT-Notation as $\hat{\mathbf{E}} = [E_{11} \ E_{22} \ E_{33} \ 2E_{12} \ 2E_{13} \ 2E_{23}]^T$. It is a symmetrical second-order tensor and vanishes for rigid-body translations or rotations. The first variation of the strains is obtained by the directional derivative as

$$\delta \mathbf{E} = \frac{1}{2} (\delta \mathbf{F}^T \mathbf{F} + \mathbf{F}^T \delta \mathbf{F}), \quad (2.10)$$

which can also be expressed in index or matrix notation

$$\delta E_{ij} = \frac{1}{2} (\delta F_{ki} F_{kj} + F_{ki} \delta F_{kj}) \quad \text{and} \quad \delta \hat{\mathbf{E}} = \check{\mathbf{F}} \delta \hat{\mathbf{F}}, \quad (2.11)$$

respectively. Here, the matrix $\check{\mathbf{F}} \in \mathbb{R}^{6 \times 9}$ has been introduced, such that

$$\delta \hat{\mathbf{E}} = \begin{bmatrix} \delta E_{11} \\ \delta E_{22} \\ \delta E_{33} \\ 2 \delta E_{12} \\ 2 \delta E_{13} \\ 2 \delta E_{23} \end{bmatrix} = \begin{bmatrix} F_{11} & 0 & 0 & 0 & F_{21} & 0 & F_{31} & 0 & 0 \\ 0 & F_{22} & 0 & F_{12} & 0 & 0 & 0 & 0 & F_{32} \\ 0 & 0 & F_{33} & 0 & 0 & F_{13} & 0 & F_{23} & 0 \\ F_{12} & F_{21} & 0 & F_{11} & F_{22} & 0 & F_{32} & 0 & F_{31} \\ F_{13} & 0 & F_{31} & 0 & F_{23} & F_{11} & F_{33} & F_{21} & 0 \\ 0 & F_{23} & F_{32} & F_{13} & 0 & F_{12} & 0 & F_{22} & F_{33} \end{bmatrix} \begin{bmatrix} \delta F_{11} \\ \delta F_{22} \\ \delta F_{33} \\ \delta F_{12} \\ \delta F_{21} \\ \delta F_{13} \\ \delta F_{31} \\ \delta F_{23} \\ \delta F_{32} \end{bmatrix}. \quad (2.12)$$

By replacing δ with Δ in Eq. 2.10 the linearisation reads

$$\Delta \mathbf{E} = \frac{1}{2} (\Delta \mathbf{F}^T \mathbf{F} + \mathbf{F}^T \Delta \mathbf{F}). \quad (2.13)$$

Expressing Eq. 2.9 in terms of the displacement gradient \mathbf{H} as

$$\mathbf{E} = \frac{1}{2} (\mathbf{H} + \mathbf{H}^T + \mathbf{H}^T \mathbf{H}) \quad (2.14)$$

reveals, that for small deformations ($\|\mathbf{H}\| \ll 1$) the GREEN-LAGRANGE strain tensor \mathbf{E}

reduces to a linear strain measure

$$\mathbf{E} \approx \boldsymbol{\varepsilon}^{lin} = \frac{1}{2} (\mathbf{H} + \mathbf{H}^T). \quad (2.15)$$

The deformation of a body \mathcal{B} usually evokes stresses within the body. A stress is defined as the force acting per unit area. To build a work conjugate pair to the GREEN-LAGRANGE strain the second PIOLA-KIRCHHOFF stress is introduced

$$\hat{\mathbf{S}} = [S_{11} \ S_{22} \ S_{33} \ S_{12} \ S_{13} \ S_{23}]^T. \quad (2.16)$$

It is a symmetric tensor related to the reference configuration; however, it has no physical interpretation. Alternative stress measures that are commonly used are, for example, the CAUCHY stress $\boldsymbol{\sigma}$ or the first PIOLA-KIRCHHOFF stress \mathbf{P} . The two PIOLA-KIRCHHOFF stresses can be related to each other using the deformation gradient

$$\mathbf{S} = \mathbf{F}^{-1} \mathbf{P}. \quad (2.17)$$

For further stress measures and their relation to each other refer to [3, 71].

The stresses and strains are related to each other by means of constitutive laws. In the case of ST. VENANT KIRCHHOFF material, which is an isotropic linear-elastic material law, the relation between the second PIOLA-KIRCHHOFF stress and the GREEN-LAGRANGE strain reads

$$\mathbf{S} = \mathbb{C} : \mathbf{E}. \quad (2.18)$$

Where \mathbb{C} is a fourth-order tensor and is referred to as the material tangent. The second PIOLA-KIRCHHOFF stress can be expressed as the derivative of the strain energy density function Ψ with respect to the GREEN-LAGRANGE strain. Consequently, the material tangent can be written as the derivative of the second PIOLA-KIRCHHOFF with respect to the GREEN-LAGRANGE strain. The relations read

$$\mathbf{S} = \frac{\partial \Psi(\mathbf{E})}{\partial \mathbf{E}} \quad \text{and} \quad \mathbb{C} = \frac{\partial \mathbf{S}(\mathbf{E})}{\partial \mathbf{E}}. \quad (2.19)$$

The strain energy density function describes the strain energy per unit volume of a material, for ST. VENANT-KIRCHHOFF it reads

$$\Psi(\mathbf{E}) = \frac{\Lambda}{2} (\text{tr} \mathbf{E})^2 + \mu (\text{tr} \mathbf{E}^2). \quad (2.20)$$

Λ and μ denote the LAMÉ parameters, which can be related to the YOUNG'S modulus E and the POISSON'S ratio ν by

$$\Lambda = \frac{\nu E}{(1 + \nu)(1 - 2\nu)} \quad \text{and} \quad \mu = \frac{E}{2(1 + \nu)}. \quad (2.21)$$

μ is the shear modulus which can be alternatively denoted by G . From this, the material

tangent in matrix notation can be derived for the ST. VENANT KIRCHHOFF material as

$$\hat{\mathbf{C}} = \frac{E}{(1+\nu)(1-2\nu)} \begin{bmatrix} 1-\nu & \nu & \nu & 0 & 0 & 0 \\ \nu & 1-\nu & \nu & 0 & 0 & 0 \\ \nu & \nu & 1-\nu & 0 & 0 & 0 \\ 0 & 0 & 0 & \frac{1-\nu}{2} & 0 & 0 \\ 0 & 0 & 0 & 0 & \frac{1-\nu}{2} & 0 \\ 0 & 0 & 0 & 0 & 0 & \frac{1-\nu}{2} \end{bmatrix}. \quad (2.22)$$

By defining different strain energy density functions, multiple constitutive laws can be specified. The reader is referred to [18, 108, 154] for the derivation of an isotropic elastoplastic material used later in this work.

2.3 Weak form of equilibrium and linearisation

The fundamental balance principles: conservation of mass, balance of linear and angular momentum, balance of energy and the principle of entropy inequality must be satisfied at all times t for any material. In the scope of this work the balance principles are not discussed, instead reference is made to standard publications on continuum mechanics [3, 71].

The equilibrium condition evolves from the balance of linear momentum and can be written as

$$\text{Div } \mathbf{P} + \mathbf{b}_0 = \mathbf{0} \quad \text{in } \Omega \quad (2.23)$$

with respect to the reference configuration, where \mathbf{b}_0 denotes the body force and measures force per unit reference volume. The equilibrium condition is referred to as *strong form* and its derivation can be found for example in [178, 186]. It serves as the starting point for the derivation of the weak form. Note, that for the quasi-static problems considered in this work, the inertia term is neglected.

To solve the differential equation using a numerical method, the strong form has to be transformed into a weak formulation, which fulfils the the differential equation in an integral sense. To do so, the local equilibrium condition in Eq. 2.23 is multiplied with a test function $\delta \mathbf{u}$ and integrated over the domain Ω . Partial integration and application of the divergence theorem yields the weak form.

$$g(\mathbf{u}, \delta \mathbf{u}) = \delta W_{int} - \delta W_{ext} = \int_{\Omega} \delta \hat{\mathbf{E}}^T \hat{\mathbf{S}} dV - \int_{\Omega} \delta \mathbf{u}^T \mathbf{b}_0 dV - \int_{\Gamma} \delta \mathbf{u}^T \mathbf{t}_0 dA = 0 \quad (2.24)$$

In engineering context it is often referred to as principle of virtual work. For the quasi-static problems considered in the scope of this work, it states that the internal virtual work is equal to the external virtual work. The body force vector \mathbf{b}_0 refers to the reference

volume of the domain Ω and \mathbf{t}_0 denotes the traction vector acting on the boundary Γ . The DIRICHLET and NEUMANN boundary conditions are given by

$$\begin{aligned} \mathbf{u} &= \bar{\mathbf{u}} \text{ on } \Gamma_u \quad \text{and} \\ \mathbf{t}_0 &= \bar{\mathbf{t}}_0 \text{ on } \Gamma_t, \end{aligned} \tag{2.25}$$

respectively. Where the boundary Γ of the domain Ω is decomposed (component-wise) into a DIRICHLET boundary Γ_u and a NEUMANN boundary Γ_t such that

$$\Gamma = \Gamma_u \cup \Gamma_t \quad \text{with} \quad \Gamma_u \cap \Gamma_t = \emptyset. \tag{2.26}$$

When geometric and/or physical nonlinearities are taken into account, a nonlinear system of equations is obtained. The solution of this nonlinear system necessitates an iterative procedure such as the NEWTON-RAPHSON scheme. This procedure requires the linearisation of the weak form (Eq. 2.24), which is obtained by terminating the TAYLOR series expansion after the linear term, such that

$$L[g(\mathbf{v}, \delta\mathbf{v}), \Delta\mathbf{v}] := g(\mathbf{v}, \delta\mathbf{v}) + D[g(\mathbf{v}, \delta\mathbf{v})] \cdot \Delta\mathbf{v} \approx 0. \tag{2.27}$$

Assuming conservative loads, which means they are independent of the deformation and vanish during linearisation, the GÂTEAUX derivative is obtained as

$$D[g(\mathbf{u}, \delta\mathbf{u})] \cdot \Delta\mathbf{u} = \int_{\Omega} \delta\hat{\mathbf{E}}^T \hat{\mathbf{C}} \Delta\hat{\mathbf{E}} + \Delta\delta\hat{\mathbf{E}}^T \hat{\mathbf{S}} dV. \tag{2.28}$$

The first term represents the material and the second term the geometric stress contribution. The derivation of the necessary equations has been presented in an abbreviated form. For a more comprehensive explanation, the reader is once again referred to the standard literature on continuum mechanics [3, 71].

To conclude, the internal virtual work of the microscopic scale, which will be incorporated into the homogenisation process (as will be discussed in sec. 4.3), follows from Eq. 2.24 as

$$\delta W_{int}^m = \int_{\Omega} \delta\hat{\mathbf{E}}^T \hat{\mathbf{S}} dV. \tag{2.29}$$

Here, the superscript $(\cdot)^m$ is introduced, to refer to the microscopic scale.

Chapter 3

Nonlinear shell theory

Shells are thin surface-like structures, which are characterized by the fact that their thickness is significantly smaller than the dimensions in the other two spatial directions. Typically, shells can have arbitrary curvatures and can be loaded in all three spatial directions. The structural behaviour is mainly described by the membrane and bending stiffness. Due to their ability to carry high loads while demanding minimal material usage, shell structures find extensive applications across various fields. In civil engineering, shells were typically used for the construction of domes, such as the Pantheon in Rome.

In the following, the geometry of the shell is described by means of its mid-surface and a director field, which describes the thickness direction. The presented shell model is based on the works of Gruttmann and Wagner [61], Klinkel et al. [95] and Wagner and Gruttmann [174]. To prevent locking effects, a mixed formulation following the HU-WASHIZU principle is employed. However, since locking effects are not discussed in the scope of this work, the following chapter is limited to the fundamental relations of a nonlinear shell formulation.

In the context of numerical homogenisation, the introduced formulation will be employed for the analysis of the macroscopic shell structure. The principles from continuum mechanics in chap. 2 are transferred to shell kinematics. To begin with, the fundamental assumptions are briefly summarised.

3.1 Assumptions

The employed assumptions for the presented REISSNER-MINDLIN shell formulation are briefly summarised:

- the thickness is smaller than the smallest radius of the shell geometry ($h \ll R_{min}$),
- the shells are assumed to be inextensible, i.e. the director is inextensible ($|\mathbf{d}| = 1$) and therefore the normal strain vanishes ($E_{33} = 0$),

- the normal stress in thickness direction is neglected ($S_{33} = 0$),
- the rotation of the director vector is described using the EULER-RODRIGUEZ formula,
- the rotations are moderate ($|\boldsymbol{\omega}| \leq 7^\circ$),
- the strains are small ($|\mathbf{E}| \leq 5\%$),
- large deformations are admissible.

3.2 Kinematics

Shells are defined by a reference surface and a director vector in the three-dimensional Euclidean space. The basis system $\mathbf{e}_i = \{\mathbf{e}_1, \mathbf{e}_2, \mathbf{e}_3\}$ is defined for reference and current configuration. Simplifying the shell to two-dimensions allows the description of the reference surface by means of two convective coordinates ξ^α and a coordinate ζ in thickness direction. Note that greek indices α, β can take the values 1, 2, while latin indices can take the values 1, 2, 3. EINSTEIN'S summation convention is employed, which indicates summation over repeated indices. In contrast to the basis system \mathbf{e}_i , the convective coordinate system $\boldsymbol{\xi}_i = \{\xi^1, \xi^2, \zeta\}$ deforms in accordance with the shell. In the reference configuration (at time $t = 0$) the reference surface Ω with boundary Γ describes a shell occupying the shell body \mathcal{B} , refer to Fig. 3.1. Analogously, in the current configuration (at any time t) the reference surface Ω_t with boundary Γ_t describes a shell occupying the shell body \mathcal{B}_t .

In the following, the reference surface of a shell with thickness h^M will always be the mid-surface, therefore $-h^M/2 \leq \zeta \leq h^M/2$. The director vector \mathbf{D} is introduced in the reference configuration as unit normal vector to the reference surface Ω . Assuming inextensibility, the shell is unable to expand in thickness direction. Consequently, also the director vector \mathbf{d} in the current configuration is a unit vector

$$|\mathbf{D}| = |\mathbf{d}| = 1. \quad (3.1)$$

In contrast to \mathbf{D} , which is perpendicular to Ω , \mathbf{d} is not required to be perpendicular to the reference surface Ω_t . This allows for transversal shear deformation.

$$\mathbf{D} = \mathbf{N} \quad (3.2)$$

Any point of the shell can be described either by the basis \mathbf{e}_i or using the convective coordinates. Using convective coordinates, a combination of a position vector to a point in the reference surface \mathbf{X} and the director vector \mathbf{D} are used in the reference configuration, see Fig. 3.1. Thus, any point $\boldsymbol{\Phi}$ can be written as

$$\boldsymbol{\Phi}(\xi^\alpha, \zeta) = \Phi_i \mathbf{e}_i = \mathbf{X}(\xi^\alpha) + \zeta \mathbf{D}(\xi^\alpha) \quad (3.3)$$

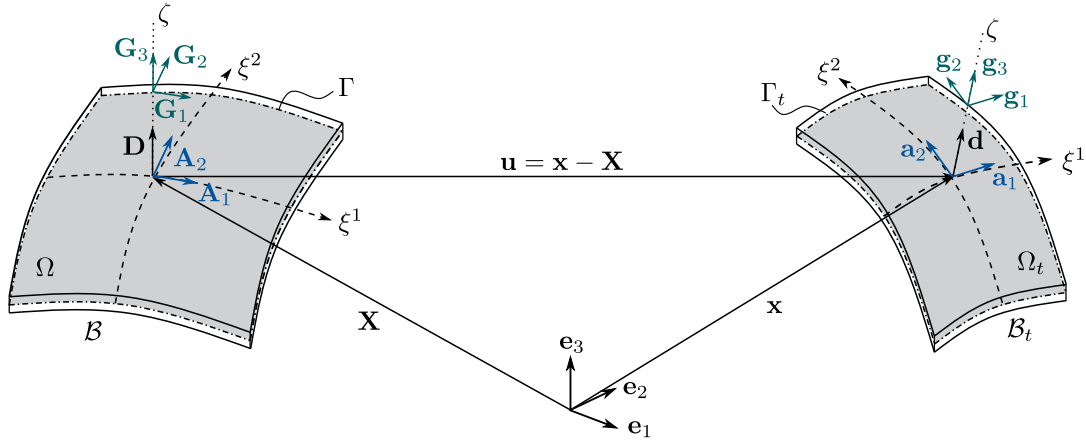


Figure 3.1: Reference and current configuration of a shell

For the current configuration a point \mathbf{x} and the director \mathbf{d} are employed. Points ϕ in the current configuration are identified in a similar way.

$$\phi(\xi^\alpha, \zeta) = \phi_i \mathbf{e}_i = \mathbf{x}(\xi^\alpha) + \zeta \mathbf{d}(\xi^\alpha) \quad (3.4)$$

From the difference of the position vectors the displacement field \mathbf{u} can be derived as

$$\phi - \Phi = \mathbf{x} - \mathbf{X} + \zeta (\mathbf{d} - \mathbf{D}) = \mathbf{u} + \zeta (\mathbf{d} - \mathbf{D}). \quad (3.5)$$

For any point of the shell, the tangents to the convective coordinate system ξ_i form a covariant basis \mathbf{G}_i and \mathbf{g}_i for the reference and current configuration, respectively.

$$\begin{aligned} \mathbf{G}_i &= \frac{\partial \Phi}{\partial \xi_i} & \mathbf{G}_\alpha &= \frac{\partial \Phi}{\partial \xi^\alpha} = \Phi_{,\alpha} = \mathbf{X}_{,\alpha} + \zeta \mathbf{D}_{,\alpha} \\ \mathbf{G}_3 &= \frac{\partial \Phi}{\partial \zeta} = \Phi_{,3} = \mathbf{D} \end{aligned} \quad (3.6)$$

$$\begin{aligned} \mathbf{g}_i &= \frac{\partial \phi}{\partial \xi^i} & \mathbf{g}_\alpha &= \frac{\partial \phi}{\partial \xi^\alpha} = \phi_{,\alpha} = \mathbf{x}_{,\alpha} + \zeta \mathbf{d}_{,\alpha} \\ \mathbf{g}_3 &= \frac{\partial \phi}{\partial \zeta} = \phi_{,3} = \mathbf{d} \end{aligned} \quad (3.7)$$

From the orthogonality conditions, the contravariant basis can be obtained.

$$\mathbf{G}_i \cdot \mathbf{G}^j = \delta_{ij} \quad \mathbf{g}_i \cdot \mathbf{g}^j = \delta_{ij} \quad (3.8)$$

Where δ_{ij} is the KRONECKER-Delta which is defined as

$$\delta_{ij} = \begin{cases} 0 & i \neq j \\ 1 & i = j \end{cases}.$$

For the reference plane, a local orthonormal basis system \mathbf{A}_i and \mathbf{a}_i can be defined. It is obtained by evaluating the covariant basis from Eqs. 3.6 and 3.7 at $\zeta = 0$.

$$\begin{aligned} \mathbf{A}_\alpha &= \mathbf{G}_\alpha(\xi^\alpha, \zeta = 0) = \mathbf{X}_{,\alpha} & \mathbf{a}_\alpha &= \mathbf{g}_\alpha(\xi^\alpha, \zeta = 0) = \mathbf{x}_{,\alpha} \\ \mathbf{A}_3 &= \mathbf{G}_3(\xi^\alpha, \zeta = 0) = \mathbf{D} & \mathbf{a}_3 &= \mathbf{g}_3(\xi^\alpha, \zeta = 0) = \mathbf{d} \end{aligned} \quad (3.9)$$

The shifter tensors $\mathbf{Z} = \mathbf{G}_i \otimes \mathbf{A}^i$ and $\bar{\mathbf{Z}} = \mathbf{g}_i \otimes \mathbf{a}^i$ are introduced to establish a relationship between the bases in the shell and the bases on the reference surface

$$\mathbf{G}_i = \mathbf{Z} \mathbf{A}_i \quad \text{and} \quad \mathbf{g}_i = \bar{\mathbf{Z}} \mathbf{a}_i. \quad (3.10)$$

Using the determinant of the shifter tensor

$$\bar{\mu} = \det \mathbf{Z} = \sqrt{\frac{G}{A}} \quad (3.11)$$

a volume integral can be written as an integral over the reference surface via

$$\begin{aligned} \int_V \square \, dV &= \int_V \square \frac{dV}{dA} \, dA = \int_\Omega \int_\zeta \square \bar{\mu} \, d\zeta \, dA \\ \text{using } \frac{dV}{dA} &= \frac{\sqrt{G} \, d\xi^1 \, d\xi^2 \, d\zeta}{\sqrt{A} \, d\xi^1 \, d\xi^2} = \bar{\mu} \, d\zeta. \end{aligned} \quad (3.12)$$

The quantities \sqrt{G} and \sqrt{A} are defined as

$$\sqrt{G} = (\mathbf{G}_1 \times \mathbf{G}_2) \cdot \mathbf{G}_3 \quad \text{and} \quad \sqrt{A} = |\mathbf{A}_1 \times \mathbf{A}_2|. \quad (3.13)$$

In the following, the factor $\bar{\mu}$ can be assumed to be $\bar{\mu} = 1$, since only plane and slightly curved shells are considered.

The director vector in the current configuration \mathbf{d} can be related to the one in the reference configuration \mathbf{D} by a rotation tensor \mathbf{R} , which describes the rotation of the director during deformation through

$$\mathbf{d} = \mathbf{R} \mathbf{D} = (\mathbf{a}_i \otimes \mathbf{A}_i) \mathbf{D}, \quad \text{where } \mathbf{R} \in \mathbb{R}^{3 \times 3}, \quad \mathbf{R}^T = \mathbf{R}^{-1} \quad \text{and} \quad \det \mathbf{R} = 1 \quad (3.14)$$

applies. Here, the orthogonal tensor \mathbf{R} is expressed using the EULER-RODRIGUEZ formula, however, other formulations are possible [23]. The EULER-RODRIGUEZ formula is frequently used, because it is free of singularities for $\omega < 2\pi$ [89]. Finite rotations with $\omega > 2\pi$ are not considered in the scope of this work.

$$\mathbf{R} = \mathbf{I} + \frac{\sin \omega}{\omega} \boldsymbol{\Omega} + \frac{1 - \cos \omega}{\omega^2} \boldsymbol{\Omega}^2, \quad \text{with } \omega = |\boldsymbol{\omega}| \quad \text{and} \quad \boldsymbol{\Omega} = \text{skew}(\boldsymbol{\omega}). \quad (3.15)$$

The rotational parameters $\boldsymbol{\omega} = [\omega_1 \ \omega_2 \ \omega_3]^T$ describe the rotations about the ξ^1, ξ^2, ζ -axis, respectively. In shell theory, ω_3 is usually omitted, however it can be beneficial for

describing thin-walled structures with non-smooth edges [67]. The skew-symmetric tensor $\boldsymbol{\Omega}$ is defined as

$$\boldsymbol{\Omega} = \text{skew}(\boldsymbol{\omega}) = \begin{bmatrix} 0 & -\omega_3 & \omega_2 \\ \omega_3 & 0 & -\omega_1 \\ -\omega_2 & \omega_1 & 0 \end{bmatrix} = [\boldsymbol{\omega}]_{\times}. \quad (3.16)$$

For moderate rotations Eq. 3.15 simplifies to $\mathbf{R} = \mathbf{I} + \boldsymbol{\Omega}$ and thus,

$$\mathbf{d} = \mathbf{R} \mathbf{D} = (\mathbf{I} + \boldsymbol{\Omega}) \mathbf{D} = \mathbf{D} + \boldsymbol{\Omega} \mathbf{D}. \quad (3.17)$$

The rotational degrees of freedom $\boldsymbol{\omega}$ can be combined with the translations \mathbf{u} from Eq. 3.5 into a vector \mathbf{v}

$$\mathbf{v} = [\mathbf{u} \quad \boldsymbol{\omega}]^T. \quad (3.18)$$

3.3 Strains

To describe the deformation of the shell, suitable strain measures must be introduced. The GREEN-LAGRANGE strain tensor from Eq. 2.9 is adapted for the shell kinematics.

$$\mathbf{E} = \frac{1}{2}(\mathbf{F}^T \mathbf{F} - \mathbf{I}) = E_{ij} \mathbf{G}^i \otimes \mathbf{G}^j \quad \text{with} \quad E_{ij} = \frac{1}{2}(\boldsymbol{\phi}_{,i} \cdot \boldsymbol{\phi}_{,j} - \boldsymbol{\Phi}_{,i} \cdot \boldsymbol{\Phi}_{,j}) \quad (3.19)$$

Using Eqs. 3.6 and 3.7 the components of E_{ij} can be written as

$$\begin{aligned} 2 E_{\alpha\beta} &= (\mathbf{x}_{,\alpha} + \zeta \mathbf{d}_{,\alpha}) \cdot (\mathbf{x}_{,\beta} + \zeta \mathbf{d}_{,\beta}) - (\mathbf{X}_{,\alpha} + \zeta \mathbf{D}_{,\alpha}) \cdot (\mathbf{X}_{,\beta} + \zeta \mathbf{D}_{,\beta}) \\ &= 2 \varepsilon_{\alpha\beta} + 2 \zeta \kappa_{\alpha\beta} + 2 \zeta^2 \rho_{\alpha\beta} \\ 2 E_{\alpha 3} &= \gamma_{\alpha} = \mathbf{x}_{,\alpha} \cdot \mathbf{d} - \mathbf{X}_{,\alpha} \cdot \mathbf{D} \\ E_{33} &= 0, \end{aligned} \quad (3.20)$$

where $\alpha, \beta = 1, 2$ applies. In Eq. 3.20 the membrane strains $\varepsilon_{\alpha\beta}$, curvatures $\kappa_{\alpha\beta}$, second-order curvatures $\rho_{\alpha\beta}$ and transverse shear strains γ_{α} are introduced. These are defined as

$$\begin{aligned} \varepsilon_{\alpha\beta} &= \frac{1}{2}(\mathbf{x}_{,\alpha} \cdot \mathbf{x}_{,\beta} - \mathbf{X}_{,\alpha} \cdot \mathbf{X}_{,\beta}), \\ \kappa_{\alpha\beta} &= \frac{1}{2}(\mathbf{x}_{,\alpha} \cdot \mathbf{d}_{,\beta} + \mathbf{x}_{,\beta} \cdot \mathbf{d}_{,\alpha} - \mathbf{X}_{,\alpha} \cdot \mathbf{D}_{,\beta} - \mathbf{X}_{,\beta} \cdot \mathbf{D}_{,\alpha}), \\ \rho_{\alpha\beta} &= \frac{1}{2}(\mathbf{d}_{,\alpha} \cdot \mathbf{d}_{,\beta} - \mathbf{D}_{,\alpha} \cdot \mathbf{D}_{,\beta}), \\ \gamma_{\alpha} &= \mathbf{x}_{,\alpha} \cdot \mathbf{d} - \mathbf{X}_{,\alpha} \cdot \mathbf{D}. \end{aligned} \quad (3.21)$$

For thin shells the second-order curvatures $\rho_{\alpha\beta}$ can be neglected. The relevant shell strains can be written in VOIGT notation as

$$\boldsymbol{\varepsilon} = [\varepsilon_{11} \quad \varepsilon_{22} \quad 2 \varepsilon_{12} \quad \kappa_{11} \quad \kappa_{22} \quad 2 \kappa_{12} \quad \gamma_1 \quad \gamma_2]^T. \quad (3.22)$$

To summarise, the shell strains $\boldsymbol{\varepsilon}$ can be related to the GREEN-LAGRANGE strains \mathbf{E} via the assembly matrix $\check{\mathbf{A}}$, such that

$$\hat{\mathbf{E}} = \begin{bmatrix} E_{11} \\ E_{22} \\ 2E_{12} \\ 2E_{13} \\ 2E_{23} \end{bmatrix} = \begin{bmatrix} 1 & 0 & 0 & \zeta & 0 & 0 & 0 & 0 \\ 0 & 1 & 0 & 0 & \zeta & 0 & 0 & 0 \\ 0 & 0 & 1 & 0 & 0 & \zeta & 0 & 0 \\ 0 & 0 & 0 & 0 & 0 & 0 & 1 & 0 \\ 0 & 0 & 0 & 0 & 0 & 0 & 0 & 1 \end{bmatrix} \begin{bmatrix} \varepsilon_{11} \\ \varepsilon_{22} \\ 2\varepsilon_{12} \\ \kappa_{11} \\ \kappa_{22} \\ 2\kappa_{12} \\ \gamma_1 \\ \gamma_2 \end{bmatrix} = \check{\mathbf{A}} \boldsymbol{\varepsilon}. \quad (3.23)$$

Because no normal strain in thickness direction occurs (i.e. $E_{33} = 0$), it is neglected in $\hat{\mathbf{E}}$. Furthermore,

$$\delta \hat{\mathbf{E}} = \check{\mathbf{A}} \delta \boldsymbol{\varepsilon} \quad (3.24)$$

applies. Note, that the components of $\hat{\mathbf{E}}$ and $\delta \hat{\mathbf{E}}$ refer to the local, convective coordinate system, see Eq. 3.19.

3.4 Stresses and stress resultants

One key assumption of REISSNER-MINDLIN shell kinematics is that no normal stresses in thickness direction occur, i.e. $S_{33} = 0$. Therefore, similar to $\hat{\mathbf{E}}$, it is neglected in the definition of the second PIOLA-KIRCHHOFF stress $\hat{\mathbf{S}}$.

$$\hat{\mathbf{S}} = [S_{11} \quad S_{22} \quad S_{12} \quad S_{13} \quad S_{23}]^T \quad (3.25)$$

The internal work is defined as the scalar product of the work conjugate pair \mathbf{S} and \mathbf{E} . Inserting Eqs. 3.12 and 3.23 into the virtual internal work from Eq. 2.24 gives:

$$\delta W_{int} = \int_V \mathbf{S} : \delta \mathbf{E} dV = \int_{\Omega} \int_{\zeta} \delta \hat{\mathbf{E}}^T \hat{\mathbf{S}} \bar{\mu} d\zeta dA = \int_{\Omega} \delta \boldsymbol{\varepsilon}^T \int_{\zeta} \check{\mathbf{A}}^T \hat{\mathbf{S}} \bar{\mu} d\zeta dA = \int_{\Omega} \delta \boldsymbol{\varepsilon}^T \boldsymbol{\sigma} dA. \quad (3.26)$$

Here, the vector of stress resultants is introduced

$$\boldsymbol{\sigma} = \int_{\zeta} \check{\mathbf{A}}^T \hat{\mathbf{S}} \bar{\mu} d\zeta. \quad (3.27)$$

It contains the membrane forces $n_{\alpha\beta} = n_{\beta\alpha}$, bending moments $m_{\alpha\beta} = m_{\beta\alpha}$ and shear forces q_{α} .

$$\boldsymbol{\sigma} = [n_{11} \quad n_{22} \quad n_{12} \quad m_{11} \quad m_{22} \quad m_{12} \quad q_1 \quad q_2]^T \quad (3.28)$$

Note, that while $\boldsymbol{\sigma}$ was initially introduced as CAUCHY stress in sec. 2.2, it subsequently denotes the stress resultants of the shell.

3.5 Constitutive relation

As discussed in sec. 2.2, the second PIOLA-KIRCHHOFF stress can be related to the GREEN-LAGRANGE strain using the material tangent \mathbb{C} . For ST. VENANT-KIRCHHOFF material the constitutive law from Eq. 2.18 reads

$$\hat{\mathbf{S}} = \hat{\mathbb{C}} \hat{\mathbf{E}} = \hat{\mathbb{C}} \check{\mathbf{A}} \boldsymbol{\varepsilon} \quad (3.29)$$

in matrix notation. For the shell formulation, it has to be accounted for $S_{33} = 0$ and $E_{33} = 0$ in the constitutive relation. Therefore, the elasticity matrix $\hat{\mathbb{C}}$ from Eq. 2.22 for ST. VENANT-KIRCHHOFF material can be rewritten as

$$\hat{\mathbb{C}} = \frac{E}{1-\nu^2} \left[\begin{array}{ccc|cc} 1 & \nu & 0 & 0 & 0 \\ \nu & 1 & 0 & 0 & 0 \\ 0 & 0 & \frac{1-\nu}{2} & 0 & 0 \\ \hline 0 & 0 & 0 & \frac{1-\nu}{2} & 0 \\ 0 & 0 & 0 & 0 & \frac{1-\nu}{2} \end{array} \right] = \left[\begin{array}{c|c} \hat{\mathbb{C}}_m^{(3 \times 3)} & \mathbf{0} \\ \hline \mathbf{0} & \hat{\mathbb{C}}_s^{(2 \times 2)} \end{array} \right]. \quad (3.30)$$

Inserting Eq. 3.29 into Eq. 3.27, the constitutive relation between the stress resultants of the shell and the shell strains can be derived

$$\boldsymbol{\sigma} = \int_{\zeta} \check{\mathbf{A}}^T \hat{\mathbf{S}} \bar{\mu} d\zeta = \int_{\zeta} \check{\mathbf{A}}^T \hat{\mathbb{C}} \check{\mathbf{A}} \bar{\mu} d\zeta \boldsymbol{\varepsilon} = \hat{\mathbb{D}} \boldsymbol{\varepsilon}. \quad (3.31)$$

$\hat{\mathbb{D}}$ denotes the material matrix of the shell, it is symmetric ($\hat{\mathbb{D}} = \hat{\mathbb{D}}^T$), and can be split in membrane, bending and shear sub-matrices $\hat{\mathbb{D}}_m^{(3 \times 3)}$, $\hat{\mathbb{D}}_b^{(3 \times 3)}$ and $\hat{\mathbb{D}}_s^{(2 \times 2)}$, respectively.

$$\hat{\mathbb{D}} = \int_{\zeta} \check{\mathbf{A}}^T \hat{\mathbb{C}} \check{\mathbf{A}} \bar{\mu} d\zeta = \int_{\zeta} \left[\begin{array}{ccc} \hat{\mathbb{C}}_m & \zeta \hat{\mathbb{C}}_m & \mathbf{0} \\ \zeta \hat{\mathbb{C}}_m & \zeta^2 \hat{\mathbb{C}}_m & \mathbf{0} \\ \mathbf{0} & \mathbf{0} & \hat{\mathbb{C}}_s \end{array} \right] \bar{\mu} d\zeta = \left[\begin{array}{ccc} \hat{\mathbb{D}}_m & \hat{\mathbb{D}}_{mb} & \mathbf{0} \\ \hat{\mathbb{D}}_{mb}^T & \hat{\mathbb{D}}_b & \mathbf{0} \\ \mathbf{0} & \mathbf{0} & \hat{\mathbb{D}}_s \end{array} \right] \quad (3.32)$$

The coupling term between the membrane and bending components $\hat{\mathbb{D}}_{mb}$ is non-zero if there is an eccentricity between the mid-surface and the reference surface. This is caused by the fact that for curved shells $\bar{\mu} \neq \text{const.}$ and therefore

$$\hat{\mathbb{D}}_{mb} = \int_{\zeta} \zeta \hat{\mathbb{C}}_m \bar{\mu}(\zeta) d\zeta \neq 0 \quad (3.33)$$

For homogeneous shells, when the mid-surface is chosen as reference surface ($-h^M/2 \leq \zeta \leq h^M/2$) and $\bar{\mu} = 1$ holds, the sub-matrices can be written as

$$\hat{\mathbb{D}}_m = h^M \hat{\mathbb{C}}_m, \quad \hat{\mathbb{D}}_b = \frac{(h^M)^3}{12} \hat{\mathbb{C}}_m \quad \text{and} \quad \hat{\mathbb{D}}_s = \kappa h^M \hat{\mathbb{C}}_s. \quad (3.34)$$

κ denotes the shear correction factor, which is usually assumed to be $\kappa = 5/6$ for rectangular, homogeneous cross-sections. It reduces the shear stiffness, which is overestimated due to the assumption of plane cross-sections remaining plane.

3.6 Weak form of equilibrium and linearisation

The weak form of equilibrium is defined as the difference between the internal and external virtual work, refer to Eq. 2.24. For REISSNER-MINDLIN shells the definition of the internal virtual work (Eq. 3.26) is substituted, such that

$$g(\mathbf{v}, \delta\mathbf{v}) = \delta W_{int} - \delta W_{ext} = \int_{\Omega} \delta\boldsymbol{\varepsilon}^T \boldsymbol{\sigma} \, dA - \int_{\Omega} \delta\mathbf{v}^T \bar{\mathbf{p}} \, dA - \int_{\Gamma} \delta\mathbf{v}^T \bar{\mathbf{f}} \, dS = 0. \quad (3.35)$$

Note, that $\delta\mathbf{u}$ from Eq. 2.24 has been replaced by $\delta\mathbf{v}$, because the degrees of freedom of the shell are defined according to Eq. 3.18. Furthermore, the surface loads $\bar{\mathbf{p}}$ and boundary loads $\bar{\mathbf{f}}$ acting on the reference surface of the shell are introduced instead of the body forces \mathbf{b}_0 and the traction vector \mathbf{t}_0 .

$$\begin{aligned} \bar{\mathbf{p}} &= [p_1 \quad p_2 \quad p_3 \quad 0 \quad 0]^T \\ \bar{\mathbf{f}} &= [f_1 \quad f_2 \quad f_3 \quad m_1 \quad m_2]^T \end{aligned} \quad (3.36)$$

The variation of the shell strains follows from Eq. 3.21 as

$$\delta\boldsymbol{\varepsilon} = \begin{bmatrix} \delta\varepsilon_{11} \\ \delta\varepsilon_{22} \\ 2\delta\varepsilon_{12} \\ \delta\kappa_{11} \\ \delta\kappa_{22} \\ 2\delta\kappa_{12} \\ \delta\gamma_1 \\ \delta\gamma_2 \end{bmatrix} = \begin{bmatrix} \delta\mathbf{x}_{,1} \cdot \mathbf{x}_{,1} \\ \delta\mathbf{x}_{,2} \cdot \mathbf{x}_{,2} \\ \delta\mathbf{x}_{,1} \cdot \mathbf{x}_{,2} + \delta\mathbf{x}_{,2} \cdot \mathbf{x}_{,1} \\ \delta\mathbf{x}_{,1} \cdot \mathbf{d}_{,1} + \delta\mathbf{d}_{,1} \cdot \mathbf{x}_{,1} \\ \delta\mathbf{x}_{,2} \cdot \mathbf{d}_{,2} + \delta\mathbf{d}_{,2} \cdot \mathbf{x}_{,2} \\ \delta\mathbf{x}_{,1} \cdot \mathbf{d}_{,2} + \delta\mathbf{x}_{,2} \cdot \mathbf{d}_{,1} + \delta\mathbf{d}_{,1} \cdot \mathbf{x}_{,2} + \delta\mathbf{d}_{,2} \cdot \mathbf{x}_{,1} \\ \delta\mathbf{x}_{,1} \cdot \mathbf{d} + \delta\mathbf{d} \cdot \mathbf{x}_{,1} \\ \delta\mathbf{x}_{,2} \cdot \mathbf{d} + \delta\mathbf{d} \cdot \mathbf{x}_{,2} \end{bmatrix}. \quad (3.37)$$

The linearisation of the weak form is needed for the iterative solution procedure within the finite element framework, refer to Eq. 2.27. Again, assuming conservative loads, the GÂTEAUX derivative for the shell formulation is obtained as

$$D[g(\mathbf{v}, \delta\mathbf{v})] \cdot \Delta\mathbf{v} = \int_{\Omega} \left(\delta\boldsymbol{\varepsilon}^T \hat{\mathbb{D}} \Delta\boldsymbol{\varepsilon} + \Delta\delta\boldsymbol{\varepsilon}^T \boldsymbol{\sigma} \right) \, dA. \quad (3.38)$$

The linearisation $\Delta\boldsymbol{\varepsilon}$ of the shell strains $\boldsymbol{\varepsilon}$ is obtained analogously to $\delta\boldsymbol{\varepsilon}$. The linearisation $\Delta\delta\boldsymbol{\varepsilon}$ of the virtual shell strains $\delta\boldsymbol{\varepsilon}$ can be found e.g. in [174] and reads

$$\Delta\delta\boldsymbol{\varepsilon} = \begin{bmatrix} \delta\mathbf{u}_{,1} \cdot \Delta\mathbf{u}_{,1} \\ \delta\mathbf{u}_{,2} \cdot \Delta\mathbf{u}_{,2} \\ \delta\mathbf{u}_{,1} \cdot \Delta\mathbf{u}_{,2} + \delta\mathbf{u}_{,2} \cdot \Delta\mathbf{u}_{,1} \\ \delta\mathbf{u}_{,1} \cdot \Delta\mathbf{d}_{,1} + \delta\mathbf{d}_{,1} \cdot \Delta\mathbf{u}_{,1} \\ \delta\mathbf{u}_{,2} \cdot \Delta\mathbf{d}_{,2} + \delta\mathbf{d}_{,2} \cdot \Delta\mathbf{u}_{,2} \\ \delta\mathbf{u}_{,1} \cdot \Delta\mathbf{d}_{,2} + \delta\mathbf{u}_{,2} \cdot \Delta\mathbf{d}_{,1} + \delta\mathbf{d}_{,1} \cdot \Delta\mathbf{u}_{,2} + \delta\mathbf{d}_{,2} \cdot \Delta\mathbf{u}_{,1} \\ \Delta\mathbf{d} \cdot \delta\mathbf{u}_{,1} + \Delta\mathbf{u}_{,1} \cdot \delta\mathbf{d} \\ \Delta\mathbf{d} \cdot \delta\mathbf{u}_{,2} + \Delta\mathbf{u}_{,2} \cdot \delta\mathbf{d} \end{bmatrix}. \quad (3.39)$$

To conclude, the internal virtual work of the macroscopic scale, which will be incorporated into the homogenisation process, follows from Eq. 3.35 as

$$\delta W_{int}^M = \int_{\Omega} \delta\boldsymbol{\varepsilon}^T \boldsymbol{\sigma} \, dA. \quad (3.40)$$

The superscript $(\cdot)^M$ is introduced, to denote the macroscopic internal virtual work.

Chapter 4

Fundamentals of computational homogenisation

In the following, the basic principles of computational homogenisation are outlined. A first-order homogenisation approach is employed. The energetic consistency between the scales is ensured by the HILL-MANDEL condition, which will be presented.

4.1 Basic principles

Materials are often heterogeneous at smaller scales, even though they appear to be homogeneous on a macroscopic scale. These heterogeneities can be cracks, pores, or phases of different materials. Some of these heterogeneities become visible on close examination of the material, while others only appear when examined under a microscope. In fact, any

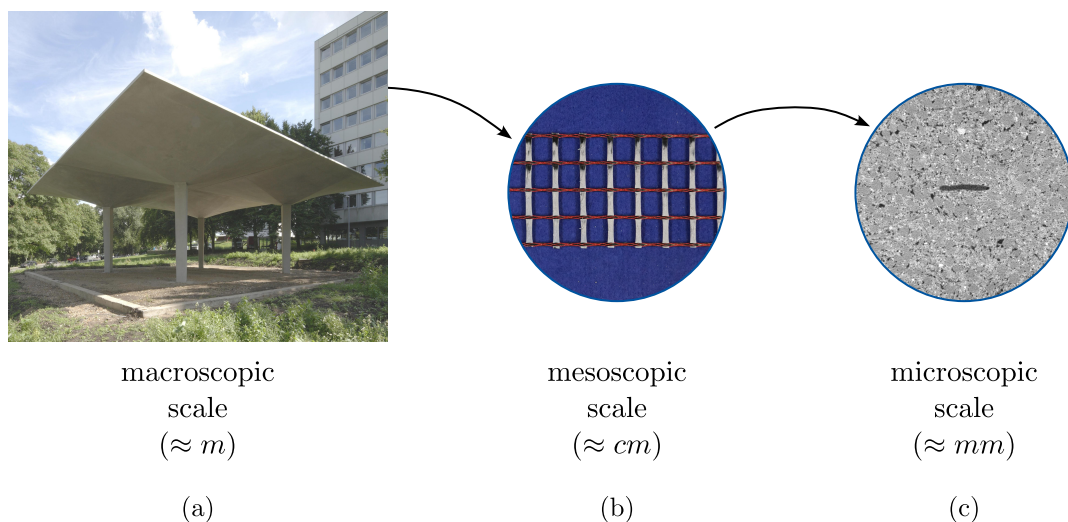


Figure 4.1: Visualization of the scale separation principle using a textile-reinforced shell structure ((a) - © IMB, RWTH Aachen; (b) - © ibac, RWTH Aachen; (c) - © F. Wagner, TU Dresden)

material can be analysed at multiple different length scales, and each defect influences the overall behaviour of the material.

A well-known example from civil engineering is a reinforced concrete specimen. From a distance, a homogeneous structural element is observed; however, upon closer investigation, the reinforcement and concrete of the component become obvious. Further magnification reveals the constituents of the concrete, such as the cement matrix and aggregate. This process can be repeated until the material is viewed at the atomic level.

However, it is not feasible to consider multiple defects at different length scales when analysing a specimen. Therefore, different length scales can be introduced. Classically, the macroscopic scale is considered to be homogeneous, while the microscopic scale contains detailed information about the heterogeneous material. The choice of macroscopic and microscopic length scale depends on the problem investigated.

Figure 4.1 depicts the construction phase of the T3-Pavilion at RWTH Aachen University. Its roof is a textile-reinforced shell structure, which is treated as homogeneous and serves as the macroscopic scale in this context. Within this shell, the textile reinforcement has dimensions on the order of centimetres, classifying it as a mesoscopic scale. Upon closer examination, the concrete constituents become visible on an even smaller length scale, on the order of millimetres, which represents the microscopic scale.

Homogenisation is the determination of averaged material properties for the macroscopic scale on the basis of the microscopic scale. Today, numerical homogenisation methods are widely used. One of them is the first-order computational homogenisation, which is a coupled multiscale method. This method requires the definition of a volume element that is representative of the microscopic material composition. Hence, this volume element is referred to as representative volume element (RVE). To each macroscopic point an RVE is assigned, which can be used to determine the local material response.

In first-order computational homogenisation, the macroscopic and the microscopic scale can be analysed using the finite element method (FEM); then, the method is often referred to as FE^2 [52].

In principle, to analyse a structure using FE^2 the following steps must be taken:

1. Defining an RVE,
2. Applying the macroscopic strains or stresses to the RVE through appropriate boundary conditions,
3. Solving a boundary value problem on the microscopic scale with any appropriate numerical method,
4. Calculating the macroscopic output quantities, i.e. the effective material properties and the corresponding stress or strain state, according to the selected input state.

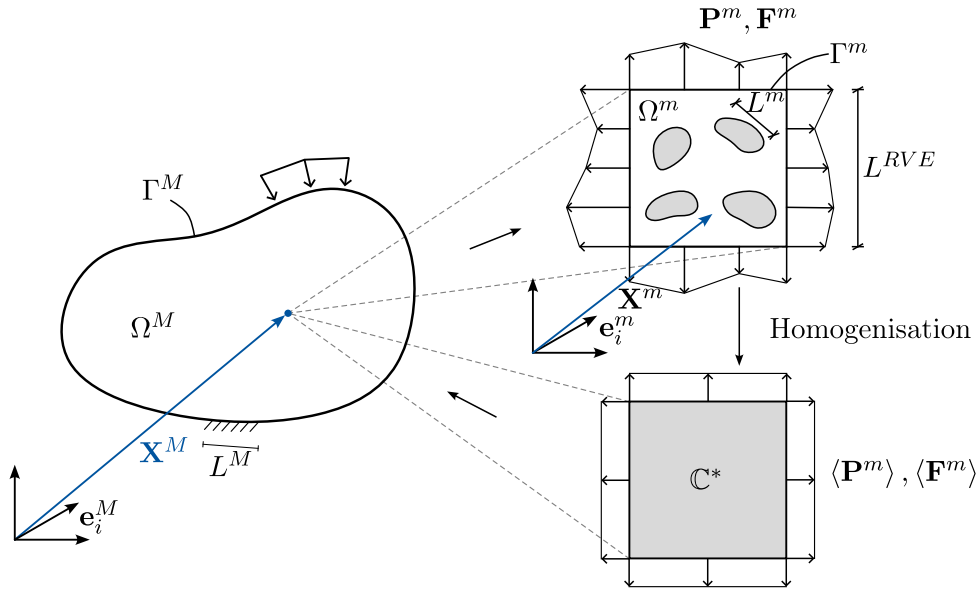


Figure 4.2: Homogenisation principle and characteristic length scales.

Applying the macroscopic values to the RVE is a critical step. Today, the HILL-MANDEL [70] condition is the most widely known homogenisation condition, whereas the approaches of Voigt [168] and Reuss [142] serve as upper and lower bounds for the homogenised stiffness components. More recently, homogenisation procedures based on the IRVING-KIRKWOOD theory [78] have been proposed [113, 125].

4.2 Representative volume element (RVE)

Magnifying any point \mathbf{X}^M on the macroscale, the microstructure with its heterogeneities becomes visible (Fig. 4.2). Determining the effective material behaviour of a homogeneous body Ω^M with boundary Γ^M requires the analysis of the magnified section. This section captures the heterogeneities on the microscopic scale and describes their material properties as well as their geometry. Thus, in contrast to analytical approaches, the structural properties of the microscale are considered in the RVE. In the scope of a homogenisation process, a microscopic section must fulfil two conditions to function as an RVE [45, 84]:

1. *Representativeness:* The size of the RVE must be chosen large enough to ensure that all relevant heterogeneities are taken into account. The average of a microscopic parameter of the RVE should be equal to the average of the microscopic parameter of the whole microscopic structure. Therefore, the characteristic length of the RVE L^{RVE} must be significantly larger than the microscopic length scale L^m .
2. *Scale separation:* The characteristic length of the macroscopic scale (L^M) must be significantly larger than the length of the RVE (L^{RVE}). This condition allows a pointwise link between the two scales.

These two conditions indicate that not just any size can be chosen for the RVE. In summary, the requirements on the size of the RVE size can be defined as

$$L^M \gg L^{RVE} \gg L^m, \quad (4.1)$$

and define an upper and a lower boundary. Finding the optimal size for an RVE is a rather complex task and can affect the quality of the solution significantly. Many publications are concerned with the determination of an appropriate RVE, see for example Gitman et al. [57] and Saeb et al. [147].

It has to be noted, that the RVE loses its representativeness for material softening or failure [57], which can be related to localisation phenomena within the RVE. Various methods to incorporate damage into a multiscale framework have been proposed in the literature [13, 105, 128]. However, this work predominantly concentrates on investigating the pre-failure behaviour.

For the definition of an RVE it is important to distinguish between global and local periodicity. Most homogenisation approaches assume global periodicity, i.e. that the entire macroscopic structure consists of the same repeating material. For global periodicity, the *unit cell* is introduced, which is a special case of a representative volume element. It is defined as the smallest repeating part of the microstructure. Therefore, the microscopic area can be divided into identical unit cells, not only identical in an averaged sense. In contrast, local periodicity assumes that the microscopic structure is repeated in the immediate vicinity of each macroscopic point. Overall, however, different microscopic structures are possible.

Not only can the material distribution vary for different points on the macroscopic scale, also the loading history varies. To incorporate this, an independent RVE is considered for each macroscopic point of evaluation, which is usually an integration point in the context of FEM.

Once a suitable RVE has been determined, the macroscopic and microscopic scale can be analysed. The equilibrium conditions for both scales are given in Tab. 4.1. \square^M denotes a macroscopic and \square^m a microscopic value, respectively. The equilibrium condition results from the balance of momentum and have been introduced in sec. 2.3. The boundary conditions needed for the solution are additionally given in Tab. 4.1. They prescribe tractions \mathbf{t}_0 on the boundary Γ_t and displacements \mathbf{u} on Γ_u .

From Tab. 4.1 it becomes obvious, that the strong form to be solved is the same on both scales and differs only in the term $\bar{\mathbf{b}}_0^M$, which denotes the macroscopic body forces. This indicates, that there are no external forces acting on the microscopic scale, as it is only used to define the effective material properties. Any external forces are applied at the macroscopic scale.

The boundary value problem on the microscopic scale is treated as quasi-static well-posed problem, which implies that coercivity is always fulfilled. In a discrete setting this means, that the stiffness matrix is positive definite. For nonlinear problems geometric instabilities

Table 4.1: Definition of boundary value problems on macroscopic and microscopic scale

macroscopic scale	microscopic scale
$\text{Div } \mathbf{P}^M + \mathbf{b}_0^M = \mathbf{0} \quad \text{in } \Omega^M$ $\mathbf{t}_0^M = \bar{\mathbf{t}}_0^M \quad \text{on } \Gamma_t^M$ $\mathbf{u}^M = \bar{\mathbf{u}}^M \quad \text{on } \Gamma_u^M$	$\text{Div } \mathbf{P}^m = \mathbf{0} \quad \text{in } \Omega^m$ $\mathbf{t}_0^m = \bar{\mathbf{t}}_0^m \quad \text{on } \Gamma_t^m$ $\mathbf{u}^m = \bar{\mathbf{u}}^m \quad \text{on } \Gamma_u^m$

should be excluded on the fine scale to ensure coercivity.

The macroscopic quantities can be related to their microscopic counterpart. The following definitions comply with the derivation in Klarmann [89] for the reference configuration. The derivation regarding the current configuration can be found, for example, in Gross and Seelig [59]. The macroscopic PIOLA-KIRCHHOFF stress \mathbf{P} and the deformation gradient \mathbf{F} can be defined at each point as the volume average of their microscopic counterparts

$$\mathbf{P}^M = \langle \mathbf{P}^m \rangle = \frac{1}{V^m} \int_{\Omega^m} \mathbf{P}^m \, dV \quad \text{and} \quad \mathbf{F}^M = \langle \mathbf{F}^m \rangle = \frac{1}{V^m} \int_{\Omega^m} \mathbf{F}^m \, dV. \quad (4.2)$$

The operator $\langle \square \rangle$ is introduced as

$$\langle \square \rangle = \frac{1}{V^m} \int_{\Omega^m} \square \, dV \quad \text{with} \quad V^m = \int_{\Omega^m} dV. \quad (4.3)$$

Since no body forces act on the microscopic scale, $\text{Div } \mathbf{P}^m = P_{ik,k}^m = \mathbf{0}$ applies, see Tab. 4.1. Further, $\text{Grad } \mathbf{X}^m = X_{j,k}^m = \delta_{jk}$ is used, such that

$$P_{ij}^m = X_{j,k}^m P_{ik}^m + X_j \underbrace{P_{ik,k}^m}_{=0} = (X_j^m P_{ik}^m)_{,k}. \quad (4.4)$$

Inserting Eq. 4.4 and transforming the volume integrals into surface integrals over the RVE boundary Eq. 4.2 can be written as

$$\begin{aligned} \mathbf{P}^M &= \frac{1}{V^m} \int_{\Omega^m} (X_j^m P_{ik}^m)_{,k} \, dV = \frac{1}{V^m} \int_{\Gamma^m} X_j^m P_{ik}^m N_k^m \, dA = \frac{1}{V^m} \int_{\Gamma^m} \mathbf{t}_0^m \otimes \mathbf{X}^m \, dA, \\ \mathbf{F}^M &= \frac{1}{V^m} \int_{\Omega^m} \text{Grad } \mathbf{x}^m \, dV = \frac{1}{V^m} \int_{\Gamma^m} \mathbf{x}^m \otimes \mathbf{N} \, dA. \end{aligned} \quad (4.5)$$

\mathbf{N} denotes the outward pointing normal vector on the RVE boundary Γ^m . In Gross and Seelig [59] it is shown that the application of the divergence theorem, which has been used to transform the volume integral into a surface integral, is also valid for RVEs with inhomogeneities, although the differentiability in the whole domain Ω^m is not given. The displacement field is required to be continuous, i.e. the material phases are perfectly bonded. Equations 4.5 show, that the macroscopic first PIOLA-KIRCHHOFF stress and

the deformation gradient can be applied directly on the RVE boundaries and, in turn, that the averaged microscopic values can be obtained from the RVE boundaries.

4.3 HILL-MANDEL condition

To relate the averaged microstructural fields to the macroscopic ones, the HILL-MANDEL condition [70] can be used, which is one of the most commonly used homogenisation approaches. It requires energetic equivalence between the two scales and can be written as [147]

$$\underbrace{\langle \mathbf{P}^m : \delta \mathbf{F}^m \rangle}_{\delta W_{int}^m} - \underbrace{\langle \mathbf{P}^m \rangle : \langle \delta \mathbf{F}^m \rangle}_{\delta W_{int}^M} = 0. \quad (4.6)$$

It states, that the averaged internal virtual work on the microscopic scale δW_{int}^m is equal to the internal virtual work of a point on the macroscopic scale δW_{int}^M . Fluctuations about the mean values of the microscopic fields, denoted by $(\tilde{\square})$, can be introduced as

$$\tilde{\mathbf{P}}^m + \langle \mathbf{P}^m \rangle = \mathbf{P}^m \quad \text{and} \quad \tilde{\mathbf{F}}^m + \langle \mathbf{F}^m \rangle = \mathbf{F}^m. \quad (4.7)$$

Inserting these into Eq. 4.6 yields

$$\langle \tilde{\mathbf{P}}^m : \delta \tilde{\mathbf{F}}^m \rangle = 0, \quad (4.8)$$

which shows, that the fluctuations of the microscopic fields do not affect the macroscopic fields. Therefore, the fluctuating fields on a heterogeneous RVE are equivalent to the averaged fields acting on a homogeneous RVE. This is also illustrated in Fig. 4.2. However, this is only valid if the RVE is large enough and satisfies the representativeness condition from sec. 4.2.

In the homogenisation process the macroscopic strain of a specific point, e.g. the deformation gradient \mathbf{F}^M , must be applied to the RVE. Following VOIGT [168] a constant strain $\mathbf{F}^M = \mathbf{F}^0$ is assumed for the whole RVE, such that

$$\mathbf{x}^m = \mathbf{F}^0 \mathbf{X}^m \quad \text{in} \quad \Omega^m \quad (4.9)$$

applies, while REUSS [142] assumes a constant stress $\mathbf{P}^m = \mathbf{P}^M = \mathbf{P}^0$ in the whole domain

$$\mathbf{t}_0^m = \mathbf{P}^0 \mathbf{N} \quad \text{in} \quad \Omega^m. \quad (4.10)$$

However, these approaches give only rough estimates of the effective material behaviour [99]. Classically, in computational homogenisation three different types of boundary conditions can be defined, which are used to apply the macroscopic fields on the RVE boundaries. These can be obtained by rewriting the HILL-MANDEL condition using the

divergence theorem as

$$\langle \mathbf{P}^m : \delta \mathbf{F}^m \rangle - \langle \mathbf{P}^m \rangle : \langle \delta \mathbf{F}^m \rangle = \frac{1}{V^m} \int_{\Gamma^m} (\delta \mathbf{x}^m - \delta \mathbf{F}^M \mathbf{X}^m) \cdot (\mathbf{t}_0^m - \mathbf{P}^M \mathbf{N}) \, dA = 0. \quad (4.11)$$

The derivation can be found, for example, in [89]. The boundary conditions for the lateral surfaces of the RVE follow as:

1. linear displacement boundary conditions

$$\mathbf{x}^m = \mathbf{F}^M \mathbf{X}^m \quad \text{on} \quad \Gamma^m, \quad (4.12)$$

2. constant traction boundary conditions

$$\mathbf{t}_0^m = \mathbf{P}^M \mathbf{N} \quad \text{on} \quad \Gamma^m, \quad (4.13)$$

3. periodic boundary conditions

$$\begin{aligned} \mathbf{x}^{m^+} - \mathbf{x}^{m^-} &= \mathbf{F}^M (\mathbf{X}^{m^+} - \mathbf{X}^{m^-}) & \text{and} \\ \mathbf{t}^{m^+} &= -\mathbf{t}^{m^-} & \text{on} \quad \Gamma^m. \end{aligned} \quad (4.14)$$

To impose periodic boundary conditions, the RVE must be symmetric, so that the boundary can be split into opposing boundaries $\Gamma^m = \Gamma^{m^+} \cup \Gamma^{m^-}$. Then $\mathbf{N}^+ = -\mathbf{N}^-$ denote equal and opposite unit normal vectors to the RVE boundary for two corresponding points $\mathbf{x}^{m^+} \in \Gamma^{m^+}$ and $\mathbf{x}^{m^-} \in \Gamma^{m^-}$. All proposed boundary conditions fulfil the HILL-MANDEL condition, which is shown in Appendix A.

The implementation of traction boundary conditions is not straightforward [99]. Here, they are included for the sake of completeness only.

In order to employ the homogenisation approach for shell structures, in the following it has to be discussed how the macroscopic shell strains are transferred to the microscopic RVE. Furthermore, it will be shown that the internal virtual work derived for both scales in chapters 2 and 3 fulfil the HILL-MANDEL condition. Additionally, the peculiarities arising from the coupling of a macroscopic shell formulation with a continuum formulation on the mesoscopic scale are treated.

Chapter 5

Homogenisation of shear deformable shells

In the following chapter, the principles of homogenisation which were discussed in chap. 4 are applied to shear deformable shell structures on the macroscale. The schematic procedure is shown in Fig. 5.1. The shell strains $\boldsymbol{\varepsilon}$ are applied to the representative volume element (RVE). The boundary value problem (BVP) is solved using scaled boundary isogeometric analysis. From this, the stress resultants $\boldsymbol{\sigma}$ and the homogenised material tensor of the shell \mathbb{D} are obtained for every macroscopic integration point (denoted by 'GP').

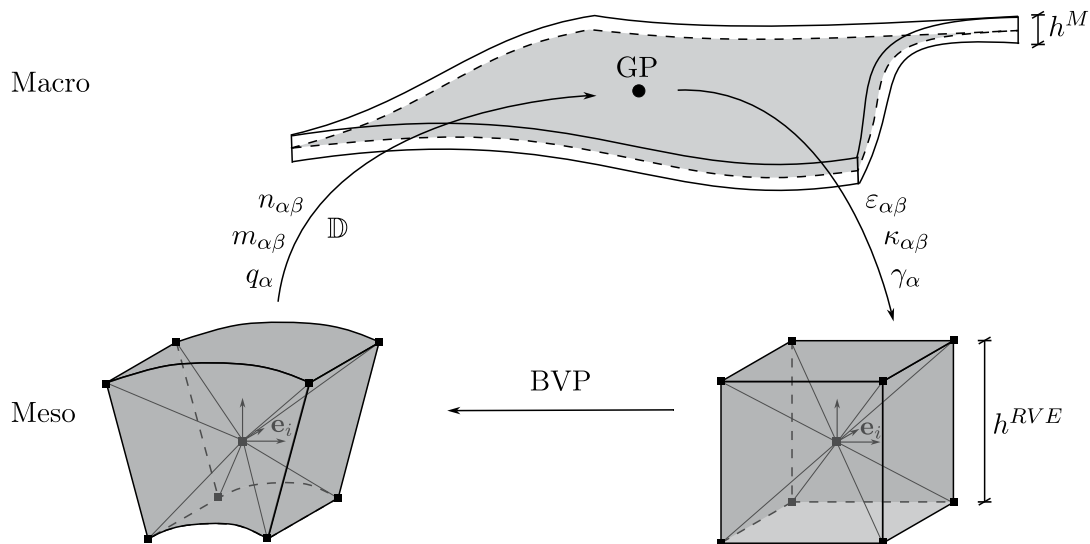


Figure 5.1: Schematic procedure of homogenisation for shells

One of the main characteristic features of homogenisation for shell structures is, that the RVE thickness represents the full shell thickness ($h^M = h^{RVE}$). Therefore, in the following the term *mesoscopic* is used instead of *microscopic*. However, the superscript \square^m is kept.

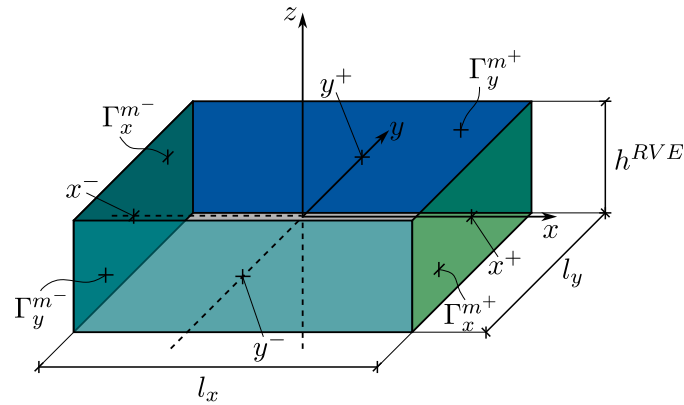


Figure 5.2: RVE with dimensions $l_x \times l_y \times h^{RVE}$ and lateral boundaries Γ^m

In the following, further distinctive properties resulting from the coupling of a structural element with a solid element formulation will be discussed. The presented approach is based on the work of Gruttmann and Wagner [62] who proposed a first-order homogenisation framework for Reissner-Mindlin shells. The introduced additional constraints are based on the previous works of Klarmann [89] for beam structures.

First, the necessary relations to prescribe the shell strains on the RVE are presented. It is then shown that the HILL-MANDEL condition, which was introduced in sec. 4.3 for continua, is satisfied for shell homogenisation. In the following, only displacement and periodic boundary conditions are discussed, since a deformation-driven homogenisation approach is chosen. Finally, the peculiarities arising from the coupling of a shell formulation on the macroscopic scale to a continuum formulation on the mesoscopic scale are discussed, and possible solutions to circumvent these problems are introduced.

5.1 Macro-Meso transition

To begin with, an exemplary RVE is depicted in Fig. 5.2. It occupies the space

$$-l_x/2 \leq x \leq l_x/2 \quad -l_y/2 \leq y \leq l_y/2 \quad -h^{RVE}/2 \leq z \leq h^{RVE}/2, \quad (5.1)$$

where the origin of the Cartesian coordinate system is centrally aligned in all three axes. The x - and y -axes denote the in-plane directions of the RVE and refer to the reference surface of the shell, while the z -axis corresponds to the thickness direction. The lateral boundaries are split into opposing boundaries $\Gamma^m = \Gamma^{m+} \cup \Gamma^{m-}$. Displacement boundary conditions can be applied to these lateral surfaces, while zero-traction boundary conditions are applied to the lower and upper surface ($z = \pm h^{RVE}/2$). This is a distinctive feature in the homogenisation of shell structures. If the upper and lower surfaces of the shell structure are free of surface loads, they are traction-free and since the RVE extends through the full thickness of the shell, this imposes zero-traction boundary conditions on the upper and lower surfaces of the RVE.

Following Gruttmann and Wagner [62], for small strains the relationship between the macroscopic strains and the prescribed lateral displacements can be written as

$$\begin{bmatrix} \bar{u}_x \\ \bar{u}_y \\ \bar{u}_z \end{bmatrix} = \begin{bmatrix} \varepsilon_{xx} + z \kappa_{xx} & \varepsilon_{xy} + z \kappa_{xy} & \frac{1}{2} \gamma_x \\ \varepsilon_{xy} + z \kappa_{xy} & \varepsilon_{yy} + z \kappa_{yy} & \frac{1}{2} \gamma_y \\ \frac{1}{2} \gamma_x & \frac{1}{2} \gamma_y & 0 \end{bmatrix} \begin{bmatrix} x \\ y \\ z \end{bmatrix}. \quad (5.2)$$

Note, that the indices of the shell quantities $\alpha, \beta = 1, 2$ have been replaced with $\alpha, \beta = x, y$. Because the RVE is defined in the orthonormal basis system \mathbf{e}_i , while the shell is defined in the local orthonormal basis system \mathbf{A}_i , the indices can be exchanged without further consequences.

Gruttmann and Wagner [62] have observed restraints for particular membrane and bending modes when prescribing the lateral displacements according to Eq. 5.2. Therefore, in the following, the displacements in the thickness direction u_z are not prescribed and Eq. 5.2 is rewritten so that

$$\begin{bmatrix} \bar{u}_x \\ \bar{u}_y \end{bmatrix} = \begin{bmatrix} \varepsilon_{xx} + z \kappa_{xx} & \varepsilon_{xy} + z \kappa_{xy} & \gamma_x \\ \varepsilon_{xy} + z \kappa_{xy} & \varepsilon_{yy} + z \kappa_{yy} & \gamma_y \end{bmatrix} \begin{bmatrix} x \\ y \\ z \end{bmatrix}. \quad (5.3)$$

Alternatively, the relation can be expressed using the vector of shell strains $\boldsymbol{\varepsilon}$ from Eq. 3.22

$$\begin{bmatrix} \bar{u}_x \\ \bar{u}_y \end{bmatrix} = \begin{bmatrix} x & 0 & \frac{1}{2} y & x z & 0 & \frac{1}{2} y z & z & 0 \\ 0 & y & \frac{1}{2} x & 0 & y z & \frac{1}{2} x z & 0 & z \end{bmatrix} \begin{bmatrix} \varepsilon_{xx} \\ \varepsilon_{yy} \\ 2 \varepsilon_{xy} \\ \kappa_{xx} \\ \kappa_{yy} \\ 2 \kappa_{xy} \\ \gamma_x \\ \gamma_y \end{bmatrix} \quad (5.4)$$

$$\bar{\mathbf{u}} = \mathbf{A} \boldsymbol{\varepsilon}$$

The deformed RVE for each strain state can be obtained from this relationship. The deformation modes are schematically depicted in Fig. 5.3.

Instead of prescribing certain shell strains via displacements of the lateral surfaces, the rotation of these surfaces can be prescribed. The surfaces Γ_x^{m+} and Γ_x^{m-} can be rotated about the y -axis. Similarly, the surfaces Γ_y^{m+} and Γ_y^{m-} can be rotated about the x -axis. The rotations are defined as

$$\omega_y = \frac{\partial u_x}{\partial z} \quad \text{and} \quad \omega_x = \frac{\partial u_y}{\partial z}, \quad (5.5)$$

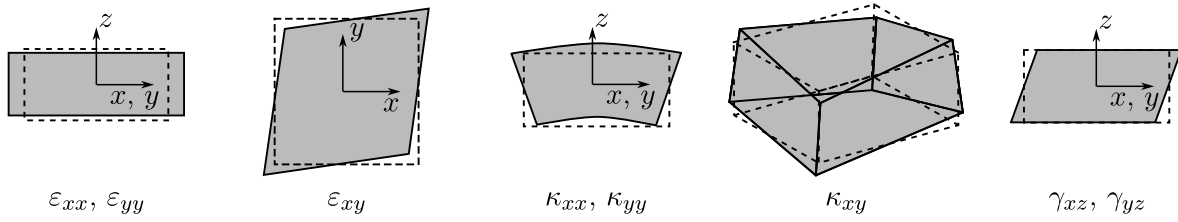


Figure 5.3: Deformation modes of the RVE subjected to the shell strains

respectively.

As an example, the curvature κ_{xx} can be applied either as a displacement

$$\bar{u}_x = \kappa_{xx} x z \quad (5.6)$$

or as rotation of the boundary surface

$$\bar{\omega}_y = \frac{\partial \bar{u}_x}{\partial z} = \kappa_{xx} x. \quad (5.7)$$

The deformation of an RVE for an applied curvature κ_{xx} is depicted in Fig. 5.4.

Generally, all curvatures and transverse shear strains may be applied as surface rotation. Therefore, the following relation can be deduced.

$$\begin{bmatrix} \bar{\omega}_x \\ \bar{\omega}_y \end{bmatrix} = \begin{bmatrix} 0 & 0 & 0 & 0 & -y & -\frac{1}{2}x & 0 & -1 \\ 0 & 0 & 0 & x & 0 & \frac{1}{2}y & 1 & 0 \end{bmatrix} \boldsymbol{\epsilon}. \quad (5.8)$$

In order to apply these rotations to the RVE boundaries, a transition element, which has been presented in [117] and is based on [89], is introduced. Using LAGRANGE multipliers, it enforces the deformation of the lateral surfaces in an integral sense. The algorithmic treatment of the transition element is discussed in sec. 6.3.

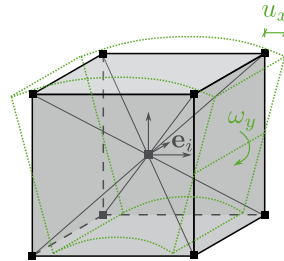


Figure 5.4: Deformation of an RVE due to an applied curvature κ_{xx}

5.2 HILL-MANDEL condition

The macroscopic stress resultants in shell theory are obtained by a through-thickness integration. Therefore, for the homogenisation of shells only an in-plane homogenisation is required. The HILL-MANDEL [70] condition from Eq. 4.6 has to be adapted, such that the mesoscopic internal work is averaged over the RVEs mid-surface instead of the RVE volume [38]. In the following, the operator $\langle \square \rangle$ denotes the average over the mid-surface A^m . However, the integration is still performed over the three-dimensional RVE volume Ω^m .

$$\langle \square \rangle = \frac{1}{A^m} \int_{\Omega^m} \square \, dV \quad (5.9)$$

Here, A^m corresponds to the in-plane area ($l_x \times l_y$) of the RVE. Nevertheless, the HILL-MANDEL condition is still written as

$$\langle \mathbf{P}^m : \mathbf{F}^m \rangle - \langle \mathbf{P}^m \rangle : \langle \mathbf{F}^m \rangle = 0, \quad (5.10)$$

as presented in Eq. 4.6 and the derived boundary conditions, see Eq. 4.12 - 4.14, remain unchanged.

For the macroscopic shell, the internal work is expressed in terms of shell strains and stress resultants, refer to Eq. 3.40. For the mesoscopic scale, SBIGA is employed and therefore the internal work from Eq. 2.29 is used. Inserting these into Eq. 5.10 yields

$$\underbrace{\langle \delta \hat{\mathbf{E}}^T \hat{\mathbf{S}} \rangle}_{\text{SBIGA}} = \underbrace{\delta \boldsymbol{\varepsilon}^T \boldsymbol{\sigma}}_{\text{shell}}. \quad (5.11)$$

Note, that for the macroscopic internal virtual work the integration over the reference surface is dropped, because the HILL-MANDEL condition requires the internal virtual work in each macroscopic point to be equal to the total internal virtual work in an RVE. It has to be shown, that the chosen boundary conditions from sec. 5.1 fulfil the HILL-MANDEL condition. Following Wagner and Gruttmann [175], the left hand side of Eq. 5.11 can be rewritten.

$$\delta \hat{\mathbf{E}}^T \hat{\mathbf{S}} = \mathbf{S} : \delta \mathbf{E} = \mathbf{P} : \delta \mathbf{F} = \mathbf{P} : \text{Grad } \delta \mathbf{u} = \text{Div} (\mathbf{P} \delta \mathbf{u}) - \underbrace{\text{Div} (\mathbf{P})}_{=0} \cdot \delta \mathbf{u}, \quad (5.12)$$

where $\text{Div} (\mathbf{P}) = 0$ because no external forces act at the mesoscopic scale, refer to Tab. 4.1. Inserting Eq. 5.12 into Eq. 5.11 and using the divergence theorem, the volume integral can be transformed into a surface integral.

$$\langle \mathbf{S} : \delta \mathbf{E} \rangle = \frac{1}{A^m} \int_{\Omega^m} \text{Div} (\mathbf{P} \delta \mathbf{u}) \, dV = \frac{1}{A^m} \int_{\Gamma^m} \mathbf{P} : \delta \mathbf{u} \otimes \mathbf{N} \, dA = \frac{1}{A^m} \int_{\Gamma^m} \mathbf{t}_0 \cdot \delta \mathbf{u} \, dA \quad (5.13)$$

where: $\mathbf{t}_0 = \mathbf{P} \mathbf{N}$ = surface tractions

$\mathbf{N} = [n_x \ n_y \ n_z]^T$ = normal vector of the RVE in the reference configuration.

From Eq. 2.17 it follows, that for small strains $\hat{\mathbf{P}} = \hat{\mathbf{S}} = [S_{11} \ S_{22} \ S_{33} \ S_{12} \ S_{13} \ S_{23}]^T$ applies. Therefore, the surface tractions can be written in matrix notation as

$$\begin{bmatrix} t_x \\ t_y \\ t_z \end{bmatrix} = \begin{bmatrix} n_x & 0 & 0 & n_y & n_z & 0 \\ 0 & n_y & 0 & n_x & 0 & n_z \\ 0 & 0 & n_z & 0 & n_x & n_y \end{bmatrix} \hat{\mathbf{S}}. \quad (5.14)$$

Since the displacements in thickness direction u_z are not applied, compare Eq. 5.3, t_z does not contribute to the work performed and Eq. 5.14 reduces to

$$\begin{bmatrix} t_x \\ t_y \end{bmatrix} = \begin{bmatrix} n_x & 0 & 0 & n_y & 0 & 0 \\ 0 & n_y & 0 & n_x & 0 & 0 \end{bmatrix} \hat{\mathbf{S}} \\ \mathbf{t} = \check{\mathbf{N}}^T \hat{\mathbf{S}}. \quad (5.15)$$

Using Eq. 5.4 the displacements on the lateral surfaces of the RVE can be prescribed, thus $\delta \mathbf{u} = \delta \bar{\mathbf{u}} = \mathbf{A} \delta \boldsymbol{\varepsilon}$. Consequently, Eq. 5.13 can be expressed using the macroscopic shell strains, such that

$$\langle \mathbf{S} : \delta \mathbf{E} \rangle = \frac{1}{A^m} \int_{\Gamma^m} \mathbf{t} \cdot \delta \bar{\mathbf{u}} dA = \frac{1}{A^m} \int_{\Gamma^m} \mathbf{A}^T \check{\mathbf{N}}^T \hat{\mathbf{S}} dA \cdot \delta \boldsymbol{\varepsilon}. \quad (5.16)$$

The matrix product $\mathbf{A}^T \check{\mathbf{N}}^T \hat{\mathbf{S}}$ can be written as

$$\mathbf{A}^T \check{\mathbf{N}}^T \hat{\mathbf{S}} = \begin{bmatrix} x n_x S_{11} + x n_y S_{12} \\ y n_y S_{22} + y n_x S_{12} \\ \frac{1}{2} y n_x S_{11} + \frac{1}{2} x n_y S_{22} + \frac{1}{2} (y n_y + x n_x) S_{12} \\ x z n_x S_{11} + x z n_y S_{12} \\ y z n_y S_{22} + y z n_x S_{12} \\ \frac{1}{2} y z n_x S_{11} + \frac{1}{2} x z n_y S_{22} + \frac{1}{2} (y z n_y + x z n_x) S_{12} \\ z n_x S_{11} + z n_y S_{12} \\ z n_y S_{22} + z n_x S_{12} \end{bmatrix}. \quad (5.17)$$

First, integrating over the two opposite surfaces where $x = \pm l_x/2$ and $\mathbf{N} = [\pm 1 \ 0 \ 0]^T$,

the integral from Eq. 5.16 simplifies to

$$\int_{-l_y/2}^{l_y/2} \int_{h^-}^{h^+} \mathbf{A}^T \check{\mathbf{N}}^T \hat{\mathbf{S}} dA = l_x l_y \int_{h^-}^{h^+} \begin{bmatrix} S_{11} \\ 0 \\ \frac{1}{2} S_{12} \\ z S_{11} \\ 0 \\ \frac{1}{2} z S_{12} \\ z \Delta S_{11}/l_x \\ z \Delta S_{12}/l_x \end{bmatrix} dz = A^m \begin{bmatrix} n_{11} \\ 0 \\ \frac{1}{2} n_{12} \\ m_{11} \\ 0 \\ \frac{1}{2} m_{12} \\ \Delta m_{11}/l_x \\ \Delta m_{12}/l_x \end{bmatrix}. \quad (5.18)$$

Analogously, it is integrated over the two perpendicular surfaces $y = \pm l_y/2$, where $\mathbf{N} = [0 \ \pm 1 \ 0]^T$.

$$\int_{-l_x/2}^{l_x/2} \int_{h^-}^{h^+} \mathbf{A}^T \check{\mathbf{N}}^T \hat{\mathbf{S}} dA = l_x l_y \int_{h^-}^{h^+} \begin{bmatrix} 0 \\ S_{22} \\ \frac{1}{2} S_{12} \\ 0 \\ z S_{22} \\ \frac{1}{2} z S_{12} \\ z \Delta S_{12}/l_y \\ z \Delta S_{22}/l_y \end{bmatrix} dz = A^m \begin{bmatrix} 0 \\ n_{22} \\ \frac{1}{2} n_{12} \\ 0 \\ m_{22} \\ \frac{1}{2} m_{12} \\ \Delta m_{12}/l_y \\ \Delta m_{22}/l_y \end{bmatrix}. \quad (5.19)$$

To integrate over all lateral surfaces the matrices of Eqs. 5.18 and 5.19 are summarised and the definition of the shear force

$$\begin{aligned} q_1 &= \frac{\Delta m_{11}}{l_x} + \frac{\Delta m_{12}}{l_y}, \\ q_2 &= \frac{\Delta m_{22}}{l_y} + \frac{\Delta m_{12}}{l_x}, \end{aligned} \quad (5.20)$$

is employed. Using Eq. 5.20, the averaged internal virtual work on the mesoscopic scale can be finally expressed as

$$\langle \mathbf{S} : \delta \mathbf{E} \rangle = \frac{1}{A^m} A^m \boldsymbol{\sigma} \cdot \delta \boldsymbol{\varepsilon}, \quad (5.21)$$

which proves that the HILL-MANDEL condition from Eq. 5.11 is fulfilled.

5.3 Peculiarities arising from the transverse shear deformation

5.3.1 Rigid body rotation of the RVE

When prescribing the shear strains γ_α as displacement of the lateral surfaces of the RVE according to Eq. 5.4, this allows a rigid body rotation of the RVE instead of a shear deformation. As a result, no stresses occur and, accordingly, the system possesses no stiffness against transverse shear strains. This has been discussed in the literature and different measures to circumvent the problem have been proposed. Geers et al. [55] impose a weak constraint on each lateral surface which requires that the averaged microscopic shear of each surface is equal to the macroscopic transverse shear strain. Klarmann [89] and Zoller [187] introduce an additional condition that restricts the averaged rotation of the RVE cross-section. For beams, the rotation about the y -axis is restricted at $x = 0$ [89], while for shells the rotation about the y -axis and the x -axis are restricted at $x = 0$ and $y = 0$ [187], respectively. Here, the approach proposed by Gruttmann and Wagner [62] is employed, which applies antisymmetric link conditions for the displacements in thickness direction \bar{u}_z . This means, that the displacement in thickness direction of the two opposing lateral surfaces have to correspond to each other. Each control point on a lateral surface is associated with a control point on the opposing boundary. In this way, rigid body rotations about the x - and y -axis are avoided.

$$\begin{aligned}\bar{u}_z(l_x/2, y, z) &= \bar{u}_z(-l_x/2, -y, z) \\ \bar{u}_z(x, l_y/2, z) &= \bar{u}_z(-x, -l_y/2, z)\end{aligned}\tag{5.22}$$

The link conditions must be applied in an antisymmetric way, because otherwise a wrong warping deformation is obtained and the homogenised torsional stiffness D_b^{33} converges against a wrong value [62].

The described problem of rigid body rotation of the RVE only occurs if the shear strains are prescribed as boundary displacements. If they are prescribed as rotation of the lateral surfaces using Eq. 5.8, the problem does not arise. Therefore, depending on the chosen boundary conditions, link conditions have to be introduced. These are presented in sec. 6.6.

5.3.2 RVE size dependence of shear stiffness components

In addition to the problem of rigid body rotation, a length dependence of the homogenised shear stiffnesses on the in-plane dimensions of the RVE occurs. This can be related to the application of the transverse shear strain to the lateral surfaces of the RVE. Following Zoller [187], an RVE with large in-plane dimensions is considered. For demonstration purposes, both in-plane axes are simplified to a fully clamped beam, such that the RVE

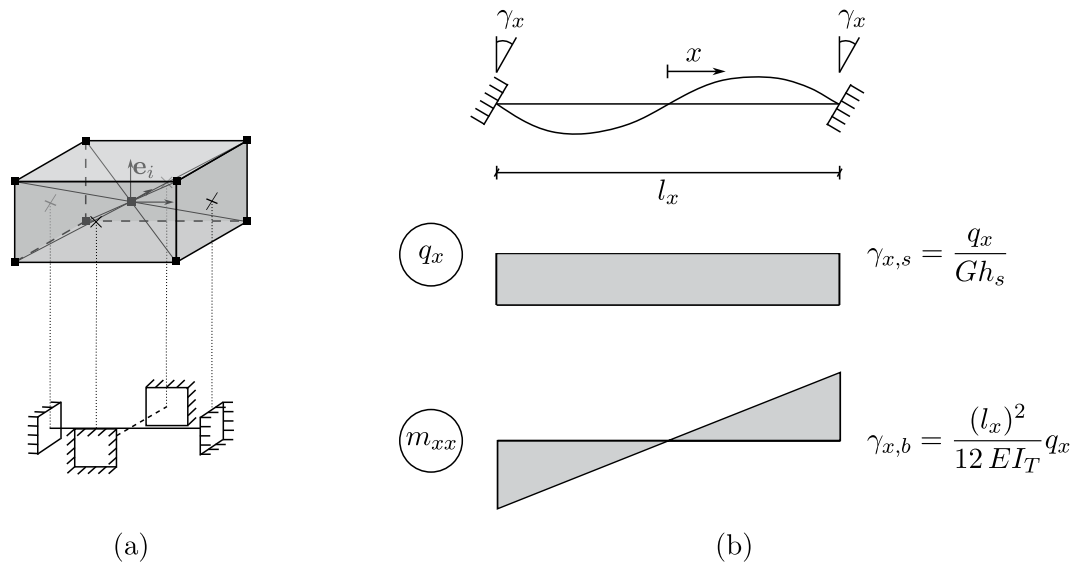


Figure 5.5: (a) Beam analogy for an RVE (b) Beam undergoing shear deformation, resulting shear force distribution q_x and bending moment distribution m_{xx} (Adapted from [117])

can be reduced to the equivalent system shown in Fig. 5.5 (a). For this purpose, the influences from torsional moments and lateral contraction are neglected. Furthermore, boundary effects are not considered when examining the centre axes of the RVE.

The boundary conditions of the beams have to be chosen according to how the macroscopic strains are applied on the RVE [89]. Because the in-plane and out-of-plane displacements are prescribed, the support of the equivalent beam is modelled as clamped.

From shell kinematics a linear relationship between the shear force and shear strain results, compare Eq. 3.31. For linear-elastic, isotropic material it reads

$$q_x = D_s^{11} \gamma_x = G h_s \gamma_x, \quad (5.23)$$

where: G = shear modulus

$$h_s = \kappa h^{RVE}$$

κ = shear correction factor.

Using Eq. 5.4 the macroscopic shear strain γ_x is applied to the RVE by prescribing the displacements of the lateral surface as

$$\bar{u}_x = \gamma_x z. \quad (5.24)$$

Using the introduced beam analogy, prescribing the displacements of the lateral surfaces results in a rotation of the clamped support, as shown in Fig. 5.5 (b). According to beam theory, a coupling between shear force and moment occurs. Thus, a constant shear force distribution and a linear moment distribution are obtained, as illustrated in Fig. 5.5 (b).

For each, a transverse shear strain component can be deduced. For the shear force

$$\gamma_{x,s} = \frac{q_x}{Gh_s} \quad (5.25)$$

is obtained, while

$$\gamma_{x,b} = \frac{(l_x)^2}{12 EI_T} q_x \quad (5.26)$$

denotes the bending moment contribution. Addition of both components relates the shear force q_x to the transverse shear strain γ_x via

$$q_x = \underbrace{\frac{12 EI_T Gh_s}{(l_x)^2 Gh_s + 12 EI_T}}_{(D_s^{11})^*} \gamma_x, \quad (5.27)$$

where: E = Young's modulus

$$I_T = (h^{RVE})^3 / 12 = \text{second moment of area.}$$

Comparison of Eq. 5.23 and Eq. 5.27 illustrates the inconsistency between the macroscopic shell kinematics and the applied kinematics for the RVE, since

$$D_s^{11} = Gh_s \neq \frac{12 EI_T Gh_s}{(l_x)^2 Gh_s + 12 EI_T} = (D_s^{11})^*. \quad (5.28)$$

Furthermore, it can be seen, that the in-plane RVE dimension l_x has a quadratic influence on the homogenised shear stiffness $(D_s^{11})^*$ – the larger the in-plane dimension the smaller is the homogenised shear stiffness. The homogenised stiffnesses should be, however, independent of the size of the RVE.

Different measures can be taken to reduce the length dependence of the homogenised shear stiffness. For example, Heller and Gruttmann [68] apply length-dependent shear correction factors for the homogenisation of sandwich composites. Hii and El Said [69] propose a volumetric constraint on the fluctuation moment within a second-order homogenisation framework for thick shells.

The present work extends the approach proposed by Klarmann and Gruttmann [90] for beams to a shell formulation. From Eq. 5.26 it becomes obvious that the length-dependent contribution is related to the linear bending moment distribution. Therefore, an additional constraint is introduced which suppresses the linear moment distribution. Then, $\gamma_{x,b}$ vanishes and a consistent macro-meso transition, assuming a linear relationship between displacement and strain (Eq. 5.24), becomes possible.

Here, the problem has been shown for the transverse shear strain γ_x . Consequently, the same phenomenon applies to the second in-plane axis, the y -axis. Therefore, the constraint that reduces the linear bending moment distribution is formulated for both in-plane axes as

$$\int_{l_x} m_{xx} x \, dx = 0 \quad \text{and} \quad \int_{l_y} m_{yy} y \, dy = 0, \quad (5.29)$$

respectively. The constraint reduces the length dependence of the homogenised shear stiffness on the RVE size. For the special case of homogeneous RVEs, the length dependence can be removed completely. The numerical treatment is discussed in sec. 6.4 and the necessity of the constraint will be emphasized using a numerical example in sec. 7.1.1.

Chapter 6

Finite Element Formulation

In the previous chapters, the basic equations for a three-dimensional continuum and a nonlinear shell formulation have been derived. The initial boundary value problem can be solved using approximation methods, like the finite element method. The previously derived weak form of equilibrium forms the basis for numerical methods and its discretisation yields a set of nonlinear equations. Here, the NEWTON-RAPHSON method is applied for the solution of the nonlinear system of equations, which requires the linearisation of the weak form. The main equations are briefly summarised below. For further details on the finite element method, the reader is referred to [9, 42, 178, 186].

The finite element method is based on the idea, that any body Ω can be partitioned into a number of finite elements Ω_e , which approximate the geometry of the whole body.

$$\Omega \approx \Omega^h = \bigcup_{e=1}^{numel} \Omega_e \quad (6.1)$$

The number of elements is given by $numel$. The superscript h indicates the approximation of a value.

The isoparametric concept is used for all finite element formulations employed in the scope of this work, i.e. both the geometry and the displacement field are approximated by the same shape functions. Lagrangian shape functions are used for the macroscopic shell formulation, while NURBS basis functions are used for the RVE at the mesoscopic scale.

The shape functions are generally denoted by N_K , so that the position vectors in the reference and current configuration can be approximated as

$$\mathbf{X}^h = \sum_{K=1}^{nel} N_K \mathbf{X}_K \quad \text{and} \quad \mathbf{x}^h = \sum_{K=1}^{nel} N_K \mathbf{x}_K, \quad (6.2)$$

respectively. nel denotes the number of nodes of each element e . \mathbf{X}_K and \mathbf{x}_K denote the position vector of each node K . Analogous to Eq. 6.2, the degrees of freedom and their

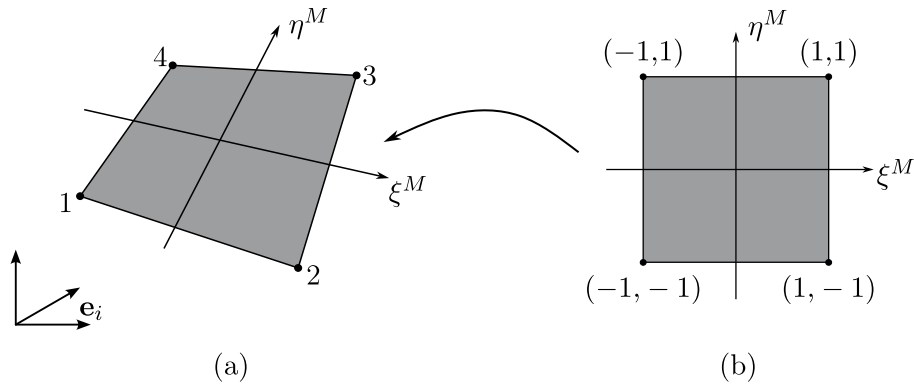


Figure 6.1: 4-node shell element (a) in the physical space and (b) parameter space

variation can be approximated.

$$\mathbf{v}^h = \sum_{K=1}^{nel} N_K \mathbf{v}_K \quad \delta \mathbf{v}^h = \sum_{K=1}^{nel} N_K \delta \mathbf{v}_K \quad (6.3)$$

\mathbf{v}_K is the vector containing the degrees of freedom of the node K ; its dimensions depend on the element formulation.

The approximation and linearisation of the weak form results in the element stiffness matrix \mathbf{k}_e and the element residual vector \mathbf{f}_e , which are specified for the corresponding element formulation in the following. These can be assembled into a global stiffness matrix and a global residual vector using the assembly operator.

$$\mathbf{K} = \mathbf{A}_{e=1}^{numel} \mathbf{k}_e \quad \mathbf{f} = \mathbf{A}_{e=1}^{numel} \mathbf{f}_e \quad (6.4)$$

The linear system of equations

$$\mathbf{K} \Delta \mathbf{V} = \mathbf{f} \quad (6.5)$$

can be solved using the NEWTON-RAPHSON scheme. $\Delta \mathbf{V}$ contains the increment of the degrees of freedom for every iteration step.

For all numerical formulations used, the relevant degrees of freedom have to be identified, suitable interpolation functions have to be chosen and finally the element stiffness matrix and the element residual vector have to be defined. The macroscopic shell formulation is discussed first, before the formulations used at the mesoscopic scale are presented. The homogenisation algorithm couples both scales numerically. To conclude, three types of boundary conditions are presented that are used to apply the macroscopic strain to the RVE.

6.1 Geometric Nonlinear Shell Element

The reference surface of the macroscopic shell is discretised using $numel$ quadrilateral elements. The element formulation will be briefly summarised in the following and is presented in more depth in [174].

Figure 6.1 (b) shows a unit square, which is defined in parameter space $\xi^M, \eta^M \in [-1,1]$. The superscript \square^M is introduced to indicate that the shell is used for the description of the macroscale within the homogenisation framework and to distinguish the shell parametric space from the mesoscopic parameter space. The unit square is mapped to the reference surface of the shell (Fig. 6.1 (a)) and the parametric coordinates correspond to the in-plane coordinates of the shell $\xi^M := \xi^1$ and $\eta^M := \xi^2$.

Each element has $nel = 4$ nodes, which are denoted by \bullet in Fig. 6.1 and correspond to index K . Following Eq. 3.18 the nodal degrees of freedom of the shell compose three displacements and three rotations

$$\mathbf{v}_K = [u_x \quad u_y \quad u_z \quad \omega_x \quad \omega_y \quad \omega_z]_K^T. \quad (6.6)$$

However, for smooth surfaces the formulation can be reduced to five degrees of freedom

$$\mathbf{v}_K = [u_x \quad u_y \quad u_z \quad \omega_1 \quad \omega_2]_K^T \quad \text{and} \quad \omega_{3K} = 0, \quad (6.7)$$

where ω_{1K}, ω_{2K} are the rotations with respect to a local orthonormal basis \mathbf{A}_{iK} for each node K .

For the approximation of the geometry and the field variables \mathbf{v}_K bilinear LAGRANGE shape functions are used, which read

$$N_K(\xi, \eta) = \frac{1}{4} (1 + \xi_K \xi) (1 + \eta_K \eta). \quad (6.8)$$

These can be arranged in the shape function matrix for the macroscopic scale

$$\mathbf{N}^M = [N_1 \mathbf{I} \quad N_2 \mathbf{I} \quad N_3 \mathbf{I} \quad N_4 \mathbf{I}]. \quad (6.9)$$

To avoid shear locking, the approach of BATHE-DVORKIN [48] is used for the interpolation of the shear strain. More detailed information on the shear strain interpolation can be found in [174].

The approximation of the field variables is inserted into the linearisation of the weak form from Eq. 2.27 which results in

$$\begin{aligned} \mathbb{L} [g(\mathbf{v}^h, \delta \mathbf{v}^h), \Delta \mathbf{v}^h] &= g(\mathbf{v}^h, \delta \mathbf{v}^h) + \mathbb{D} [g(\mathbf{v}^h, \delta \mathbf{v}^h)] \cdot \Delta \mathbf{v}^h \\ &= \sum_{e=1}^{numel} \delta \mathbf{v}_e^T [\mathbf{f}_e + \mathbf{k}_e \Delta \mathbf{v}_e] = 0. \end{aligned} \quad (6.10)$$

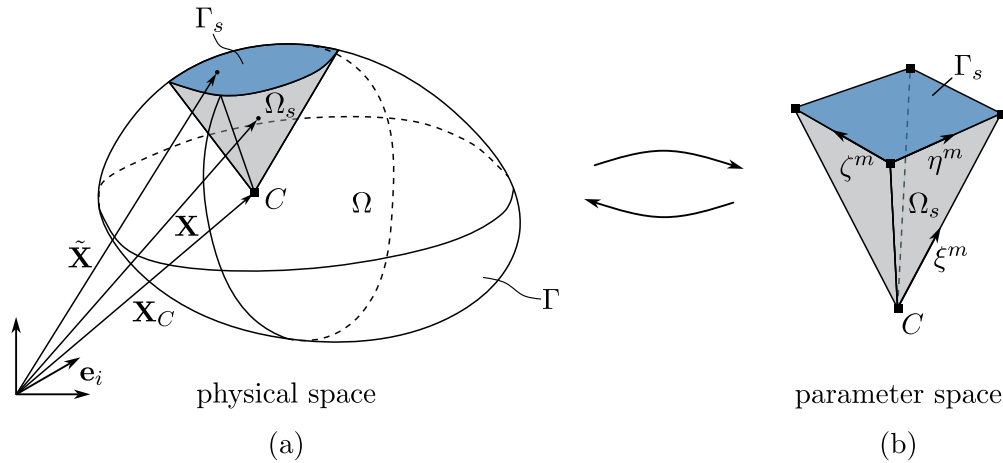


Figure 6.2: Domain in the physical and parametric space

The tangential stiffness matrix and element residual vector for the shell read

$$\begin{aligned} \mathbf{k}_e &= \int_{\Omega_e} \mathbf{B}^T \mathbb{D} \mathbf{B} + \mathbf{G} \, dA, \\ \mathbf{f}_e &= \int_{\Omega_e} \mathbf{B}^T \boldsymbol{\sigma} - \mathbf{N}^{M^T} \bar{\mathbf{p}} \, dA - \int_{\Gamma_e} \mathbf{N}^{M^T} \bar{\mathbf{f}} \, dS. \end{aligned} \quad (6.11)$$

The strain-displacement matrix \mathbf{B} and the geometric matrix \mathbf{G} are defined e.g. in [174]. Following the definitions in chap. 3, the vector $\boldsymbol{\sigma}$ denotes the stress resultants of the shell, refer to Eq. 3.27, and $\bar{\mathbf{p}}$ and $\bar{\mathbf{f}}$ denote the external forces acting on the reference surface of the shell, see Eq. 3.36.

Note, that for the approximation of the shell only linear shape functions are used in the scope of this work. In the homogenisation framework, overall convergence is ensured by mesh refinement at the macroscopic shell.

6.2 Scaled Boundary Isogeometric Analysis

The weak form of equilibrium on the mesoscopic scale is approximated using the scaled boundary isogeometric analysis (SBIGA) [30]. To directly adopt the boundary representation from Computer Aided Design (CAD) for analysis, a scaling centre C is introduced. It is placed in a location from which the boundary of the whole domain must be visible. This requires the geometries to be *star-convex*. Fulfilling this condition, the interior of the domain can be described by a scaling parameter that runs from the scaling centre to the boundary.

The domain Ω from Fig. 2.1 is assumed to be star-convex. Therefore, in the reference configuration it can be described by a scaling centre C and its boundaries Γ , see Fig. 6.2 (a). The domain can be partitioned into a number of n_{sec} sections according to the boundary surfaces. Thus, $\Omega = \bigcup^{n_{sec}} \Omega_s$ applies. A section Ω_s is bounded by the surface Γ_s . Three

directions are parameterised, the interior by means of the scaling parameter $\xi^m \in [0,1]$ and the two boundary directions by means of the parameters $\eta^m \in [0,1]$ and $\zeta^m \in [0,1]$, refer to Fig. 6.2 (b). The position of the scaling centre is defined by the position vector \mathbf{X}_C in the reference configuration while any point on the boundary is defined by the position vector $\tilde{\mathbf{X}}$. Consequently, any point of the section can be expressed as

$$\mathbf{X}(\xi, \eta, \zeta) = \mathbf{X}_C + \xi \left(\tilde{\mathbf{X}}(\eta, \zeta) - \mathbf{X}_C \right) \quad \text{in } \Omega_s. \quad (6.12)$$

The JACOBIAN matrix is introduced to relate the partial derivatives with respect to the Cartesian coordinates to those with respect to parametric coordinates. For the scaled boundary parameterisation it can be split multiplicatively, such that

$$\mathbf{J} = \begin{bmatrix} X_{1,\xi} & X_{2,\xi} & X_{3,\xi} \\ X_{1,\eta} & X_{2,\eta} & X_{3,\eta} \\ X_{1,\zeta} & X_{2,\zeta} & X_{3,\zeta} \end{bmatrix} = \begin{bmatrix} 1 & 0 & 0 \\ 0 & \xi & 0 \\ 0 & 0 & \xi \end{bmatrix} \underbrace{\begin{bmatrix} \tilde{X}_1 - X_{C1} & \tilde{X}_2 - X_{C2} & \tilde{X}_3 - X_{C3} \\ \tilde{X}_{1,\eta} & \tilde{X}_{2,\eta} & \tilde{X}_{3,\eta} \\ \tilde{X}_{1,\zeta} & \tilde{X}_{2,\zeta} & \tilde{X}_{3,\zeta} \end{bmatrix}}_{\tilde{\mathbf{J}}(\eta, \zeta)}. \quad (6.13)$$

Thus, the determinant can also be written as a product

$$\det \mathbf{J} = \xi^2 \det(\tilde{\mathbf{J}}) = \xi^2 \tilde{J}. \quad (6.14)$$

A volume element can then be transformed from physical to parametric space via $dV = \xi^2 \tilde{J} d\xi d\eta d\zeta$. Using the JACOBIAN matrix, the differential operator from Eq. 2.6 can be rewritten as

$$\mathcal{D} = \mathbf{b}_1 \frac{\partial}{\partial \xi} + \frac{1}{\xi} \left(\mathbf{b}_2 \frac{\partial}{\partial \eta} + \mathbf{b}_3 \frac{\partial}{\partial \zeta} \right). \quad (6.15)$$

The definition of the matrices \mathbf{b}_1 , \mathbf{b}_2 and \mathbf{b}_3 can be found in Appendix B.

Compared to the "classical" finite element method, the use of scaled boundary isogeometric analysis introduces two significant changes. On the one hand, that concerns the introduced discretisation. On the other hand, the use of isogeometric analysis implicates the use of NURBS basis functions for approximation, which is directly related to the use of CAD models to describe the geometry.

These changes result in a slightly different terminology. The star-shaped geometry is divided into a number of sections (n_{sec}) instead of elements. The boundaries of the sections are described by NURBS basis functions. Their coefficients are denoted as *control points* and can be interpreted as being equivalent to nodes from the finite element formulations. However, the control points are not interpolated by B-spline curves. Instead, linear interpolation of the control points yields the so-called *control polygon*.

Figure 6.3 (a) shows the exploded view of a cylinder, which is described by its boundaries and a scaling centre. As an example, Fig. 6.3 (b) illustrates the control polygon of one section. Control points are denoted by \blacksquare . In Fig. 6.3 (c) the section Ω_s is depicted in the parameter space $\xi^m, \eta^m, \zeta^m \in [0,1]$ together with the NURBS basis functions, which can

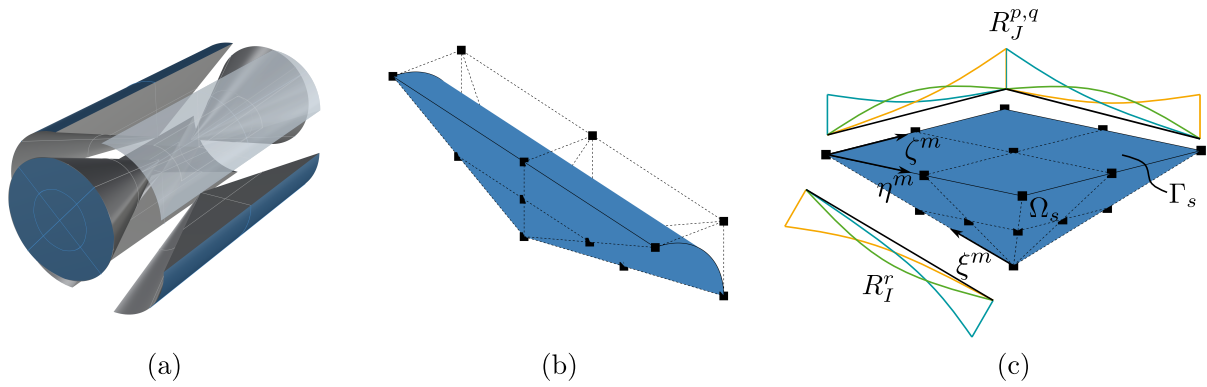


Figure 6.3: (a) Exploded view of a cylinder (b) Plot of section with control points for polynomial degree $p = q = r = 2$, $n_{bc} = 3 \times 3$ boundary control points and $n_{cp} = 3$ control points along each scaling line (c) Illustration of NURBS basis functions in the parameter space of a section Ω_s

be adopted from the CAD model. To comply with the principles of IGA, these are used to describe the geometry and the displacement. In the remainder of this chapter and for the sake of legibility, the superscript \square^m will be dropped for the parametric coordinates. Each control point possesses three displacements as degrees of freedom.

$$\mathbf{v}_K = [u_x \quad u_y \quad u_z]_K^T \quad (6.16)$$

Therefore, the vector containing the degrees of freedom \mathbf{v}_K of each control point can be interchanged with the vector of displacements of each control point \mathbf{u}_K without any further consequence.

The boundary of the RVE is described by the polynomial order of the boundary NURBS $p_b = p = q$ and the number of elements n_b in each boundary direction. Similarly, the scaling direction has the polynomial order $p_c = r$ and the number of elements n_c . A conforming discretisation is chosen, which means that the scaling direction and the two boundary directions are always discretised in the same manner, i.e. $p_c = p_b$. In general, a non-conforming discretisation is possible in order to allow for a more efficient discretisation. However, this requires a coupling approach [6, 29, 44], which is not treated in the present work.

To describe the interior, basis splines (B-Splines) are employed. These consist of piecewise polynomial curves and are denoted as

$$R_I^r(\xi). \quad (6.17)$$

where: r = polynomial degree in scaling direction ξ
 I = number of control point = $1, \dots, n_{cp}$
 n_{cp} = total number of control points along each scaling line

For the description of the boundary, NURBS basis functions are used. They are constructed using B-Splines and allow for a rational basis. Therefore, they can represent

conic sections. The basis function of a NURBS surface reads

$$R_J^{p,q}(\eta,\zeta). \quad (6.18)$$

where: p, q = polynomial degree in boundary directions η, ζ
 J = number of control point = $1, \dots, n_{bc}$
 n_{bc} = total number of control points on the boundary

How to construct B-Spline curves and NURBS surfaces is described in the literature, see e.g. [134]. In Eq. 6.12 the position vector for any point on the boundary $\tilde{\mathbf{X}}$ was introduced, which can be rewritten using Eq. 6.18, such that

$$\tilde{\mathbf{X}} = \sum_{J=1}^{n_{bc}} R_J^{p,q}(\eta,\zeta) \mathbf{X}_{b,J} = \mathbf{N}_b \mathbf{X}_b. \quad (6.19)$$

The vector $\mathbf{X}_{b,J}$ contains the coordinates of control point J on the boundary and can be assembled into a vector \mathbf{X}_b . \mathbf{N}_b is the shape function matrix for the boundary and has size $[3 \times 3 n_{bc}]$, since three degrees of freedom are assigned to each control point.

$$\mathbf{N}_b(\eta,\zeta) = [R_1^{p,q} \mathbf{I}, \dots, R_{n_{bc}}^{p,q} \mathbf{I}] \quad (6.20)$$

Following the isoparametric concept, the displacements can be written analogously to Eq. 6.19 as

$$\mathbf{v}^h = \sum_{J=1}^{n_{bc}} R_J^{p,q}(\eta,\zeta) \mathbf{U}_{b,J} = \mathbf{N}_b(\eta,\zeta) \mathbf{U}_b(\xi). \quad (6.21)$$

$\mathbf{U}_{b,J}$ contains the displacements of the control point with index J and can be rearranged in the vector \mathbf{U}_b . Employing the B-Splines from Eq. 6.17 the displacement vector $\mathbf{U}_{b,J}$ can be approximated as

$$\mathbf{U}_{b,J} = \sum_{I=1}^{n_{cp}} R_I^r(\xi) \mathbf{U}_I, \quad (6.22)$$

where the vector \mathbf{U}_I contains the control point displacements along each scaling line. Defining the vector \mathbf{v}_s which contains all control point displacements of the section Ω_s and rearranging the basis functions R_I^r in a matrix with dimensions $[3 n_{bc} \times 3 n_{bs}]$

$$\mathbf{N}_s(\xi) = \begin{bmatrix} R_1^r \mathbf{I} & \dots & R_{n_{cp}}^r \mathbf{I} & \mathbf{0} & \dots \\ \mathbf{0} & \dots & \mathbf{0} & R_1^r \mathbf{I} & \dots \\ \vdots & \ddots & \vdots & \vdots & \ddots \end{bmatrix}, \quad (6.23)$$

Eq. 6.21 can be written as

$$\mathbf{v}^h(\xi,\eta,\zeta) = \mathbf{N}_b(\eta,\zeta) \mathbf{N}_s(\xi) \mathbf{v}_s = \mathbf{N}^m(\eta,\zeta,\xi) \mathbf{v}_s. \quad (6.24)$$

$n_{bs} = n_{bc} \cdot n_{cp}$ denotes the total number of control points describing one section. \mathbf{N}^m is the consolidated shape function matrix for the mesoscale and has size $[3 \times 3 n_{bs}]$. The vector

\mathbf{v}_s contains all displacements of a section. Finally, for the scaled boundary isogeometric analysis Eq. 6.3 reads

$$\mathbf{v}^h = \sum_{K=1}^{n_{bs}} N_K \mathbf{v}_K = \mathbf{N}^m \mathbf{v}_s \quad \text{and} \quad \delta \mathbf{v}^h = \sum_{K=1}^{n_{bs}} N_K \delta \mathbf{v}_K = \mathbf{N}^m \delta \mathbf{v}_s. \quad (6.25)$$

To approximate the weak form of equilibrium from Eq. 2.24 the variation of the GREEN-LAGRANGE strain $\delta \hat{\mathbf{E}}$ has to be rewritten. To do so, the approximation of the virtual displacements, Eq. 6.25, is used to write the interpolation of the gradient of the virtual displacements $\delta \hat{\mathbf{F}}$. Following Eq. 2.5 it is a vector with nine components.

$$\delta \hat{\mathbf{F}} = \mathcal{D} \delta \mathbf{u} = \mathcal{D} \mathbf{N}^m \delta \mathbf{v}_s = \mathbf{B} \delta \mathbf{v}_s \quad (6.26)$$

\mathbf{B} is the strain-displacement matrix and using the definition of \mathcal{D} from Eq. 6.15 it reads

$$\mathbf{B} = \frac{1}{\det \tilde{\mathbf{J}}} \left[\mathbf{b}_1 \mathbf{N}_b \mathbf{N}_{s,\xi} + \frac{1}{\xi} (\mathbf{b}_2 \mathbf{N}_{b,\eta} \mathbf{N}_s + b_3 \mathbf{N}_{b,\zeta} \mathbf{N}_s) \right]. \quad (6.27)$$

Consequently, the approximation of the weak form follows as

$$\begin{aligned} g(\mathbf{v}^h, \delta \mathbf{v}^h) &= \sum_{s=1}^{n_{sec}} \delta \mathbf{v}_s^T \left[\int_{\Omega_s^{RVE}} \mathbf{B}^T \check{\mathbf{F}}^T \hat{\mathbf{S}} dV \right] \\ &= \sum_{s=1}^{n_{sec}} \delta \mathbf{v}_s^T \mathbf{f}_s, \end{aligned} \quad (6.28)$$

where the external virtual work has been neglected, since body forces and tractions act only on the macroscopic shell. Analogously, the GÂTEAUX derivative from Eq. 2.28 can be approximated, which yields the stiffness matrix for each section.

$$\begin{aligned} \mathbf{D} [g(\mathbf{v}^h, \delta \mathbf{v}^h)] \cdot \Delta \mathbf{v}^h &= \sum_{s=1}^{n_{sec}} \delta \mathbf{v}_s^T \int_{\Omega_s^{RVE}} \xi^2 \mathbf{B}^T \left(\check{\mathbf{F}}^T \hat{\mathbf{C}} \check{\mathbf{F}} + \check{\mathbf{S}} \right) \mathbf{B} \det \tilde{\mathbf{J}} dV \Delta \mathbf{v}_s \\ &= \sum_{s=1}^{n_{sec}} \delta \mathbf{v}_s^T \mathbf{k}_s \Delta \mathbf{v}_s \end{aligned} \quad (6.29)$$

The $[9 \times 9]$ matrix $\check{\mathbf{S}}$ has been introduced, which results from $\Delta \check{\mathbf{F}}^T \mathbf{S} = \check{\mathbf{S}} \Delta \hat{\mathbf{F}}$ and is defined, for example, in [30].

The initial discretisation is determined by the CAD model but can be refined using different refinement techniques from IGA, such as knot insertion or order elevation, see e.g. [40, 76].

To evaluate the integral over the sectional domain in Eq. 6.28 and 6.29 the standard GAUSS quadrature scheme with $n_{GP} \geq (p+1) \times (q+1) \times (r+1)$ integration points per direction is used. Generally, this integration rule is not able to exactly integrate NURBS, however, the induced error vanishes with increasing number of integration points. Alter-

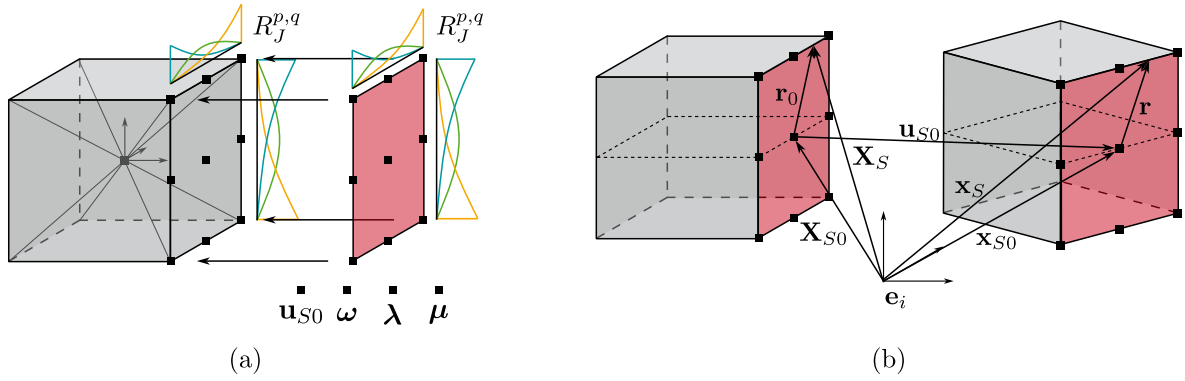


Figure 6.4: (a) Application of transition element on RVE (b) Kinematic relations of transition element (Adapted from [116])

native integration rules to integrate NURBS are discussed, for example, in [77].

6.3 Transition element

As shown in sec. 5.1, the macroscopic shell strains can be applied on the lateral surface of the RVE by prescribing rotations instead of displacements. This can be achieved using the transition element of [117], which is based on [91]. It enforces the deformation of the lateral surface in an integral sense by means of LAGRANGE multipliers. Here, it was adopted to comply with the SBIGA concept at mesoscopic scale.

The transition element is a two-dimensional element that exactly coincides with the geometry of the lateral surface of the RVE, compare Fig. 6.4 (a). Before the numerical description can be obtained, the kinematics and the weak form of the transition element must be derived. The position vector of any point belonging to the RVE in the current configuration is denoted by \mathbf{x}_V and the position vector of the transition element is described by \mathbf{x}_S .

To describe the kinematics, a point \mathbf{X}_{S0} is introduced, which lies on the reference plane of the RVE (at $z = 0$ when $-h^{RVE}/2 \leq z \leq h^{RVE}/2$), see Fig. 6.4 (b). It can be related to the current configuration via

$$\mathbf{x}_{S0} = \mathbf{X}_{S0} + \mathbf{u}_{S0}. \quad (6.30)$$

Any point on the lateral surface in the reference and current configuration can be related to the point \mathbf{X}_{S0} using the vector \mathbf{r}_0 in the reference and $\mathbf{r} = \boldsymbol{\omega} \times \mathbf{r}_0$ in the current configuration, respectively.

$$\begin{aligned} \mathbf{X}_S &= \mathbf{X}_{S0} + \mathbf{r}_0, \\ \mathbf{x}_S &= \mathbf{x}_{S0} + \mathbf{r} = \mathbf{X}_{S0} + \mathbf{u}_{S0} + \boldsymbol{\omega} \times \mathbf{r}_0, \end{aligned} \quad (6.31)$$

where the vector $\boldsymbol{\omega}$ contains the rotations. The geometry of the lateral surface can be described using the volumetric description of the RVE (denoted by \mathbf{x}_V) and the description of the two-dimensional transition element (denoted by \mathbf{x}_S), which have to correlate such that

$$\mathbf{x}_V = \mathbf{x}_S. \quad (6.32)$$

For a numerical description the translation \mathbf{u}_{S0} and rotation $\boldsymbol{\omega}$ are introduced as additional degrees of freedom, together with the two LAGRANGE parameters $\boldsymbol{\lambda}$ and $\boldsymbol{\mu}$. These are globally defined for each transition element and are illustrated in Fig. 6.4 (a). The translation and rotation of the transition element, \mathbf{u}_{S0} and $\boldsymbol{\omega}$, are associated to the point \mathbf{X}_{S0} .

Since the geometry corresponds to the RVE, where SBIGA is used, the same NURBS surface description with n_{bc} control points is employed, indicated in Fig. 6.4 (a). In total, each transition element possesses $3 \times (n_{bc} + 4)$ degrees of freedom. To incorporate the additional constraint on the mesoscopic scale, the weak form can be written as variation of a potential Π .

$$g(\mathbf{v}, \delta \mathbf{v}) = \delta \Pi(\mathbf{v}) \quad (6.33)$$

To enforce the geometric equivalence from Eq. 6.32, using the LAGRANGE parameters $\boldsymbol{\lambda}$ and $\boldsymbol{\mu}$, the potential is extended by

$$\begin{aligned} \Pi &= \dots + \int_{\Gamma^{RVE}} \boldsymbol{\Lambda} \cdot (\mathbf{x}_V - \mathbf{x}_S) \, dA = 0 \\ &= \dots + \int_{\Gamma^{RVE}} (\boldsymbol{\lambda} + \boldsymbol{\mu} \times \mathbf{r}_0) \cdot (\mathbf{x}_V - \mathbf{X}_{S0} - \mathbf{u}_{S0} - \boldsymbol{\omega} \times \mathbf{r}_0) \, dA = 0, \end{aligned} \quad (6.34)$$

with $\boldsymbol{\Lambda} = \boldsymbol{\lambda} + \boldsymbol{\mu} \times \mathbf{r}_0$. The parameter $\boldsymbol{\lambda}$ can be interpreted as force per area and $\boldsymbol{\mu}$ is equivalent to a bending moment. Therefore, $\boldsymbol{\Lambda}$ corresponds to a stress vector [89].

Following Eq. 6.34, the geometric equivalence is fulfilled in an integral sense allowing the cross-section to deform freely. If, in contrast, the constraint would be fulfilled in a point-wise manner, the cross-section would remain plane after deformation. For each transition element the six parameters $\boldsymbol{\lambda}$ and $\boldsymbol{\mu}$ can be chosen as constant values. However, this assumption neglects the geometry and material properties of the cross-section and is therefore only valid for homogenous, linear-elastic RVEs. If stiffness jumps occur across the thickness of the RVE and the LAGRANGE parameters are chosen to be globally constant, the layers with different stiffnesses will deform to a different extent, refer to Fig. 6.5 (a). Instead, the assumption can be relaxed, such that the LAGRANGE parameters are constant for each section. This can be achieved by scaling the LAGRANGE parameter with the local stiffness of the material. Figure 6.5 (b) shows, that this approach allows for a consistent displacement figure. The resulting normal stress distribution from $\boldsymbol{\lambda}$ and $\boldsymbol{\mu}$ is shown in Fig. 6.6. It further shows, that the reference point \mathbf{x}_{S0} is not required to be positioned at the mid-plane of the RVE. The formulation for the transition element is formulated in a general way, which is advantageous because the position where the stress becomes zero does not have to be determined a priori. However, commonly \mathbf{x}_{S0} is

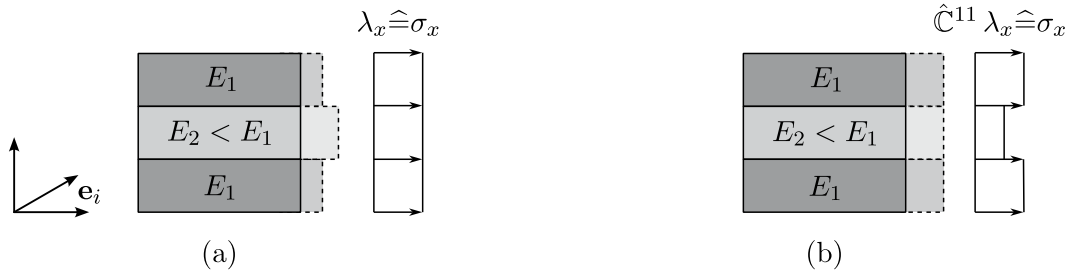


Figure 6.5: Deformation and normal stress distribution of layered RVE with stiffness jumps over the thickness - (a) globally constant LAGRANGE parameter (b) LAGRANGE parameters are scaled with local stiffness contribution and are element-wise constant

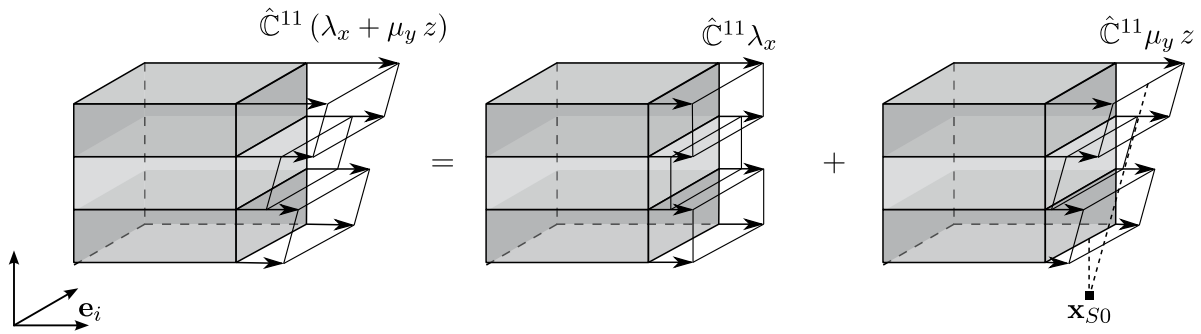


Figure 6.6: Resulting normal stress distribution for a layered RVE with softer core

positioned at the mid-plane of the RVE.

Note, that scaling the LAGRANGE parameters with the local stiffness, is a simplifying assumption, which is only valid for linear material behaviour. For nonlinear material this assumption may not be valid. Nevertheless, it is a sufficient estimation and improves functionality of the transition element. Assuming a linear-elastic constitutive law, here \hat{C}^{11} is used as suitable scaling parameter. \hat{C}^{11} denotes the first entry of the material tangent \hat{C} from Eq. 2.22.

To obtain the weak form, the variation of the potential from Eq. 6.34 has to be found. The extended weak form reads

$$\begin{aligned}
 g(\mathbf{v}, \delta \mathbf{v}) = \dots + \int_{\Gamma^{RVE}} & \delta \mathbf{x}_V^T (\boldsymbol{\lambda} + \boldsymbol{\mu} \times \mathbf{r}_0) + \delta \mathbf{u}_{S_0}^T (-\boldsymbol{\lambda} - \boldsymbol{\mu} \times \mathbf{r}_0) \\
 & + \delta \boldsymbol{\omega}^T (\boldsymbol{\lambda} \times \mathbf{r}_0 + \mathbf{r}_0 \times (\mathbf{r}_0 \times \boldsymbol{\mu})) \\
 & + \delta \boldsymbol{\lambda}^T (\mathbf{x}_V - \mathbf{X}_{S_0} - \mathbf{u}_{S_0} - \boldsymbol{\omega} \times \mathbf{r}_0) \\
 & + \delta \boldsymbol{\mu}^T \mathbf{r}_0 \times (\mathbf{x}_V - \mathbf{X}_{S_0} - \mathbf{u}_{S_0} - \boldsymbol{\omega} \times \mathbf{r}_0) dA = 0
 \end{aligned} \tag{6.35}$$

and accordingly the GÂTEAUX derivative is written as

$$\begin{aligned}
D[g(\mathbf{v}, \delta\mathbf{v})] \cdot \Delta\mathbf{v} = & \dots + \int_{\Gamma^{RVE}} \delta\mathbf{x}_V^T (\Delta\boldsymbol{\lambda} - \mathbf{r}_0 \times \Delta\boldsymbol{\mu}) + \delta\mathbf{u}_{S0}^T (-\Delta\boldsymbol{\lambda} + \mathbf{r}_0 \times \Delta\boldsymbol{\mu}) \\
& + \delta\boldsymbol{\omega}^T (-\mathbf{r}_0 \times \Delta\boldsymbol{\lambda} + \mathbf{r}_0 \times (\mathbf{r}_0 \times \Delta\boldsymbol{\mu})) \\
& + \delta\boldsymbol{\lambda}^T (\Delta\mathbf{x}_V - \Delta\mathbf{u}_{S0} + \mathbf{r}_0 \times \Delta\boldsymbol{\omega}) \\
& + \delta\boldsymbol{\mu}^T \mathbf{r}_0 \times (\Delta\mathbf{x}_V - \Delta\mathbf{u}_{S0} + \mathbf{r}_0 \times \Delta\boldsymbol{\omega}) \, dA.
\end{aligned} \tag{6.36}$$

The following definitions have been employed

$$\begin{aligned}
\delta\mathbf{x}_V &= \delta\mathbf{u}_V, & \Delta\mathbf{x}_V &= \Delta\mathbf{u}_V, \\
\delta\mathbf{x}_{S0} &= \delta\mathbf{u}_{S0}, & \Delta\mathbf{x}_{S0} &= \Delta\mathbf{u}_{S0}.
\end{aligned} \tag{6.37}$$

To obtain the tangential stiffness matrix and the residual vector the field variables need to be approximated. Since the geometry of the transition element and the lateral RVE boundary coincide, the same NURBS shape functions are used for interpolation, see \mathbf{N}^m from Eq. 6.24. Where the scaling parameter is $\xi = 1$ since only values on the boundary are considered. Thus, the field variables can be approximated as

$$\begin{aligned}
\mathbf{x}_V^h &= \sum_{J=1}^{n_{bc}} N_J \mathbf{x}_{VJ} = \sum_{J=1}^{n_{bc}} N_J (\mathbf{X}_{VJ} + \mathbf{v}_J), \\
\delta\mathbf{x}_V^h &= \sum_{J=1}^{n_{bc}} N_J \delta\mathbf{x}_{VJ} = \sum_{J=1}^{n_{bc}} N_J \delta\mathbf{v}_J, \\
\Delta\mathbf{x}_V^h &= \sum_{J=1}^{n_{bc}} N_J \Delta\mathbf{x}_{VJ} = \sum_{J=1}^{n_{bc}} N_J \Delta\mathbf{v}_J, \\
\mathbf{r}_0^h &= \sum_{J=1}^{n_{bc}} N_J \mathbf{X}_{VJ} - \mathbf{X}_{S0}.
\end{aligned} \tag{6.38}$$

n_{bc} corresponds to the number of control points per transition element. The additional control points do not count into n_{bc} . \mathbf{v}_J is the displacement vector of control point J of the transition element and $\delta\mathbf{v}_J$ and $\Delta\mathbf{v}_J$ are the variation and linearisation, respectively.

Finally, the residual vector for each section can be written as

$$\tilde{\mathbf{f}}_s = \begin{bmatrix} \mathbf{f}_a \\ \mathbf{f}_b \\ \mathbf{f}_c \\ \mathbf{f}_d \\ \mathbf{f}_e \end{bmatrix} = \int_{\Gamma_s^{RVE}} \begin{bmatrix} \mathbf{N}^{mT} (\boldsymbol{\lambda} + \boldsymbol{\mu} \times \mathbf{r}_0^h) \\ \mathbf{x}_V^h - \mathbf{X}_S - \mathbf{u}_{S0} - \boldsymbol{\omega} \times \mathbf{r}_0^h \\ \mathbf{r}_0^h (\mathbf{x}_V^h - \mathbf{X}_S - \mathbf{u}_{S0} - \boldsymbol{\omega} \times \mathbf{r}_0^h) \\ -\boldsymbol{\lambda} - \boldsymbol{\mu} \times \mathbf{r}_0^h \\ \boldsymbol{\lambda} \times \mathbf{r}_0^h + \mathbf{r}_0^h \times (\mathbf{r}_0^h \times \boldsymbol{\mu}) \end{bmatrix} dA, \tag{6.39}$$

and the stiffness matrix as

$$\begin{aligned} \tilde{\mathbf{k}}_s &= \begin{bmatrix} \mathbf{0} & \mathbf{k}_{ab} & \mathbf{k}_{ac} & \mathbf{0} & \mathbf{0} \\ \mathbf{k}_{ba} & \mathbf{0} & \mathbf{0} & \mathbf{k}_{bd} & \mathbf{k}_{be} \\ \mathbf{k}_{ca} & \mathbf{0} & \mathbf{0} & \mathbf{k}_{cd} & \mathbf{k}_{ce} \\ \mathbf{0} & \mathbf{k}_{db} & \mathbf{k}_{dc} & \mathbf{0} & \mathbf{0} \\ \mathbf{0} & \mathbf{k}_{eb} & \mathbf{k}_{ec} & \mathbf{0} & \mathbf{0} \end{bmatrix} \\ &= \int_{\Gamma_s^{RVE}} \begin{bmatrix} \mathbf{0} & \mathbf{N}^{mT} \mathbf{I} & \mathbf{N}^{mT} [\mathbf{r}_0^h]^T & \mathbf{0} & \mathbf{0} \\ \mathbf{I} \mathbf{N}^m & \mathbf{0} & \mathbf{0} & -\mathbf{I} & [\mathbf{r}_0^h]_\times \\ [\mathbf{r}_0^h]_\times \mathbf{N}^m & \mathbf{0} & \mathbf{0} & [\mathbf{r}_0^h]^T & [\mathbf{r}_0^h]_\times [\mathbf{r}_0^h]_\times \\ \mathbf{0} & -\mathbf{I} & [\mathbf{r}_0^h]_\times & \mathbf{0} & \mathbf{0} \\ \mathbf{0} & [\mathbf{r}_0^h]^T & [\mathbf{r}_0^h]_\times [\mathbf{r}_0^h]_\times & \mathbf{0} & \mathbf{0} \end{bmatrix} dA. \end{aligned} \quad (6.40)$$

The integral $\int_{\Gamma_s^{RVE}} \square dA$ is applied component-wise. $[\square]_\times$ denotes the skew-symmetric matrix of a vector and is defined as

$$[\mathbf{a}]_\times = \begin{bmatrix} 0 & -a_3 & a_2 \\ a_3 & 0 & -a_1 \\ -a_2 & a_1 & 0 \end{bmatrix}. \quad (6.41)$$

The zero-entries on the diagonal of the stiffness-matrix in Eq. 6.40 indicate that the problem becomes indefinite because the constraint is enforced using LAGRANGE parameters. To solve this system of equations the PARDISO solver is used. It can be used for the parallel solution of sparse linear systems of equations [149, 150]. Alternatively, an Augmented Lagrange method could be used, which incorporates an additional penalty term to improve convergence behaviour [177].

For inhomogeneous material the stiffness matrix and residual vector for each section are scaled using the stiffness contribution in normal direction. For linear-elastic material behaviour and small deformations the entries from the material tangent $\hat{\mathbf{C}}$, see Eq. 2.22, can be used. Thus, for surfaces with normal vector parallel to the x -axis $\hat{\mathbf{C}}^{11}$ is employed and $\hat{\mathbf{C}}^{22}$ for the y -direction, respectively. Therefore,

$$\begin{aligned} \mathbf{k}_s &= \hat{\mathbf{C}}^{11} \tilde{\mathbf{k}}_s \quad \text{and} \quad \mathbf{f}_s = \hat{\mathbf{C}}^{11} \tilde{\mathbf{f}}_s, \quad \text{when} \quad \mathbf{N} = [1 \ 0 \ 0]^T, \quad \text{and} \\ \mathbf{k}_s &= \hat{\mathbf{C}}^{22} \tilde{\mathbf{k}}_s \quad \text{and} \quad \mathbf{f}_s = \hat{\mathbf{C}}^{22} \tilde{\mathbf{f}}_s, \quad \text{when} \quad \mathbf{N} = [0 \ 1 \ 0]^T \end{aligned} \quad (6.42)$$

applies.

6.4 Moment reduction constraint

As has been discussed in sec. 5.3.2 the homogenised shear stiffness components exhibit a dependence on the RVE size, which can be related to a linear bending moment distribution. This will be enforced to be zero by an additional constraint, which is based on [91].

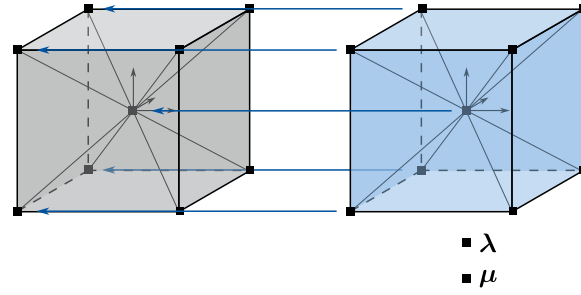


Figure 6.7: Discretisation of the MRC coincides with the RVE geometry

It is called 'moment reduction constraint' in the following and is abbreviated as MRC. The spurious bending moment distributions occur for both in-plane axes, therefore the constraint is applied for both directions. The moment which has to be removed results from the normal stress in the respective direction, such that the constraints are written as

$$\begin{aligned} \int_{l_x} \int_{\Gamma^{RVE}} \sigma_x (\lambda_x + \mu_y z) \, dA \, dL & \quad \int_{l_y} \int_{\Gamma^{RVE}} \sigma_y (\lambda_y - \mu_x z) \, dA \, dL \\ = \int_{\Omega^{RVE}} \sigma_x (\lambda_x + \mu_y z) \, dV = 0 & \quad = \int_{\Omega^{RVE}} \sigma_y (\lambda_y - \mu_x z) \, dV = 0 \end{aligned} \quad (6.43)$$

In the following, the derivation is restricted to the σ_x -component, but can be carried out for σ_y similarly. Again, the constraint is incorporated by extension of the potential.

$$\begin{aligned} \Pi &= \dots + \int_{\Omega^{RVE}} \sigma_x (\lambda_x + \mu_y z) \, dV \\ &= \dots + \int_{\Omega^{RVE}} \sigma_x \check{\mathbf{p}}_x \cdot \mathbf{\Lambda}^{MRC} \, dV \end{aligned} \quad (6.44)$$

Where the position vector $\check{\mathbf{p}}_x = [1 \quad z]^T$ and the vector of LAGRANGE parameters $\mathbf{\Lambda}^{MRC} = [\lambda_x \quad \mu_y]^T$ have been introduced. Here, the LAGRANGE parameters are interpreted as a strain λ_x and a curvature μ_y [89]. The first variation of the potential yields the contribution to the weak form of equilibrium.

$$g(\mathbf{v}, \delta \mathbf{v}) = \dots + \int_{\Omega^{RVE}} (\delta \sigma_x \check{\mathbf{p}}_x \cdot \mathbf{\Lambda}^{MRC} + \sigma_x \check{\mathbf{p}}_x \cdot \delta \mathbf{\Lambda}^{MRC}) \, dV \quad (6.45)$$

The GÂTEAUX derivative follows as

$$D[g(\mathbf{v}, \delta \mathbf{v})] \cdot \Delta \mathbf{v} = \dots + \int_{\Omega^{RVE}} (\delta \sigma_x \check{\mathbf{p}}_x \cdot \Delta \mathbf{\Lambda}^{MRC} + \Delta \sigma_x \check{\mathbf{p}}_x \cdot \delta \mathbf{\Lambda}^{MRC}) \, dV. \quad (6.46)$$

The integration is performed over the whole RVE domain, therefore the whole domain needs to be discretised. Since the moment reduction constraint is introduced on RVE level, the same SBIGA discretisation can be used, which is depicted in Fig. 6.7. Two

additional control points are introduced, which relate to the globally defined LAGRANGE parameters.

Corresponding to the SBIGA discretisation in sec. 6.2 the vector of degrees of freedom for each control point reads

$$\mathbf{v}_K = [u_x \quad u_y \quad u_z]_K^T. \quad (6.47)$$

Assuming material and geometric linear behaviour as well as small deformations the stress component can be written as

$$\delta\sigma_x = \sum_{K=1}^{n_{bs}} \hat{\mathbf{C}}^{1\Box} \mathbf{B}_K \delta\mathbf{v}_K. \quad (6.48)$$

$\hat{\mathbf{C}}^{1\Box}$ denotes the first row of the linear-elastic material tangent in matrix notation from Eq. 2.22. Corresponding to sec. 6.2, n_{bs} are the total number of control points per section. The strain-displacement matrix \mathbf{B}_K for each control point K is derived from Eq. 6.27. It necessitates the interpolation functions \mathbf{N}^m from Eq. 6.24. The displacement field is approximated according to Eq. 6.25 as

$$\mathbf{v}^h = \sum_{K=1}^{n_{bs}} N_K \mathbf{v}_K = \mathbf{N}^m \mathbf{v}_s, \quad \delta\mathbf{v}^h = \sum_{K=1}^{n_{bs}} N_K \delta\mathbf{v}_K = \mathbf{N}^m \delta\mathbf{v}_s. \quad (6.49)$$

Again, the vector \mathbf{v}_s contains all degrees of freedom of a section s . The LAGRANGE parameters are approximated with shape functions that comply with the resulting bending moment distribution. Following sec. 5.3.2 a linear distribution is obtained, therefore

$$N_\Lambda^{MRC} = x. \quad (6.50)$$

Note, that in accordance with sec. 5.1 the coordinate system is defined to be centrally aligned within the RVE. The approximation of the LAGRANGE parameters can be deduced as

$$(\mathbf{\Lambda}^{MRC})^h = N_\Lambda^{MRC} \mathbf{\Lambda}^{MRC}, \quad (\delta\mathbf{\Lambda}^{MRC})^h = N_\Lambda^{MRC} \delta\mathbf{\Lambda}^{MRC}. \quad (6.51)$$

Inserting the approximations from Eq. 6.49 and Eq. 6.51 into the weak form (Eq. 6.45) results in the element residual vector.

$$\begin{aligned} & \int_{\Omega^{RVE}} (\delta\sigma_x \check{\mathbf{p}}_x \cdot (\mathbf{\Lambda}^{MRC})^h + \sigma_x \check{\mathbf{p}}_x \cdot (\delta\mathbf{\Lambda}^{MRC})^h) dV \\ &= \sum_{s=1}^{n_{sec}} \begin{bmatrix} \delta\mathbf{v}_s \\ \delta\mathbf{\Lambda}_s \end{bmatrix}^T \underbrace{\left[\int_{\Omega_s^{RVE}} \mathbf{B}^T \hat{\mathbf{C}}^{1\Box T} \check{\mathbf{p}}_x \cdot \mathbf{\Lambda}_s dV \right]}_{\mathbf{f}_s} \end{aligned} \quad (6.52)$$

Here, the vector $\mathbf{\Lambda}_s$ summarizes the LAGRANGE parameters per section. Analogously

inserting the approximations into the GÂTEAUX derivative from Eq. 6.46 gives

$$\int_{\Omega^{RVE}} (\delta\sigma_x \check{\mathbf{p}}_x \cdot \Delta\boldsymbol{\Lambda}^{MRC} + \sigma_x \check{\mathbf{p}}_x \cdot \delta\boldsymbol{\Lambda}^{MRC}) dV = \sum_{s=1}^{n_{sec}} \begin{bmatrix} \delta\mathbf{v}_s \\ \delta\boldsymbol{\Lambda}_s \end{bmatrix}^T \underbrace{\begin{bmatrix} \mathbf{0} & \mathbf{k}_{ab} \\ \mathbf{k}_{ab}^T & \mathbf{0} \end{bmatrix}}_{\mathbf{k}_s} \begin{bmatrix} \Delta\mathbf{v}_s \\ \Delta\boldsymbol{\Lambda}_s \end{bmatrix}, \quad (6.53)$$

where

$$\mathbf{k}_{ab} = \int_{\Omega^{RVE}} \mathbf{B}^T \hat{\mathbf{C}}^{1\Box^T} \check{\mathbf{p}}_x^T N_{\Lambda}^{MRC} dV. \quad (6.54)$$

In Eq. 6.52 and Eq. 6.54 the residual vector and stiffness matrix for each section of the moment reduction constraint have been derived.

6.5 Homogenisation algorithm

The algorithm coupling the macroscopic shell with the mesoscopic RVE is based on [62]. To each macroscopic integration point $i = 1, \dots, n_{GP}$ in every element $e = 1, \dots, numel$ an RVE is assigned. The weak form of equilibrium of the macroscopic shell is extended with the homogenised mesoscopic model. External loads are acting solely on the macroscopic scale. To employ the NEWTON-RAPHSON scheme the linearisation is required, which reads for the coupled system

$$\begin{aligned} & \mathbb{L} [g(\mathbf{v}, \delta\mathbf{v}), \Delta\mathbf{v}] \\ &= g(\mathbf{v}, \delta\mathbf{v}) + \mathbb{D} [g(\mathbf{v}, \delta\mathbf{v})] \cdot \Delta\mathbf{v} \\ &= \int_{\Omega} \delta\boldsymbol{\varepsilon}^{M^T} \boldsymbol{\sigma}^M dA + (\text{external loads}) + \int_{\Omega} \delta\boldsymbol{\varepsilon}^{M^T} \hat{\mathbb{D}} \Delta\boldsymbol{\varepsilon}^M + \Delta\delta\boldsymbol{\varepsilon}^{M^T} \boldsymbol{\sigma}^M dA \\ &+ \sum_{e=1}^{numel} \sum_{i=1}^{n_{GP}} \left[\frac{1}{A_i} \left(\int_{\Omega_i^{RVE}} \delta\hat{\mathbf{E}}^T \hat{\mathbf{S}} dV + \int_{\Omega_i^{RVE}} \delta\hat{\mathbf{E}}^T \hat{\mathbf{C}} \Delta\hat{\mathbf{E}}^T + \Delta\delta\hat{\mathbf{E}}^T \hat{\mathbf{S}} dV \right) \right]_e. \end{aligned} \quad (6.55)$$

The superscript \Box^M indicates macroscopic quantities. For the sake of legibility no superscript has been introduced for the mesoscopic values. On the macroscale integration is performed over the shell reference surface Ω , while on the mesoscale integration is carried out over the RVE volume Ω^{RVE} and averaged over its mid-surface A_i .

Using the introduced interpolation functions for both scales the linearised weak form can be written as the following system of equations.

$$\mathbb{L} [g(\mathbf{v}^h, \delta\mathbf{v}^h), \Delta\mathbf{v}^h] = \sum_{e=1}^{numel} \begin{bmatrix} \delta\mathbf{v}^M \\ \delta\mathbf{V}_1 \\ \vdots \\ \delta\mathbf{V}_{n_{GP}} \end{bmatrix}_e^T \left\{ \begin{bmatrix} \mathbf{k}^M & \mathbf{0} & \dots & \mathbf{0} \\ \mathbf{0} & \mathbf{K}_1 & \dots & \mathbf{0} \\ \vdots & \vdots & \ddots & \vdots \\ \mathbf{0} & \mathbf{0} & \dots & \mathbf{K}_{n_{GP}} \end{bmatrix} \begin{bmatrix} \Delta\mathbf{v}^M \\ \Delta\mathbf{V}_1 \\ \vdots \\ \Delta\mathbf{V}_{n_{GP}} \end{bmatrix} + \begin{bmatrix} \mathbf{f}^M \\ \mathbf{F}_1 \\ \vdots \\ \mathbf{F}_{n_{GP}} \end{bmatrix} \right\}_e \quad (6.56)$$

The first row corresponds to the macroscopic boundary value problem for shell element e , where the element stiffness matrix and the element residual vector correspond to Eq. 6.11. All other rows refer to a mesoscopic boundary value problem for GAUSS point $1 \leq i \leq nGP$ of shell element e .

$$\delta \mathbf{V}_i (\mathbf{K}_i \Delta \mathbf{V}_i + \mathbf{F}_i) = \frac{1}{A_i} \sum_{s=1}^{n_{sec}} \delta \mathbf{v}_s^T (\mathbf{k}_s \Delta \mathbf{v}_s + \mathbf{f}_s) \quad (6.57)$$

\mathbf{f}_s and \mathbf{k}_s are the element residual vector and element tangential stiffness matrix of the mesoscopic scale from Eq. 6.28 and Eq. 6.29, respectively. Again, n_{sec} denotes the total number of sections for each RVE. The macroscopic quantities $\mathbf{k}^M(\hat{\mathbb{D}}_i)$ and $\mathbf{f}^M(\boldsymbol{\sigma}_i)$ depend on the mesoscopic homogenised shell material tangent matrix $\hat{\mathbb{D}}_i$ and the stress resultants $\boldsymbol{\sigma}_i$, respectively.

For static condensation, the displacement vector \mathbf{v}_s at the mesoscopic scale is split into two parts. A vector \mathbf{v}_a , which comprises all degrees of freedom of a section without boundary conditions and a vector \mathbf{v}_b containing all boundary displacements. The internal degrees of freedom are related to the global displacement vector \mathbf{V}_i using the assembly matrix \mathbf{a}_s . The boundary displacements \mathbf{v}_b can be related to the macroscopic strains $\boldsymbol{\varepsilon}^M$ using $\mathbf{A}_s(x, y, z)$.

$$\mathbf{v}_s = \begin{bmatrix} \mathbf{v}_a \\ \mathbf{v}_b \end{bmatrix} = \begin{bmatrix} \mathbf{a}_s \mathbf{V}_i \\ \mathbf{A}_s \boldsymbol{\varepsilon}^M \end{bmatrix} \quad (6.58)$$

The variation and linearisation can be derived accordingly.

$$\begin{bmatrix} \delta \mathbf{v}_a \\ \delta \mathbf{v}_b \end{bmatrix} = \begin{bmatrix} \mathbf{a}_s & \mathbf{0} \\ \mathbf{0} & \mathbf{A}_s \end{bmatrix} \begin{bmatrix} \delta \mathbf{V}_i \\ \delta \boldsymbol{\varepsilon}^M \end{bmatrix} \quad \begin{bmatrix} \Delta \mathbf{v}_a \\ \Delta \mathbf{v}_b \end{bmatrix} = \begin{bmatrix} \mathbf{a}_s & \mathbf{0} \\ \mathbf{0} & \mathbf{A}_s \end{bmatrix} \begin{bmatrix} \Delta \mathbf{V}_i \\ \Delta \boldsymbol{\varepsilon}^M \end{bmatrix} \quad (6.59)$$

Introducing $\mathbf{k}_{\alpha\beta}$ and \mathbf{f}_α with $\alpha, \beta = a, b$ as submatrices of \mathbf{k}_s and \mathbf{f}_s , Eq. 6.57 can be rewritten, such that

$$\begin{aligned} \delta \mathbf{V}_i (\mathbf{K}_i \Delta \mathbf{V}_i + \mathbf{F}_i) &= \frac{1}{A_i} \sum_{s=1}^{n_{sec}} \begin{bmatrix} \delta \mathbf{V}_i \\ \delta \boldsymbol{\varepsilon}_i^M \end{bmatrix}_s^T \left\{ \begin{bmatrix} \mathbf{a}_s^T \mathbf{k}_{aa} \mathbf{a}_s & \mathbf{a}_s^T \mathbf{k}_{ab} \mathbf{A}_s \\ \mathbf{A}_s^T \mathbf{k}_{ba} \mathbf{a}_s & \mathbf{A}_s^T \mathbf{k}_{bb} \mathbf{A}_s \end{bmatrix} \begin{bmatrix} \Delta \mathbf{V}_i \\ \Delta \boldsymbol{\varepsilon}_i^M \end{bmatrix} + \begin{bmatrix} \mathbf{a}_s^T \mathbf{f}_a \\ \mathbf{A}_s^T \mathbf{f}_b \end{bmatrix} \right\}_s \\ &= \frac{1}{A_i} \sum_{s=1}^{n_{sec}} \begin{bmatrix} \delta \mathbf{V}_i \\ \delta \boldsymbol{\varepsilon}_i^M \end{bmatrix}_s^T \left\{ \begin{bmatrix} \mathbf{K} & \mathbf{L} \\ \mathbf{L}^T & \mathbf{M} \end{bmatrix} \begin{bmatrix} \Delta \mathbf{V}_i \\ \Delta \boldsymbol{\varepsilon}_i^M \end{bmatrix} + \begin{bmatrix} \mathbf{F}_a \\ \mathbf{F}_b \end{bmatrix} \right\}_s = 0. \end{aligned} \quad (6.60)$$

The internal degrees of freedom can be statically condensed using

$$\Delta \mathbf{V}_i = -\mathbf{K}^{-1} (\mathbf{L} \Delta \boldsymbol{\varepsilon}_i^M + \mathbf{F}_a), \quad (6.61)$$

when $\delta \mathbf{V}_i \neq 0$. Using appropriate boundary conditions, rigid body motions are constrained, such that \mathbf{K}^{-1} exists. Finally, the mesoscopic boundary value problem can be

written as

$$\begin{aligned} \delta \mathbf{V}_i (\mathbf{K}_i \Delta \mathbf{V}_i + \mathbf{F}_i) &= \frac{1}{A_i} \delta \boldsymbol{\varepsilon}_i^{M^T} \left[(\mathbf{M} - \mathbf{L}^T \mathbf{K}^{-1} \mathbf{L}) \Delta \boldsymbol{\varepsilon}_i^{M^T} + (\mathbf{F}_b - \mathbf{L}^T \mathbf{K}^{-1} \mathbf{F}_a) \right] \\ &= \delta \boldsymbol{\varepsilon}_i^{M^T} \left(\hat{\mathbb{D}}_i \Delta \boldsymbol{\varepsilon}_i^M + \boldsymbol{\sigma}_i \right) = 0. \end{aligned} \quad (6.62)$$

The homogenised stress resultants $\boldsymbol{\sigma}_i$ and shell material tangent matrix $\hat{\mathbb{D}}_i$ for each GAUSS point i are introduced as

$$\boldsymbol{\sigma}_i = \frac{1}{A_i} (\mathbf{F}_b - \mathbf{L}^T \mathbf{K}^{-1} \mathbf{F}_a) \quad (6.63)$$

$$\hat{\mathbb{D}}_i = \frac{1}{A_i} (\mathbf{M} - \mathbf{L}^T \mathbf{K}^{-1} \mathbf{L}) \quad (6.64)$$

They contribute to the macroscopic scale through $\mathbf{f}^M(\boldsymbol{\sigma}_i)$ and $\mathbf{k}^M(\hat{\mathbb{D}}_i)$ and inserting back into Eq. 6.56 yields

$$\begin{aligned} &L [g(\mathbf{v}^h, \delta \mathbf{v}^h), \Delta \mathbf{v}^h] \\ &= \sum_{e=1}^{numel} \begin{bmatrix} \delta \mathbf{v}^M \\ \delta \boldsymbol{\varepsilon}_1^M \\ \vdots \\ \delta \boldsymbol{\varepsilon}_{nGP}^M \end{bmatrix}_e^T \left\{ \begin{bmatrix} \mathbf{k}^M(\hat{\mathbb{D}}_i) & \mathbf{0} & \dots & \mathbf{0} \\ \mathbf{0} & \hat{\mathbb{D}}_1 & \dots & \mathbf{0} \\ \vdots & \vdots & \ddots & \vdots \\ \mathbf{0} & \mathbf{0} & \dots & \hat{\mathbb{D}}_{nGP} \end{bmatrix} \begin{bmatrix} \Delta \mathbf{v}^M \\ \Delta \boldsymbol{\varepsilon}_1^M \\ \vdots \\ \Delta \boldsymbol{\varepsilon}_{nGP}^M \end{bmatrix} + \begin{bmatrix} \mathbf{f}^M(\boldsymbol{\sigma}_i) \\ \boldsymbol{\sigma}_1 \\ \vdots \\ \boldsymbol{\sigma}_{nGP} \end{bmatrix} \right\}_e \end{aligned} \quad (6.65)$$

from which the macro-meso coupling becomes evident. The mesoscopic system of equations depend on the macroscopic strains, compare the second until last row of Eq. 6.65. On the other hand the homogenised values $\hat{\mathbb{D}}_i$ and $\boldsymbol{\sigma}_i$ are required to solve the macroscopic problem, as can be seen from the first row of Eq. 6.65. However, the mesoscopic problems are independent of each other and can be solved simultaneously. The systems are solved using the NEWTON iteration scheme, which is only terminated when macroscopic and mesoscopic equilibrium is achieved.

6.6 Boundary conditions for the RVE

The macroscopic shell strains have to be applied on the RVE by means of appropriate boundary conditions. As has been discussed in sec. 5.1, for the top and bottom surface of the RVE ($z = \pm h^{RVE}/2$) zero-traction boundary conditions apply. Thus, the strains will be applied on the lateral surfaces, where the $x - y$ -plane always corresponds to the shell reference surface. The RVE size is determined by the in-plane dimensions l_x and l_y , which can be generally chosen independently. Here, for demonstration purposes $l_x = l_y = L^{RVE}$ applies. Refer to Fig. 5.2 for an illustration of an RVE.

Equation 5.4 prescribes the macroscopic shell strains $\boldsymbol{\varepsilon}^M$ as lateral displacement for every

control point K by means of a matrix \mathbf{A}_K .

$$\bar{\mathbf{u}}_K = \mathbf{A}_K(x,y,z)\boldsymbol{\varepsilon}^M \quad (6.66)$$

The matrices \mathbf{A}_K are submatrices of \mathbf{A}_s from Eq. 6.58. Since the strains can be either applied directly as displacement of the RVE geometry or by means of the introduced transition element from sec. 6.3, the matrix is split into a part relating to the RVE geometry $\tilde{\mathbf{A}}_s$ and a relational matrix for applying the strains through the transition element $\check{\mathbf{A}}_s$.

$$\mathbf{A}_s = \begin{bmatrix} \tilde{\mathbf{A}}_s^T & \check{\mathbf{A}}_s^T \end{bmatrix}^T \quad (6.67)$$

Depending on the type of boundary conditions, which will be presented subsequently, either part may vanish. The matrix $\tilde{\mathbf{A}}_s$ is defined as

$$\tilde{\mathbf{A}}_s = \begin{bmatrix} \delta_1 \tilde{\mathbf{A}}_1 \\ \vdots \\ \delta_K \tilde{\mathbf{A}}_K \\ \vdots \\ \delta_{n_{bs}} \tilde{\mathbf{A}}_{n_{bs}} \end{bmatrix} \quad \text{with} \quad \delta_K = \begin{cases} 1 & \text{if control point } K \text{ has fixed DOFs} \\ 0 & \text{else} \end{cases}. \quad (6.68)$$

The total number of control points per section is given by n_{bs} . Similarly, the matrix for the transition element is defined.

$$\check{\mathbf{A}}_s = \begin{bmatrix} \delta_1 \check{\mathbf{A}}_1 \\ \vdots \\ \delta_L \check{\mathbf{A}}_L \\ \vdots \\ \delta_{nt} \check{\mathbf{A}}_{nt} \end{bmatrix} \quad \text{with} \quad \delta_L = \begin{cases} 1 & \text{if transition element } L \text{ has fixed DOFs} \\ 0 & \text{else} \end{cases}. \quad (6.69)$$

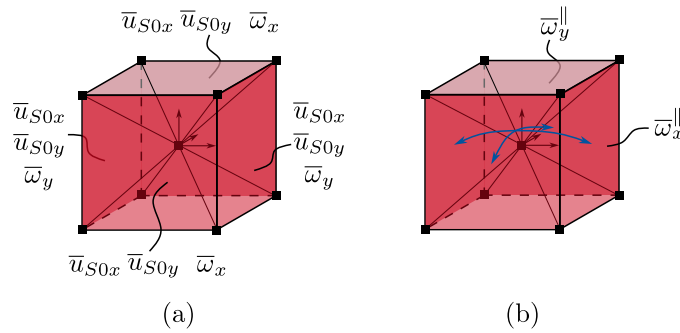
nt denotes the number of transition elements used in the formulation of the boundary conditions.

In addition to prescribing displacements or rotations, it can be required that the deformation on opposing RVE boundaries correlate. This is achieved by link conditions. These can be applied either symmetrically, which is indicated by \square^{\parallel} , or in an antisymmetric manner, denoted by \square^{\times} . In both cases, each control point is associated with a specific control point on the opposing boundary.

For all types of boundary conditions, an arbitrary node is fixed in the z -direction to avoid rigid body motions. Furthermore, the presented moment reduction constraint from sec. 6.4 is used for all three types of boundary conditions presented to reduce the length dependence of the homogenised shear stiffness component on the RVE size L^{RVE} . The necessity of this constraint has been shown in [116] and will be further discussed in sec. 7.1.1.

Table 6.1: Notation of in-plane and out-of-plane displacements and rotations

	$x = \pm l_x/2$	$y = \pm l_y/2$
	$\mathbf{N} = [1 \ 0 \ 0]^T$	$\mathbf{N} = [0 \ 1 \ 0]^T$
displacements		
in-plane	\bar{u}_y	\bar{u}_x
out-of-plane	\bar{u}_x	\bar{u}_y
rotations		
in-plane	$\bar{\omega}_y$	$\bar{\omega}_x$
out-of-plane	$\bar{\omega}_x$	$\bar{\omega}_y$

**Figure 6.8:** Boundary and link conditions for traction boundary conditions (tbc) - (a) prescribed displacements and rotations using transition element (b) link conditions for in-plane rotation

For clarity, the definition of the in-plane and out-of-plane displacements and rotations is summarised in Tab. 6.1 for the lateral surfaces.

6.6.1 Traction Boundary Conditions

The first type of boundary conditions employs the introduced transition element on all four faces of the RVE, thus $nt = 4$. The macroscopic strains are applied by prescribing the translation \mathbf{u}_{S0} and rotation $\boldsymbol{\omega}$ of the transition element. The deformation is enforced using LAGRANGE parameters, see sec. 6.3. This method causes constant tractions on the boundaries, which is why this type of boundary condition will be referred to as 'traction boundary conditions' (*tbc*) in the following.

It must be clarified that this type of boundary condition is not a 'true' stress boundary condition, which has been derived from the HILL-MANDEL condition, see Eq. 4.13. Instead of applying tractions directly to the RVE, as it would be the case for 'true' stress boundary conditions, here macroscopic strains are applied to the RVE using the introduced transition element, refer to sec. 6.3. This invokes constant tractions on the boundary of the RVE.

As the transition element is applied on all four lateral surfaces and the shell strains are

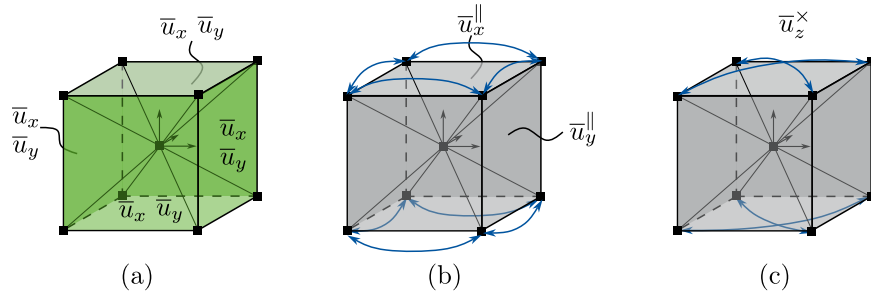


Figure 6.9: Boundary and link conditions for shell boundary conditions (sbc) - (a) prescribed displacements (b) symmetric link conditions for in-plane displacement (c) antisymmetric link conditions for displacement in thickness direction

only applied using the additional degrees of freedom, the relational matrix \mathbf{A}_s reduces to

$$\mathbf{A}_s = \check{\mathbf{A}}_s. \quad (6.70)$$

Figure 6.8 shows the RVE with the applied transition elements. For each lateral surface L the membrane strains $\varepsilon_{\alpha\beta}$ are applied to the RVE using the two translations u_{S0x} and u_{S0y} . By prescribing the in-plane rotation of each surface the macroscopic curvatures $\kappa_{\alpha\beta}$ and the transverse shear strains γ_α are applied. Here, the in-plane rotation is the rotation about the axis perpendicular to the normal of the surface, see Fig. 6.8 (a) and refer to Tab. 6.1.

It is also required that the out-of-plane rotations correspond on opposite sides, i.e.

$$\begin{aligned} \omega_x(L^{RVE}/2, y, z) &= \omega_x(-L^{RVE}/2, y, z) \quad \text{and} \\ \omega_y(x, L^{RVE}/2, z) &= \omega_y(x, -L^{RVE}/2, z). \end{aligned} \quad (6.71)$$

This link condition is denoted by $\bar{\omega}^{\parallel}$ and is illustrated in Fig. 6.8 (b).

The relationship between the macroscopic shell strains and the translational and rotational nodes for each transition element L can be derived from Eq. 5.4 and Eq. 5.8. The matrix \mathbf{A}_L can be written as

$$\begin{bmatrix} \bar{u}_{S0x} \\ \bar{u}_{S0y} \\ \bar{\omega}_x \\ \bar{\omega}_y \end{bmatrix}_L = \underbrace{\begin{bmatrix} x & 0 & \frac{1}{2}y & 0 & 0 & 0 & 0 & 0 \\ 0 & y & \frac{1}{2}x & 0 & 0 & 0 & 0 & 0 \\ 0 & 0 & 0 & 0 & -y & -\frac{1}{2}x & 0 & -1 \\ 0 & 0 & 0 & x & 0 & \frac{1}{2}y & 1 & 0 \end{bmatrix}}_{\mathbf{A}_L^{tbc}} \boldsymbol{\varepsilon}^M. \quad (6.72)$$

Table 6.2: Shell boundary conditions (sbc) - boundary and link conditions for the lateral surface

K on lateral surface	Boundary conditions	Link conditions
$x = \pm l_x/2$	$\bar{\mathbf{u}}_K = \mathbf{A}_K^{sbc}(x,y,z)\boldsymbol{\varepsilon}^M$	$u_y(l_x/2,y,z) = u_y(-l_x/2,y,z)$ $u_z(l_x/2,y,z) = u_z(-l_x/2, -y,z)$
$y = \pm l_y/2$	$\bar{\mathbf{u}}_K = \mathbf{A}_K^{sbc}(x,y,z)\boldsymbol{\varepsilon}^M$	$u_x(x,l_y/2,z) = u_x(x, -l_y/2,z)$ $u_z(x,l_y/2,z) = u_z(-x, -l_y/2,z)$

6.6.2 Shell Boundary Conditions

The 'shell boundary conditions' (*sbc*) have been adapted from Gruttmann and Wagner [62]. It is necessary to adapt the boundary conditions of Gruttmann and Wagner [62] if there are inhomogeneities intersecting the boundary of the RVE that do not span over its entire width. The importance of the adjustment is demonstrated by an example in sec. 7.1.2.

For the shell boundary conditions no transition element is introduced and the shell strains are applied only by means of prescribing the boundary displacements of the RVE, see Fig. 6.9 (a). Thus, Eq. 6.67 reads

$$\mathbf{A}_s = \tilde{\mathbf{A}}_s \quad (6.73)$$

and following Eq. 5.4 the displacements for each control point K is given by

$$\begin{bmatrix} \bar{u}_x \\ \bar{u}_y \end{bmatrix}_K = \underbrace{\begin{bmatrix} x & 0 & \frac{1}{2}y & xz & 0 & \frac{1}{2}yz & z & 0 \\ 0 & y & \frac{1}{2}x & 0 & yz & \frac{1}{2}xz & 0 & z \end{bmatrix}}_{\mathbf{A}_K^{sbc}} \boldsymbol{\varepsilon}^M. \quad (6.74)$$

The out-of-plane displacements of each lateral surface is prescribed and the in-plane displacements are linked symmetrically to the opposing boundary (superscript \square^{\parallel}), see also Fig. 6.9 (b). To avoid a rigid body rotation of the RVE, while allowing for the correct warping deformation, the displacement in the thickness direction \bar{u}_z is linked in an anti-symmetric way (indicated by \square^{\times}), as discussed in sec. 5.3.1. The boundary and link conditions for the shell boundary conditions are summarised in Table 6.2.

6.6.3 Periodic Boundary Conditions

Using the 'periodic boundary conditions' (*pb*), the macroscopic strains are applied by prescribing the boundary displacements of the lateral RVE surfaces, refer to Fig. 6.10 (a). Additionally, the macroscopic transverse shear strains $\boldsymbol{\gamma}$ are prescribed as rotations using two transition elements ($nt = 2$). These are applied to the positive RVE surfaces ($x = l_x/2$ and $y = l_y/2$) as shown in Fig. 6.10 (b).

Both matrices $\tilde{\mathbf{A}}_s$ and $\check{\mathbf{A}}_s$ from Eq. 6.67 need to be defined, as the macroscopic strains are applied to the RVE by prescribing the displacements as well as by using the transition

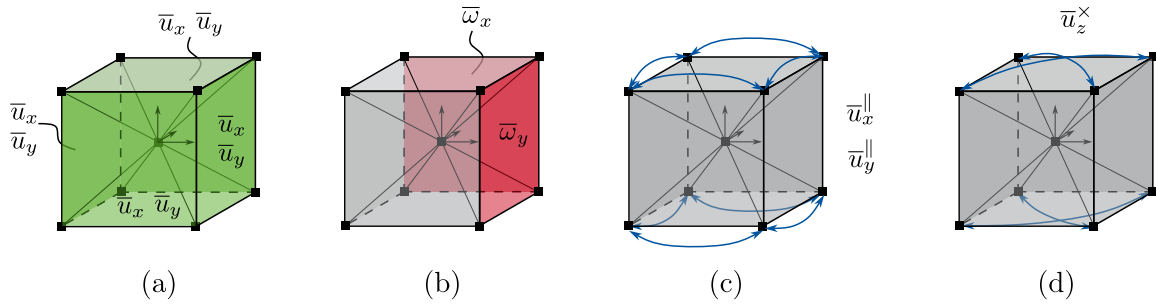


Figure 6.10: Boundary and link conditions for periodic boundary conditions (pbc) - (a) prescribed boundary conditions (b) prescribed rotations using transition element (c) symmetric in-plane link conditions (d) antisymmetric link conditions for thickness direction

Table 6.3: Periodic boundary conditions (pbc) - boundary and link conditions for the lateral surface

K on lateral surface	Boundary conditions	Link conditions
$x = \pm l_x/2$	$\bar{\mathbf{u}}_K = \tilde{\mathbf{A}}_K^{pbc}(x,y,z)\boldsymbol{\varepsilon}^M$	$u_x(l_x/2,y,z) = u_x(-l_x/2,y,z)$ $u_y(l_x/2,y,z) = u_y(-l_x/2,y,z)$ $u_z(l_x/2,y,z) = u_z(-l_x/2,-y,z)$
$y = \pm l_y/2$	$\bar{\mathbf{u}}_K = \tilde{\mathbf{A}}_K^{pbc}(x,y,z)\boldsymbol{\varepsilon}^M$	$u_x(x,l_y/2,z) = u_x(x,-l_y/2,z)$ $u_y(x,l_y/2,z) = u_y(x,-l_y/2,z)$ $u_z(x,l_y/2,z) = u_z(-x,-l_y/2,z)$

element. In accordance with Eq. 5.4 the displacements are prescribed as

$$\begin{bmatrix} \bar{u}_x \\ \bar{u}_y \end{bmatrix}_K = \underbrace{\begin{bmatrix} \Delta x & 0 & \frac{1}{2}\Delta y & \Delta x z & 0 & \frac{1}{2}\Delta y z & 0 & 0 \\ 0 & \Delta y & \frac{1}{2}\Delta x & 0 & \Delta y z & \frac{1}{2}\Delta x z & 0 & 0 \end{bmatrix}}_{\tilde{\mathbf{A}}_K^{pbc}} \boldsymbol{\varepsilon}^M. \quad (6.75)$$

Using the transition element the rotation of the lateral surfaces is prescribed following Eq. 5.8.

$$\begin{bmatrix} \bar{w}_x \\ \bar{w}_y \end{bmatrix}_L = \underbrace{\begin{bmatrix} 0 & 0 & 0 & 0 & -y & -\frac{1}{2}x & 0 & -1 \\ 0 & 0 & 0 & x & 0 & \frac{1}{2}y & 1 & 0 \end{bmatrix}}_{\check{\mathbf{A}}_L^{pbc}} \boldsymbol{\varepsilon}^M \quad (6.76)$$

Because for periodic boundary conditions $\mathbf{x}^+ = \mathbf{x}^- + \mathbf{F}(\mathbf{X}^+ - \mathbf{X}^-)$ applies, in Eq. 6.75 $\Delta \mathbf{X} = \mathbf{X}^+ - \mathbf{X}^-$ has been introduced. It corresponds to the in-plane dimensions of the RVE, thus $\Delta x = l_x$ and $\Delta y = l_y$.

For the periodic boundary conditions, the boundary displacements are linked symmetrically to the opposite lateral surface \bar{u}_x^{\parallel} and \bar{u}_y^{\parallel} , as illustrated in Fig. 6.10 (c). The vertical displacement \bar{u}_z^{\times} is again linked in an anti-symmetric manner to avoid rigid body rotations (see Fig. 6.10 (d)). The boundary and linking conditions are summarised in Table 6.3.

Chapter 7

Numerical Examples

The presented multiscale approach has been implemented in the academic finite element analysis software FEAP [163]. In the following the presented three types of boundary conditions will be tested and compared to each other by means of appropriate examples.

To begin with, the assumptions made for the derivation of the boundary conditions are verified by a set of preliminary, simple examples. First, the necessity of the MRC is shown with an example and the beam analogy from sec. 5.3.2 is justified. Afterwards, the shell boundary conditions are demarcated from the boundary conditions according to Gruttmann and Wagner [62]. Finally, all three types of boundary conditions are compared in terms of the way they apply shear deformations on the RVE and the shear stress distribution is examined.

As a next step, it is to be shown, that the proposed homogenisation approach yields correct homogenised stiffness components for an RVE. For the chosen examples the numerical solution is verified using analytical expressions. Following Eq. 3.32, the components of the symmetric material tangent matrix read

$$\hat{\mathbb{D}} = \begin{bmatrix} \hat{\mathbb{D}}_m & \hat{\mathbb{D}}_{mb} & \mathbf{0} \\ \hat{\mathbb{D}}_{mb}^T & \hat{\mathbb{D}}_b & \mathbf{0} \\ \mathbf{0} & \mathbf{0} & \hat{\mathbb{D}}_s \end{bmatrix} = \begin{bmatrix} D_m^{11} & D_m^{12} & D_m^{13} & D_{mb}^{11} & D_{mb}^{12} & D_{mb}^{13} & 0 & 0 \\ & D_m^{22} & D_m^{23} & D_{mb}^{21} & D_{mb}^{22} & D_{mb}^{23} & 0 & 0 \\ & & D_m^{33} & D_{mb}^{31} & D_{mb}^{32} & D_{mb}^{33} & 0 & 0 \\ & & & D_b^{11} & D_b^{12} & D_b^{13} & 0 & 0 \\ & & & & D_b^{22} & D_b^{23} & 0 & 0 \\ & & & & & D_b^{33} & 0 & 0 \\ & & & & & & D_s^{11} & D_s^{12} \\ & & & & & & & D_s^{22} \end{bmatrix}. \quad (7.1)$$

The obtained material tangent matrix should be independent of the exact choice of the RVE, i.e. its size, as long as it reflects the microstructural behaviour sufficiently. To investigate this issue, the RVE size is incrementally increased. Since the thickness of the RVE always corresponds to the macroscopic shell thickness, only the in-plane dimensions are adapted. Here, for demonstration purposes $L^{RVE} = l_x = l_y$ is chosen. Generally,

the two in-plane lengths of the RVE may be independent of each other. In the scope of this work global periodicity is assumed for all examples, such that an RVE of size $l_x \times l_y \times h^{RVE} = 1 \times 1 \times 1$ can be treated as *unit cell*. Nevertheless, it will be referred to as RVE in the following. To increase the in-plane dimensions of an RVE, multiple unit cells will be placed next to each other.

Once the homogenisation algorithm has been verified on the mesoscopic scale, multiscale simulations will be conducted. The coupled multiscale problems are compared to analytical and full-scale solutions. Displacement-based volume elements with LAGRANGE interpolation functions are used as reference.

On the macroscopic scale the 5/6-parameter, 4-node shell elements from sec. 6.1 are used for discretisation. The mesoscopic RVE is modelled and analysed using the SBIGA formulation from sec. 6.2. For this, the scaling centre is always chosen to be placed in the centre of mass of the respective geometry. The sections are discretised conforming and the same number of elements and the same polynomial degree are chosen in boundary and scaling direction ($n_b = n_c$, $p_b = p_c$). The mesoscopic discretisation can significantly influence the overall multiscale solution. A preliminary study was carried out to investigate the convergence behaviour of the RVE. In the following, the mesoscopic scale is considered as sufficiently fine discretised to yield converged solutions. Typically, $p_b = p_c = 3$ and $n_b = n_c = 8$ is chosen, if not stated otherwise. A throughout convergence study on the mesoscopic scale is out of the scope of this work. For refinement strategies in IGA one is referred to [41, 76] or to [30] for SBIGA.

Throughout the chapter, the units are presumed to be chosen consistent for each example and are therefore not explicitly stated. The data presented in the following are made available through OpARA [114].



7.1 Preliminary Examples

7.1.1 Necessity of the moment reduction constraint (MRC)

In sec. 5.3.2 it was discussed that the homogenised shear stiffness component D_s^{11} depends on the in-plane dimensions of the RVE. To investigate this problem and to underline the functionality of the proposed moment reduction constraint a homogeneous RVE is considered. The in-plane dimensions $L^{RVE} = l_x = l_y$ are chosen to be equal and are subsequently increased while the height $h^{RVE} = 1$ is kept constant. Linear-elastic material behaviour for the RVE is assumed with the properties summarised in Tab. 7.1.

The macroscopic transverse shear strain $\gamma_x^M = 0.2$ is applied on the RVE using the three proposed types of boundary conditions. The homogenised shear stiffness $(D_s^{11})^*$

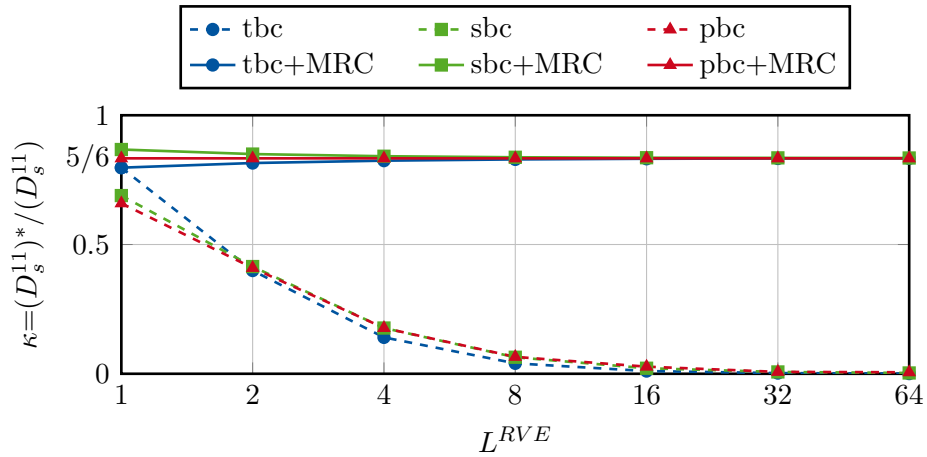


Figure 7.1: Shear correction factor for homogeneous RVE with varying in-plane dimension L^{RVE} for the three boundary conditions with and without the presented moment reduction constraint (MRC) ([117])

is compared to the analytical solution $D_s^{11} = Gh$. Note, that here the shear correction factor κ is neglected in the analytical solution. Thus, comparing the numerical solution to the analytical solution yields the shear correction factor

$$\kappa = \frac{(D_s^{11})^*}{D_s^{11}}. \quad (7.2)$$

In Fig. 7.1 the obtained shear correction factor is plotted for increasing RVE lengths $L^{RVE} = 1, 2, 4, 8, 16, 32, 64$ and for all three types of boundary conditions, both with and without the additional constraint. Without the moment reduction constraint the obtained homogenised stiffness $(D_s^{11})^*$ reduces to zero for increasing RVE size L^{RVE} . This is in line with the derivation in Eq. 5.27. Application of the MRC yields the expected shear correction factor $\kappa = 5/6$ for homogeneous cross-sections for increasing in-plane lengths.

Figure 7.2 shows the displacement in thickness direction u_z and the transverse shear stress distribution τ_{xz} for an RVE with dimensions $l_x \times l_y \times h^{RVE} = 32 \times 32 \times 1$ using periodic boundary conditions. In Fig. 7.2 (a) and (b) the results without using the moment reduction constraint are shown, while Fig. 7.2 (c) and (d) depict the results using the MRC for comparison. The displacement in thickness direction u_z in Fig. 7.2 (a) corresponds to the beam analogy from sec. 5.3.2, compare also Fig. 5.5. Figure 7.2 (b) shows that the transverse shear stress is non-uniformly distributed over the RVE and spurious stresses occur at the edges. Application of the proposed constraint reduces the displacement in

Table 7.1: Material properties for homogeneous RVE

Young's modulus E in N/mm^2	Poisson's ratio
100	0.3

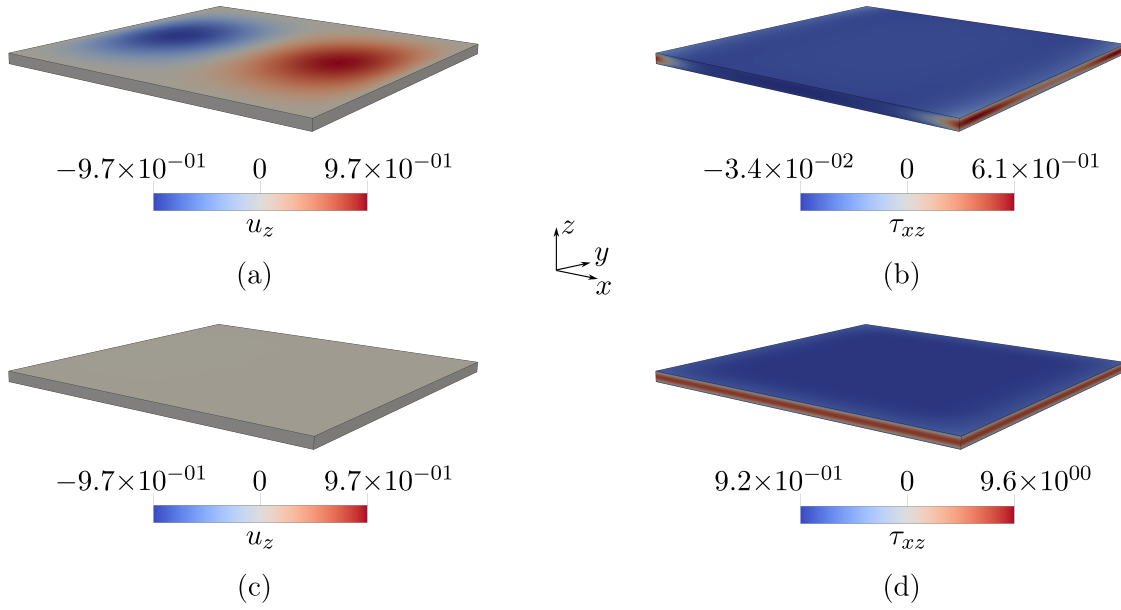


Figure 7.2: Homogeneous RVE with size $l_x \times l_y \times h^{RVE} = 32 \times 32 \times 1$ - $\gamma_x^M = 0.2$ using periodic boundary conditions (a) u_z without MRC (b) τ_{xz} without MRC (c) u_z with MRC (d) τ_{xz} with MRC

thickness direction and evokes a uniform shear stress distribution, see Fig. 7.2 (c) and (d). From the example it can be seen that the proposed moment reduction constraint is able to effectively reduce the dependence of the homogenised shear stiffness $(D_s^{11})^*$ on the RVE size L^{RVE} . Consequently, the unphysical displacement in thickness direction, which is associated to the coupled bending moment, is reduced and a uniform shear stress distribution is obtained. Therefore, the proposed constraint is incorporated in combination with every type of boundary condition (tbc, sbc or pbc) on the mesoscopic scale.

7.1.2 Adaption of Shell Boundary Conditions

As has been discussed in sec. 6.6.2 the boundary conditions from Gruttmann and Wagner [62] have to be adapted when RVEs are investigated where the inhomogeneities do not span the full width of the RVE. The necessity is to be presented by means of an exemplary RVE with cylindrical inclusion, as depicted in Fig. 7.3 (a). It has dimensions $l_x \times l_y \times h^{RVE} = 1 \times 1 \times 1$ and the inclusion is centrally aligned within the RVE, is of cylindrical shape and has radius $r = 0.25$. For both constituents linear-elastic material behaviour is assumed. The surrounding matrix material has the properties $E_M = 100$ and $\nu = 0.3$. The cylindrical inclusion, also referred to as *fibres*, behaves 100 times stiffer ($E_F = 10000$, $\nu = 0.3$).

The macroscopic membrane strain $\varepsilon_{yy}^M = 0.2$ is applied on the RVE using the boundary conditions from Gruttmann and Wagner [62] and using the proposed shell boundary conditions from sec. 6.6.2. The corresponding deformations are depicted in Fig. 7.3 (b)

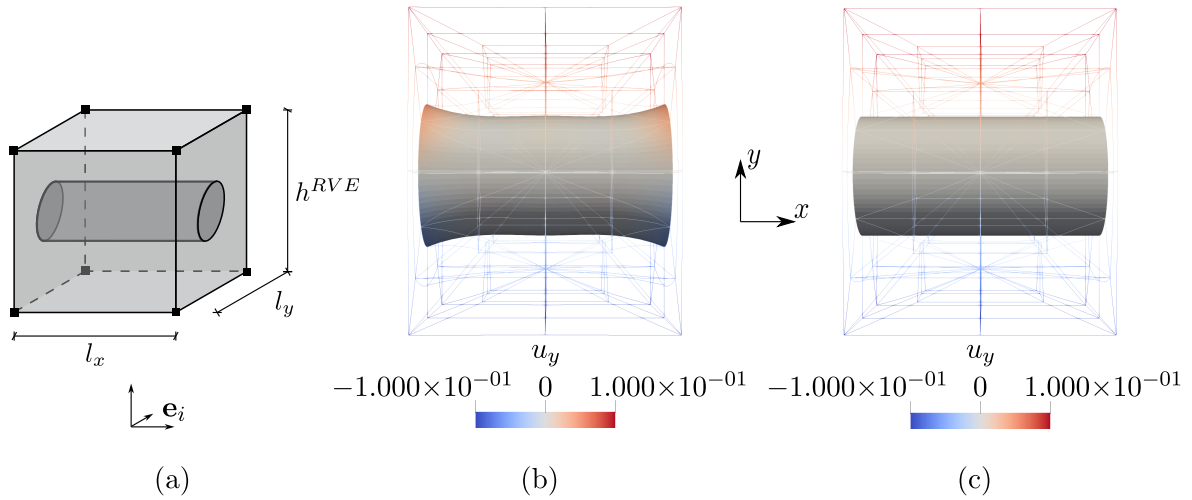


Figure 7.3: (a) Exemplary RVE with dimensions $l_x \times l_y \times h^{RVE} = 1 \times 1 \times 1$ and cylindrical inclusion (b) Deformation mode when ϵ_{yy}^M is applied using the boundary conditions from [62] (c) Deformation mode when ϵ_{yy}^M is applied using the proposed shell boundary conditions (Adapted from [117])

and (c), respectively. To examine the deformation of the inclusion, only the outline of the surrounding matrix is depicted.

From the applied macroscopic strain an extension in y -direction is expected, which can be observed in both configurations. Using the boundary conditions from [62] the in-plane displacements (here u_y on the surfaces where $x = \pm l_x/2$) are prescribed, which yields to unphysical behaviour for cases where the inhomogeneity does not span the whole width. This can be observed in Fig. 7.3 (b) as the inclusion deforms at the boundary. However, since the fibre material is significantly stiffer compared to the surrounding matrix material this is not reasonable. By relaxing this constraint using link conditions for the in-plane displacements (here u_y), as proposed in sec. 6.6.2, the overall deformation of the RVE remains the same while the inclusion does not deform at the boundaries, compare Fig. 7.3 (c).

The example shows, that linking the in-plane displacements, rather than prescribing them, allows more flexibility of the mesoscopic structures under consideration. It is an important enhancement of the boundary conditions proposed by [62].

7.1.3 Comparison of boundary conditions

To compare the three presented boundary conditions an RVE with dimensions $l_x \times l_y \times h^{RVE} = 1 \times 1 \times 1$ and homogeneous, linear-elastic material is examined. The RVE is shown in Fig. 7.4 and the material parameters are given in Table 7.1. One of the main differences of the boundary conditions is how the macroscopic transversal shear strains are applied. Either as displacements, as for the shell boundary conditions, or as rotation

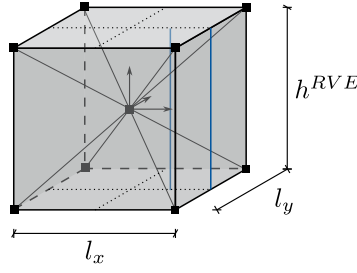


Figure 7.4: Exemplary homogeneous RVE with dimensions $l_x \times l_y \times h^{RVE} = 1 \times 1 \times 1$ with lines of evaluation indicated

of the lateral surface, as is the case for the traction and periodic boundary conditions. Therefore, in this preliminary example a transverse shear strain of $\gamma_x^M = 0.2$ is applied to emphasize the differences between the three boundary conditions.

For comparison the analytical shear stress distribution and the displacement can be derived.

$$\begin{aligned}\tau_{xz} &= \frac{3}{2} \frac{q}{A} \left(1 - \frac{4z^2}{h^{RVE^2}} \right) \\ &= \frac{3}{2} \frac{G \kappa h^{RVE} \gamma_x^M}{A} \left(1 - \frac{4z^2}{h^{RVE^2}} \right)\end{aligned}\quad (7.3)$$

where: A = cross-sectional area of lateral surface

G = shear modulus = $E/(2(1 + \nu))$

q = shear force = $G (\kappa h^{RVE}) \gamma_x^M$ see Eq. 5.23

κ = shear correction factor - for rectangular cross-sections $\kappa = 5/6$

Equation 7.3 reveals a quadratic shear stress distribution over the height of the RVE. To obtain the maximum shear stress it is evaluated at $z = 0$ and the geometric properties ($A = 1$, $h^{RVE} = 1$) are taken into account.

$$\tau_{xz,max}(z = 0) = \frac{3}{2} G \kappa \gamma_x^M = 9.615 \quad (7.4)$$

The displacement distribution can be obtained analytically by integrating the shear strain distribution $\gamma(z) = \tau(z)/G$ over the RVE thickness. It yields

$$u_x = \int_{h^{RVE}} \gamma(z) dz = \frac{5}{4} \gamma_x^M \left(z - \frac{4}{3} z^3 \right). \quad (7.5)$$

The maximum displacement occurs at the top and bottom surface, where $z = \pm h^{RVE}/2$,

$$u_{x,max}(z = \pm h^{RVE}/2) = \pm 0.08\bar{3}. \quad (7.6)$$

For the comparison of the boundary conditions the RVE is discretised with $n_c = 2$ and $n_b = 6$ elements and polynomial order $p_c = p_b = 4$. The macroscopic transversal shear strain $\gamma_x^M = 0.2$ is applied using all three types of boundary conditions, and the shear

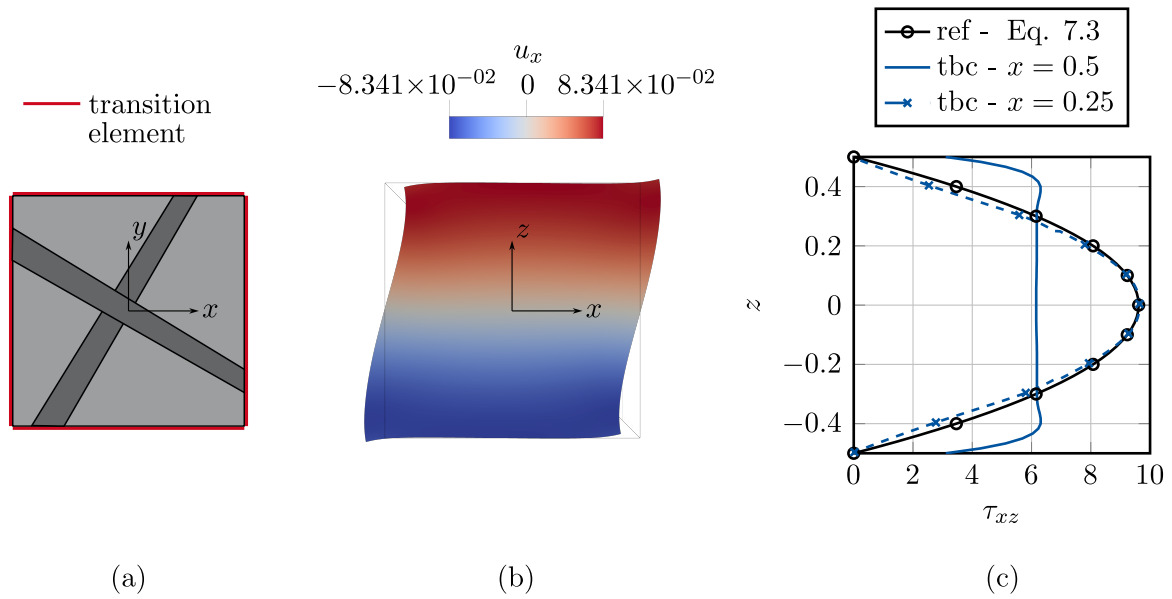


Figure 7.5: Traction boundary conditions - (a) plane view of RVE indicating the symmetry requirements (b) deformation figure for applied transverse shear strain $\gamma_x^M = 0.2$ (c) shear stress distribution over RVE height (Adapted from [117])

stress distribution, the deformation mode and the symmetry requirements are discussed. The shear stress distribution is evaluated over the thickness of the RVE at two positions ($(x,y) = (0.25,0)$ and $(x,y) = (0.5,0)$), which are indicated in Fig. 7.4.

In the following, only the shear deformation of the RVE is discussed. For the sake of completeness, the deformation modes for all macroscopic strains and all three types of boundary conditions are depicted in Appendix C. However, the deformation modes do not show any significant difference for the different boundary conditions, except for the transverse shear deformation.

Traction boundary conditions Using the traction boundary conditions the macroscopic strains are applied using the transition element on all four lateral faces of the RVE, indicated as red line in Fig. 7.5 (a). There is no link conditions applied on the control points of the RVE; therefore, no symmetry requirements have to be met. This is indicated in the $x - y$ -view of the RVE in Fig. 7.5 (a) by two randomly distributed inclusions.

Figure 7.5 (b) depicts the deformed RVE due to the transverse shear strain. From the figure two things become apparent: since the transition element applies the deformation in an integral sense using LAGRANGE multipliers, cross-sectional warping is permissible. Furthermore, the analytical maximum displacement from Eq. 7.6 is well approximated.

Examination of Fig. 7.5 (c) yields why the term *traction boundary condition* is justified. The shear stress distribution on the surface of the RVE, at $(x,y) = (0.5,0)$, is almost constant over the RVE height (here z -axis). Towards the centre of the RVE the boundary effects vanish and the shear stress parabola from Eq. 7.3 is well approximated. Addi-

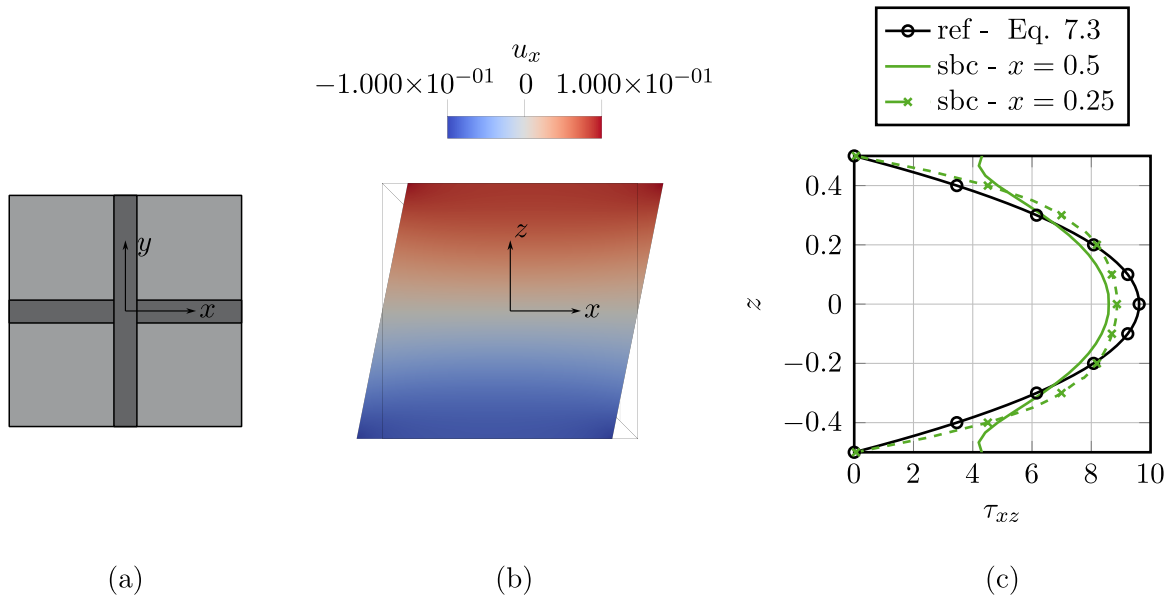


Figure 7.6: Shell boundary conditions - (a) plane view of RVE indicating the symmetry requirements (b) deformation figure for applied transverse shear strain $\gamma_x^M = 0.2$ (c) shear stress distribution over RVE height (Adapted from [117])

tionally, it can be observed that the stress at the top and bottom surface of the RVE ($z = \pm 0.5$) tends to zero, which indicates that the zero-traction boundary condition is fulfilled, which has been identified as characteristic feature of the shell homogenisation approach in sec. 5.1

Shell boundary conditions As has been described in sec. 6.6.2 the shell boundary conditions link the in-plane displacements symmetrically and the displacements in thickness direction antisymmetric. It follows that the $x - y$ -plane of the RVE must be axisymmetric to the x and y axes. In addition, the $x - y$ -plane must be point symmetric with respect to the centre. Thus, the two inclusions cannot be randomly distributed as can be seen from Fig. 7.6 (a).

Using the shell boundary conditions the out-of-plane displacement is directly prescribed. From Eq. 6.74 a linear relation between displacement and macroscopic strain becomes apparent, which can also be observed in the deformation figure in Fig. 7.6 (b). Thus, the cross-section cannot warp. Consequently, the maximum displacement $u_{x,max}$ directly corresponds to this linear relationship and overestimates the reference solution from Eq. 7.6.

Figure 7.6 (c) shows the shear stress distribution over the RVE height at the two locations for the shell boundary conditions. At both locations the parabolic shape from Eq. 7.3 is approximated. On the lateral surface, at $(x,y) = (0.5,0)$, the peak of the shear stress is too low and at the top and bottom surface ($z = \pm 0.5$) boundary effects can be observed. Towards the centre of the RVE the parabolic approximation of the shear stress distribution becomes more accurate and the shear stress at the top and bottom surface reduces to zero,

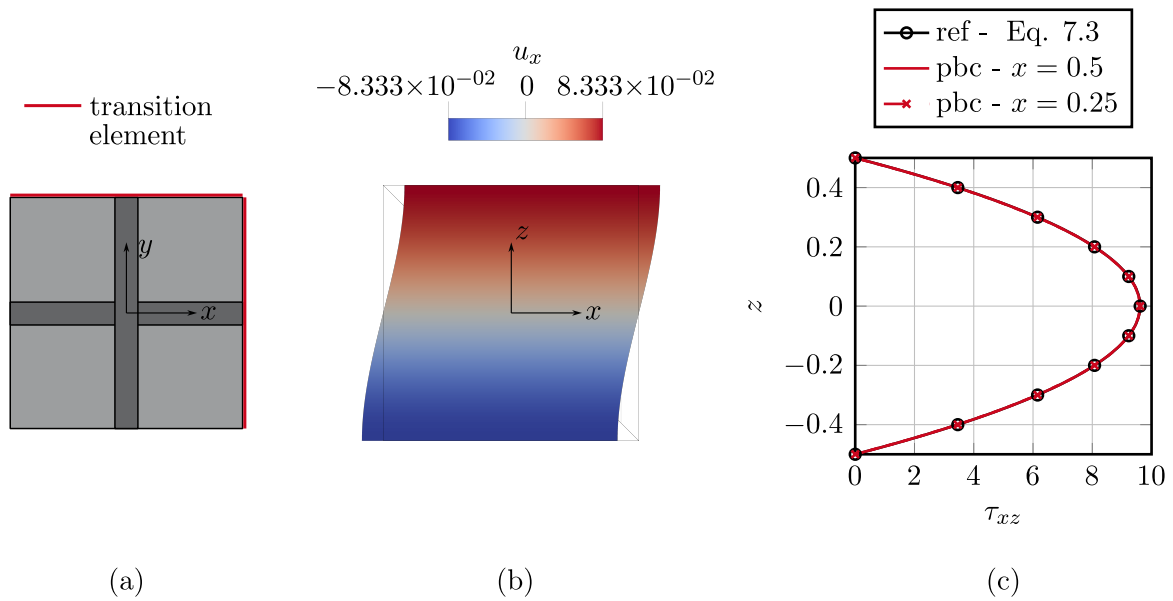


Figure 7.7: Periodic boundary conditions - (a) plane view of RVE indicating the symmetry requirements (b) deformation figure for applied transverse shear strain $\gamma_x^M = 0.2$ (c) shear stress distribution over RVE height (Adapted from [117])

thus the zero-traction boundary conditions are fulfilled.

Periodic boundary conditions The periodic boundary conditions require in-plane symmetry and point-symmetry of the RVE due to their link conditions. Similar to the shell boundary conditions any inclusions cannot be randomly distributed, see Fig. 7.7 (a).

Figure 7.7 (b) shows the deformation of the RVE for an applied transverse shear strain $\gamma_x^M = 0.2$. Because the transverse shear strains are applied as rotation of the lateral surface using the transition element, compare Eq. 6.76, warping of the cross-section is admissible. Furthermore, the maximum displacement corresponds to the analytical solution (Eq. 7.6).

Furthermore, using the periodic boundary conditions the shear stress distribution on the lateral surface and inside the RVE closely approximates the reference solution, see Fig. 7.7 (c). For both positions the shear stress is zero at the top and bottom surface of the RVE, which shows that the zero-traction boundary conditions are fulfilled.

Comparison From applying the transverse shear strains by means of all three boundary conditions on a homogeneous RVE some characteristic properties as well as similarities and differences have emerged.

- **Symmetry** The traction boundary conditions impose no symmetry requirement on the RVE, while shell and periodic boundary conditions require the RVEs to be symmetric with respect to the in-plane axes and symmetric to the centre point.

- **Shear deformation** Applying the transverse shear γ^M by means of the transition element (tbc and pbc) allows for cross-sectional warping, which is expected (compare Eq. 7.5).
- **Zero-traction boundary conditions** In sec. 5.1 the zero-traction boundary conditions at the top and bottom surface of the RVE have been identified as one characteristic feature of shell homogenisation. All three proposed types of boundary conditions fulfil this requirement.
- **Boundary effects of the shear stress distribution** Depending on the chosen boundary conditions the shear stress distribution on the RVE boundary will be approximated well (pbc) or not so well (tbc and sbc). Towards the centre of the RVE the boundary effects decay, such that the shear stress distribution is sufficiently approximated for all three types of boundary conditions.

7.2 Mesoscopic Scale

In the following, the homogenised material response is evaluated for a homogeneous and a layered RVE, because the stiffness values can be compared to analytical values. All three types of boundary conditions will be compared to each other. The homogenised stiffness components correspond to the shell material tangent and can be obtained analytically according to Eq. 3.32 - 3.34. The mid-surface of the RVE corresponds to the reference surface of the shell and is always chosen to be at $z = 0$, such that the coupling terms vanish ($\mathbb{D}_{mb} = \mathbf{0}$).

7.2.1 Homogeneous, linear-elastic RVE

The same homogenous RVE with dimensions $l_x \times l_y \times h^{RVE} = 1 \times 1 \times 1$ and linear-elastic material behaviour as in sec. 7.1.1 is investigated. The material properties are given in Tab. 7.1. Following Eq. 3.32 - 3.34, the analytical stiffness components are obtained as

$$\begin{aligned} D_m^{11} = D_m^{22} &= 109.8901, & D_b^{11} = D_b^{22} &= 9.1575, & D_s^{11} = D_s^{22} &= 38.4615, \\ D_m^{12} = D_m^{21} &= 32.9670, & D_b^{12} = D_b^{21} &= 2.7472, & & \\ D_m^{33} &= 38.4615, & D_b^{33} &= 3.2051. & & \end{aligned} \quad (7.7)$$

The shear correction factor of the homogeneous cross-section is $\kappa_{ref} = 5/6$.

The in-plane RVE size L^{RVE} is consecutively increased from $L^{RVE} = 1, 2, 4, 8, 16$ to $L^{RVE} = 32$. The homogenised stiffness components are compared to the analytical values from Eq. 7.7 and the results are summarised in Tab. 7.2.

Independent of the RVE size and of the chosen type of boundary conditions the membrane components \mathbb{D}_m as well as the bending components $D_b^{11} = D_b^{22}, D_b^{12}$ are obtained with machine precision (referred to as *exact* in Tab. 7.2).

The torsional stiffness D_b^{33} is obtained correctly using shell and periodic boundary conditions. Using traction boundary conditions a length dependence can be observed, see Fig. 7.8 (a). Nevertheless, with increasing RVE dimensions the stiffness converges towards the correct value.

The transverse shear stiffnesses $D_s^{11} = D_s^{22}$ are obtained correctly using periodic boundary conditions, irrespective of the RVE size. For the traction and shell boundary conditions

Table 7.2: Homogeneous RVE - comparison of stiffness components

	tbc	sbc	pbc
\mathbb{D}_m	exact	exact	exact
$D_b^{11}, D_b^{22}, D_b^{12}$	exact	exact	exact
D_b^{33}	Fig. 7.8 (a)	exact	exact
$D_s^{11} = D_s^{22}$	Fig. 7.8 (b)	Fig. 7.8 (b)	exact

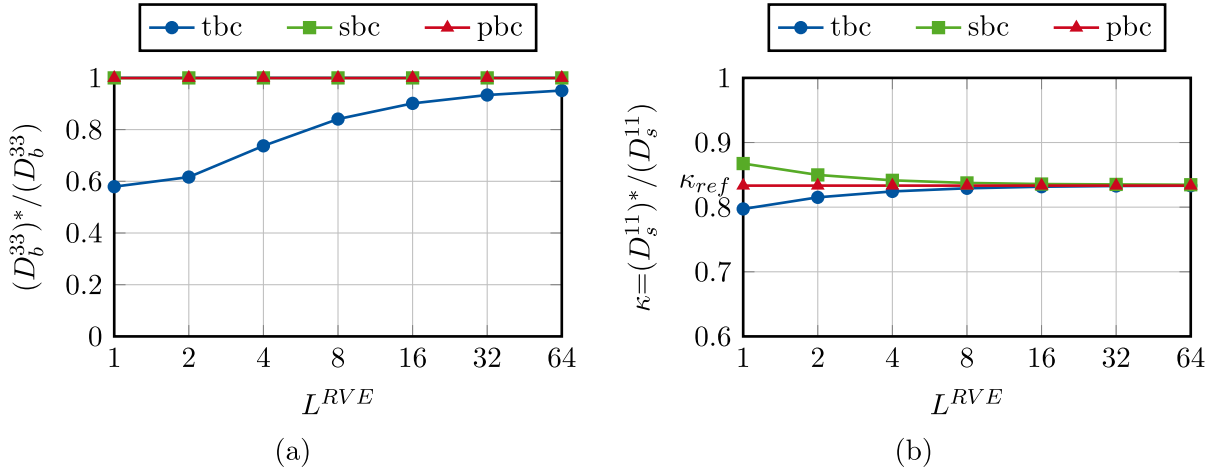


Figure 7.8: Homogeneous RVE - Influence of the RVE size on the homogenised (a) torsional stiffness $(D_b^{33})^*$ and the (b) transverse shear stiffness $(D_s^{11})^* = (D_s^{22})^*$ for different RVE boundary conditions ([117])

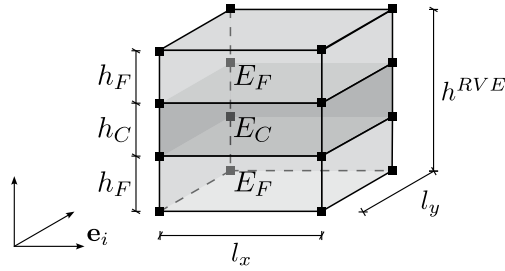


Figure 7.9: Layered RVE with dimensions $l_x \times l_y \times h^{RVE} = 1 \times 1 \times 1$ and $h_F = h_C = 1/3$

a length dependence is observed, which is visualized in Fig. 7.8 (b). As in sec. 7.1.1, the homogenised shear stiffness $(D_s^{11})^* = (D_s^{22})^*$ is compared to the analytical value $D_s^{11} = D_s^{22}$, such that the shear correction factor κ is obtained. In fact, Fig. 7.8 (b) corresponds to Fig. 7.1.

7.2.2 Layered, linear-elastic RVE

Next, an RVE with three layers is investigated. An exemplary RVE with dimensions $l_x \times l_y \times h^{RVE} = 1 \times 1 \times 1$ is depicted in Fig. 7.9, where the face layers and the core layer take equal thicknesses $h_F = h_C = 1/3$. The total height of the RVE reads $h^{RVE} = h_C + 2h_F$. Generally, the height of the different layers depends on the core fraction ρ_C . It describes the ratio between the core height and the RVE height $\rho_C = h_C/h^{RVE}$.

For both, core and face layers, linear-elastic material behaviour is assumed. The Young's moduli can be related to each other via $E_C = \alpha_M E_F$. An analytical solution for the shear correction factor can be calculated following Vlachoutsis [167].

Table 7.3: Material properties for layered RVE

Young's modulus in N/mm^2		Poisson's ratio
E_F	E_C	ν
100	1000	0.3

7.2.2.1 Effective properties

To begin with, the homogenised stiffness components for a layered RVE are to be examined for the three types of boundary conditions. The face layers and the core layer take equal thicknesses $h_F = h_C = 1/3$, while the total height of the RVE is kept at $h^{RVE} = 1$, compare Fig. 7.9. The in-plane dimensions are increased consecutively from $L^{RVE} = 1, 2, 4, 8, 16$ to 32.

The core is assumed to be stiffer than the face sheets ($\alpha_M = 10$). The material parameters are summarised in Table 7.3. Using Eq. 3.32 - 3.34, the analytical stiffness components are obtained as

$$\begin{aligned}
D_m^{11} = D_m^{22} &= 439.5604, & D_b^{11} = D_b^{22} &= 12.2100, & D_s^{11} = D_s^{22} &= 153.8462, \\
D_m^{12} = D_m^{21} &= 131.8681, & D_b^{12} = D_b^{21} &= 3.6630, & & \\
D_m^{33} &= 153.8462, & D_b^{33} &= 4.2735. & &
\end{aligned} \tag{7.8}$$

According to Vlachoutsis [167] the shear correction factors for layered cross-sections can be calculated analytically as

$$\kappa_{ref} = \frac{4}{9} \frac{T_1^2}{T_2 T_4}. \tag{7.9}$$

Where the quantities T_1, T_2 and T_4 are obtained from

$$\begin{aligned}
T_1(\rho_C) &= (1 - \rho_C^3) + \rho_C^3 \alpha_M \\
T_2(\rho_C) &= \frac{(1 - \rho_C)}{\alpha_M} + \rho_C \\
T_3(\rho_C) &= (1 - \rho_C^2)^2 + \frac{8}{15} \alpha_M^2 \rho_C^4 + \frac{4}{3} \alpha_M \rho_C^2 (1 - \rho_C^2). \\
T_4(\rho_C) &= A(\rho_C) \alpha_M + \rho_C T_3 \\
A(\rho_C) &= \frac{(1 - \rho_C)^3}{15} (3\rho_C^3 + 9\rho_C + 8)
\end{aligned} \tag{7.10}$$

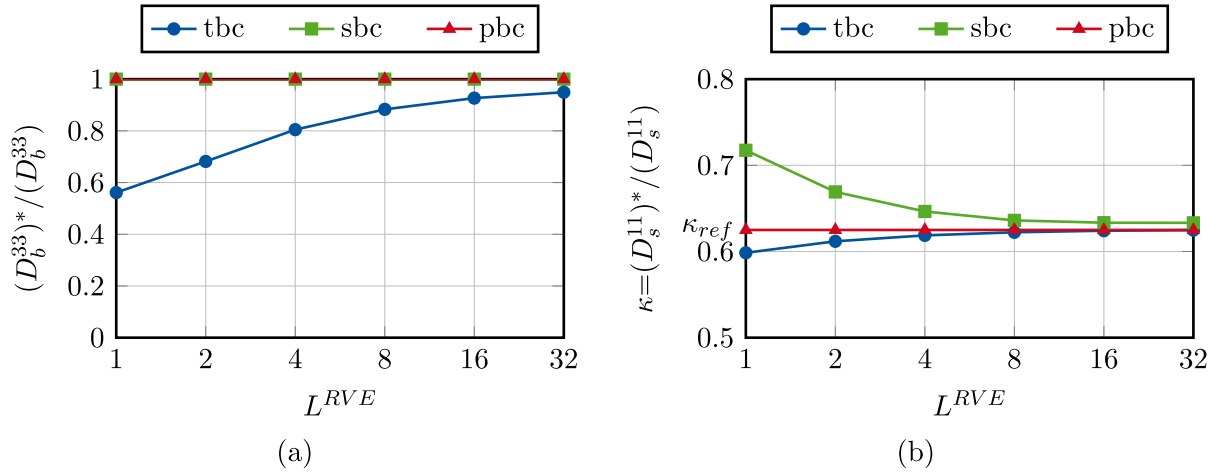
For the layered cross-section with $\rho_C = 1/3$ and $\alpha_M = 10$ the shear correction factor can be calculated as $\kappa_{ref} = 0.625$ [167].

The non-zero homogenised stiffness components are compared to the analytical solution from Eq. 7.8 and the findings are summarised in Table 7.4.

As for the homogeneous RVE, the membrane and bending components ($\mathbb{D}_m, D_b^{11}, D_b^{22}, D_b^{12}$) are obtained with machine precision, irrespective of the type of boundary conditions or

Table 7.4: Layered RVE - comparison of stiffness components

	tbc	sbc	pbc
\mathbb{D}_m	exact	exact	exact
$D_b^{11}, D_b^{22}, D_b^{12}$	exact	exact	exact
D_b^{33}	Fig. 7.10 (a)	exact	exact
$D_s^{11} = D_s^{22}$	Fig. 7.10 (b)	Fig. 7.10 (b)	exact

**Figure 7.10:** Layered RVE - Influence of the RVE size on the homogenised (a) bending stiffness $(D_b^{33})^*$ and the (b) transverse shear stiffness $(D_s^{11})^* = (D_s^{22})^*$ for different boundary conditions ([117])

the in-plane RVE size.

Again, shell and periodic boundary conditions yield the correct torsional stiffness D_b^{33} , while the traction boundary conditions possess a dependence on L^{RVE} , which can be observed in Fig. 7.10 (a). Similar to the homogeneous case, large in-plane dimensions are needed to obtain sufficient accuracy for the torsional stiffness.

Applying periodic boundary conditions also yields the homogenised transverse shear stiffnesses $(D_s^{11})^* = (D_s^{22})^*$ with sufficient accuracy. The length-dependent behaviour of the traction and shell boundary conditions are illustrated in Fig. 7.10 (b).

7.2.2.2 Shear correction factor

So far, the periodic boundary conditions have yielded the correct homogenised stiffness values irrespective of the RVE size for the homogeneous and the layered RVE. To investigate this further, the core fraction ρ_C and stiffness ratio α_M are varied and the shear correction factor κ is numerically obtained using periodic boundary conditions. Different core fractions $\rho_C = 0.2, 0.4, 0.6, 0.8$ and stiffness ratios $\alpha_M = 0.1, 0.5, 10$ are investigated. For the cases of $\rho_C = 0$ and $\rho_C = 1$ the RVE is homogeneous, which has been treated in sec. 7.2.1.

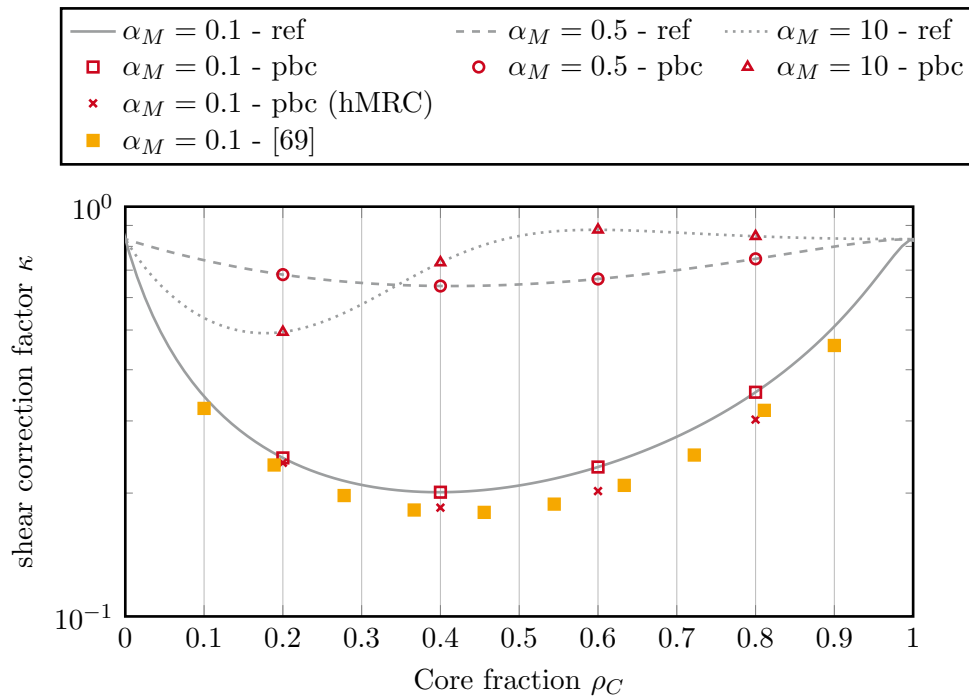


Figure 7.11: Layered RVE - Shear correction factor κ for varying core fractions ρ_C and stiffness ratios α_M ([117])

The results are presented in Fig. 7.11. Good agreement between the numerically obtained values using the periodic boundary conditions and the analytical reference from Vlachoutsis [167] can be observed.

The moment reduction constraint accounts for stiffness jumps over the thickness of the RVE, compare Eq. 6.54. To investigate the necessity of this, the constraint is treated as homogeneous (abbreviated as 'hMRC'). This is achieved by not accounting for the local stiffness contribution. The results are included in Fig. 7.11 for $\alpha_M = 0.1$. It becomes obvious, that the consideration of the local stiffness contribution over the RVE thickness is a significant feature of the proposed method, because the results incorporating the stiffness jumps lie considerably closer to the analytical values.

Additionally, the shear correction factors obtained by Hii and El Said [69] using a second-order homogenisation approach are included. These results show good agreement with the ones obtained when neglecting the stiffness jumps ('hMRC'). This indicates that the constraint on the fluctuation moment introduced by Hii and El Said [69] is comparable to the moment reduction constraint when disregarding the stiffness differences over the thickness of the RVE.

7.2.3 Findings from the mesoscopic scale

Before continuing with the evaluation of the homogenisation approach using coupled problems, the main findings of the investigations carried out on the mesoscopic scale are sum-

marised.

- **Torsional stiffness** The homogenised torsional stiffness component $(D_b^{33})^*$ exhibits a severe dependence on the RVE size when using the traction boundary conditions. For the smallest investigated RVE, the stiffness is underestimated by about 40%. For shell and periodic boundary conditions this effect does not occur.
- **Transversal shear stiffness** Using the shell and traction boundary conditions the homogenised transversal shear stiffness $(D_s^{11})^* = (D_s^{22})^*$ exhibits a dependence on the in-plane RVE size and is overestimated or underestimated, respectively, when investigating the smallest considered RVE ($L^{RVE} = 1$). The effect is more distinct for the layered RVE. The periodic boundary conditions yield the analytical shear stiffness independent of the RVE size.
- **Incorporation of stiffness in MRC** For the periodic boundary conditions and a layered RVE with different core fractions and stiffness ratios it has been shown, that the incorporation of the stiffness jumps in the moment reduction constraint is an essential characteristic of the approach which significantly improves the quality of the solution.

7.3 Multiscale

In the following, four coupled problems will be investigated with regard to the applicability of the proposed boundary conditions. A key feature of the approach is, that the macroscopic shell thickness always corresponds to the height of the RVE ($h^M = h^{RVE}$). For the examples where linear-elastic material behaviour is employed, the macroscopic material tangent matrix is obtained by homogenisation of a single RVE. In this way, the mesoscopic boundary value problem does not have to be solved in every integration point and every iteration step, which reduces the computational cost remarkably. The macroscopic shell is discretised comparably fine, because the focus of the examples is on the comparison of the three types of boundary conditions and the influence of the size of the RVE on the macroscopic behaviour. This motivates a fine discretisation on the macroscopic scale in order to avoid effects from macroscopic mesh refinement.

The main aim of this section is to evaluate to which extent the observed length dependencies from the mesoscopic scale are transferred to the macroscopic scale and which type of boundary condition is the most suitable for the homogenisation of shear-deformable shells.

7.3.1 Beam

To begin with, a clamped beam with two lengths $L = 6$ and $L = 20$ is examined, which serves as benchmark example. The height and width are kept constant at $h^M = 1$ and $B = 1$, respectively. It is clamped on one side and subjected to a distributed load $p = 1$ at the free end. The geometry of the macroscopic scale is shown in Fig. 7.12. Two different beam lengths are investigated, because it is known from beam theory that the influence of the shear stiffness on the overall bending behaviour is lower for larger length to height ratios.

Three different kinds of mesostructure are considered. A homogeneous RVE (Fig. 7.12 (a)), an RVE with circular inclusion parallel to the beam axis (Fig. 7.12 (b)) and an RVE with circular inclusion perpendicular to the same (Fig. 7.12 (c)). The inclusion has the radius $r = 0.106$ and is centrally aligned. This is physically meaningless for the example; however, it is considered sufficient, as it serves only to demonstrate the differences between the fibre orientations. The RVEs depicted in Fig. 7.12 have dimensions $l_x \times l_y \times h^{RVE} = 1 \times 1 \times 1$ and serve as unit cell.

The maximum vertical tip displacement $u_z(x = L)$ is used for comparison. For the homogeneous case the numerical solution is compared to the analytical solution. For the cases with circular inclusion a full-scale reference solution is obtained.

Homogeneous RVE For the homogeneous mesostructure, linear-elastic material behaviour with $E = 100$ and $\nu = 0.3$ is assumed. After conducting a convergence study, the

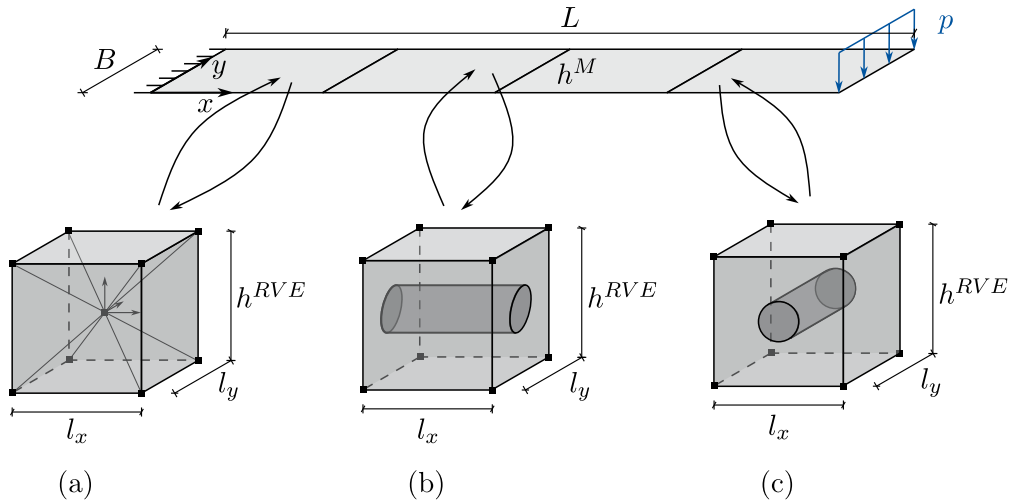


Figure 7.12: Clamped beam subjected to a load p with three different mesostructures - (a) homogeneous (b) longitudinally reinforced and (c) transversally reinforced

macroscopic shell is discretised using $32 \cdot L \times 1$ ($L \times B$) elements. The in-plane RVE size is chosen as $L^{RVE} = 1, 2, 4$ and 8 , and the height is constant at $h^{RVE} = 1$.

From beam kinematics, the analytical solution for the maximum vertical deflection u_z can be calculated as

$$u_z = u_{z,B} + u_{z,S} = \frac{FL^3}{3EI_T} + \frac{FL}{GA_s} \quad (7.11)$$

where: $F = p \cdot B$ = resulting load
 $I_T = (B(h^M)^3)/12$ = second moment of area
 $G = E/(2(1 + \nu))$ = shear modulus
 $A_s = \kappa A$ = cross-sectional shear area
 $\kappa = 5/6$ = shear correction factor for homogeneous cross-section.

The subscripts \square_B and \square_S denote the bending and shear contribution, respectively. The maximum deflections are obtained as

$$\begin{aligned} L = 6 : \quad u_{z,ref} &= 8.827 \quad \text{and} \\ L = 20 : \quad u_{z,ref} &= 320.624. \end{aligned} \quad (7.12)$$

The analytical solution from beam kinematics serves as reference solution in this case, because the shell kinematic is equivalent to the beam kinematic for this case. The numerical analysis is carried out using all three types of boundary conditions and different RVE sizes on mesoscopic level. The relative error to the analytical solution is plotted in Fig. 7.13 (a) for the beam with length $L = 6$ and in Fig. 7.13 (b) for $L = 20$. For both macroscopic beam lengths the solutions using traction and shell boundary conditions converge towards the analytical solution with increasing RVE size. The periodic boundary conditions yield a good fit to the reference solution irrespective of L^{RVE} and the macroscopic beam length. Note, that for the long beam the error is a factor ten smaller compared to the short beam.

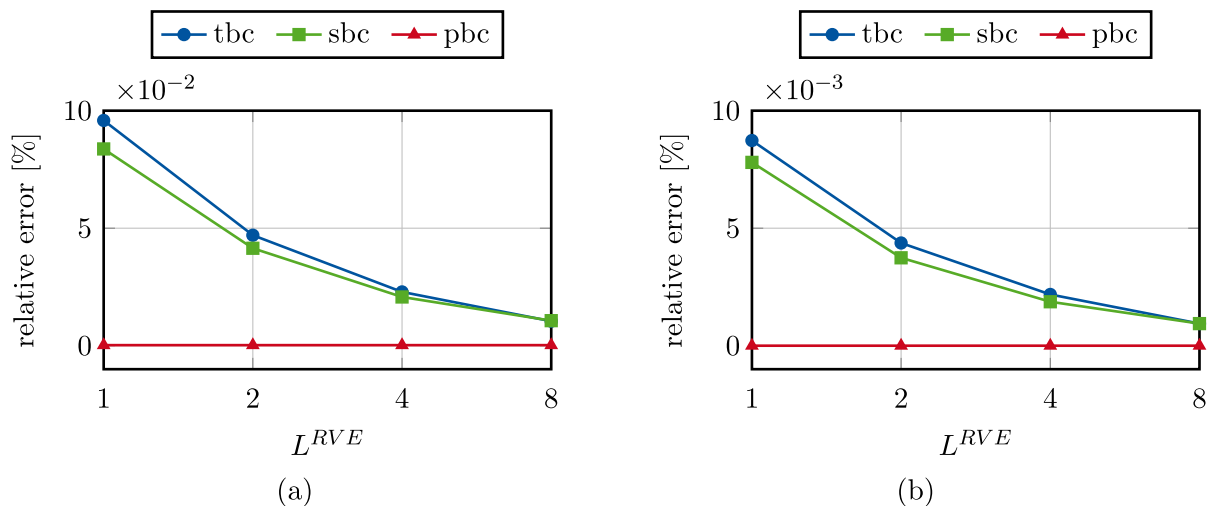


Figure 7.13: Relative error of the vertical tip displacement u_z for different RVE sizes and different boundary conditions for (a) $L = 6$ and (b) $L = 20$ ([117])

Table 7.5: Material properties for RVE with circular inclusion

	Matrix	Fibre
Young's modulus E	27,000	142,000
Poissons ratio ν	0.2	0.35

This can be related to the reduced influence of the shear stiffness on the overall bending behaviour, compare Eq. 7.11. The dependence of the solution on the RVE size for tbc and sbc can be directly related to the observed dependence of the shear stiffness on the RVE size, which has been investigated for a homogeneous RVE in sec. 7.2.1 and is documented in Fig. 7.8 (b). Nevertheless, for both beam configurations the error is considered small for all RVE sizes and boundary conditions. Therefore, one can conclude, that all proposed boundary conditions are suitable for the homogenisation of the shown example.

Longitudinally reinforced RVE In a next step, the RVE is reinforced using a cylindrical inclusion, referred to as 'fibre', parallel to the beam axis (see Fig. 7.12 (b)). Linear-elastic material behaviour is used for both components, matrix and fibre, where the fibre is assumed to be approximately five times stiffer than the surrounding material. The material parameters are summarised in Table 7.5. Again, the macroscopic shell is discretised using $32 \cdot L \times 1$ ($L \times B$) elements and the in-plane RVE size is chosen as $L^{RVE} = 1, 2, 4$ while the height is $h^{RVE} = 1$.

An analytical solution is not available for this configuration. Therefore, a full-scale model is used to obtain a reference solution. Standard hexahedral elements with quadratic shape functions are used. The beam is discretised using 38,160 elements and 126,864 elements for $L = 6$ and $L = 20$, respectively. The circumferential direction of the fibre is discretised using 16 elements. To compare the full-scale solution to the macroscopic shell the

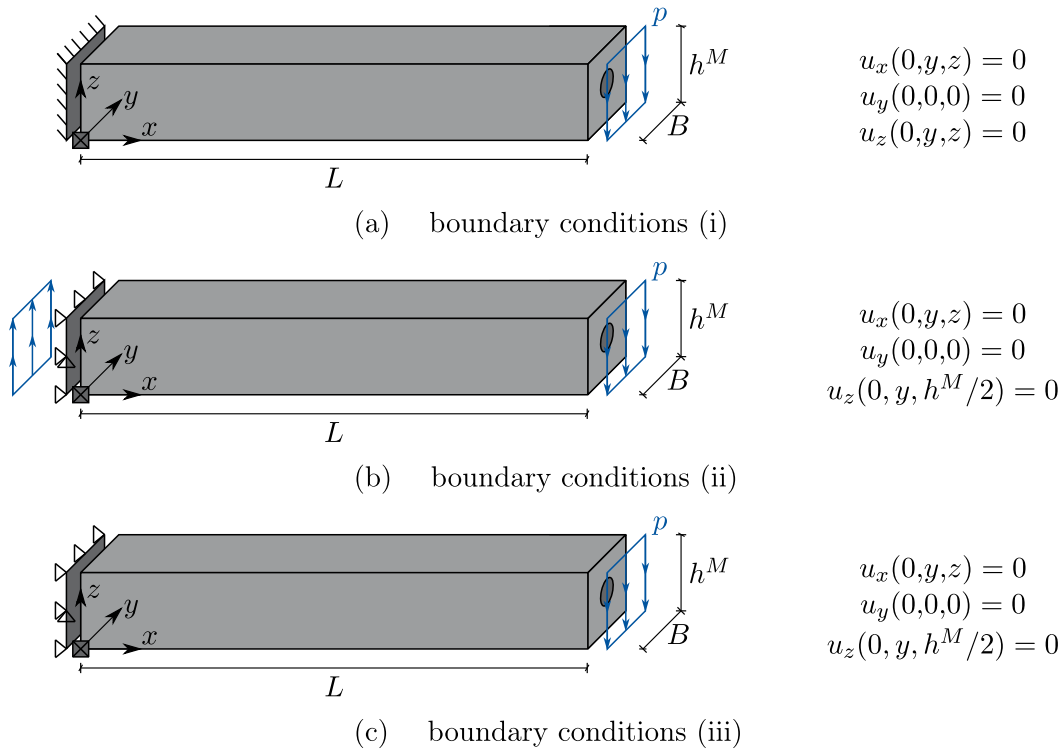


Figure 7.14: Full-scale volumetric model of the longitudinal reinforced beam with different boundary conditions (Adapted from [117])

boundary conditions have to be chosen carefully. Here, three different kinds of boundary conditions are proposed for the full-scale model. For illustration purposes, these are presented in Fig. 7.14. The displacement in length direction of the beam (x -axis) is fixed for all cases at $x = 0$. To allow for contraction of the cross-section of the beam, the displacement u_y is restrained at only one point at $x = 0$. The boundary conditions mainly differ in their treatment of the displacement u_z and are summarised in Fig. 7.14. For case (ii) the load p is additionally applied at the support in opposite direction to enforce global equilibrium in thickness direction. The three types of boundary conditions yield an upper (iii), a lower (i) and an intermediate (ii) value for the reference solution. The tip displacement u_z at $x = L$ is averaged over the thickness of the beam for comparison. The boundary conditions (i) and (iii) exhibit a stress singularity at $x = 0$. Therefore, the boundary conditions (ii) are best suited for the comparison to the beam kinematics. Nevertheless, boundary conditions (i) and (iii) are included to serve as an upper and lower bound.

The absolute displacement u_z is compared for the three mesoscopic boundary conditions and varying RVE size L^{RVE} for both beam lengths. The results for $L = 6$ and $L = 20$ are presented in Fig. 7.15 (a) and (b), respectively. The reference solutions from the full-scale model are indicated by dashed lines. All numerical solutions lie within the upper and lower bound of the reference, or in close proximity. For the shorter beam the upper and lower reference solution differ by 0.388%, while for the long beam the difference is 0.067%.

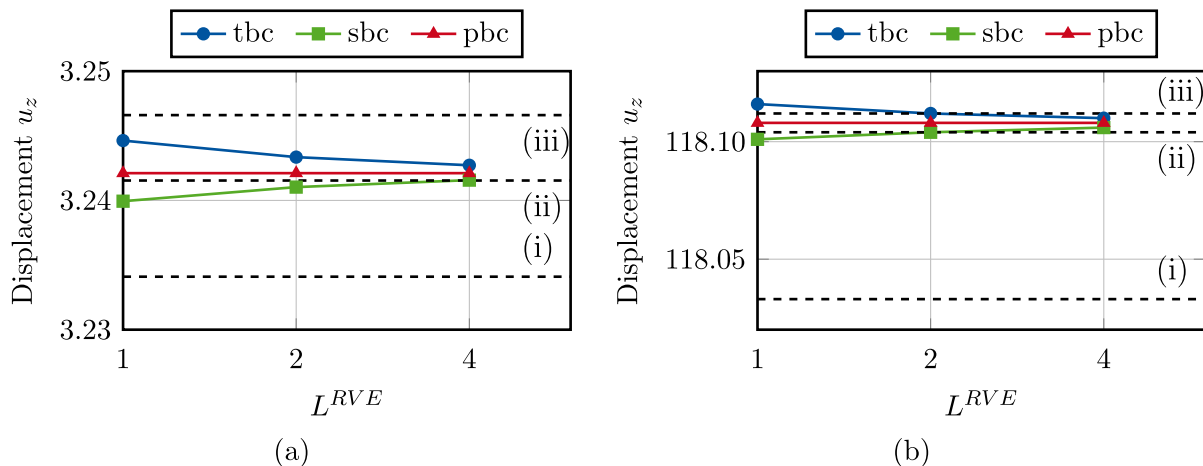


Figure 7.15: Comparison of vertical tip displacement u_z of longitudinally reinforced beam for different RVE sizes and different boundary conditions for (a) $L = 6$ and (b) $L = 20$ ([117])

The difference between the reference solutions is smaller for the long beam, because the effects from the boundary conditions decay over the length of the beam.

The traction and shell boundary conditions exhibit a dependence on the in-plane RVE size L^{RVE} , which is more severe for the shorter beam. This can, again, be related to the dependence of the shear stiffness on the RVE size, compare Figs. 7.8 (b) and 7.10 (b). The periodic boundary conditions yield constant results for varying RVE size.

Transversally reinforced RVE To conclude the beam example, the RVE is rotated by 90° about the z -axis so that the beam is now transversally reinforced, compare Fig. 7.12 (c). The geometric and material properties are kept constant, and the macroscopic and mesoscopic meshes for the numerical solution remain unchanged.

Consequently, also the full-scale reference solution is calculated using the same type of boundary conditions and the same number of elements (38,160 for $L = 6$ and 126,864 for $L = 20$).

As for the longitudinally reinforced RVE the absolute displacement u_z resulting from the homogenisation approach is compared to the full-scale solution. Again, the RVE boundary conditions and the in-plane size are varied. The results are illustrated in Fig. 7.16. The obtained numerical solutions lie within or in close proximity to the proposed reference solutions. In contrast to the longitudinally reinforced beam, now the displacement u_z exhibits a dependence on the in-plane RVE size L^{RVE} for all three types of mesoscopic boundary conditions. However, the dependence of the periodic boundary conditions is rather small compared to the traction and shell boundary conditions and is even less distinct for the long beam compared to the shorter one.

This observation can be explained by the assumption of a linear bending moment (see Fig. 5.5) for the moment reduction constraint. If inhomogeneities are present in the RVE, this linear assumption is not valid anymore, because differences in the RVE stiffness induce jumps in the moment distribution. However, as long as the inhomogeneity stretches

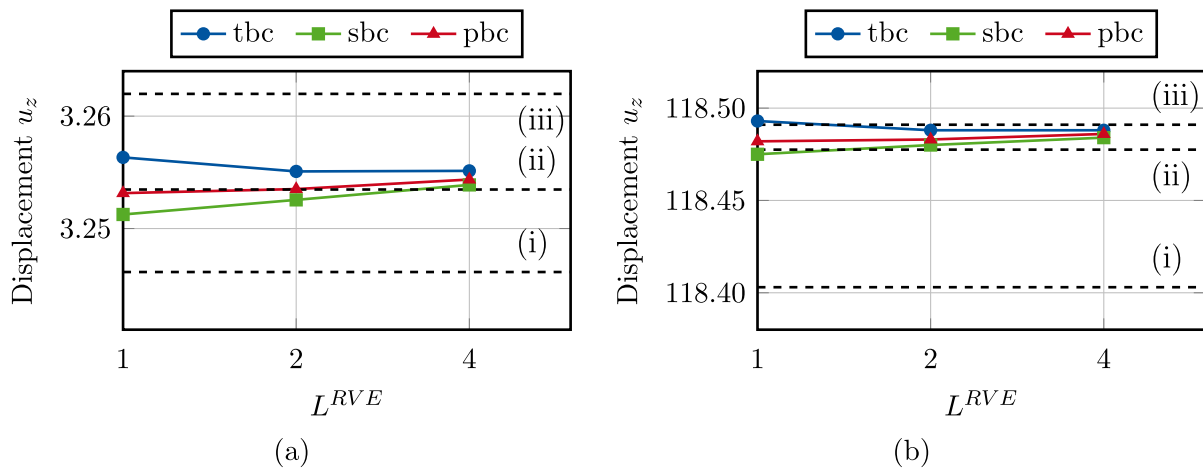


Figure 7.16: Comparison of vertical tip displacement u_z of transversally reinforced beam for different RVE sizes and different boundary conditions for (a) $L = 6$ and (b) $L = 20$ ([117])

over the whole width, the shear stiffness in the respective direction is calculated correctly. This is the case for the longitudinal reinforcement; therefore, the problem becomes only obvious when the beam is transversally reinforced. For the present example the induced length dependence is considered neglectable. However, for larger inclusions or larger stiffness differences between matrix and fibre the dependence on the RVE size may become more severe, even for the periodic boundary conditions. For these cases, the assumption of a linear moment distribution in the RVE is not sufficient.

7.3.2 Layered cylindrical shell

The quarter of a cylindrical composite shell is investigated, similar to [62]. Figure 7.17 illustrates the problem with length $L = 300$, radius $R = 100$ and thickness $h^M = 1$. The three layers have equal thicknesses and the angles are given by $[90^\circ/0^\circ/90^\circ]$, where 0° refers to the circumferential direction of the cylinder and 90° to the length direction. Transversal isotropic material behaviour is assumed, with

$$\begin{aligned}
 E_1 &= 125,000 & G_{12} &= 4,800 \\
 E_2 &= 7,400 & G_{23} &= 2,700. \\
 \nu_{12} &= 0.34
 \end{aligned} \tag{7.13}$$

Geometrical nonlinearity is considered for this example. The computations are performed displacement controlled by prescribing u_z , as indicated in Fig. 7.17. The force F is obtained as the reaction force for the prescribed displacement.

For the coupled computation the macroscopic, homogeneous shell is discretised using 16 elements in circumferential and length direction. The RVE accounts for the three layers, see Fig. 7.9, and each is discretised using $p_c = p_b = 4$ and $p_b = p_c = 2$.

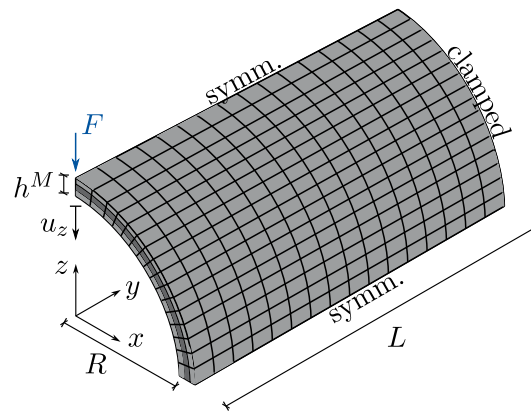


Figure 7.17: Quarter of layered, cylindrical shell ([116])

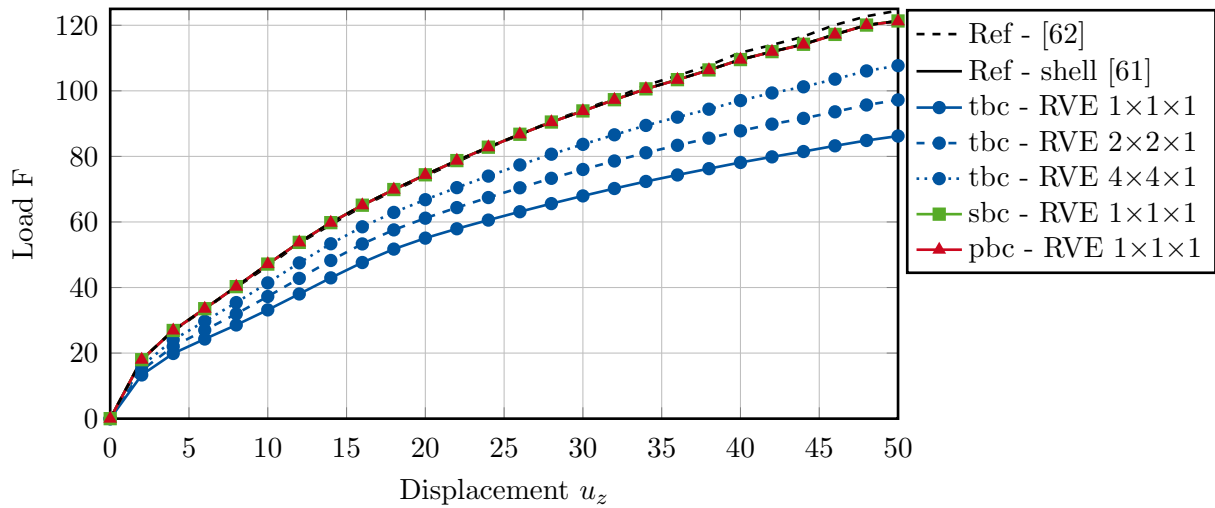


Figure 7.18: Load-displacement curve for the layered cylindrical shell for different mesoscopic boundary conditions ([117])

For comparison the homogenised solution from Gruttmann and Wagner [62] is used and a reference solution is calculated using the shell element [61] with four elements in thickness direction per layer.

Figure 7.18 presents the load-displacement curve. Using the periodic and shell boundary conditions with RVE size $1 \times 1 \times 1$ reveals good agreement with the reference solutions. The traction boundary conditions yield too soft behaviour; therefore, the in-plane RVE dimensions have been increased, which consecutively improves the accuracy of the solution.

The dependence of the accuracy of the solution on the RVE size using traction boundary conditions can be related to the torsional stiffness D_b^{33} , see Fig. 7.8 (a) and Fig. 7.10 (a). On the mesoscopic scale the torsional stiffness component was underestimated by $\approx 40\%$ for an RVE with size $1 \times 1 \times 1$. In this example the solution is $\approx 30\%$ too soft. Thus, the mesoscopic error is mitigated by the contribution of the other stiffness components.

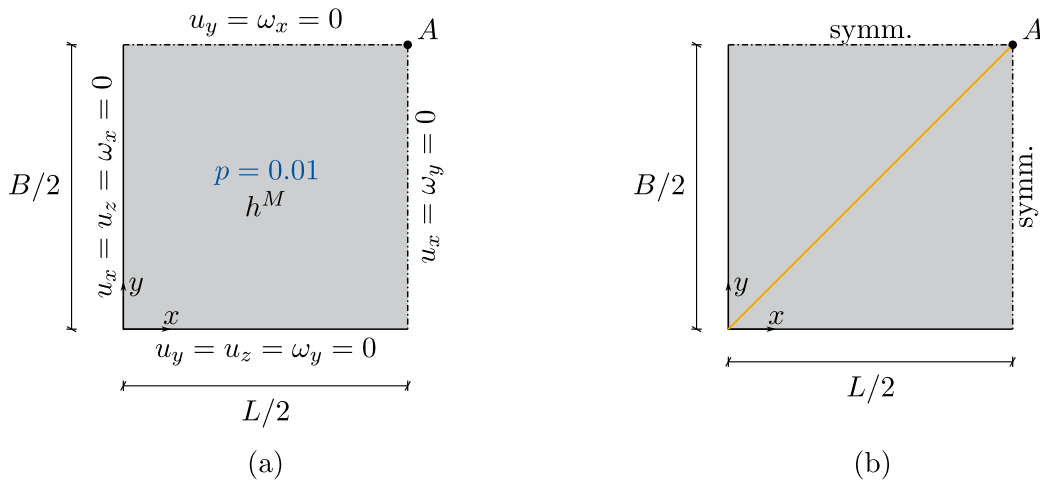


Figure 7.19: (a) Geometry and boundary conditions of quarter of the plate (b) Analytical yield line for the quarter of the plate

Nevertheless, the traction boundary conditions are not suitable for the homogenisation of the layered shell.

The shell and periodic boundary conditions are appropriate for the homogenisation of the curved shell including geometric nonlinearities.

7.3.3 Plate - elasto-plastic material

To investigate physically nonlinear behaviour a homogeneous, thin plate with dimensions $B = L = 100$ and thickness $h^M = 1$ is examined. Only a quarter of the plate is modelled, taking advantage of the symmetry. The geometry and the applied boundary conditions are illustrated in Fig. 7.19. As a material law, VON MISES plasticity is used. The parameters for the employed small strain elasto-plastic isotropic material are

$$E = 210,000, \quad \nu = 0 \quad \text{and} \quad f_{y,k} = 240. \quad (7.14)$$

$f_{y,k}$ denotes the yield stress. The plate is subjected to a uniformly distributed load $p = 0.01$.

For the coupled multiscale approach the macroscopic shell is discretised using 4×4 elements, while the RVE is discretised using $p_c = p_b = 3$ and $n_c = n_b = 2$ per direction. Here, the RVE size is chosen as $l_x \times l_y \times h^{RVE} = 1 \times 1 \times 1$.

The yield line theory (YLT) [180] is used for comparison. The plastic moment of the yield line can be derived as

$$m_{pl} = \frac{1}{4}(h^M)^2 f_{y,k} = 60 \quad (7.15)$$

and the expected yield line is illustrated in Fig. 7.19 (b). Using the principle of virtual displacements the ultimate load for the investigated simply supported plate, can be

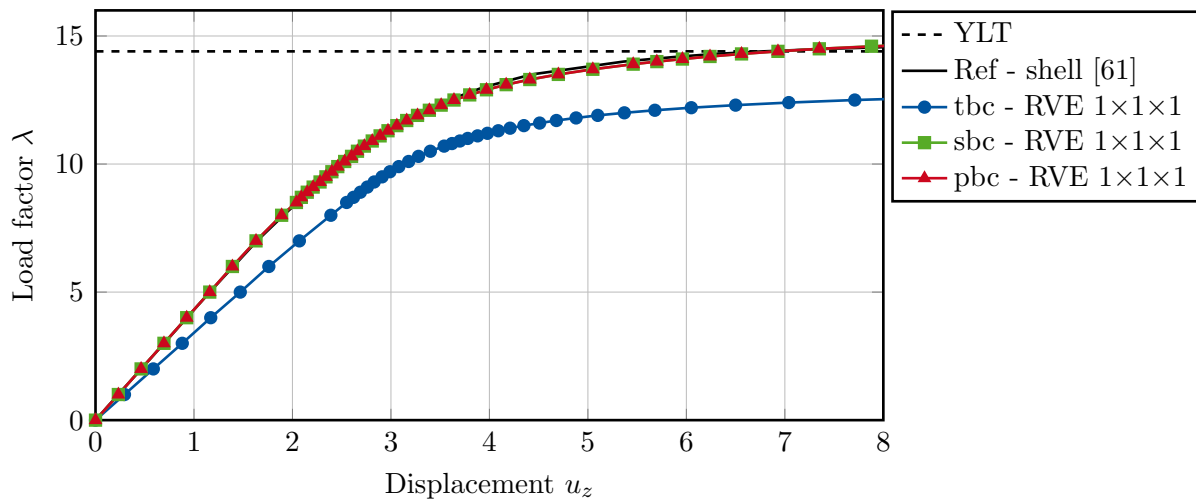


Figure 7.20: Load factor λ versus displacement u_z in the centre of the plate (Adapted from [117])

determined [180]. Hence, the ultimate load factor λ results in

$$\begin{aligned}\lambda p &= 24 \frac{m_{pl}}{L^2} = 0.144 \\ \lambda &= 14.4.\end{aligned}\tag{7.16}$$

Additional to the analytical load factor from yield line theory, the shell element from [61] with a fine discretisation of 32×32 elements for the in-plane directions and seven layers in thickness direction is used for comparison.

The results are presented in Fig. 7.20 by plotting the load factor λ versus the vertical displacement u_z in the centre of the plate (point A in Fig. 7.19). The coupled simulation using shell and periodic boundary conditions closely correlate with the shell formulation [61] used as reference. Furthermore, the ultimate load factor from yield line theory (compare Eq. 7.16) is closely approximated. Using the traction boundary conditions, the solution is underestimated by $\approx 14\%$. This can, again, be related to the torsional stiffness component, which can not be properly homogenised using traction boundary conditions on an RVE with size $1 \times 1 \times 1$. Here, the error using the traction boundary conditions is "only" $\approx 14\%$, compared to $\approx 30\%$ in the previous example of the cylindrical shell. This indicates, that the quality of the solution using traction boundary conditions largely depends upon the macroscopic problem and the principal load transfer mechanisms.

To further evaluate the coupled multiscale method, the contour plot and the distribution of the equivalent von Mises stress σ_v are examined at load factor $\lambda = 14.4$ for the shell formulation from [61], which is used as reference. Figure 7.21 (a) shows the displacement u_z of the quarter plate for the load factor $\lambda = 14.4$ in the boundary layers ($z = \pm(h^M)/2$) of the shell. A maximum displacement of $u_{z,max,ref} = 6.7824$ is obtained.

Figures 7.21 (b) and (c) illustrate the equivalent von Mises stress distribution at mid-

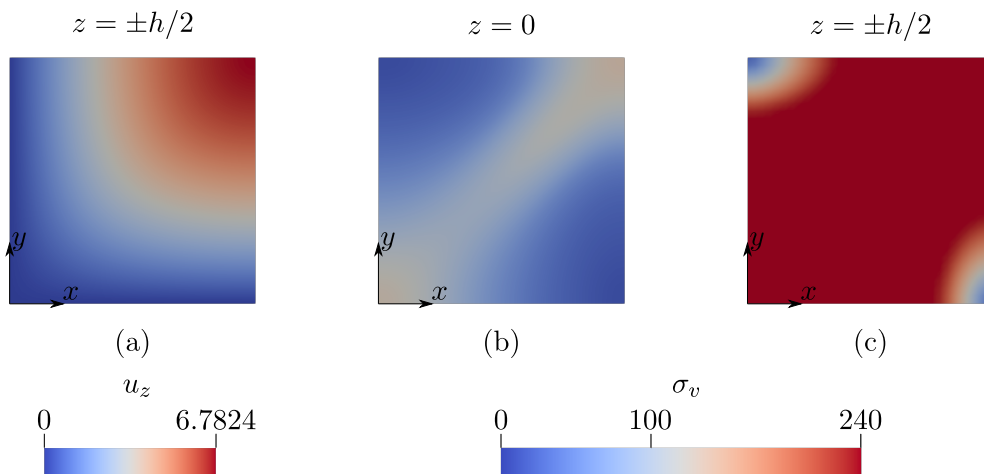


Figure 7.21: Reference shell formulation [61] - Contour plot at $\lambda = 14.4$ for (a) the displacement u_z at the boundary layers $z = \pm h/2$, (b) the von Mises stress σ_v at the mid-surface $z = 0$ and (c) the von Mises stress σ_v at the boundary layers $z = \pm h/2$ ([117])

surface ($z = 0$) and at the boundary layers ($z = \pm(h^M)/2$), respectively. It is observed that at the boundary layers the yield stress $f_{y,k} = 240$ is reached in most regions, while this is not the case for the mid-surface. At the mid-surface a region with increased equivalent stress spans diagonally across the plate. This corresponds to the expected yield line from yield line theory [180], compare Fig. 7.19 (b).

Figure 7.22 presents the contour plots for the macroscopic displacement u_z for the shell and the equivalent von Mises stress on four RVEs in the corners of the plate for load factor $\lambda = 14.4$. The result is obtained using periodic boundary conditions on the mesoscopic scale. The contour plots can be qualitatively compared to the ones of the reference shell formulation in Fig. 7.21. The displacement of the macroscopic shell shows good agreement with the displacement of the boundary layers of the reference shell. The maximum displacements $u_{z,max}$ and $u_{z,max,ref}$ correlate. Examination of the von Mises stress in the RVEs shows, that the RVEs placed on the diagonal from $(x,y) = (0,0)$ to $(x,y) = (L/2,B/2)$ have reached the yield stress in the boundary layers. The RVEs placed on the orthogonal diagonal have not reached the yield stress yet. This is in line with the yield line theory (Fig. 7.19 (b)) and the reference solution (Fig. 7.21 (b) and (c)).

7.3.4 Plate - longitudinally reinforced

As a last example, a plate with dimensions $B = L = 50$ and thickness $h^M = 1$ is investigated. It is unidirectionally reinforced using cylindrical inclusions with radius $r = 0.106$. These are positioned vertically centred and the distance between their centre lines is 1. For the mesoscopic scale, the RVE from sec. 7.3.1 (see Fig. 7.12) is employed. For comparison a full-scale model of the plate is used. As in the previous example, symmetry is exploited. Both models are illustrated in Fig. 7.23.

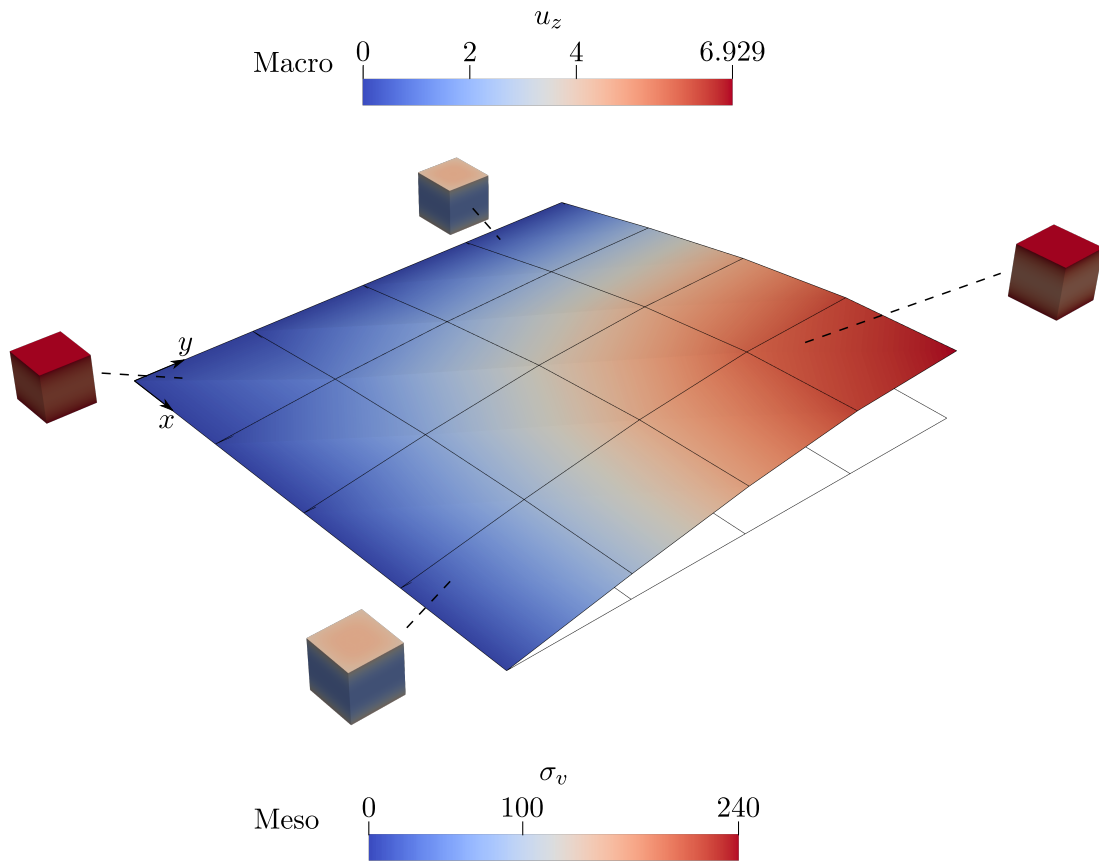


Figure 7.22: Coupled multiscale approach - Contour plot at $\lambda = 14.4$ for the displacement u_z of the macroscopic shell and the von Mises stress σ_v for four exemplary RVEs ([117])

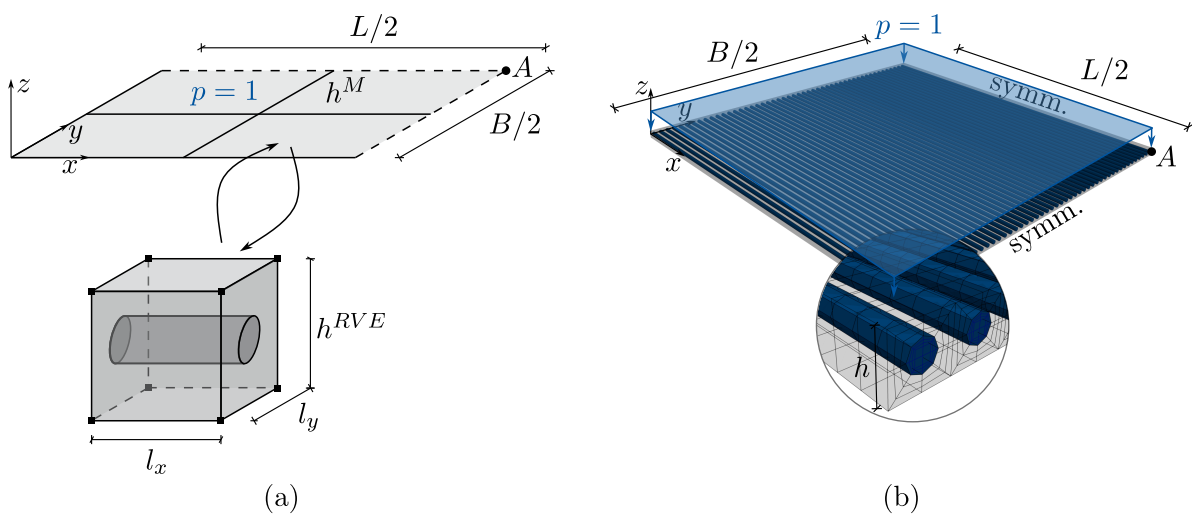


Figure 7.23: (a) Coupled multiscale model of the unidirectionally stiffened plate (b) Full-scale model of the plate used for comparison (Adapted from [117])

Table 7.6: Boundary conditions for the unidirectionally stiffened plate

(x,y)	Macroscale (FE ²)	Full-scale
$(0,y)$	$u_z = 0$	$u_z = 0$
$(x,0)$	$u_z = 0$	$u_z = 0$
$(L/2,y)$	$u_x = 0, \omega_y = 0$	$u_x = 0$
$(x,B/2)$	$u_y = 0, \omega_x = 0$	$u_y = 0$

The boundary conditions for the macroscopic shell and for the full-scale model are summarized in Tab. 7.6. For the volumetric model, the boundary conditions are applied at the mid-plane ($z = 0$, where $-h^M/2 \leq z \leq h^M/2$). Linear-elastic material behaviour is assumed for both constituents, the parameters can be taken from Tab. 7.5. The plate is subjected to a uniformly distributed load $p = 1$.

The coupled simulation is carried out using $numel = 2^2, 4^2, 8^2, 16^2, 32^2, 64^2, 128^2, 256^2, 512^2$ and 1024^2 macroscopic shell elements. The size of the RVE is varied from $L^{RVE} = 1, 2$ to 4 by placing multiple unit cells next to each other.

The full-scale model shown in Fig. 7.23 (b) yields a converged solution using 370,000 hexahedral elements with quadratic shape functions, where the circumferential direction of the circular inclusion is modelled with 16 elements.

The vertical displacement u_z in point A (see Fig. 7.23) is compared. Here, the reference solution from the full-scale model is obtained as the average of the displacement at the top surface of the shell ($z = h^M/2$) and the displacement of the mid-surface ($z = 0$). The average displacement is taken, because in the full-scale reference model thickness strains may occur, which are neglected in the shell formulation used to describe the macroscopic scale. It has to be kept in mind, that the solution from the volumetric model is not directly comparable to the solution obtained using a shell model, due to the different model assumptions regarding e.g. boundary and loading conditions. The chosen set of boundary and loading conditions have been verified by means of a homogeneous example.

Figure 7.24 plots the vertical displacement u_z versus the number of macroscopic shell elements ($numel$). In the upper diagram the results of all three types of boundary conditions (tbc, sbc and pbc) are shown for the three different RVE sizes. The lower diagram enlarges the dotted region and focuses on the homogenised results using the shell and periodic boundary conditions. It becomes obvious that the results using the traction boundary conditions strongly depend on the RVE size, while the results using the shell and periodic boundary conditions are independent of L^{RVE} . The overestimation of the displacement using the traction boundary conditions can be related to the underestimation of the torsional stiffness, compare Fig. 7.8 (a) and Fig. 7.10 (a). Furthermore, it can be seen, that the extensive macroscopic mesh refinement is not necessary. Even with coarser discretisation sufficient approximation of the reference solution is possible using shell or periodic boundary conditions.

To evaluate the efficiency of the proposed homogenisation approach, the complexity is used

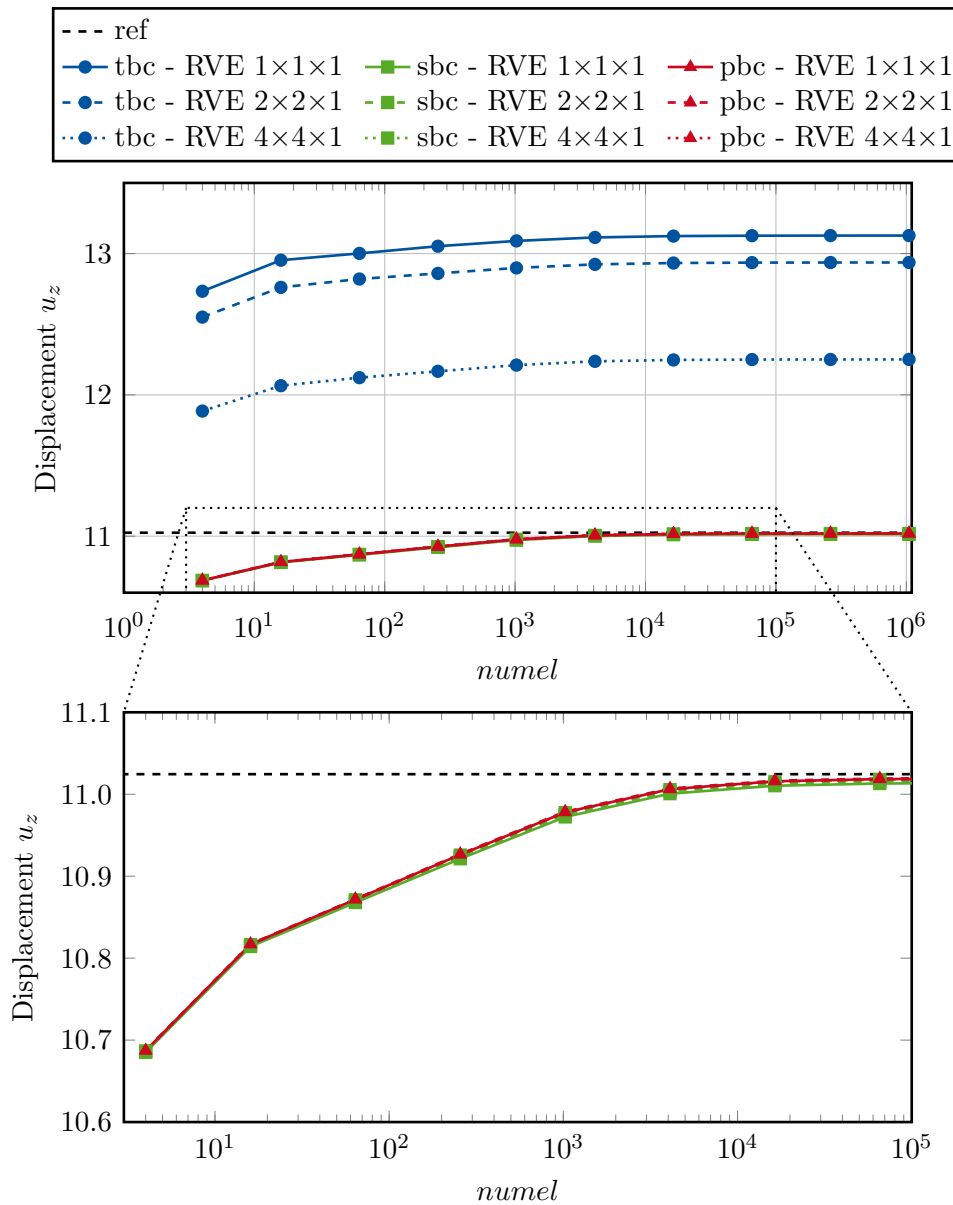


Figure 7.24: Comparison of the vertical displacement u_z in point A for different macroscopic discretisations, different mesoscopic boundary conditions and different RVE sizes ([117])

as a measure of the required computational effort. Considering the complete system of equations results in n^3 operations. If the sparsity is taken into account, e.g. by employing the PARDISO solver [149], this can be reduced to a complexity of about $\mathcal{O}(n^2)$ [58], where n denotes the number of equations. For the full-scale model, the total number of equations corresponds to all equations in the system n_{eq} . For the coupled approach, the total number of equations is a summation of the equations to be solved on the macroscopic and the mesoscopic scales, i.e. the number of equations describing the macroscopic problem (n_{eq}^M) and the number of equations of each RVE (n_{eq}^m) multiplied by the number of GAUSS integration points (n_{GP}). Table 7.7 compares the complexity of the two approaches. The error of the numerical solution with respect to the full-scale reference solution is

Table 7.7: Numerical complexity of the different approaches

FE ²	Full-scale
$\mathcal{O}\left((n_{eq}^M)^2 + n_{GP} \cdot (n_{eq}^m)^2\right)$	$\mathcal{O}(n_{eq}^2)$

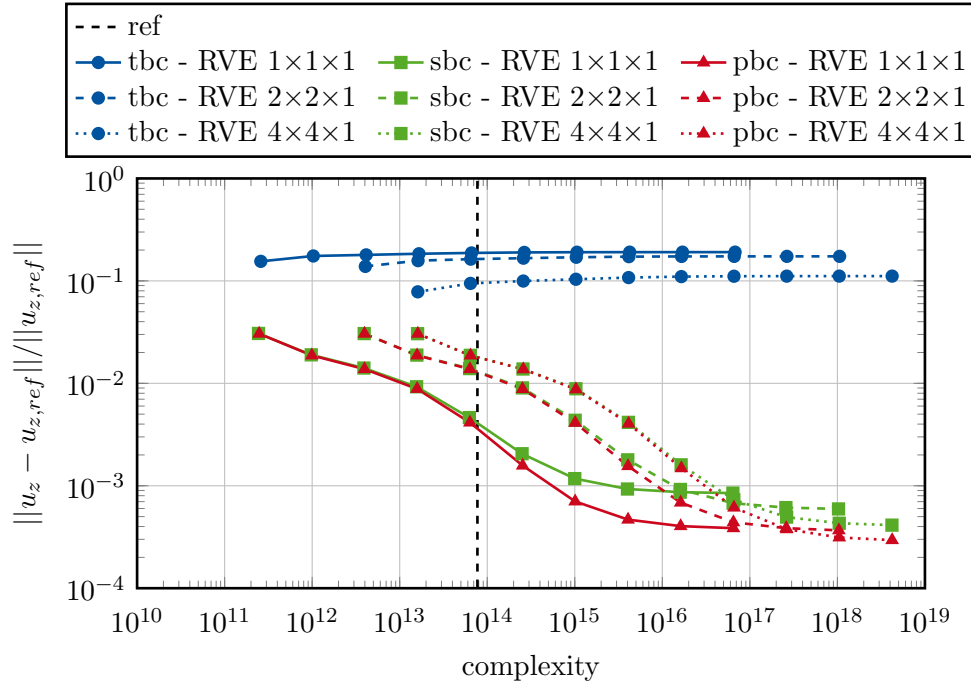


Figure 7.25: Error of the FE² solution compared to the full-scale reference solution plotted against the complexity of the system of equations for different boundary conditions and RVE sizes ([117])

plotted against the complexity in Fig. 7.25. Again, different boundary conditions and different RVE sizes are analysed. The dashed, vertical line represents the complexity of the full-scale reference solution ($\mathcal{O}(n_{eq}^2)_{ref} = 7.7252 \times 10^{13}$). In this figure, increasing complexity corresponds to finer discretisation of the macroscopic shell. As has been also observed in Fig. 7.24, the traction boundary conditions fail to sufficiently approximate the displacement u_z , even with increasing RVE size. When using shell boundary conditions, increasing the RVE size increases the accuracy of the solution. More significantly, however, the complexity increases. For the periodic boundary conditions, the RVE size has almost no effect on the accuracy of the displacement u_z compared to the reference. Solely the complexity increases remarkably.

From Fig. 7.25 it can be seen, that using a coupled model with the same complexity as the full-scale model, which corresponds to a macroscopic discretisation of 32×32 elements and an RVE size of $1 \times 1 \times 1$, the error is around 0.4%. This can be considered a good agreement, bearing in mind that there are naturally some differences between the shell and the volumetric model due to the kinematic assumptions.

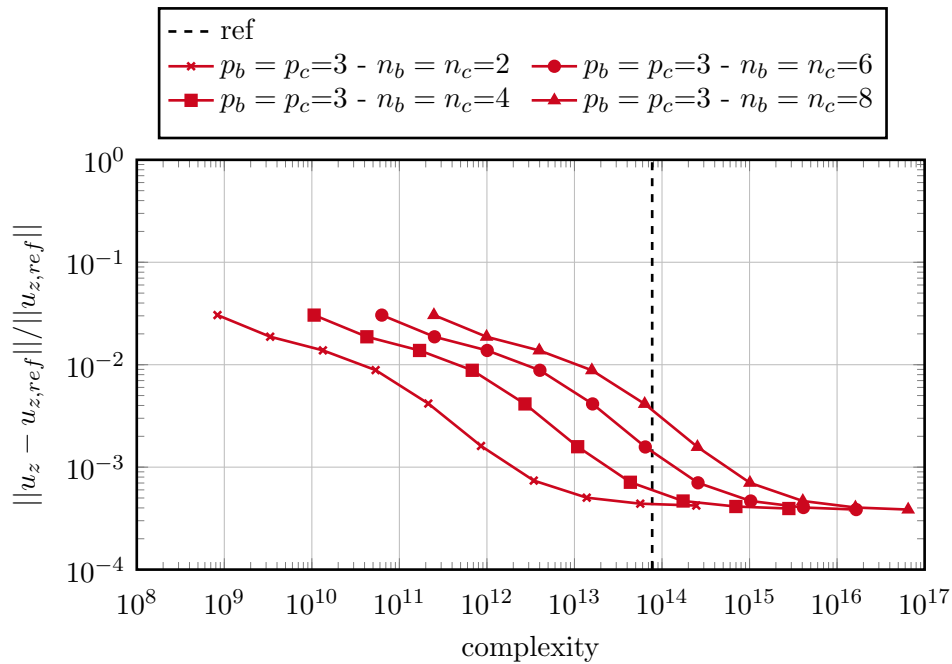


Figure 7.26: Error of the FE² solution compared to the full-scale reference solution plotted against the complexity of the system of equations for periodic boundary conditions and different RVE discretisations ([117])

To conclude this example, the discretisation of the RVE is closer examined. So far all calculations have been carried out using polynomial order $p_b = p_c = 3$ and $n_c = n_b = 8$ elements. However, the more efficient the mesoscale is discretised, the more efficient is the solution of the coupled problem. An RVE with size $l_x = l_y = h^{RVE} = 1 \times 1 \times 1$ is employed in the homogenisation framework using periodic boundary conditions. The number of elements on the RVE is varied from $n_c = n_b = 2, 4, 6$ to 8. Again, the error of the numerical solution is plotted against the complexity of the algorithm, see Fig. 7.26. It can be noticed, that the mesoscopic discretisation does not significantly improve the quality of the solution, but rather influences the overall complexity. Reducing the number of elements from $n_c = n_b = 8$ to $n_c = n_b = 2$, the same accuracy (error of $\approx 0.4\%$) can be kept, while the complexity is approximately 400 times lower. Thus, it can be concluded that the mesoscopic discretisation significantly influences the complexity of the problem. In the case of periodic boundary conditions, the macroscopic discretisation has a stronger influence on the accuracy of the solution than the mesoscopic discretisation. Therefore, a good balance between macroscopic and mesoscopic mesh refinement has to be found in order to obtain the most accurate results at low complexity.

7.4 Discussion

The presented multiscale examples have shown that the proposed approach is able to homogenise planar and curved macroscopic structures with different mesoscopic compositions, incorporating geometrically and physically nonlinear behaviour. To summarise the numerical examples, the main findings are discussed taking the results from the mesoscopic scale into account.

Effect of the mesoscopic length dependence of the RVE on the macroscopic structural behaviour

It can be concluded, that the dependence of the stiffness components on the in-plane RVE size influences the macroscopic structural behaviour. However, the extent to which the macroscopic behaviour is affected depends largely on the problem definition. For example, the more slender the shell structure, the less distinct is the length dependent behaviour of the shear contribution as seen in sec. 7.3.1. Furthermore, the RVE size dependence of the individual stiffness component is mitigated due to the influence of several stiffness components on the macroscopic structural behaviour.

Applicability of the moment reduction constraint

The moment reduction constraint has proven to effectively reduce the dependence of the homogenised shear stiffness on the in-plane RVE size. However, it is based on the assumption of a linear moment distribution along each RVE axis. This assumption is only valid, if the material is homogeneously distributed along the axis. Nevertheless, for small inclusions and moderate stiffness jumps, the constraint is still able to reduce the dependence. It has to be kept in mind, that this assumption may not be valid if highly heterogeneous RVEs are to be investigated.

Periodic boundary conditions

For the shown examples the periodic boundary conditions give the most accurate results irrespective of the RVE size. Nevertheless, they require the RVE to be symmetric with respect to the in-plane axes and symmetric to the centre point, which is a major restriction on the choice of RVE.

Shell boundary conditions

The shell boundary conditions yield good results, as long as the shear stiffness is not dominating the problem. In comparison to the periodic boundary conditions they are less universal, because attention has to be paid which load transfer mechanisms occur in the investigated macroscopic shell. The advantage of the shell boundary conditions is, that even though they also require symmetry, they are easier to apply on the RVE, because they do not require any linking conditions.

Traction boundary conditions

It has been shown, that problems with a dominant torsional stiffness contribution cannot be solved with sufficient accuracy using traction boundary conditions. Even increasing

the size of the RVE may not yield adequate results. Nevertheless, for problems where the torsional stiffness does not dominate, traction boundary conditions are still valuable. And they offer a major advantage compared to the shell and periodic boundary conditions: they do not impose any symmetry requirements on the RVE, thus giving the RVE model a high degree of flexibility.

Influence of the macroscopic and mesoscopic discretisation

This aspect has only been investigated in detail for the periodic boundary conditions, but it is assumed that the results can be generalized for the other type of boundary conditions. For the investigated periodic boundary conditions, a finer macroscopic discretisation with a coarser mesoscopic discretisation is preferable, in terms of accuracy of the solution and in terms of complexity of the system of equations.

Chapter 8

Image-based modelling

So far, a numerical homogenisation approach for shear-deformable shells has been proposed and verified using academic examples. As has been discussed in chap. 1, shell structures are applied in many different fields and composite materials are often used to maximize their load-bearing behaviour. To incorporate detailed information about the mesostructure, computed tomography data can be used.

Computed tomography (CT) is a three-dimensional imaging technique, which allows the digital reconstruction of an object. The object is exposed to X-radiation and detectors measure the X-ray attenuation of the material. The projection data is gathered as axial slices. These can be used for the three-dimensional digital reconstruction of the object. Compared to classical CT, commonly known for example from medical engineering, μ -CT offers a higher resolution. Therefore, μ -CT is ideal for the non-destructive analysis of objects.

In civil engineering, textile-reinforced concrete can be used for the construction of shell structures. Due to the increased corrosion resistance of the textile, compared to steel reinforcement, the component thickness can be significantly reduced. However, slender constructions require high precision in the reinforcement placement. Therefore, μ -CT data can be used to evaluate the position of the textile within the concrete shell.

A procedure to incorporate the μ -CT data of textile-reinforced concrete specimens in the shell homogenisation approach has been proposed in [173]. In the following, the procedure to obtain μ -CT data of textile-reinforced concrete specimens is briefly explained. From the digital reconstruction the textile needs to be extracted. This is done using machine learning techniques. The information of the extracted textile can be incorporated into the RVE. The developed approach from [173] will be recapitulated. It has to be noted, that the results presented were developed within the CRC/TRR 280 in cooperation with Franz Wagner from the Institute of Photogrammetry and Remote Sensing at TU Dresden. The steps from the generation of the μ -CT data to the representation of the extracted textile were investigated at TU Dresden.

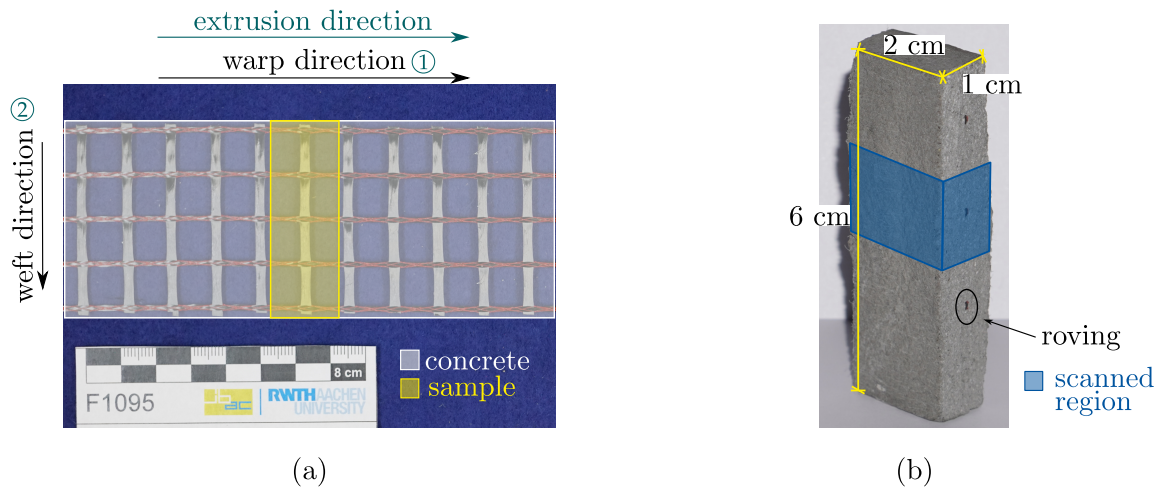


Figure 8.1: (a) Schematic illustration of the extruded specimen with extrusion direction indicated (b) Sample with region scanned by μ -CT device indicated (Adapted from [173])

8.1 Microtomography and Roving Extraction

8.1.1 Specimen

The procedure for embedding μ -CT data in the RVE is described in the following using one specimen as example. It was produced as part of the CRC/TRR 280 using extrusion, an innovative manufacturing technique. More information on the production process using a Laboratory Mortar Extruder (LabMorTex) can be found in [81, 82, 83]. During extrusion, concrete and textile are continuously pressed through a rectangular mouthpiece, forming a component of $6 \times X \times 1 \text{ cm}^3$, where X denotes the extrusion length. From this component, a sample of size $6 \times 2 \times 1 \text{ cm}^3$ is taken. Figure 8.1 (a) illustrates the textile grid which is used for extrusion. The weft and warp direction, as well as the extrusion direction and the sample size are specified. Additionally, the sample to be examined is shown in Fig. 8.1 (b).

In the sample, the textile SITgrid044 VL by WILHELM KNEITZ Solutions in Textile GmbH is embedded. It is a biaxial carbon textile, which means that the rovings in warp and weft direction are positioned perpendicular to each other. The position of the rovings is fixed with a knitting thread, which runs along the roving in warp direction and is indicated in red in Fig. 8.1 (a). The textile has a yarn spacing of 16.2 mm (warp) \times 14.7 mm (weft). The yarn spacing is defined as the distance between the centre lines of two parallel rovings. According to the data sheet of the manufacturer, the cross-sectional area of the rovings in warp and weft direction is 35.25 mm^2 per meter length perpendicular to the roving axis. The SITgrid044 VL is impregnated using polystyrene to increase the durability and the bond strength.

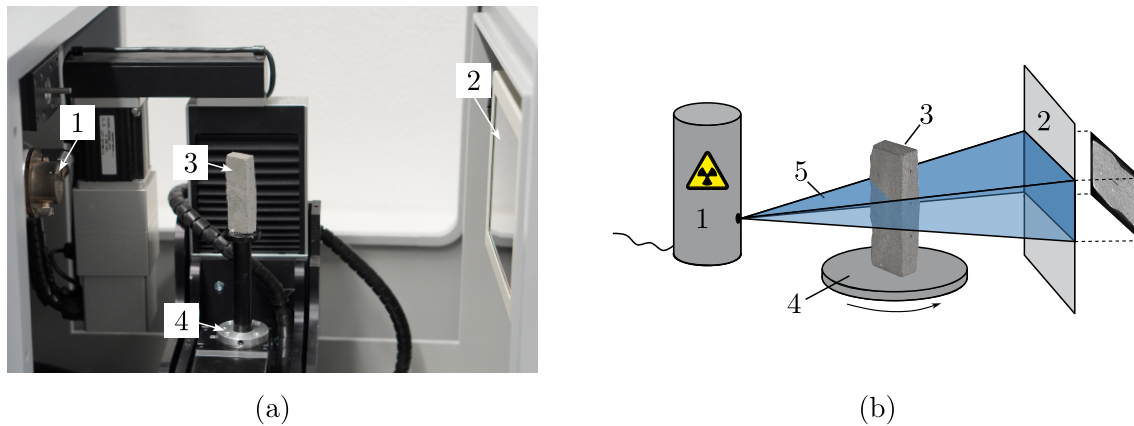


Figure 8.2: (a) Computed tomography (CT) device (Procon CT-XPRESS) (b) Schematic illustration of functionality - 1: X-ray source, 2: X-ray detector 3: sample, 4: rotating sample plate, 5: X-rays ((a) Adapted from [173])

8.1.2 Microtomography

A μ -CT device, namely the Procon CT-XPRESS, was utilized to investigate the internal characteristics of the sample. The device is depicted in Fig. 8.2 (a) and the functionality is schematically illustrated in Fig. 8.2 (b). It consists of an X-ray source (1) and a detector (2). The sample (3) is placed on a rotating sample plate (4). During the scanning process, the sample is rotated about 360° and subjected to X-radiation (5). The radiation usually consists of several different wavelengths and is referred to as *polychromatic* [173].

The scanning procedure produces a series of two-dimensional images, so-called *slices*. Using the software X-AID 2023 by MITOS GmbH, these slices can be utilized for the three-dimensional digital reconstruction of the sample. Depending on the placement of the sample relative to the X-ray source and the detector only a section of the sample is scanned. The scanned region of the sample is indicated in Fig. 8.1 (b). One exemplary slice, the stacking procedure and the 3D reconstruction of the scanned region are presented in Fig. 8.3. Using the Procon CT-XPRESS a nominal resolution of $5\ \mu\text{m}$ per voxel can be achieved [136]. That means, that each pixel, in a two-dimensional image, or each voxel, in a three-dimensional reconstruction, corresponds to $5\ \mu\text{m}$ of the sample.

8.1.3 Segmentation

Image segmentation is the process of classifying voxels, and thus partitioning the image into multiple segments. In the present case, the carbon grid is to be extracted. The most intuitive approach is the application of a threshold. Because the roving and the concrete have different greyscale values, as can be observed in Fig. 8.3 (a), applying a threshold can reveal a first indication which regions belong to the roving. However, due to cupping effects [173], the greyscale range is not constant across the two-dimensional image. This makes a reliable segmentation of the carbon grid difficult. A manual extraction of the

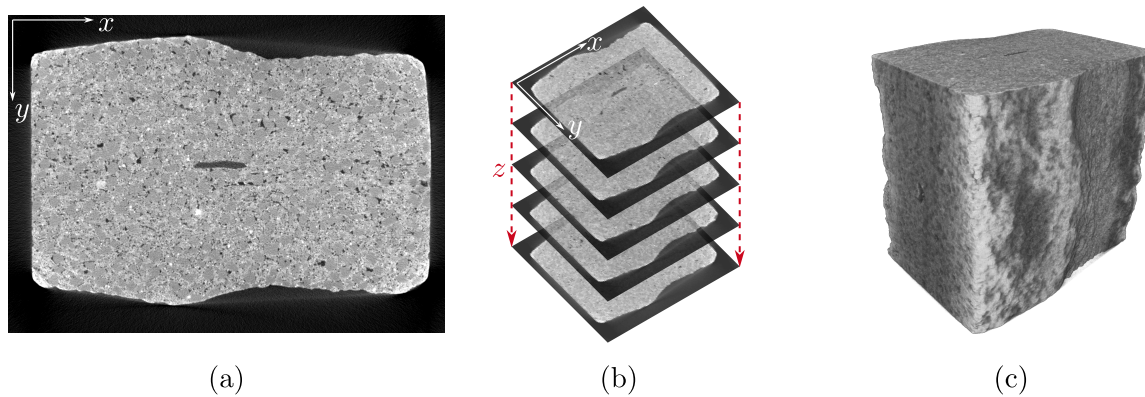


Figure 8.3: (a) Exemplary two-dimensional image (*slice*) (b) Stacking procedure of two-dimensional images to obtain (c) Digital 3D reconstruction of the scanned area ((a),(c) Adapted from [173])

roving is also possible, but is very time-consuming.

Neural networks can be employed to automate the process of image segmentation [8, 25, 31, 35, 37, 145]. Wagner and Maas [172] have compared different network architectures and have come to the conclusion that the 3D U-Net [35] is suited best for the segmentation of the carbon grid.

Before the convolutional neural network (CNN) can be used to extract the roving from the specimen it has to be trained, which means it is fed with a dataset that has been manually segmented. A dataset has been made available by [170]. It can be artificially extended to be more diverse by using data augmentation techniques. This includes, for example, scaling, flipping, rotating or cropping of the images. More detailed information on the employed augmentation techniques can be found in [173]. Generally, augmentation techniques are applied to prevent overfitting of the CNN. A CNN is said to be overfitting, if it describes the training data exceptionally well but is not able to generalize to new data.

After the CNN has been trained it can be used to extract the roving from the 3D reconstruction of the specimen, compare Fig. 8.3 (c). Due to the lack of available training data, the CNN was trained with strong augmentation. This resulted in the segmentation of regions that visually resembled a roving, known as artefacts, but were not part of actual roving geometry. To remove these artefacts, a software called Roving Surface Extractor [171] was used. The software determines connected voxels, by finding common corners or edges. Finally, the cluster consisting of the most voxels is identified as the carbon grid. The accurate extraction of the roving introduces unwanted complexity, which is further increased in regions where the knitting thread is present. To smooth the roving surface and remove further artefacts, a 3D Gaussian filter with standard deviation of 10 was applied on the binary roving. Figure 8.4 illustrates the procedure exemplarily for one slice. In Fig. 8.4 (a) one slice obtained during the μ -CT scanning process is shown, where the roving, the knitting thread and some air inclusions are indicated. Fig. 8.4 (b) shows the segmentation which is obtained using the CNN. Multiple artefacts are present and the

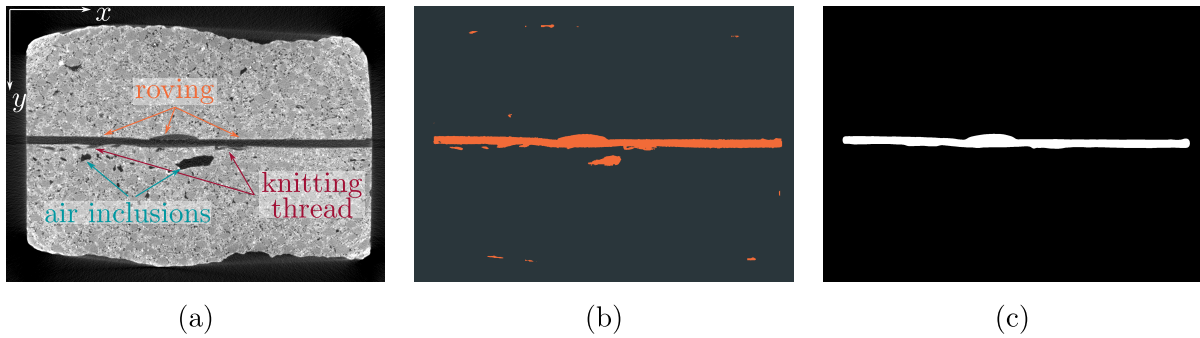


Figure 8.4: (a) Exemplary two-dimensional image (*slice*) (b) Segmentation obtained using CNN (c) Binary representation of roving after using Gaussian filter

outline of the roving is complex. Applying the described post-processing steps the binary representation of the roving depicted in Fig. 8.4 (c) is obtained.

As a last step, the marching cube algorithm [106] is applied on the 3D volume to extract a point cloud only describing the surface of the roving.

The obtained information from computed tomography of the scanned specimen and the extracted roving is available in the form of:

- a point cloud describing the surface of the extracted roving,
- binary cross-sectional images of
 - the roving (i.e. all pixels belonging to the roving are white, compare Fig. 8.4 (c)),
 - the sample (i.e. all pixels within the boundary of the sample are white).

8.2 Parameterised RVE and determination of characteristic properties

From the presented first-order shell homogenisation approach from chapters 4 and 5, the periodic boundary conditions have shown to perform best. Therefore, they will be employed in the following. However, the use of periodic boundary conditions imposes two major restrictions on the RVE geometry. They require the RVE to be symmetric with regard to the in-plane axes and point symmetric with regard to the in-plane centre point. Furthermore, using scaled boundary isogeometric analysis requires the RVE geometry to be star-shaped, as has been discussed in sec. 6.2.

Hence, a parameterised RVE fulfilling these criteria has been developed. It represents one roving intersection, such that it can serve as unit cell. The main characteristic features of the RVE are derived from the computed tomography data or from data sheets provided by the manufacturer of the carbon textile.

For illustration purposes a parameterised RVE is depicted in Fig. 8.5. The characteristic properties include the grid opening in warp and weft directions l_1 and l_2 , the height of the RVE h^{RVE} , the concrete cover c_0 , as well as the roving dimensions. The cross-section of the roving is assumed to be elliptical [184]. Thus, their geometry can be described by a semi-major axis (b_1/b_2) and a semi-minor axis (h_1/h_2) for the warp and weft directions, respectively.

The model is parameterised using the plug-in Grasshopper[®] within the CAD software Rhinoceros[®] and has been published on Zenodo [115].



Note, that the coordinate systems of the parameterised RVE and the μ -CT data do not necessarily coincide. From μ -CT data the z -direction corresponds to the stacking direction, while for the RVE the z -direction is the thickness direction. Therefore, the dimensions will be extracted for warp and weft direction and are then transferred to the RVE.

8.2.1 Assumptions

Before explaining how to derive the characteristic properties from the μ -CT data, the assumptions made for the parameterised RVE are summarised.

1. Only one roving intersection is considered.
2. Rovings are orthogonal to each other.
3. Rovings are approximated as elliptical cylinders.

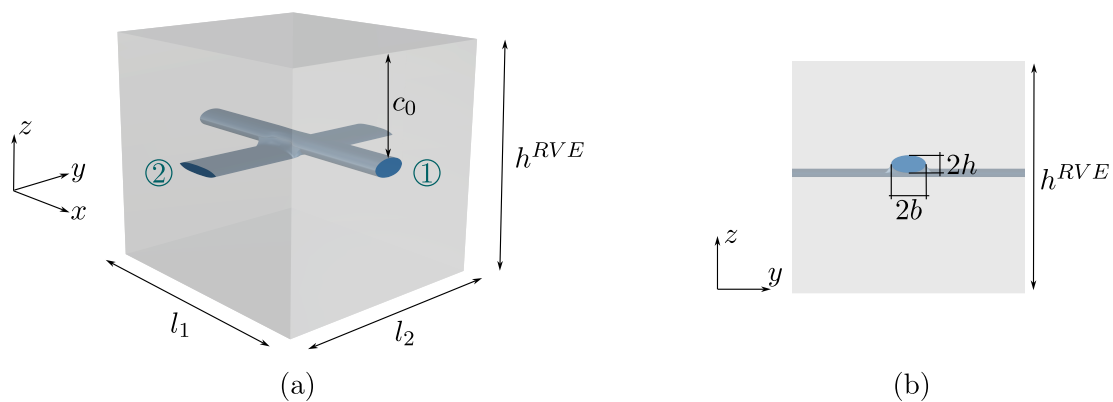


Figure 8.5: (a) Perspective and (b) plane view ($y - z$ - plane) of parameterized RVE with dimensions (1: warp direction, 2: weft direction) ([173])

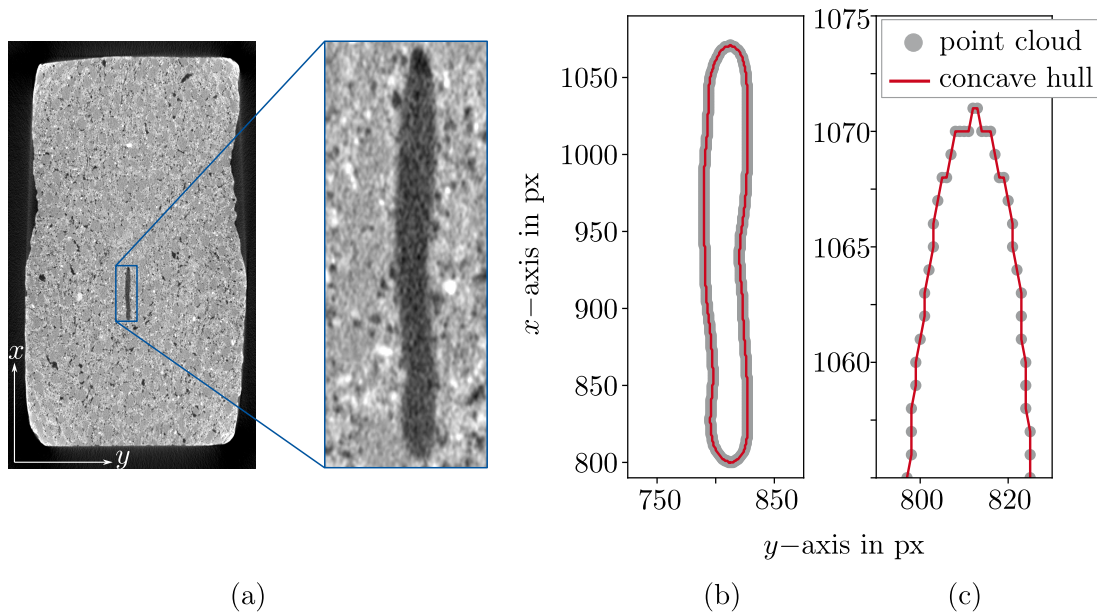


Figure 8.6: (a) Exemplary cross-sectional image of sample with magnification of roving (b) Corresponding point cloud and concave hull (c) Magnification of point cloud and concave hull ([173])

4. The lower edge of the roving in warp direction coincides with the centre line of the roving in weft direction.

Generally, any symmetric and point-symmetric reinforcement can be investigated. Here, the investigations are restricted to grid-like textile orientations.

8.2.2 Roving dimensions

The rovings are approximated as elliptical cylinders, their cross-sections are described by a semi-major axis b and a semi-minor axis h . Thus, the width of the roving is described by $2b$ and its height by $2h$, refer to Fig. 8.5 (b). The indices \square_1 and \square_2 correspond to the quantities in warp and weft direction, respectively.

To determine the cross-sectional properties of the roving from the CT-data, the point cloud is utilized. From observation the two main axes of the rovings can be determined. Variation of the coordinate along one main axis allows the investigation of the boundary point cloud of the roving. Application of the concave hull algorithm, based on [132], facilitates the derivation of a polygon describing the outline of the roving.

Figure 8.6 illustrates a cross-sectional image of the sample alongside with the corresponding point cloud and derived boundary polygon. For the boundary polygon the area A_i and its centroid $\mathbf{x}_{centroid,i}$ can be determined. Furthermore, the width $2b_i$ and height $2h_i$ are calculated as the difference between the maximum and minimum coordinate.

The procedure can be repeated for a number of n_{slice} coordinates along each axis and the

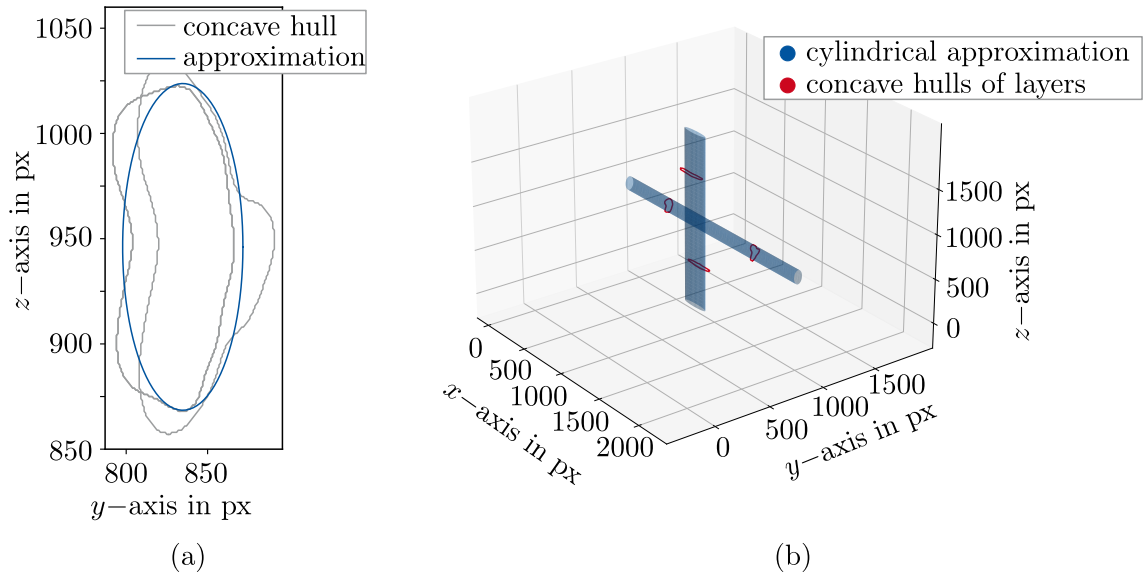


Figure 8.7: (a) Plane view of approximated ellipse from two concave hulls describing the roving (b) Perspective view of derived elliptical cylinders with concave hulls used for approximation ([173])

roving properties can be averaged.

$$\begin{aligned}\bar{A}_1 &= \frac{\sum_i^{n_{slice}} A_i}{n_{slice}}, & \bar{\mathbf{x}}_1 &= \frac{\sum_i^{n_{slice}} \mathbf{x}_{centroid,i}}{n_{slice}}, \\ \bar{b}_1 &= \frac{\sum_i^{n_{slice}} b_i}{n_{slice}}, & \bar{h}_1 &= \frac{\sum_i^{n_{slice}} h_i}{n_{slice}}.\end{aligned}\quad (8.1)$$

From the averaged values an aspect ratio between the semi-major and the semi-minor axis can be derived as

$$\mathcal{X}_{roving} = \bar{h}_1 : \bar{b}_1. \quad (8.2)$$

Using the averaged cross-sectional area and the aspect ratio, the dimensions of the approximating ellipse can be determined as

$$\begin{aligned}A_1 &= \bar{A}_1, & \mathcal{X}_1 &= \mathcal{X}_{roving} \\ b_1 &= \sqrt{\frac{A_1}{\pi \cdot \mathcal{X}_1}}, & h_1 &= \mathcal{X}_1 \cdot b_1.\end{aligned}\quad (8.3)$$

Here, the equations have been derived for the roving in warp direction (\square_1), the roving dimensions for the weft direction are obtained accordingly. Using the dimensions from Eq. 8.3 the rovings can be approximated as elliptical cylinder. For illustration purposes, Fig. 8.7 (a) shows the derived cross-sectional ellipse from two concave hulls in the $y-z$ -plane. In Fig. 8.7 (b) the two derived elliptical cylinders are depicted in perspective view. For both directions $n_{slice} = 2$ has been used.

8.2.3 In-Plane Dimensions

The derived RVE is to serve as unit cell, i.e. it describes the smallest repeating part possible. Therefore, the in-plane dimensions of the RVE can be directly related to the properties of the textile. The lengths l_1 and l_2 correspond to the thread spacing specified on the manufacturer's data sheet and indicate the distance between the centre lines of two rovings.

In order to validate the thread spacing using μ -CT data a larger sample and larger scanning region would be required. However, due to the knitting thread and polystyrene coating of the textile it is assumed to be geometrically stable. Therefore, the thread spacing is expected to be consistent throughout the extruded specimen.

8.2.4 Shell Thickness

The height of the RVE (h^{RVE}) corresponds to the height of the sample and is typically defined prior to production. Using the obtained μ -CT data the achieved sample thickness can be evaluated. This evaluation can be beneficial for assessing the production methods.

The binary images describing the whole sample are employed for this purpose, all pixels within the boundary of the sample are set to the value 255 (white), all pixels outside are set to the value 0 (black), compare Fig. 8.8 (a). Note, that on each side 10% of the width of the sample $a_{x,max}$ are neglected, such that only the shaded area is used for the determination of the top and bottom of the sample. This is due to the fact, that the extrusion process introduces imperfections due to which the sample is not perfectly rectangular.

The averaged top coordinate $y_{t,sample}$ and the averaged bottom coordinate $y_{b,sample}$ are determined and the distance between them is identified as shell thickness h_i^{RVE} of the slice. Again, this procedure can be repeated for multiple slices and the shell thickness h^{RVE} is averaged over the number of slices.

8.2.5 Concrete Cover

The concrete cover describes the distance from the top of the RVE to the top of the roving and is typically, similar to the shell thickness, defined before production of the component. Using μ -CT data the concrete cover can be determined and, for example, the accuracy of the production process can be assessed. This is particularly important for thin shells, as the positioning of the textile within the specimen largely influences the load-bearing behaviour.

To determine the concrete cover c_0 a binary representation of a cross-sectional slice is utilized, where the pixels belonging to the roving take the value 255 (white) and all others have value 0 (black), compare Fig. 8.8 (b). The first white pixel in y -direction indicates the top of the roving ($y_{t,roving}$). To determine the concrete cover the averaged

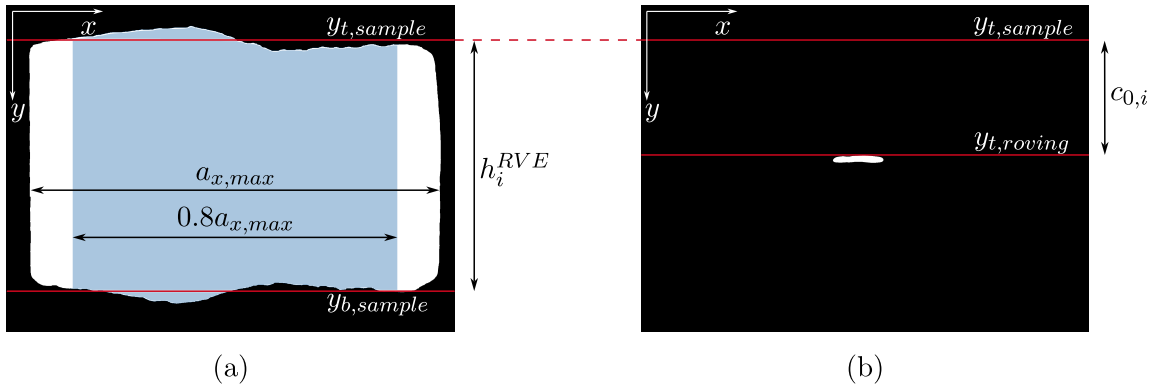


Figure 8.8: (a) Binary image of sample (pixels belonging to sample have value 255 (white)) (b) Binary image of the roving contained in sample (pixels belonging to roving have value 255 (white)) ([173])

coordinate of the top of the sample $y_{t,sample}$ from sec. 8.2.4 (Fig. 8.8 (a)) is employed, such that

$$c_{0,i} = y_{t,roving} - y_{t,sample}. \quad (8.4)$$

Similarly, the procedure is repeated for multiple slices and an average concrete cover c_0 is determined.

8.3 Examples

In the following, two tensile tests on carbon-reinforced concrete specimens are investigated using the proposed multiscale approach for shear deformable shell structures. The presented periodic boundary conditions are used to apply the macroscopic strains on the parameterised RVE.

The first example analyses the extruded specimen introduced in sec. 8.1.1. The characteristic properties for the parameterised RVE are derived using available CT data. For this example, the multiscale analysis is restricted to the linear-elastic regime. The primary objective of this initial example is to validate the proposed procedure for deriving the parameterised RVE by comparing them to reference values.

As a second example another tensile test is investigated, which has been conventionally cast. Because no computed tomography data is available for this sample the characteristic properties are derived using the data provided by the manufacturer of the textile reinforcement. For this example a microplane damage model is employed to simulate the material behaviour of concrete. It aims to integrate the nonlinear material of carbon-reinforced concrete within the multiscale method.

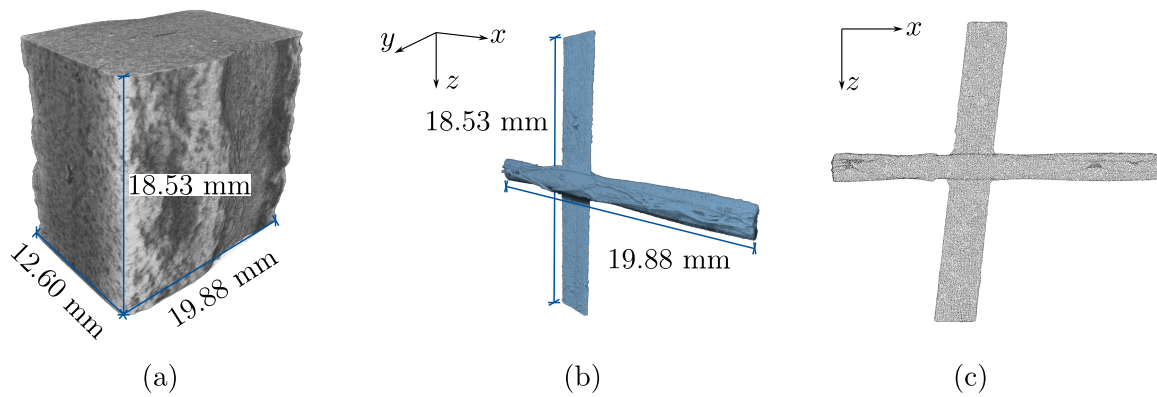


Figure 8.9: (a) 3D reconstruction of the scanned area of the sample (b) 3D representation of the segmented roving (c) Point cloud representing the surface of the textile (Adapted from [173])

8.3.1 Tensile Test - linear-elastic

The steps described for deriving the characteristic properties needed for the parameterised RVE are carried out for the specimen described in sec. 8.1.1. The segmented roving intersection had the dimensions of $19.88 \text{ mm} \times 18.53 \text{ mm}$ (warp \times weft). The three-dimensional reconstruction of the scanned region from Fig. 8.3 (c) is depicted again in Fig. 8.9 (a). The three-dimensional model of the embedded textile and the derived point cloud are shown in Fig. 8.9 (b) and (c), respectively. The voxel size of the sample is $9.5 \mu\text{m}$. From Fig. 8.9 (c) it can be observed that the two rovings are oriented along the x - and z -axis. For the parameterised RVE the x -direction corresponds to the warp direction, while the z -direction of the point cloud represents the weft direction of the textile within the RVE. Further, it can be seen, that the roving in weft direction is not parallel to the z -axis but rotated by approximately 6.325° .

The values obtained using the described steps are compared to values from the data sheet of the manufacturer and values defined prior to the extrusion process. To conclude, the parameterised RVE is embedded into the first-order homogenisation framework to investigate the linear-elastic behaviour of a tensile test.

8.3.1.1 Roving dimensions

The roving dimensions are derived using the procedure from sec. 8.2.2 for the x - and z -axis. The number of slices n_{slice} along each axis needs to be chosen large enough to ensure a constant mean value.

To investigate this issue the averaged cross-sectional area of the roving in warp (x -) and weft (z -) direction is determined for a varying number of slices. A reference solution using $n_{slice} = 100$ is obtained. The averaged cross-sectional areas are plotted versus n_{slice} in Fig. 8.10. It can be observed, that the averaged cross-sectional area \bar{A}_{roving} converges to a fixed value. In the following, $n_{slice} = 40$ was chosen to derive the roving geometry.

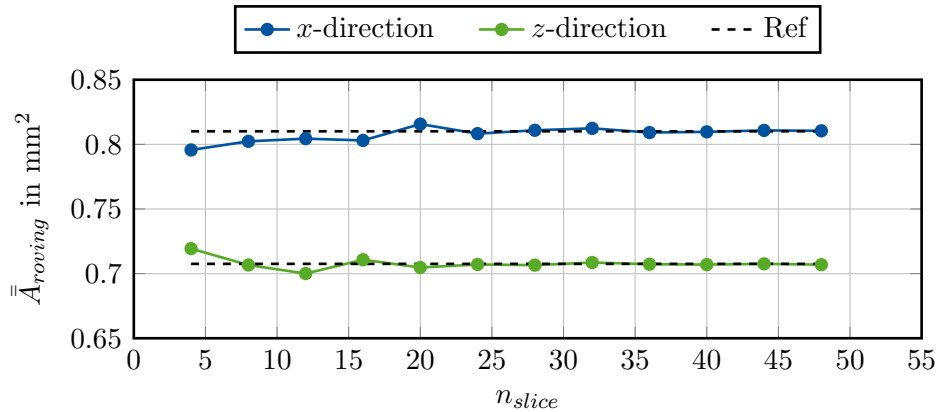


Figure 8.10: Obtained cross-sectional area of roving \bar{A}_{roving} for varying number of slices n_{slices} for warp and weft direction of sample ([173])

Table 8.1: Dimensions of cylindrical approximation of the rovings ($n_{slice} = 40$)

	A in mm ²	$2b$ in mm	$2h$ in mm	$\mathcal{X} = h : b$
warp direction	0.83	1.49	0.71	0.48
weft direction	0.71	2.45	0.37	0.15

Following Eq. 8.3 the averaged properties for both rovings can be determined. The dimensions of the approximating ellipses are summarised in Tab. 8.1.

As can be seen from Fig. 8.9 (c), the roving in weft direction is not parallel to the z -axis. Instead, it is rotated about 6.325° , which might lead to inaccurate roving dimensions. In order to quantify the deviation, the point cloud was rotated, such that the roving in weft direction is oriented parallel to the z -axis. Again, the roving dimensions were determined using $n_{slice} = 40$. The cross-sectional dimensions deviate by approximately 1.1%, which is considered neglectable in civil engineering context.

To verify the procedure, the derived cross-sectional values can be compared to the data of the manufacturer. In the chosen specimen the textile SITgrid 044 VL with yarn spacing of $16.2 \text{ mm} \times 14.7 \text{ mm}$ (warp \times weft) and cross-sectional area of $35.25 \text{ mm}^2/\text{m}$ is embedded, compare sec. 8.1.1. This results in theoretical cross-sectional areas of

$$\begin{aligned}
 \text{warp direction: } & A_{ref,1} = 0.57 \text{ mm}^2 \\
 \text{weft direction: } & A_{ref,2} = 0.52 \text{ mm}^2.
 \end{aligned} \tag{8.5}$$

These values differ significantly from the derived values in Tab. 8.1. The differences can be explained by the coating of the roving and the knitting thread. Both are not taken into account in the data of the manufacturer. However, the greyscale value of coating and knitting thread are similar to the one of the roving, compare Fig. 8.4 (a). And since the training dataset contained the knitting thread as ground truth, the CNN could not distinguish between the components during segmentation. Therefore, the derived cross-

sectional values are larger than the ones from the manufacturer.

However, since there is full bond between textile and coating, the values obtained using μ -CT data are used for further calculations.

8.3.1.2 In-Plane Dimensions

As has been discussed in sec. 8.2.3 the in-plane dimensions of the RVE correspond to the yarn spacing provided by the manufacturer in order for the RVE to serve as unit cell. For the present specimen these are

$$\begin{aligned} \text{warp direction: } l_1 &= 16.20 \text{ mm} \\ \text{weft direction: } l_2 &= 14.70 \text{ mm.} \end{aligned} \tag{8.6}$$

8.3.1.3 Shell Thickness

Using the binarised cross-sectional images as explained in sec. 8.2.4, the thickness of the specimen is obtained as

$$h^M = h^{RVE} = 13 \text{ mm.} \tag{8.7}$$

The derived thickness can be compared to the defined thickness prior to production. The specimen was extruded using the Laboratory Mortar Extruder (LabMorTex) [81] and the employed mouthpiece for extrusion had an opening height of $h_{ref} = 10$ mm. The derived component height is significantly larger than the proposed component height. However, Kalthoff et al. [81] have also observed an increased component height compared to the mouthpiece opening, which originates from the extrusion process. Therefore, the derived thickness h^{RVE} is reasonable.

8.3.1.4 Concrete Cover

Using the same locations, that have been used to determine the shell thickness, the average concrete cover is determined as

$$c_0 = 5.92 \text{ mm,} \tag{8.8}$$

using the method from sec. 8.2.5.

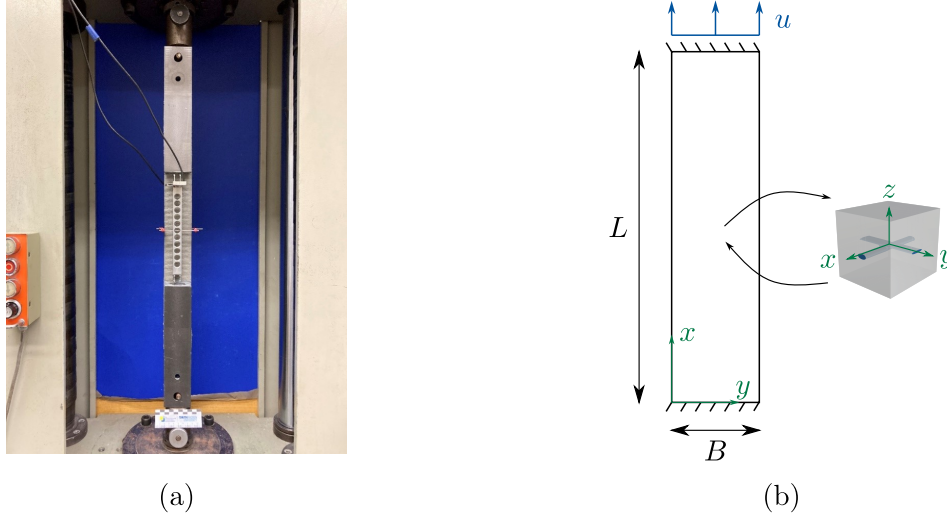
For comparison the theoretical concrete cover is calculated. During the extrusion process the textile was placed in the centre of the component [81]. Using the component thickness h^{RVE} (Eq. 8.7) and the roving properties (Tab. 8.1) that were derived from μ -CT data, the concrete cover is obtained as

$$c_{0,ref} = \frac{h^{RVE} - (2h_1 + h_2)}{2} = 6.05 \text{ mm.} \tag{8.9}$$

Since $c_0 \approx c_{0,ref}$, it can be concluded, that the textile was successfully placed centrally aligned within the component during the extrusion process.

Table 8.2: Linear-elastic material parameters for tensile test, adapted from [81]

	Roving	Concrete
Young's modulus E in N/mm^2	142,000	27,000
Poisson's ratio ν	0.35	0.2

**Figure 8.11:** (a) Experimental set-up (b) Adaption of tensile test for multiscale approach (Adapted from [116], (a) © ibac, RWTH Aachen)

8.3.1.5 Multiscale analysis

The derived properties can be used as input for the parameterised RVE model in Grasshopper. This model can be embedded in the first-order homogenisation framework developed in this work to validate the derived geometric characteristics.

The specimen, which has been scanned and for which the characteristic properties have been derived, has been taken from an extruded concrete specimen. The specimen has been tested in a tensile test [81] and has a free length of $L = 250$ mm and a width of $B = 60$ mm. The experimental test set-up is depicted in Fig. 8.11 (a).

To analyse the tensile test using the proposed first-order homogenisation framework for shells, the specimen characterises the macroscopic shell. Figure 8.11 (b) shows, how the test set-up is adapted. While the macroscopic shell is discretised using 4×1 elements, the RVE is discretised using $p_c = p_b = 3$ and $n_c = n_b = 1$ per direction. In the scope of this example, only linear-elastic material behaviour is assumed. The material parameters are given in Tab. 8.2 and were chosen according to [81].

The analysis was carried out displacement controlled with $u = 2$ mm/m, which corresponds to the experimental test set-up.

The load F is obtained as reaction force for the prescribed displacement u and is plotted versus the strain in Fig. 8.12. Good agreement in the linear-elastic regime between the ex-

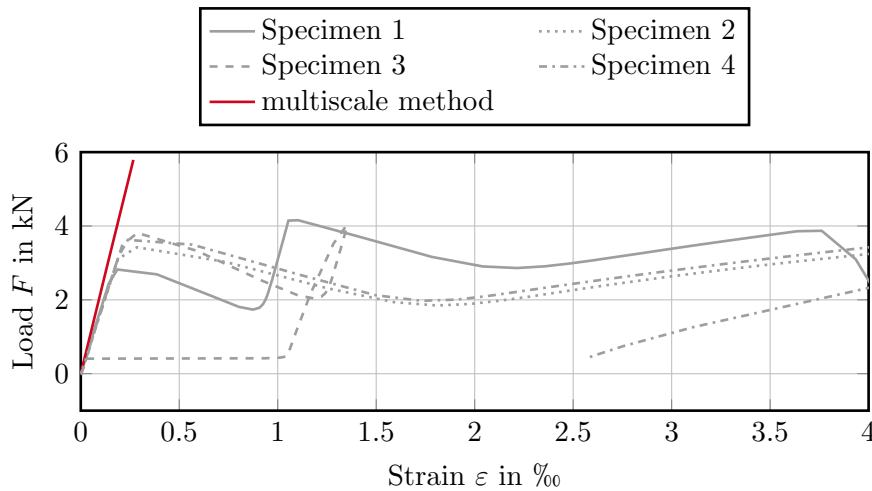


Figure 8.12: Load-strain curve for tensile test (Adapted from [173])

perimental data and the numerical analysis can be observed. This proves that the derived geometrical properties yield the correct volume fraction for the textile and concrete.

8.3.2 Tensile Test - microplane damage model

As a second example, another tensile test, carried out by the Institute of Structural Concrete, RWTH Aachen University, is examined. To incorporate the nonlinear material behaviour of concrete a microplane-damage model is used. It is based on the previous works of Bažant and Oh [11], Chudoba et al. [34], Jirásek [79] and has been presented for the analysis of carbon reinforced concrete shells using a multiscale approach in [87].

Because no image-based data is available for this example, the characteristic dimensions needed for the parameterised RVE are derived from the data sheet of the manufacturer. The textile GRID Q95-CCE-38-E5 of solidian was used in this test series, which is a textile still under development. The roving dimensions in warp and weft direction are the same for this textile.

8.3.2.1 Roving dimensions

The roving dimensions are derived from the cross-section of an individual roving given by the manufacturer. For warp and weft directions, the cross-sectional area is

$$A_{roving} = 3.62 \text{ mm}^2. \quad (8.10)$$

As a first approach, the aspect ratio between semi-major and semi-minor axis is simplified as

$$\mathcal{X}_{roving} = h : b = 0.5. \quad (8.11)$$

Using Eq. 8.3 the dimensions of the approximating ellipse can be determined, such that

$$b_1 = b_2 = \sqrt{\frac{A_{roving}}{\pi \cdot \mathcal{X}}} = 1.518 \text{ mm} \quad \text{and} \quad h_1 = h_2 = \mathcal{X} \cdot b_1 = 0.759 \text{ mm}. \quad (8.12)$$

8.3.2.2 In-plane dimensions

Again, the in-plane dimensions of the RVE correspond to the yarn spacing of the textile. For the solidian GRID Q95-CCE-38-E5 the distance in warp and weft direction are the same, therefore

$$l_1 = l_2 = 38 \text{ mm}. \quad (8.13)$$

8.3.2.3 Shell thickness

The specimens were produced using conventional concrete pouring, therefore it is assumed that the thickness determined prior to production is achieved with sufficient accuracy. Hence, the thickness of the RVE is

$$h^{RVE} = 30 \text{ mm}. \quad (8.14)$$

8.3.2.4 Concrete cover

Because no computed tomography data is available, the theoretical concrete cover is calculated. The textile was placed centrally aligned in the cross-section of the specimen, such that the concrete cover is obtained as

$$c_0 = \frac{h^{RVE} - (2h_1 + h_2)}{2} = 13.862 \text{ mm}. \quad (8.15)$$

8.3.2.5 Multiscale analysis

Again, the derived properties serve as input for the parameterised RVE model in Grasshopper. The obtained RVE is embedded in the proposed first-order homogenisation framework.

The concrete specimens have a length of 1000 mm, a width of $B = 120$ mm and a height of $h^M = 30$ mm. The samples are fixed by two clamping jaws such that the free length is $L = 530$ mm. The experimental set-up and the adaption for the simulation is depicted in Fig. 8.13, where symmetry is exploited. The macroscopic shell is discretised using 4×1 elements, while the RVE is discretised using $p_c = p_b = 3$ and $n_c = n_b = 1$ per direction.

For these samples the high-strength concrete C3-HF2-165-4 [151] is used. The characteristic properties of the concrete were determined on concrete cylinders and cubes [87]. Kikis et al. [87] calibrate the microplane-damage model using one single RVE. The material is characterised by two parameters – e_p , which denotes the elastic limit and e_f , which is

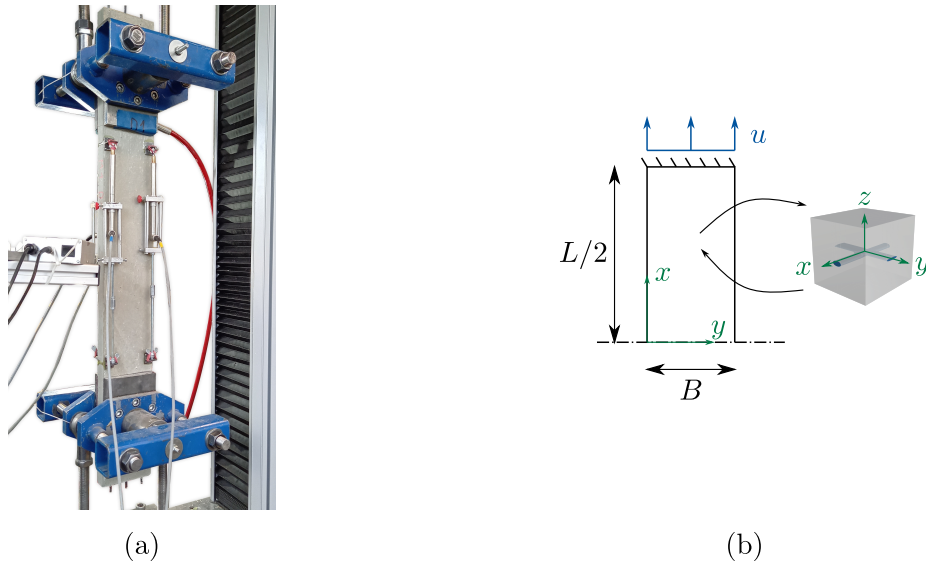


Figure 8.13: (a) Experimental set-up (b) Adaption of tensile test for multiscale approach (Adapted from [87], (a) © IMB, RWTH Aachen)

Table 8.3: Material parameters for tensile test, adapted from [87]

	Roving	Concrete
Young's modulus E in N/mm^2	247,469	42,793
Poisson's ratio ν	0.35	0.2
elastic limit e_p	-	0.00004
ductility param. e_f	-	0.02148
tensile strength f_{tm} in MPa	3,824	-

a ductility parameter [79]. The carbon textile is described using a linear-elastic material model, the characteristic material properties of the textile were determined by small scale tests. The characteristic material properties of carbon and textile are summarised in Tab. 8.3.

The experiment was carried out displacement controlled with $u = 1 \text{ mm}/\text{min}$. The load F is obtained as reaction force for the prescribed displacement. In Fig. 8.14 the load-displacement curve of both specimens as well as the numerical approximation is given.

The multiscale method using the microplane damage model is able to approximate the experimental results well. Good agreement can be observed in the linear-elastic domain. The numerical solution terminates, when the maximum tensile strength f_{tm} is reached. It is observed, that this value is too low, compared to the experimental data.

8.4 Discussion

To conclude, first the assumptions made in sec. 8.2.1 will be evaluated.

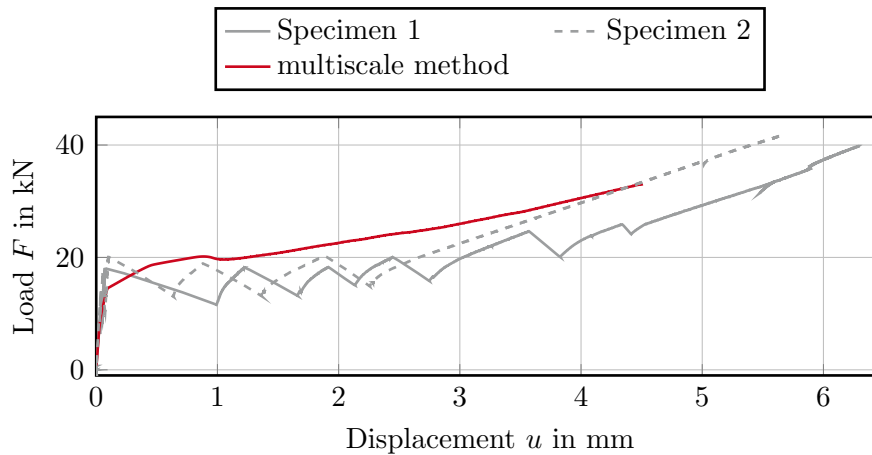


Figure 8.14: Load-displacement curve for tensile test using microplane damage model (Adapted from [87])

1. **Only one roving intersection is considered.** This assumption is valid, as long as the scanned and evaluated region is representative of the whole mesostructure. Only then, it is able to serve as unit cell. Manufacturing errors can lead to varying shell thicknesses and concrete covers; therefore, when choosing the sample that will be scanned, it should be ensured that it is representative of the whole structure. Additionally, the segmented area should be larger or equal to the RVE size, such that the averaged roving dimensions are as representative as possible.
2. **Rovings are orthogonal to each other.** The first example has shown, that the rovings were not positioned perfectly orthogonal to each other. Nevertheless, the rotation only introduced small deviations into the derived geometric properties of the roving. Furthermore, it is assumed that the distortion was introduced during the extrusion process. It is expected that using classical production processes this distortion is reduced. To conclude, the assumption of the rovings being orthogonal to each other is valid.
3. **Rovings are approximated as elliptical cylinders.** The assumption of elliptical cross-sections is in line with the literature [184] and has yielded sufficient results for the presented example. Generally, small aspect ratios \mathcal{X} should be chosen for the rovings in warp and weft direction. However, when debonding or friction between roving and concrete should be investigated, this simplification may not be sufficient.
4. **The lower edge of the roving in warp direction coincides with the centre line of the roving in weft direction.** From a technical point of view, the rovings are positioned on top of each other and do not penetrate each other. Nevertheless, due to the knitting thread and coating, the rovings are compressed at the intersecting points. For the shown examples the assumption is valid.

Alternatively, to the grid-like textile structure investigated here, multiple different rein-

forcement patterns are imaginable. To be implemented in the proposed homogenisation approach, the mesoscopic structure needs to be periodically repeating, as well as symmetric to the in-plane axes and symmetric to the centre point. Structures with multiple layers of textile may also be analysed using the proposed parameterised RVE by stacking multiple RVEs on top of each other.

The homogenisation approach offers the advantage, that technically each macroscopic integration point can be assigned an individual RVE. Enhancing the method with image-based data enables a sophisticated representation of the shell structure.

The first example has shown, that the procedure proposed to derive the characteristic RVE properties yields accurate results. The parameterised RVE was embedded in the multiscale framework, where good agreement between the numerical and the experimental solution was obtained in the linear-elastic regime.

Since no CT data was available for the second specimen, the properties needed for the parameterised RVE were derived from the manufacturer's data. A microplane damage model was employed to incorporate the nonlinear material behaviour of concrete. For the textile linear-elastic material behaviour including a maximum tensile strength was used. It was observed, that the multiscale simulation was able to approximate the experimental data well, especially in the linear-elastic regime. This indicates, that even though this approach is less accurate compared to incorporating image-based data, it is still able to account for the correct volume fractions of the individual components.

The maximum tensile strength of the simulation was reached before the experiments failed, which implies that further investigations using the microplane damage model should be conducted. Furthermore, as has been discussed in sec. 4.2, the RVE loses its representativeness when failure occurs at RVE level due to localisation. This is an issue which should be investigated further in the future. Generally, this example should be interpreted as starting point for further investigations of carbon-reinforced concrete shells using the proposed approach. Nevertheless, it underlines the benefits of the parametrised RVE model, as individual parameters can be easily changed while still retaining an analysis-suitable model that fulfils the requirements emerging from the multiscale model, i.e. star-shapedness and symmetry.

A further open point is the investigation of bending dominated problems. For these problems, the positioning of the textile has a greater affect on the overall behaviour than for tensile tests. Future work should also consider debonding between the roving and concrete. Klarmann et al. [92] have proposed a zero-thickness interface in combination with a cohesive zone model to account for the interaction mechanisms between textile reinforcement and concrete.

Chapter 9

Conclusion and Outlook

A first-order homogenisation approach has been proposed that allows the transition from three-dimensional continua describing the microscale to shear deformable shells at the macroscale. The macroscopic scale accounts for the structural behaviour and is treated as homogeneous. The material response for every macroscopic point is determined using a representative volume element, which accounts for the morphology of the microstructure. In contrast to classical homogenisation approaches, where it is distinguished between a macroscopic and a microscopic scale, a distinctive feature of the approach is that the RVE accounts for the complete thickness of the shell and is therefore referred to as mesoscale.

The macroscopic scale is described using a structural shell element in line with REISSNER-MINDLIN kinematics. The mesoscopic boundary value problem is analysed using SBIGA with conforming discretisation in scaling and boundary direction. However, it is crucial to note that the presented approach is independent of the discretisation technique employed.

The main outcome of this work can be summarised as follows.

- Three different boundary conditions suitable for the consistent coupling of the macroscopic shell element with the mesoscopic continuum formulation were developed. They differ mainly in how the transverse shear strain is applied to the lateral RVE boundaries.
- Further, a moment reduction constraint has been introduced for the RVE to counteract the dependence of the homogenised shear stiffness on the in-plane RVE size.
- To account for the mesoscopic morphology, a parameterised RVE for the analysis of carbon-reinforced concrete shell structures has been presented, incorporating image-based methods into the proposed homogenisation framework.

For the validation of the three boundary conditions presented, compliance with the zero-traction boundary conditions on the top and bottom surface of the RVE and the correct calculation of the shear stress distribution within the RVE are key features. It has been shown that all three boundary conditions satisfy these requirements towards the centre

of the RVE when boundary effects decay. The proposed periodic boundary conditions do not exhibit boundary effects.

Furthermore, the approaches for applying the macroscopic strains to the RVE were verified by means of mesoscopic benchmarks, comparing the homogenised stiffness components with analytical values. Thereby, for the traction boundary conditions a dependence on the in-plane RVE size for the torsional stiffness and the transversal shear stiffnesses was observed. The shell boundary conditions only show length dependent behaviour for the transverse shear component, whereas the periodic boundary conditions yield the correct homogenised stiffness components irrespective of the RVE size and the RVE morphology. Finally, the method was validated using four multiscale examples including geometrical and physical nonlinearities. The analyses have shown that the length dependent behaviour from the mesoscopic scale is transferred to the macroscopic scale. However, the overall behaviour largely depends on the macroscopic problem and the load transfer mechanisms of the shell structure.

In general, it can be concluded that the periodic boundary conditions yield the most promising results.

One limitation of the presented boundary condition is that only globally periodic structures have been investigated, such that all RVEs also served as unit cells and the heterogeneities were uniformly distributed. Even though the periodic boundary conditions yielded the best results, they require the RVE to be symmetric with respect to the in-plane axes and to the centre point, which must be considered a restriction but gives rise to further research in this regard.

In addition, two distinctive peculiarities arise from prescribing the transversal shear strain. On the one hand, the RVE is subject to rigid body rotations when the shear strains are prescribed as displacement of the lateral surfaces. Therefore, it possesses no shear stiffness. This problem is addressed with antisymmetric link conditions of the displacements in thickness direction. On the other hand, a dependence of the homogenised shear stiffness on the in-plane RVE size was observed. The dependence arises from an unbalanced moment distribution, which evolves from the application of the transverse shear strain on the lateral RVE surfaces. In order to overcome this issue, a moment reduction constraint is introduced, effectively reducing the dependence on the in-plane RVE size. A distinctive feature is that the constraint takes the local stiffness contribution of the material into account.

The proposed moment reduction constraint used in the homogenisation framework assumes a linear bending moment distribution along both in-plane axes. Although this assumption is only valid for homogeneous RVEs, the constraint has shown to yield sufficient results as long as the inclusions are not too large and the stiffness jumps are not severe.

Since shell structures are naturally prone to imperfections due to their thin structure, exploring the inner composition using non-destructive image-based methods can enhance the quality of the solution and evaluate novel production methods. In the scope of

this work, microtomography was utilized to investigate the inner structure of carbon-reinforced concrete shell structures. The textile reinforcement was segmented from the three-dimensional reconstruction using a convolutional neural network. The information obtained were directly incorporated into the RVE to represent the microstructure as accurately as possible.

However, the presented homogenisation framework with periodic boundary conditions imposes two restrictive requirements on the definition of the RVE. First, as SBIGA is used at the mesoscopic scale the geometries need to be star-shaped. Second, the periodic boundary conditions require the RVE to be symmetric to the in-plane axes and symmetric to the centre point. Therefore, a parameterised RVE was developed which satisfies these conditions a priori.

The characteristic features of the parameterised RVE are the dimensions of the rovings, the in-plane dimensions of the unit cell, the thickness of the shell and the concrete cover. These are determined using the data obtained from computed tomography or data provided by the manufacturer. The rovings were assumed to be of elliptical shape.

Experimental data from two tensile tests was used to validate the algorithm for deriving the characteristic RVE properties and to demonstrate the applicability of the multiscale approach for the analysis of carbon-reinforced concrete shells.

At the moment, the parameterised RVE is restricted to grid-like textiles, where the warp and weft direction are orthogonal to each other. Furthermore, the roving geometry is assumed to be elliptical, which is a simplifying assumption.

To allow for the analysis of more complex reinforced structures, the parameterised RVE has to be adapted and consequently, different boundary conditions for the homogenisation framework may be necessary. The proposed traction boundary conditions can be utilized for this purpose, since they impose no symmetry requirements on the RVE. However, they show a significant dependence of the torsional stiffness on the in-plane size of the RVE, which should be investigated further in future work.

To further improve the analysis of carbon-reinforced concrete shells in the future, a wider range of experimental tests that activate more complex load transfer mechanisms, such as bending, are required for calibration and validation of the microplane damage model. Additionally, the debonding between roving and concrete should be considered, for example using an isogeometric cohesive zone element. However, it should be noted that the consideration of complex microscopic effects is at the expense of the efficiency of the overall homogenisation procedure.

Another aspect which can be investigated in the future is the analysis of resolved shell structures. These are characterised by two outer layers and an inner structure, which can be, for instance, interpenetrating shells or folded structures. Resolved shell structures aim to offer a resource efficient alternative to conventional structural elements, such as slabs. The extension of the proposed homogenisation method can provide a starting point for the development of an efficient analysis method of resolved shell structures.

Overall, the presented work provides an accurate yet efficient analysis method for com-

posite shell structures by incorporating image-based methods into a first-order homogenisation approach. Thus, combining the detailed mesoscopic morphology of the composite material with a numerically efficient description of the structural shell element.

Nomenclature

The following notation is employed throughout the present work. Tensors and tensor products are used in a Cartesian coordinate system. Einstein's summation convention is applied over repeated indices.

Unless otherwise stated the following notation has been employed. Only the most frequently used symbols have been listed, all others will be defined upon appearance.

General notation and operators

a	scalar
\mathbf{a}	vector
\mathbf{A}	second-order tensor
$\mathbf{a} \cdot \mathbf{b}$	single contraction ($a_i b_i$)
$\underline{\mathbf{A}} : \underline{\mathbf{B}}$	double contraction ($A_{ij} B_{ij}$)
Grad \square	Gradient operator ($\frac{\square_i}{\partial X_j}$)
grad \square	Gradient operator ($\frac{\square_i}{\partial x_j}$)
Div \square	Divergence operator ($\frac{\square_{ij}}{\partial X_j}$)
div \square	Divergence operator ($\frac{\square_{ij}}{\partial x_j}$)
$\delta \square$	variation of \square
$\Delta \square$	linearisation of \square
\square^T	transpose of a second-order tensor ($A_{ij} = A_{ji}$)
$\langle \square \rangle$	volume or surface average of quantity
$[\square]_x$	skew-symmetric matrix of a vector

Latin letters

$\mathbf{a}_i, \mathbf{a}^i$	covariant/contravariant basis system on Ω_t
A	area in the reference configuration
A^m	area of the mid-surface of the RVE
$\check{\mathbf{A}}$	assembly matrix to relate $\boldsymbol{\varepsilon}$ to \mathbf{E}
\mathbf{A}	matrix to apply boundary conditions on RVE

$\tilde{\mathbf{A}}, \check{\mathbf{A}}$	submatrices of \mathbf{A}
$\mathbf{A}_i, \mathbf{A}^i$	covariant/contravariant basis system on Ω
\mathbf{b}, \mathbf{b}_0	body forces
$\mathbf{b}_1, \mathbf{b}_2, \mathbf{b}_3$	matrices containing components of $\tilde{\mathbf{J}}^{-1}$
\mathbf{B}	strain-displacement matrix
c_0	concrete cover
C	scaling centre
dA	differential area element in the reference configuration
dV	differential volume element in the reference configuration
\mathbf{d}	director vector of the shell in the current configuration
D	GÂTEAUX directional derivative
$D_s^{11}, D_s^{22}, D_s^{12}$	shear stiffness components of shell
\mathbf{D}	director vector of the shell in the reference configuration
\mathbf{e}_i	basis system in Euclidean space
E	Young's modulus
\mathbf{E}	GREEN-LAGRANGE strain
$f_{y,k}$	yield stress for elasto-plastic material
$\bar{\mathbf{f}}$	boundary loads on the shell reference surface
\mathbf{f}	global residual vector
\mathbf{f}_e	element residual vector
\mathbf{f}_s	residual vector for each section
\mathbf{F}	deformation gradient
$\check{\mathbf{F}}$	matrix notation of deformation gradient $\in \mathbb{R}^{[6 \times 9]}$
$\mathbf{g}_i, \mathbf{g}^i$	covariant/contravariant basis system in the current configuration
G	shear modulus
\mathbf{G}	geometrical matrix
$\mathbf{G}_i, \mathbf{G}^i$	covariant/contravariant basis system in the reference configuration
h^M	shell thickness

h^{RVE}	height of RVE
\mathbf{H}	displacement gradient
i, j	indices 1, 2, 3
I_T	second moment of area
I, J, K	number of control point
\mathbf{I}	identity matrix or tensor
J	determinant of the Jacobian matrix
\tilde{J}	determinant of the Jacobian matrix on the boundary
\mathbf{J}	Jacobian matrix
$\tilde{\mathbf{J}}$	Jacobian matrix on the boundary
\mathbf{k}_e	element stiffness matrix
\mathbf{k}_s	stiffness matrix for each section
\mathbf{K}	global stiffness matrix
l_x, l_y	in-plane dimensions of an RVE
L	linearisation of a functional
L	Length dimension on the macroscopic shell
L^m, L^M	characteristic length on the mesoscopic/macroscopic scale
L^{RVE}	in-plane RVE size
$m^{\alpha\beta}$	bending moments
$n^{\alpha\beta}$	normal forces
n_b	number of elements in each boundary direction
n_{bc}	total number of control points on the boundary
n_{bs}	total number of control points of one section
n_c	number of elements in scaling direction
n_{cp}	total number of control points along each scaling line
n_{GP}	number of GAUSS integration points
n_{sec}	total number of sections
n_x, n_y, n_z	components of normal vector

nel	nodes per element
$numel$	total number of elements
N_K	shape function of node/control point K
\mathbf{n}	unit normal vector in the current configuration
\mathbf{N}	unit normal vector in the reference configuration
\mathbf{N}^m	shape function matrix for SBIGA discretisation
\mathbf{N}^M	shape function matrix of the shell
\mathbf{N}_b	shape function matrix for the boundary
\mathbf{N}_s	shape function matrix for scaling line
p, q	polynomial degree of NURBS in boundary directions
p_b	polynomial degree of NURBS on the boundary
p_c	polynomial degree of B-Spline in scaling direction
$\bar{\mathbf{p}}$	surface loads acting on the reference surface of the shell
$\check{\mathbf{p}}_x$	position vector of moment reduction constraint
\mathbf{P}	first PIOLA-KIRCHHOFF stress tensor
q^α	shear forces
r	polynomial degree of B-Spline in scaling direction
R	radius of the macroscopic shell
R_I^r	B-Spline curve
$R_J^{p,q}$	basis function of a NURBS surface
\mathbf{R}	rotational tensor
\mathbf{S}	second PIOLA-KIRCHHOFF stress tensor
$\check{\mathbf{S}}$	matrix notation of second PIOLA-KIRCHHOFF stress tensor $\in \mathbb{R}^{[9 \times 9]}$
\mathbf{u}	displacement field
\mathbf{U}_b	vector containing displacements of all boundary control points
$\mathbf{U}_{b,J}$	displacement of control point J on the boundary
t	time
\mathbf{t}	CAUCHY stress vector

\mathbf{t}_0	traction vector
V	volume in the reference configuration
\mathbf{v}	vector containing the degrees of freedom
\mathbf{v}_s	vector containing the degrees of freedom of each section
\mathbf{v}_K	vector containing the degrees of freedom of node/control point K
\mathbf{V}	vector of the global degrees of freedom
δW_{int}	virtual internal work
δW_{ext}	virtual external work
x, y, z	spatial coordinates
\mathbf{x}	position vector in the current configuration
\mathbf{X}	position vector in the reference configuration
\mathbf{X}_b	vector containing coordinates of all boundary control points
$\mathbf{X}_{b,J}$	coordinates of control point J on the boundary
\mathbf{X}_C	position vector of the scaling centre in the reference configuration
$\tilde{\mathbf{X}}$	position vector of any point on the boundary of a section in the reference configuration
\mathbf{Z}	shifter tensor in the reference configuration
$\bar{\mathbf{Z}}$	shifter tensor in the current configuration

Greek letters

α, β	indices 1,2
γ_α	transversal shear strains of the shell
Γ	Boundary of a domain Ω in the reference configuration
Γ_s	Boundary of a domain Ω_s of a section in the reference configuration
Γ_t	Boundary of a domain Ω_t in the current configuration
δ_{ij}	KRONECKER-Delta
$\varepsilon_{\alpha\beta}$	membrane strains of the shell
ε	vector of shell strains

ζ	coordinate in thickness direction of shell
κ	shear correction factor
$\kappa_{\alpha\beta}$	curvatures of the shell
λ	load factor
$\boldsymbol{\lambda}$	$= \lambda_x, \lambda_y, \lambda_z$ vector of the translational LAGRANGE parameters
Λ	first LAMÉ parameter
$\mathbf{\Lambda}$	vector of the LAGRANGE parameters
μ	second LAMÉ parameter, shear modulus
$\boldsymbol{\mu}$	$= \mu_x, \mu_y, \mu_z$ vector of the rotational LAGRANGE parameters
ν	Poisson's ratio
ξ^m, η^m, ζ^m	parametric coordinates on mesoscopic scale $\in [0,1]$
ξ^M, η^M, ζ^M	parametric coordinates on macroscopic scale $\in [-1,1]$
ξ^α	convective coordinates of the shell reference surface
$\boldsymbol{\xi}_i$	convective coordinate system of the shell reference surface
ρ_0	mass density in the reference configuration
$\rho_{\alpha\beta}$	second-order curvatures of the shell
σ_v	equivalent von Mises stress
$\boldsymbol{\sigma}$	CAUCHY stress tensor (chapter 3); vector of the stress resultants of the shell (chapter 4-7)
$\boldsymbol{\phi}$	position vector in the current configuration of a shell
$\boldsymbol{\Phi}$	position vector in the reference configuration of a shell
Ψ	strain energy density function
$\boldsymbol{\omega}$	rotation vector
Ω	Spatial domain in the reference configuration
Ω_s	spatial domain of a section in the reference configuration
Ω_t	Spatial domain in the current configuration
$\boldsymbol{\Omega}$	skew-symmetric matrix

Calligraphic letters

\mathcal{B}	Domain of a continuum body in the reference configuration
\mathcal{B}_t	Domain of a continuum body in the current configuration
\mathbb{C}	material tangent - fourth order tensor
$\hat{\mathbb{C}}_m$	membrane submatrix of the material tangent
$\hat{\mathbb{C}}_s$	shear submatrix of the material tangent
\mathcal{D}	differential operator
$\hat{\mathbb{D}}$	material matrix of the shell
$\hat{\mathbb{D}}_b$	bending submatrix of the shell material matrix
$\hat{\mathbb{D}}_m$	membrane submatrix of the shell material matrix
$\hat{\mathbb{D}}_{mb}$	membrane/bending coupling submatrix of the shell material matrix
$\hat{\mathbb{D}}_s$	shear submatrix of the shell material matrix
\mathcal{O}	complexity
\mathcal{P}	material point

Indices

\square_t	value corresponding to current configuration
\square_e/\square_s	value corresponding to element/section
$\square_{,i}$	derivative of \square with respect to i
\square^h	approximation of a value
\square^m	quantity corresponding to the microscopic/mesoscopic scale
\square^M	quantity corresponding to the macroscopic scale
$\hat{\square}$	vector/matrix notation, also VOIGT notation
\square^*	homogenised value of a quantity
$\dot{\square}$	time derivative of a value
$\square^{\parallel}/\square^{\times}$	degree of freedom \square is linked symmetrically/anti-symmetric

Abbreviations

CAD	Computer Aided Design
CNN	convolutional neural network
CT	Computed tomography
FEM	Finite Element Method
IGA	Isogeometric Analysis
MRC	moment reduction constraint
NURBS	Non-Uniform Rational B-Splines
pbc	periodic boundary conditions
RVE	Representative Volume Element
sbc	shell boundary conditions
SBFEM	Scaled Boundary Finite Element Method
SBIGA	Scaled Boundary Isogeometric Analysis
tbc	traction boundary conditions
YLT	yield line theory

Appendix A

Boundary Conditions for the RVE

It is to be shown, that the boundary conditions from sec. 4.3 fulfill the Hill-Mandel condition. The main equations are briefly recapitulated. The Hill-Mandel condition from Eq. 4.6 reads

$$\langle \mathbf{P}^m : \mathbf{F}^m \rangle - \langle \mathbf{P}^m \rangle : \langle \mathbf{F}^m \rangle = 0. \quad (\text{A.1})$$

The macroscopic fields can be expressed as surface integrals following Eq. 4.5.

$$\begin{aligned} \mathbf{P}^M &= \frac{1}{V^m} \int_{\Omega^m} (X_j P_{ik}^m)_{,k} dV = \frac{1}{V^m} \int_{\Gamma^m} X_j^m P_{ik}^m N_k^m dA = \frac{1}{V^m} \int_{\Gamma^m} \mathbf{t}_0^m \otimes \mathbf{X}^m dA \\ \mathbf{F}^M &= \frac{1}{V^m} \int_{\Omega^m} \text{Grad } \mathbf{x}^m dV = \frac{1}{V^m} \int_{\Gamma^m} \mathbf{x}^m \otimes \mathbf{N} dA \end{aligned} \quad (\text{A.2})$$

Linear displacement boundary condition Using linear displacement boundary conditions the macroscopic deformation gradient \mathbf{F}^M is prescribed as constant value \mathbf{F}^0 on the lateral RVE boundaries

$$\mathbf{x}^m = \mathbf{F}^0 \mathbf{X}^m. \quad (\text{A.3})$$

The average of the internal microscopic work can be rewritten as

$$\langle \mathbf{P}^m : \mathbf{F}^m \rangle = \frac{1}{V^m} \int_{\Omega^m} \mathbf{P}^m : \mathbf{F}^m dV = \frac{1}{V^m} \int_{\Omega^m} \mathbf{P}^m : \text{Grad } \mathbf{x}^m dV. \quad (\text{A.4})$$

Using

$$\text{Div}(\mathbf{P}^m \mathbf{x}^m) = \underbrace{\text{Div}(\mathbf{P}^m)}_{=0} \mathbf{x}^m + \mathbf{P}^m : \text{Grad } \mathbf{x}^m \quad (\text{A.5})$$

Eq. A.4 can be written as

$$\begin{aligned}
\langle \mathbf{P}^m : \mathbf{F}^m \rangle &= \frac{1}{V^m} \int_{\Omega^m} \text{Div}(\mathbf{P}^m \mathbf{x}^m) \, dV = \frac{1}{V^m} \int_{\Gamma^m} \mathbf{P}^m : \mathbf{x}^m \otimes \mathbf{N} \, dA \\
&= \frac{1}{V^m} \int_{\Gamma^m} \mathbf{t}_0^m \cdot \mathbf{x}^m \, dA = \frac{1}{V^m} \int_{\Gamma^m} \mathbf{t}_0^m \cdot (\mathbf{F}^0 \mathbf{X}^m) \, dA = \underbrace{\frac{1}{V^m} \int_{\Gamma^m} \mathbf{t}_0^m \otimes \mathbf{X}^m \, dA}_{\mathbf{P}^M} : \mathbf{F}^0 \\
&= \mathbf{P}^M : \mathbf{F}^0,
\end{aligned} \tag{A.6}$$

which proves that the displacement boundary conditions fulfill the HILL-MANDEL condition.

Constant traction boundary condition Employing constant traction boundary conditions the macroscopic stress \mathbf{P}^M is applied as a constant value \mathbf{P}^0 on the RVE boundaries

$$\mathbf{t}_0^m = \mathbf{P}^0 \mathbf{N}. \tag{A.7}$$

Similar to Eq. A.6 the averaged internal work at the microscopic scale can be rewritten as

$$\langle \mathbf{P}^m : \mathbf{F}^m \rangle = \frac{1}{V^m} \int_{\Gamma^m} \mathbf{t}_0^m \cdot \mathbf{x}^m \, dA. \tag{A.8}$$

Inserting the boundary condition yields

$$\begin{aligned}
\langle \mathbf{P}^m : \mathbf{F}^m \rangle &= \frac{1}{V^m} \int_{\Gamma^m} \mathbf{t}_0^m \cdot \mathbf{x}^m \, dA = \frac{1}{V^m} \int_{\Gamma^m} (\mathbf{P}^0 \mathbf{N}) \cdot \mathbf{x}^m \, dA = \mathbf{P}^0 : \underbrace{\frac{1}{V^m} \int_{\Gamma^m} \mathbf{x}^m \otimes \mathbf{N} \, dA}_{\mathbf{F}^M} \\
&= \mathbf{P}^0 : \mathbf{F}^M,
\end{aligned} \tag{A.9}$$

which shows that the HILL-MANDEL condition is fulfilled for the constant traction boundary conditions.

Periodic boundary conditions If opposing RVE boundaries are geometrically identical, periodic boundary conditions can be employed by splitting the surface integral in a positive and a negative part. Then, periodic displacement boundary conditions and antiperiodic tractions can be applied.

$$\begin{aligned}
\mathbf{x}^{m^+} - \mathbf{x}^{m^-} &= \mathbf{F}^M \left(\mathbf{X}^{m^+} - \mathbf{X}^{m^-} \right) \quad \text{and} \\
\mathbf{t}^{m^+} &= -\mathbf{t}^{m^-} \quad \text{on } \Gamma^m
\end{aligned} \tag{A.10}$$

Again choosing Eq. A.8 as a starting point and splitting the boundary shows that the HILL-MANDEL condition is also fulfilled for the periodic boundary conditions.

$$\begin{aligned}
\langle \mathbf{P}^m : \mathbf{F}^m \rangle &= \frac{1}{V^m} \int_{\Gamma^m} \mathbf{t}_0^m \cdot \mathbf{x}^m \, dA = \frac{1}{V^m} \left[\int_{\Gamma^{m+}} \mathbf{t}_0^{m+} \cdot \mathbf{x}^{m+} \, dA + \int_{\Gamma^{m-}} \mathbf{t}_0^{m-} \cdot \mathbf{x}^{m-} \, dA \right] \\
&= \frac{1}{V^m} \int_{\Gamma^{m+}} \mathbf{t}_0^{m+} \cdot (\mathbf{x}^{m+} - \mathbf{x}^{m-}) \, dA = \frac{1}{V^m} \int_{\Gamma^{m+}} \mathbf{t}_0^{m+} \cdot \mathbf{F}^M (\mathbf{X}^{m+} - \mathbf{X}^{m-}) \, dA \\
&= \frac{1}{V^m} \int_{\Gamma^m} \underbrace{\mathbf{t}_0^m \otimes \mathbf{X}^m}_{\mathbf{P}^M} \, dA : \mathbf{F}^M
\end{aligned} \tag{A.11}$$

Appendix B

Derivation of differential operator

The differential operator from Eq. 2.6

$$\mathcal{D}^T = \begin{bmatrix} \frac{\partial}{\partial X_1} & 0 & 0 & \frac{\partial}{\partial X_2} & 0 & \frac{\partial}{\partial X_3} & 0 & 0 & 0 \\ 0 & \frac{\partial}{\partial X_2} & 0 & 0 & \frac{\partial}{\partial X_1} & 0 & \frac{\partial}{\partial X_3} & 0 & 0 \\ 0 & 0 & \frac{\partial}{\partial X_3} & 0 & 0 & 0 & \frac{\partial}{\partial X_1} & 0 & \frac{\partial}{\partial X_2} \end{bmatrix} \quad (\text{B.1})$$

can be expressed in terms of the parametric coordinates using the JACOBIAN matrix. For the scaled boundary formulation it reads

$$\mathbf{J} = \begin{bmatrix} 1 & 0 & 0 \\ 0 & \xi & 0 \\ 0 & 0 & \xi \end{bmatrix} \underbrace{\begin{bmatrix} \tilde{X}_1 - \hat{X}_1 & \tilde{X}_2 - \hat{X}_2 & \tilde{X}_3 - \hat{X}_3 \\ \tilde{X}_{1,\eta} & \tilde{X}_{2,\eta} & \tilde{X}_{3,\eta} \\ \tilde{X}_{1,\zeta} & \tilde{X}_{2,\zeta} & \tilde{X}_{3,\zeta} \end{bmatrix}}_{\tilde{\mathbf{J}}(\eta,\zeta)}. \quad (\text{B.2})$$

Its determinant is defined as $\det \mathbf{J} = \xi^2 \det(\tilde{\mathbf{J}}) = \xi^2 \tilde{J}$, where

$$\det(\tilde{\mathbf{J}}) = \left[(\tilde{X}_1 - \hat{X}_1) (\tilde{X}_{2,\eta} \tilde{X}_{3,\zeta} - \tilde{X}_{3,\eta} \tilde{X}_{2,\zeta}) + (\tilde{X}_2 - \hat{X}_2) (\tilde{X}_{3,\eta} \tilde{X}_{1,\zeta} - \tilde{X}_{1,\eta} \tilde{X}_{3,\zeta}) \right. \\ \left. + (\tilde{X}_3 - \hat{X}_3) (\tilde{X}_{1,\eta} \tilde{X}_{2,\zeta} - \tilde{X}_{2,\eta} \tilde{X}_{1,\zeta}) \right]. \quad (\text{B.3})$$

The differential operator can be written as

$$\mathcal{D} = \mathbf{b}_1 \frac{\partial}{\partial \xi} + \frac{1}{\xi} \left(\mathbf{b}_2 \frac{\partial}{\partial \eta} + \mathbf{b}_3 \frac{\partial}{\partial \zeta} \right). \quad (\text{B.4})$$

The matrices $\mathbf{b}_1, \mathbf{b}_2$ and \mathbf{b}_3 contain the components of the inverse of the jacobian $\tilde{\mathbf{J}}$.

$$\mathbf{b}_1 = \begin{bmatrix} \tilde{j}_{11} & 0 & 0 \\ 0 & \tilde{j}_{21} & 0 \\ 0 & 0 & \tilde{j}_{31} \\ \tilde{j}_{21} & 0 & 0 \\ 0 & \tilde{j}_{11} & 0 \\ \tilde{j}_{31} & 0 & 0 \\ 0 & 0 & \tilde{j}_{11} \\ 0 & \tilde{j}_{31} & 0 \\ 0 & 0 & \tilde{j}_{21} \end{bmatrix}, \quad \mathbf{b}_2 = \begin{bmatrix} \tilde{j}_{12} & 0 & 0 \\ 0 & \tilde{j}_{22} & 0 \\ 0 & 0 & \tilde{j}_{32} \\ \tilde{j}_{22} & 0 & 0 \\ 0 & \tilde{j}_{12} & 0 \\ \tilde{j}_{32} & 0 & 0 \\ 0 & 0 & \tilde{j}_{12} \\ 0 & \tilde{j}_{32} & 0 \\ 0 & 0 & \tilde{j}_{22} \end{bmatrix}, \quad \mathbf{b}_3 = \begin{bmatrix} \tilde{j}_{13} & 0 & 0 \\ 0 & \tilde{j}_{23} & 0 \\ 0 & 0 & \tilde{j}_{33} \\ \tilde{j}_{23} & 0 & 0 \\ 0 & \tilde{j}_{13} & 0 \\ \tilde{j}_{33} & 0 & 0 \\ 0 & 0 & \tilde{j}_{13} \\ 0 & \tilde{j}_{33} & 0 \\ 0 & 0 & \tilde{j}_{23} \end{bmatrix} \quad (\text{B.5})$$

The components of the inverse are defined as:

$$\begin{aligned} \tilde{j}_{11} &= \frac{1}{\det(\tilde{\mathbf{J}})} \left(\tilde{X}_{2,\eta} \tilde{X}_{3,\zeta} - \tilde{X}_{3,\eta} \tilde{X}_{2,\zeta} \right) \\ \tilde{j}_{12} &= \frac{1}{\det(\tilde{\mathbf{J}})} \left((\tilde{X}_2 - \hat{X}_2) \tilde{X}_{3,\zeta} - (\tilde{X}_3 - \hat{X}_3) \tilde{X}_{2,\zeta} \right) \\ \tilde{j}_{13} &= \frac{1}{\det(\tilde{\mathbf{J}})} \left((\tilde{X}_2 - \hat{X}_2) \tilde{X}_{3,\eta} - (\tilde{X}_3 - \hat{X}_3) \tilde{X}_{2,\eta} \right) \\ \tilde{j}_{21} &= \frac{1}{\det(\tilde{\mathbf{J}})} \left(\tilde{X}_{3,\eta} \tilde{X}_{1,\zeta} - \tilde{X}_{1,\eta} \tilde{X}_{3,\zeta} \right) \\ \tilde{j}_{22} &= \frac{1}{\det(\tilde{\mathbf{J}})} \left((\tilde{X}_1 - \hat{X}_1) \tilde{X}_{3,\zeta} - (\tilde{X}_3 - \hat{X}_3) \tilde{X}_{1,\zeta} \right) \\ \tilde{j}_{23} &= \frac{1}{\det(\tilde{\mathbf{J}})} \left((\tilde{X}_3 - \hat{X}_3) \tilde{X}_{1,\eta} - (\tilde{X}_1 - \hat{X}_1) \tilde{X}_{3,\eta} \right) \\ \tilde{j}_{31} &= \frac{1}{\det(\tilde{\mathbf{J}})} \left(\tilde{X}_{1,\eta} \tilde{X}_{2,\zeta} - \tilde{X}_{2,\eta} \tilde{X}_{1,\zeta} \right) \\ \tilde{j}_{32} &= \frac{1}{\det(\tilde{\mathbf{J}})} \left((\tilde{X}_1 - \hat{X}_1) \tilde{X}_{2,\zeta} - (\tilde{X}_2 - \hat{X}_2) \tilde{X}_{1,\zeta} \right) \\ \tilde{j}_{33} &= \frac{1}{\det(\tilde{\mathbf{J}})} \left((\tilde{X}_1 - \hat{X}_1) \tilde{X}_{2,\eta} - (\tilde{X}_2 - \hat{X}_2) \tilde{X}_{1,\eta} \right). \end{aligned} \quad (\text{B.6})$$

Appendix C

Deformation modes

A homogeneous RVE with dimensions $l_x \times l_y \times h^{RVE} = 1 \times 1 \times 1$ is investigated. Linear-elastic material behaviour with Young's modulus $E = 100$ and Poisson's ratio $\nu = 0.3$ is assumed. To compare the deformation modes of the RVE the macroscopic shell strains are applied individually using each of the presented type of boundary condition. For each case the shell strain takes the value of 0.2.

The deformation modes of the RVE for all three types of boundary conditions are presented in the following. The contour colours represent the displacement magnitude, where blue indicates the minimum values and red indicates the maximum values.

It can be observed that reasonable deformation modes are obtained for all membrane strains $\varepsilon_{\alpha\beta}$ and all curvatures $\kappa_{\alpha\beta}$ ($\alpha, \beta = x, y$), irrespective of the employed type of boundary condition. Significant differences can be observed only for the applied shear strain γ_α . These are discussed in detail in sec. 7.1.3.

C.1 Traction boundary conditions

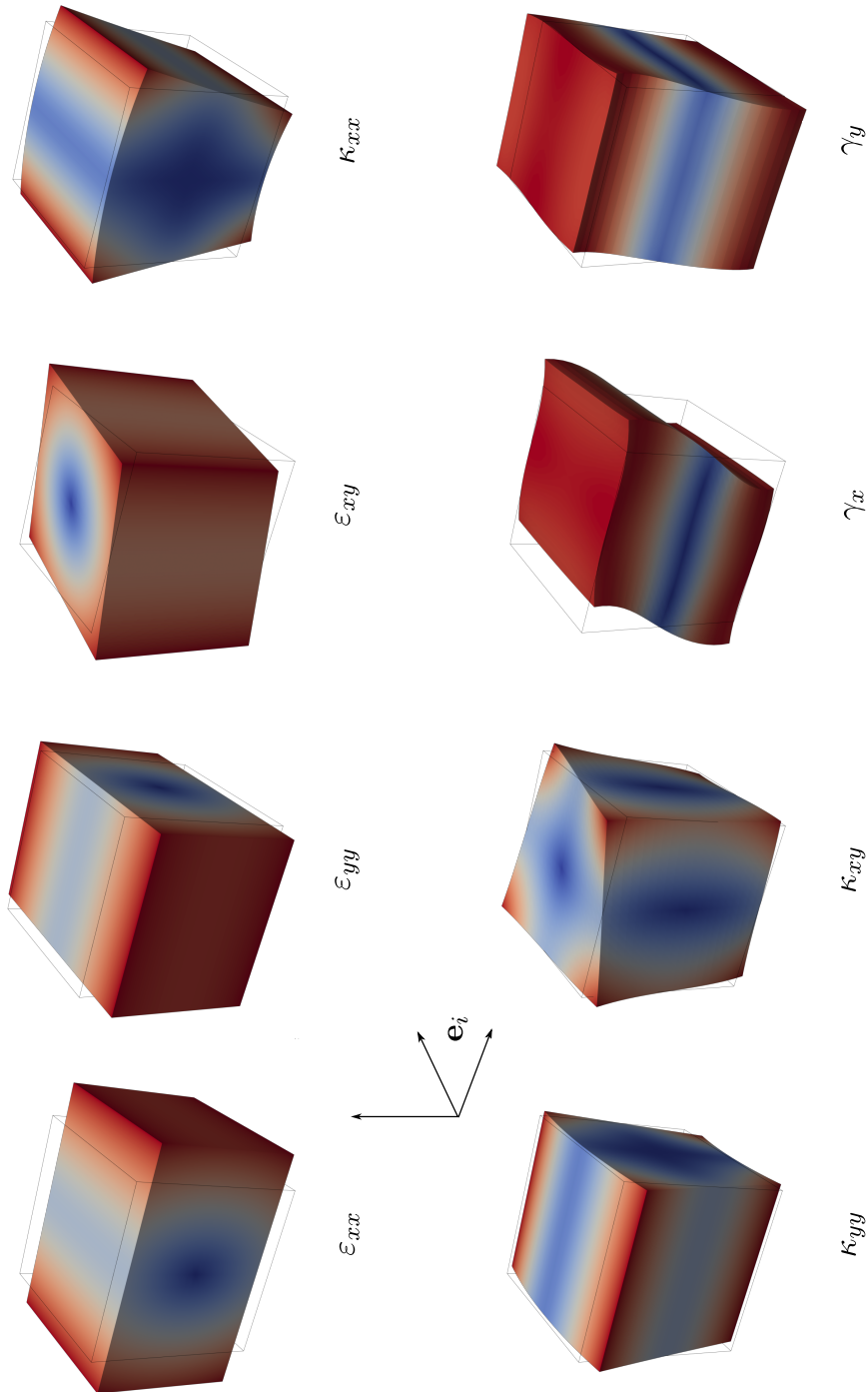


Figure C.1: Deformation modes of isotropic, homogeneous RVE using traction boundary conditions (tbc)

C.2 Shell boundary conditions

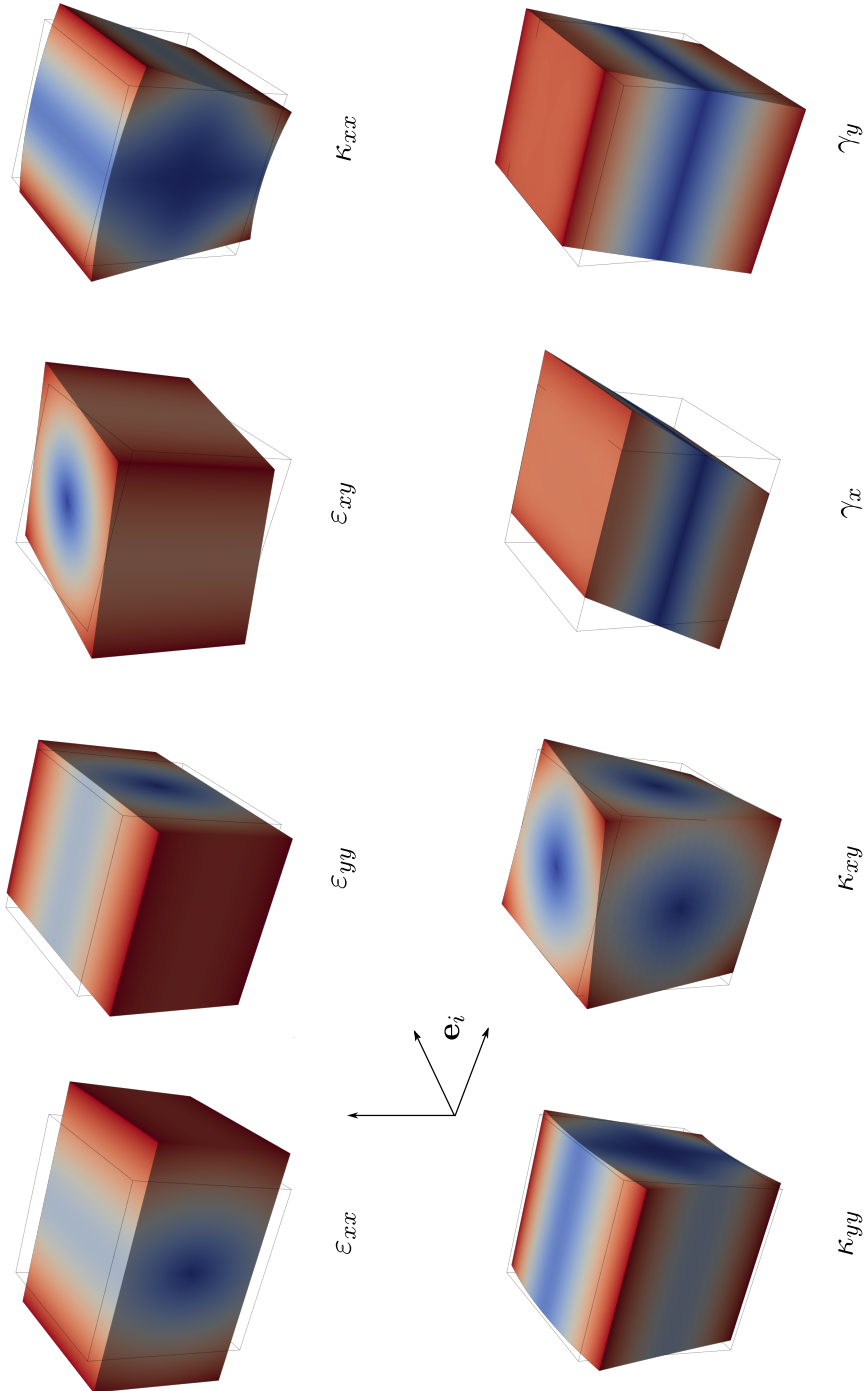


Figure C.2: Deformation modes of isotropic, homogeneous RVE using shell boundary conditions (sbc)

C.3 Periodic boundary conditions

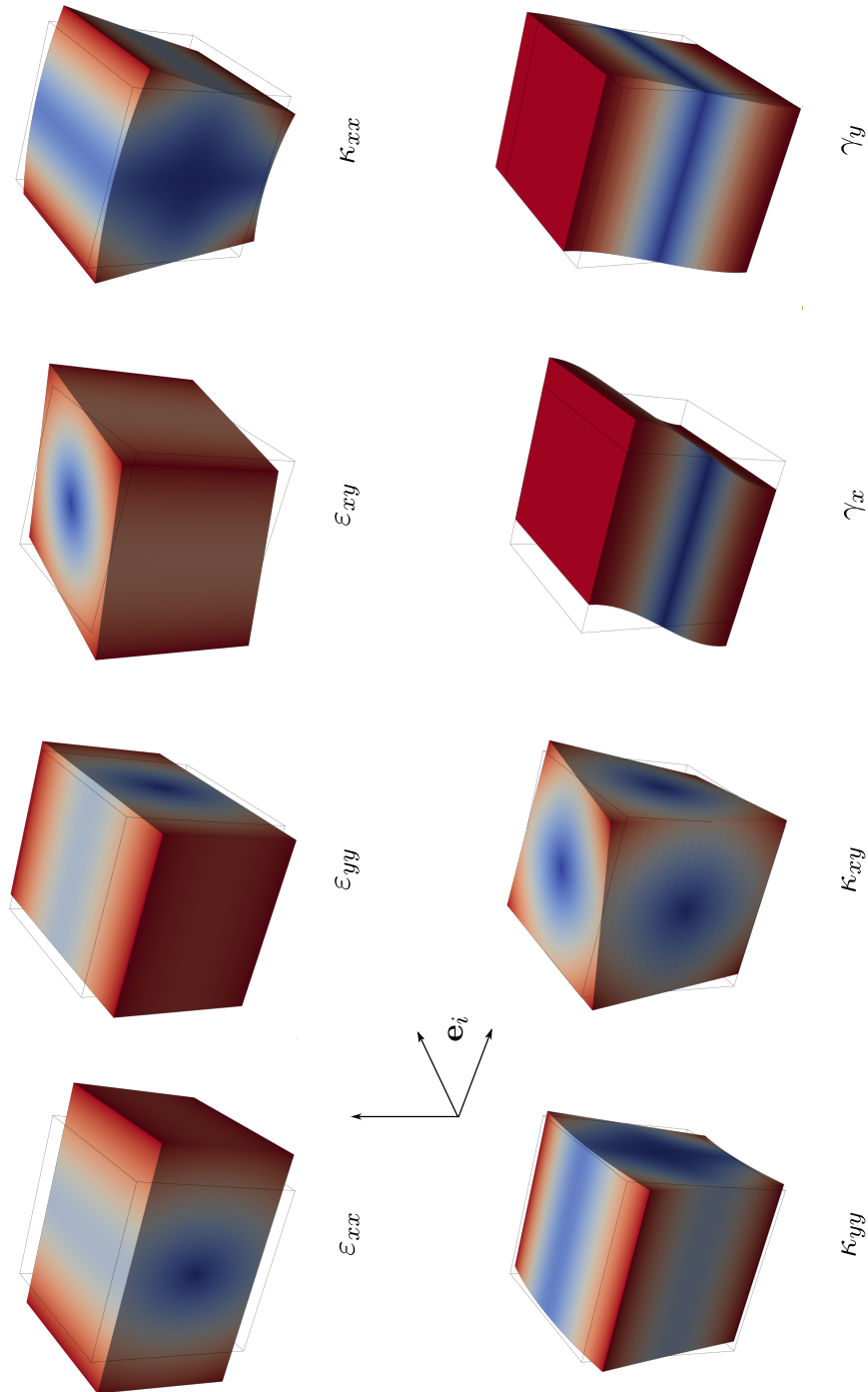


Figure C.3: Deformation modes of isotropic, homogeneous RVE using periodic boundary conditions (pbc)

Bibliography

- [1] J. Aboudi, S. M. Arnold, and B. A. Bednarczyk. *Micromechanics of Composite Materials*. Elsevier, 2013. ISBN 978-0-12-397035-0.
- [2] M. Aigner, C. Heinrich, B. Jüttler, E. Pilgerstorfer, B. Simeon, and A.-V. Vuong. Swept volume parameterization for isogeometric analysis. In: E. R. Hancock, R. R. Martin, and M. A. Sabin (eds.), *Mathematics of Surfaces XIII*, vol. 5654 of *Lecture Notes in Computer Science*, pp. 19–44. Springer, Berlin, Heidelberg, 2009. ISBN 978-3-642-03595-1.
- [3] H. Altenbach. *Kontinuumsmechanik*. Springer, Berlin, Heidelberg, 2015. ISBN 978-3-662-47069-5.
- [4] H. Altenbach, J. Chróścielewski, V. A. Eremeyev, and K. Wiśniewski (eds.). *Recent Developments in the Theory of Shells*. Advanced Structured Materials. Springer International Publishing, Cham, 2019. ISBN 978-3-030-17746-1.
- [5] J. Altenbach, H. Altenbach, and V. A. Eremeyev. On generalized cosserat-type theories of plates and shells: a short review and bibliography. *Archive of Applied Mechanics (Ingenieur Archiv)*, 80(1):73–92, 2010. DOI: 10.1007/s00419-009-0365-3.
- [6] A. Apostolatos, R. Schmidt, R. Wüchner, and K.-U. Bletzinger. A nitsche-type formulation and comparison of the most common domain decomposition methods in isogeometric analysis. *International Journal for Numerical Methods in Engineering*, 97(7):473–504, 2014. DOI: 10.1002/nme.4568.
- [7] C. Arioli, A. Shamanskiy, S. Klinkel, and B. Simeon. Scaled boundary parametrizations in isogeometric analysis. *Computer Methods in Applied Mechanics and Engineering*, 349:576–594, 2019. DOI: 10.1016/j.cma.2019.02.022.
- [8] V. Badrinarayanan, A. Handa, and R. Cipolla. SegNet: A Deep Convolutional Encoder-Decoder Architecture for Robust Semantic Pixel-Wise Labelling. *arXiv preprint*, 2015. URL <http://arxiv.org/pdf/1505.07293v1>.
- [9] K.-J. Bathe. *Finite element procedures*. Prentice Hall, Englewood Cliffs, 2014. ISBN 978-0-9790049-5-7.

- [10] B. Bauer, C. Arioli, and B. Simeon. Generating Star-Shaped Blocks for Scaled Boundary Multipatch IGA. In: H. van Brummelen, C. Vuik, M. Möller, C. Verhoosel, B. Simeon, and B. Jüttler (eds.), *Isogeometric Analysis and Applications 2018*, vol. 133 of *Lecture Notes in Computational Science and Engineering*, pp. 1–25. Springer International Publishing, Cham, 2021. ISBN 978-3-030-49835-1.
- [11] Z. P. Bažant and B. H. Oh. Microplane Model for Progressive Fracture of Concrete and Rock. *Journal of Engineering Mechanics*, 111(4):559–582, 1985. DOI: 10.1061/(ASCE)0733-9399(1985)111:4(559).
- [12] Y. Bazilevs, V. M. Calo, J. A. Cottrell, J. A. Evans, T. J. R. Hughes, S. Lipton, M. A. Scott, and T. W. Sederberg. Isogeometric analysis using T-splines. *Computer Methods in Applied Mechanics and Engineering*, 199(5-8):229–263, 2010. DOI: 10.1016/j.cma.2009.02.036.
- [13] T. Belytschko, S. Loehnert, and J.-H. Song. Multiscale aggregating discontinuities: A method for circumventing loss of material stability. *International Journal for Numerical Methods in Engineering*, 73(6):869–894, 2008. DOI: 10.1002/nme.2156.
- [14] M. Berger, A. Tagliasacchi, L. M. Seversky, P. Alliez, G. Guennebaud, J. A. Levine, A. Sharf, and C. T. Silva. A Survey of Surface Reconstruction from Point Clouds. *Computer Graphics Forum*, 36(1):301–329, 2017. DOI: 10.1111/cgf.12802.
- [15] M. Bischoff and E. Ramm. Shear deformable shell elements for large strains and rotations. *International Journal for Numerical Methods in Engineering*, 40(23):4427–4449, 1997. DOI: 10.1002/(SICI)1097-0207(19971215)40:23<4427::AID-NME268>3.0.CO;2-9.
- [16] M. Bischoff, K.-U. Bletzinger, W. A. Wall, and E. Ramm. Models and Finite Elements for Thin-Walled Structures. In: E. Stein, R. Borst, and T. J. R. Hughes (eds.), *Encyclopedia of Computational Mechanics*. Wiley, 2004. ISBN 9780470846995.
- [17] K.-U. Bletzinger, M. Bischoff, and E. Ramm. A unified approach for shear-locking-free triangular and rectangular shell finite elements. *Computers & Structures*, 75(3):321–334, 2000. DOI: 10.1016/S0045-7949(99)00140-6.
- [18] R. I. Borja. *Plasticity*. Springer, Berlin, Heidelberg, 2013. ISBN 978-3-642-38546-9.
- [19] E. Börjesson, F. Larsson, K. Runesson, J. J. Remmers, and M. Fagerström. Variationally consistent homogenisation of plates. *Computer Methods in Applied Mechanics and Engineering*, 413:116094, 2023. DOI: 10.1016/j.cma.2023.116094.
- [20] L. Bouhala, Y. Koutsawa, A. Makradi, and S. Belouettar. An advanced numerical method for predicting effective elastic properties of heterogeneous composite materials. *Composite Structures*, 117:114–123, 2014. DOI: 10.1016/j.compstruct.2014.06.028.

- [21] D. Bouvard, J. M. Chaix, R. Dendievel, A. Fazekas, J. M. Létang, G. Peix, and D. Quenard. Characterization and simulation of microstructure and properties of EPS lightweight concrete. *Cement and Concrete Research*, 37(12):1666–1673, 2007. DOI: 10.1016/j.cemconres.2007.08.028.
- [22] B. Brank. Nonlinear shell models with seven kinematic parameters. *Computer Methods in Applied Mechanics and Engineering*, 194(21-24):2336–2362, 2005. DOI: 10.1016/j.cma.2004.07.036.
- [23] N. Büchter and E. Ramm. Shell theory versus degeneration - a comparison in large rotation finite element analysis. *International Journal for Numerical Methods in Engineering*, 34(1):39–59, 1992. DOI: 10.1002/nme.1620340105.
- [24] N. Büchter, E. Ramm, and D. Roehl. Three-dimensional extension of non-linear shell formulation based on the enhanced assumed strain concept. *International Journal for Numerical Methods in Engineering*, 37(15):2551–2568, 1994. DOI: 10.1002/nme.1620371504.
- [25] T. D. Bui, J. Shin, and T. Moon. Skip-connected 3D DenseNet for volumetric infant brain MRI segmentation. *Biomedical Signal Processing and Control*, 54: 101613, 2019. DOI: 10.1016/j.bspc.2019.101613.
- [26] P. Cartraud and T. Messenger. Computational homogenization of periodic beam-like structures. *International Journal of Solids and Structures*, 43(3-4):686–696, 2006. DOI: 10.1016/j.ijsolstr.2005.03.063.
- [27] M. Chasapi and S. Klinkel. A scaled boundary isogeometric formulation for the elasto-plastic analysis of solids in boundary representation. *Computer Methods in Applied Mechanics and Engineering*, 333:475–496, 2018. DOI: 10.1016/j.cma.2018.01.015.
- [28] M. Chasapi and S. Klinkel. Geometrically nonlinear analysis of solids using an isogeometric formulation in boundary representation. *Computational Mechanics*, 65(2):355–373, 2020. DOI: 10.1007/s00466-019-01772-6.
- [29] M. Chasapi, W. Dornisch, and S. Klinkel. Patch coupling in isogeometric analysis of solids in boundary representation using a mortar approach. *International Journal for Numerical Methods in Engineering*, 121(14):3206–3226, 2020. DOI: 10.1002/nme.6354.
- [30] M. Chasapi, L. Mester, B. Simeon, and S. Klinkel. Isogeometric analysis of 3D solids in boundary representation for problems in nonlinear solid mechanics and structural dynamics. *International Journal for Numerical Methods in Engineering*, 2021. DOI: 10.1002/nme.6893.
- [31] S. Chen, K. Ma, and Y. Zheng. Med3D: Transfer Learning for 3D Medical Image Analysis. *arXiv preprint*, 2019. URL <http://arxiv.org/pdf/1904.00625v4>.

- [32] E. B. Chin and N. Sukumar. Scaled boundary cubature scheme for numerical integration over planar regions with affine and curved boundaries. *Computer Methods in Applied Mechanics and Engineering*, 380:113796, 2021. DOI: 10.1016/j.cma.2021.113796.
- [33] H.-H. Cho, Y. Cho, and H. N. Han. Finite element analysis for mechanical response of Ti foams with regular structure obtained by selective laser melting. *Acta Materialia*, 97:199–206, 2015. DOI: 10.1016/j.actamat.2015.07.003.
- [34] R. Chudoba, E. Sharei, and A. Scholzen. A strain-hardening microplane damage model for thin-walled textile-reinforced concrete shells, calibration procedure, and experimental validation. *Composite Structures*, 152:913–928, 2016. DOI: 10.1016/j.compstruct.2016.06.030.
- [35] Ö. Çiçek, A. Abdulkadir, S. S. Lienkamp, T. Brox, and O. Ronneberger. 3D U-Net: Learning Dense Volumetric Segmentation from Sparse Annotation. In: *Medical Image Computing and Computer-Assisted Intervention – MICCAI 2016: 19th International Conference, Athens, Greece, October 17-21, 2016, Proceedings, Part II 19*, pp. 424–432. Springer, 2016. URL <http://arxiv.org/pdf/1606.06650v1>.
- [36] F. Cirak, M. Ortiz, and P. Schröder. Subdivision surfaces: a new paradigm for thin-shell finite-element analysis. *International Journal for Numerical Methods in Engineering*, 47(12):2039–2072, 2000. DOI: 10.1002/(SICI)1097-0207(20000430)47:12<2039::AID-NME872>3.0.CO;2-1.
- [37] D. Cirosan, A. Giusti, L. Gambardella, and J. Schmidhuber. Deep neural networks segment neuronal membranes in electron microscopy images. *Advances in neural information processing systems*, 25, 2012.
- [38] E. Coenen, V. G. Kouznetsova, and M. G. Geers. Computational homogenization for heterogeneous thin sheets. *International Journal for Numerical Methods in Engineering*, 83(8-9):1180–1205, 2010. DOI: 10.1002/nme.2833.
- [39] Y. Cong, S. Nezamabadi, H. Zahrouni, and J. Yvonnet. Multiscale computational homogenization of heterogeneous shells at small strains with extensions to finite displacements and buckling. *International Journal for Numerical Methods in Engineering*, 104(4):235–259, 2015. DOI: 10.1002/nme.4927.
- [40] J. A. Cottrell, T. J. R. Hughes, and A. Reali. Studies of refinement and continuity in isogeometric structural analysis. *Computer Methods in Applied Mechanics and Engineering*, 196(41-44):4160–4183, 2007. DOI: 10.1016/j.cma.2007.04.007.
- [41] J. A. Cottrell, T. J. R. Hughes, and Y. Bazilevs. *Isogeometric analysis: Toward integration of CAD and FEA*. John Wiley and Sons, Chichester and Hoboken, 2009. ISBN 978-0-470-74873-2.

- [42] R. de Borst, M. A. Crisfield, J. J. C. Remmers, and C. V. Verhoosel. *Non-Linear Finite Element Analysis of Solids and Structures*. Wiley, 2012. ISBN 9780470666449.
- [43] M. R. Dörfel, B. Jüttler, and B. Simeon. Adaptive isogeometric analysis by local h-refinement with T-splines. *Computer Methods in Applied Mechanics and Engineering*, 199(5-8):264–275, 2010. DOI: 10.1016/j.cma.2008.07.012.
- [44] W. Dornisch, G. Vitucci, and S. Klinkel. The weak substitution method - an application of the mortar method for patch coupling in NURBS-based isogeometric analysis. *International Journal for Numerical Methods in Engineering*, 103(3):205–234, 2015. DOI: 10.1002/nme.4918.
- [45] W. J. Drugan and J. R. Willis. A micromechanics-based nonlocal constitutive equation and estimates of representative volume element size for elastic composites. *Journal of the Mechanics and Physics of Solids*, 44(4):497–524, 1996. DOI: 10.1016/0022-5096(96)00007-5.
- [46] A. Du Plessis and W. P. Boshoff. A review of X-ray computed tomography of concrete and asphalt construction materials. *Construction and Building Materials*, 199:637–651, 2019. DOI: 10.1016/j.conbuildmat.2018.12.049.
- [47] S. Du Rolland Roscoat, M. Decain, C. Geindreau, X. Thibault, and J.-F. Bloch. Microstructural analysis of paper using synchrotron X-ray microtomography: numerical estimation of the permeability and effective thermal conductivity. *Appita: Technology, Innovation, Manufacturing, Environment*, 61(4), 2008.
- [48] E. Dvorkin and K.-J. Bathe. A continuum mechanics based four-node shell element for general non-linear analysis. *Engineering Computations*, 1(1):77–88, 1984. DOI: 10.1108/eb023562.
- [49] J. D. Eshelby. The determination of the elastic field of an ellipsoidal inclusion, and related problems. *Proceedings of the Royal Society of London. Series A. Mathematical and Physical Sciences*, 241(1226):376–396, 1957. DOI: 10.1098/rspa.1957.0133.
- [50] L. M. Evans, E. Sözümert, B. E. Keenan, C. E. Wood, and A. Du Plessis. A review of image-based simulation applications in high-value manufacturing. *Archives of Computational Methods in Engineering*, 30(3):1495–1552, 2023. DOI: 10.1007/s11831-022-09836-2.
- [51] F. Feyel. Multiscale FE2 elastoviscoplastic analysis of composite structures. *Computational Materials Science*, 16(1-4):344–354, 1999. DOI: 10.1016/S0927-0256(99)00077-4.
- [52] F. Feyel and J.-L. Chaboche. FE2 multiscale approach for modelling the elastoviscoplastic behaviour of long fibre SiC/Ti composite materials. *Computer Methods in Applied Mechanics and Engineering*, 183(3-4):309–330, 2000. DOI: 10.1016/S0045-7825(99)00224-8.

- [53] J. Främby, J. Brouzoulis, and M. Fagerström. Assessment of two methods for the accurate prediction of transverse stress distributions in laminates. *Composite Structures*, 140:602–611, 2016. DOI: 10.1016/j.compstruct.2015.12.036.
- [54] M. G. Geers, V. G. Kouznetsova, and W. A. M. Brekelmans. Gradient-enhanced computational homogenization for the micro-macro scale transition. *Le Journal de Physique IV*, 11(PR5):Pr5–145–Pr5–152, 2001. DOI: 10.1051/jp4:2001518.
- [55] M. G. Geers, E. Coenen, and V. G. Kouznetsova. Multi-scale computational homogenization of structured thin sheets. *Modelling and Simulation in Materials Science and Engineering*, 15(4):S393–S404, 2007. DOI: 10.1088/0965-0393/15/4/S06.
- [56] M. G. Geers, V. G. Kouznetsova, and W. A. M. Brekelmans. Multi-scale computational homogenization: Trends and challenges. *Journal of Computational and Applied Mathematics*, 234(7):2175–2182, 2010. DOI: 10.1016/j.cam.2009.08.077.
- [57] I. M. Gitman, H. Askes, and L. J. Sluys. Representative volume: Existence and size determination. *Engineering Fracture Mechanics*, 74(16):2518–2534, 2007. DOI: 10.1016/j.engfracmech.2006.12.021.
- [58] G. H. Golub and C. F. van Loan. *Matrix computations*. Johns Hopkins studies in the mathematical sciences. The Johns Hopkins University Press, Baltimore, fourth edition, 2013. ISBN 978-1-4214-0859-0.
- [59] D. Gross and T. Seelig. *Bruchmechanik*. Springer, Berlin, Heidelberg, 2016. ISBN 978-3-662-46736-7.
- [60] O. Grove, K. Rajab, and L. A. Piegl. From CT to NURBS: Contour Fitting with B-spline Curves. *Computer-Aided Design and Applications*, 8(1):3–21, 2011. DOI: 10.1080/16864360.2010.10738807.
- [61] F. Gruttmann and W. Wagner. Structural analysis of composite laminates using a mixed hybrid shell element. *Computational Mechanics*, 37(6):479–497, 2006. DOI: 10.1007/s00466-005-0730-1.
- [62] F. Gruttmann and W. Wagner. A coupled two-scale shell model with applications to layered structures. *International Journal for Numerical Methods in Engineering*, 94(13):1233–1254, 2013. DOI: 10.1002/nme.4496.
- [63] F. Gruttmann, W. Wagner, and P. Wriggers. A nonlinear quadrilateral shell element with drilling degrees of freedom. *Archive of Applied Mechanics (Ingenieur Archiv)*, 62(7):474–486, 1992. DOI: 10.1007/BF00810238.
- [64] Z. Hashin and S. Shtrikman. A variational approach to the theory of the effective magnetic permeability of multiphase materials. *Journal of Applied Physics*, 33(10):3125–3131, 1962. DOI: 10.1063/1.1728579.

- [65] C. Helfen and S. Diebels. A numerical homogenisation method for sandwich plates based on a plate theory with thickness change. *ZAMM - Journal of Applied Mathematics and Mechanics / Zeitschrift für Angewandte Mathematik und Mechanik*, 93(2-3):113–125, 2013. DOI: 10.1002/zamm.201100173.
- [66] C. Helfen and S. Diebels. Computational homogenisation of composite plates: Consideration of the thickness change with a modified projection strategy. *Computers & Mathematics with Applications*, 67(5):1116–1129, 2014. DOI: 10.1016/j.camwa.2013.12.017.
- [67] D. Heller. *A nonlinear multiscale finite element model for comb-like sandwich panels*. PhD thesis, Technische Universität Darmstadt, 2016. URL <https://tuprints.ulb.tu-darmstadt.de/id/eprint/5288>.
- [68] D. Heller and F. Gruttmann. Nonlinear two-scale shell modeling of sandwiches with a comb-like core. *Composite Structures*, 144:147–155, 2016. DOI: 10.1016/j.compstruct.2016.02.042.
- [69] A. K. Hii and B. El Said. A kinematically consistent second-order computational homogenisation framework for thick shell models. *Computer Methods in Applied Mechanics and Engineering*, 398:115136, 2022. DOI: 10.1016/j.cma.2022.115136.
- [70] R. Hill. Elastic properties of reinforced solids: Some theoretical principles. *Journal of the Mechanics and Physics of Solids*, 11(5):357–372, 1963. DOI: 10.1016/0022-5096(63)90036-X.
- [71] G. A. Holzapfel. *Nonlinear solid mechanics: A continuum approach for engineering*. John Wiley & Sons Ltd, 2000. ISBN 978-0-471-82319-3.
- [72] M. Hori and S. Nemat-Nasser. On two micromechanics theories for determining micro–macro relations in heterogeneous solids. *Mechanics of Materials*, 31(10):667–682, 1999. DOI: 10.1016/S0167-6636(99)00020-4.
- [73] Z. Huang, Y. Wen, Z. Wang, J. Ren, and K. Jia. Surface reconstruction from point clouds: A survey and a benchmark. *arXiv preprint*, 2022. URL <http://arxiv.org/pdf/2205.02413v1>.
- [74] T. J. R. Hughes and W. K. Liu. Nonlinear finite element analysis of shells: Part I. three-dimensional shells. *Computer Methods in Applied Mechanics and Engineering*, 26(3):331–362, 1981. DOI: 10.1016/0045-7825(81)90121-3.
- [75] T. J. R. Hughes and T. E. Tezduyar. Finite elements based upon mindlin plate theory with particular reference to the four-node bilinear isoparametric element. *Journal of Applied Mechanics*, 48(3):587–596, 1981. DOI: 10.1115/1.3157679.

- [76] T. J. R. Hughes, J. A. Cottrell, and Y. Bazilevs. Isogeometric analysis: CAD, finite elements, NURBS, exact geometry and mesh refinement. *Computer Methods in Applied Mechanics and Engineering*, 194(39-41):4135–4195, 2005. DOI: 10.1016/j.cma.2004.10.008.
- [77] T. J. R. Hughes, A. Reali, and G. Sangalli. Efficient quadrature for NURBS-based isogeometric analysis. *Computer Methods in Applied Mechanics and Engineering*, 199(5-8):301–313, 2010. DOI: 10.1016/j.cma.2008.12.004.
- [78] J. H. Irving and J. G. Kirkwood. The statistical mechanical theory of transport processes. IV. The equations of hydrodynamics. *The Journal of Chemical Physics*, 18(6):817–829, 1950. DOI: 10.1063/1.1747782.
- [79] M. Jirásek. Comments on microplane theory. *Mechanics of Quasi-Brittle Materials and Structures*, pp. 55–77, 1999.
- [80] B. Jüttler, S. Maroscheck, M.-S. Kim, and Q. Youn Hong. Arc fibrations of planar domains. *Computer Aided Geometric Design*, 71:105–118, 2019. DOI: 10.1016/j.cagd.2019.04.010.
- [81] M. Kalthoff, M. Raupach, and T. Matschei. Investigation into the Integration of Impregnated Glass and Carbon Textiles in a Laboratory Mortar Extruder (LabMorTex). *Materials*, 14(23), 2021. DOI: 10.3390/ma14237406.
- [82] M. Kalthoff, M. Raupach, and T. Matschei. Extrusion and subsequent transformation of textile-reinforced mortar components—requirements on the textile, mortar and process parameters with a Laboratory Mortar Extruder (LabMorTex). *buildings*, 12(6):726, 2022. DOI: 10.3390/buildings12060726.
- [83] M. Kalthoff, S. Bosbach, J. G. Backes, C. Morales Cruz, M. Claßen, M. Traverso, M. Raupach, and T. Matschei. Fabrication of lightweight, carbon textile reinforced concrete components with internally nested lattice structure using 2-layer extrusion by LabMorTex. *Construction and Building Materials*, 395:132334, 2023. DOI: 10.1016/j.conbuildmat.2023.132334.
- [84] T. Kanit, S. Forest, I. Galliet, V. Mounoury, and D. Jeulin. Determination of the size of the representative volume element for random composites: Statistical and numerical approach. *International Journal of Solids and Structures*, 40(13-14): 3647–3679, 2003. DOI: 10.1016/S0020-7683(03)00143-4.
- [85] G. J. Kennedy and J. R. Martins. A homogenization-based theory for anisotropic beams with accurate through-section stress and strain prediction. *International Journal of Solids and Structures*, 49(1):54–72, 2012. DOI: 10.1016/j.ijsolstr.2011.09.012.

- [86] R. Kienzler, H. Altenbach, and I. Ott (eds.). *Theories of Plates and Shells: Critical Review and New Applications*. Springer Science & Business Media, 1 edition, 2004. ISBN 978-3-540-20997-3.
- [87] G. Kikis, L. Mester, H. Spartali, R. Chudoba, and S. Klinkel. Analyse des Trag- und Bruchverhaltens von Carbonbetonstrukturen im Rahmen des SFB/TRR 280/Analysis of the load-bearing and fracture behavior of carbon concrete structures as part of the SFB/TRR 280. *Bauingenieur*, 98(07-08):218–226, 2023. DOI: 10.37544/0005-6650-2023-07-08-40.
- [88] G. Kirchhoff. Über das Gleichgewicht und die Bewegung einer elastischen Scheibe. *Journal für die reine und angewandte Mathematik (Crelles Journal)*, 1850(40):51–88, 1850. DOI: 10.1515/crll.1850.40.51.
- [89] S. Klarmann. *Geometrisch und physikalisch nichtlineare Mehrskalenmodellierung räumlicher Stabtragwerke*. PhD thesis, Technische Universität Darmstadt, 2018. URL <https://tuprints.ulb.tu-darmstadt.de/id/eprint/7638>.
- [90] S. Klarmann and F. Gruttmann. A homogenization approach for beam-like structures with arbitrarily shaped and deformable cross-sections. In: M. Scheven, M.-A. Keip, and N. Karajan (eds.), *Proceedings of the 7th GACM Colloquium on Computational Mechanics*, vol. 7, pp. 476–479. Institute for Structural Mechanics, University of Stuttgart, Stuttgart, 2017.
- [91] S. Klarmann, F. Gruttmann, and S. Klinkel. Homogenization assumptions for coupled multiscale analysis of structural elements: Beam kinematics. *Computational Mechanics*, 65:635–661, 2020. DOI: 10.1007/s00466-019-01787-z.
- [92] S. Klarmann, G. Kikis, S. Klinkel, and R. Chudoba. Isogeometric cohesive zone modeling of interfaces in reinforced concrete structures. *PAMM*, 2023. DOI: 10.1002/pamm.202300160.
- [93] S. Klinkel. *Theorie und Numerik eines Volumen-Schalen-Elementes bei finiten elastischen und plastischen Verzerrungen*. PhD thesis, Karlsruher Institut für Technologie, Karlsruhe, 2000.
- [94] S. Klinkel, F. Gruttmann, and W. Wagner. A continuum based three-dimensional shell element for laminated structures. *Computers & Structures*, 71(1):43–62, 1999. DOI: 10.1016/S0045-7949(98)00222-3.
- [95] S. Klinkel, F. Gruttmann, and W. Wagner. A mixed shell formulation accounting for thickness strains and finite strain 3D material models. *International Journal for Numerical Methods in Engineering*, 74(6):945–970, 2008. DOI: 10.1002/nme.2199.

- [96] S. Klinkel, L. Chen, and W. Dornisch. A NURBS based hybrid collocation–Galerkin method for the analysis of boundary represented solids. *Computer Methods in Applied Mechanics and Engineering*, 284:689–711, 2015. DOI: 10.1016/j.cma.2014.10.029.
- [97] F. Koschnick. *Geometrische Lockingeffekte bei Finiten Elementen und ein allgemeines Konzept zu ihrer Vermeidung*. PhD thesis, Technische Universität München, München, 2004.
- [98] F. Koschnick, M. Bischoff, N. Camprubí, and K.-U. Bletzinger. The discrete strain gap method and membrane locking. *Computer Methods in Applied Mechanics and Engineering*, 194(21-24):2444–2463, 2005. DOI: 10.1016/j.cma.2004.07.040.
- [99] V. G. Kouznetsova. *Computational homogenization for the multi-scale analysis of multi-phase materials*. PhD thesis, Technische Universiteit Eindhoven, 2002.
- [100] V. G. Kouznetsova, M. G. Geers, and W. A. M. Brekelmans. Multi-scale second-order computational homogenization of multi-phase materials: a nested finite element solution strategy. *Computer Methods in Applied Mechanics and Engineering*, 193(48-51):5525–5550, 2004. DOI: 10.1016/j.cma.2003.12.073.
- [101] W. B. Krätzig and D. Jun. Multi-layer multi-director concepts for d-adaptivity in shell theory. *Computers & Structures*, 80(9-10):719–734, 2002. DOI: 10.1016/S0045-7949(02)00043-3.
- [102] E. Kröner. Berechnung der elastischen Konstanten des Vielkristalls aus den Konstanten des Einkristalls. *Zeitschrift für Physik*, 151(4):504–518, 1958. DOI: 10.1007/BF01337948.
- [103] R. Larsson and M. Landervik. A stress-resultant shell theory based on multiscale homogenization. *Computer Methods in Applied Mechanics and Engineering*, 263: 1–11, 2013. DOI: 10.1016/j.cma.2013.04.011.
- [104] L. Liu, Y. Zhang, T. J. R. Hughes, M. A. Scott, and T. W. Sederberg. Volumetric T-spline construction using Boolean operations. *Engineering With Computers*, 30(4):425–439, 2014. DOI: 10.1007/s00366-013-0346-6.
- [105] S. Loehnert and T. Belytschko. A multiscale projection method for macro/microcrack simulations. *International Journal for Numerical Methods in Engineering*, 71(12):1466–1482, 2007. DOI: 10.1002/nme.2001.
- [106] W. E. Lorensen and H. E. Cline. Marching cubes: A high resolution 3D surface construction algorithm. *ACM SIGGRAPH Computer Graphics*, 21(4):163–169, 1987. DOI: 10.1145/37402.37422.

- [107] A. E. H. Love. XVI. The small free vibrations and deformation of a thin elastic shell. *Philosophical Transactions of the Royal Society of London. (A.)*, 179:491–546, 1888. DOI: 10.1098/rsta.1888.0016.
- [108] J. Lubliner. *Plasticity theory*. Courier Corporation, 2008.
- [109] K. K. Mandadapu, A. Sengupta, and P. Papadopoulos. A homogenization method for thermomechanical continua using extensive physical quantities. *Proceedings of the Royal Society A: Mathematical, Physical and Engineering Sciences*, 468(2142): 1696–1715, 2012. DOI: 10.1098/rspa.2011.0578.
- [110] J. Mandel. Plasticité classique et viscoplasticité. In: *CISM Courses and Lectures*. Springer New York, 1972. URL <https://api.semanticscholar.org/CorpusID:118220241>.
- [111] K. Matouš, M. G. Geers, V. G. Kouznetsova, and A. Gillman. A review of predictive nonlinear theories for multiscale modeling of heterogeneous materials. *Journal of Computational Physics*, 330:192–220, 2017. DOI: 10.1016/j.jcp.2016.10.070.
- [112] B. C. N. Mercatoris and T. J. Massart. A coupled two-scale computational scheme for the failure of periodic quasi-brittle thin planar shells and its application to masonry. *International Journal for Numerical Methods in Engineering*, 85(9):1177–1206, 2011. DOI: 10.1002/nme.3018.
- [113] B. S. Mercer, K. K. Mandadapu, and P. Papadopoulos. Novel formulations of microscopic boundary-value problems in continuous multiscale finite element methods. *Computer Methods in Applied Mechanics and Engineering*, 286:268–292, 2015. DOI: 10.1016/j.cma.2014.12.021.
- [114] L. Mester. "Computational Homogenisation and Multiscale Modelling Employing an Image-based Approach for the Structural Analysis of Shells." - Data corresponding to publication, 2024, Technische Universität Dresden. DOI: 10.25532/OPARA-460. URL <https://opara.zih.tu-dresden.de//handle/123456789/595>.
- [115] L. Mester and S. Klinkel. Parameterized representative volume element (RVE) for textile-reinforced composites, 2023, Zenodo. DOI: 10.5281/zenodo.8340827.
- [116] L. Mester, S. Klarmann, and S. Klinkel. Homogenisation for macroscopic shell structures with application to textile-reinforced mesostructures. *PAMM*, 22(1), 2023. DOI: 10.1002/pamm.202200137.
- [117] L. Mester, S. Klarmann, and S. Klinkel. Homogenization assumptions for the two-scale analysis of first-order shear deformable shells. *Computational Mechanics*, 2023. DOI: 10.1007/s00466-023-02390-z.

- [118] L. Mester, V. Klempt, F. Wagner, S. Scheerer, S. Klarmann, I. Vakaliuk, M. Curbach, H.-G. Maas, S. Löhnert, and S. Klinkel. A comparison of multiscale methods for the modelling of carbon-reinforced concrete structures. In: A. Ilki, D. Çavunt, and Y. S. Çavunt (eds.), *Building for the Future: Durable, Sustainable, Resilient*, vol. 350 of *Lecture Notes in Civil Engineering*, pp. 1418–1427. Springer Nature Switzerland, Cham, 2023. ISBN 978-3-031-32510-6.
- [119] C. Miehe. Computational micro-to-macro transitions for discretized microstructures of heterogeneous materials at finite strains based on the minimization of averaged incremental energy. *Computer Methods in Applied Mechanics and Engineering*, 192(5-6):559–591, 2003. DOI: 10.1016/S0045-7825(02)00564-9.
- [120] C. Miehe and A. Koch. Computational micro-to-macro transitions of discretized microstructures undergoing small strains. *Archive of Applied Mechanics (Ingenieur Archiv)*, 72(4-5):300–317, 2002. DOI: 10.1007/s00419-002-0212-2.
- [121] G. W. Milton and R. V. Kohn. Variational bounds on the effective moduli of anisotropic composites. *Journal of the Mechanics and Physics of Solids*, 36(6): 597–629, 1988. DOI: 10.1016/0022-5096(88)90001-4.
- [122] R. D. Mindlin. Influence of rotatory inertia and shear on flexural motions of isotropic, elastic plates. *Journal of Applied Mechanics*, 18(1):31–38, 1951. DOI: 10.1115/1.4010217.
- [123] T. Mori and K. Tanaka. Average stress in matrix and average elastic energy of materials with misfitting inclusions. *Acta Metallurgica*, 21(5):571–574, 1973. DOI: 10.1016/0001-6160(73)90064-3.
- [124] H. Moulinec and P. Suquet. A numerical method for computing the overall response of nonlinear composites with complex microstructure. *Computer Methods in Applied Mechanics and Engineering*, 157(1-2):69–94, 1998. DOI: 10.1016/S0045-7825(97)00218-1.
- [125] M. Müller, S. Klarmann, and F. Gruttmann. A new homogenization scheme for beam and plate structures without a priori requirements on boundary conditions. *Computational Mechanics*, 70(6):1167–1187, 2022. DOI: 10.1007/s00466-022-02219-1.
- [126] S. Mulmule and A. K. Rath. Application of a multi-director displacement field approach for sandwich shell structure analysis. *Computers & Structures*, 48(4): 653–660, 1993. DOI: 10.1016/0045-7949(93)90259-G.
- [127] S. Natarajan, J. Wang, C. Song, and C. Birk. Isogeometric analysis enhanced by the scaled boundary finite element method. *Computer Methods in Applied Mechanics and Engineering*, 283:733–762, 2015. DOI: 10.1016/j.cma.2014.09.003.

- [128] V. P. Nguyen, O. Lloberas-Valls, M. Stroeven, and L. Johannes Sluys. On the existence of representative volumes for softening quasi-brittle materials – a failure zone averaging scheme. *Computer Methods in Applied Mechanics and Engineering*, 199(45-48):3028–3038, 2010. DOI: 10.1016/j.cma.2010.06.018.
- [129] C. Oddy and R. Bisschop. Multiscale modelling of heterogeneous beams. Master’s thesis, Göteborg, Sweden, 2017. URL <https://odr.chalmers.se/server/api/core/bitstreams/07e41359-b8a4-46c4-ba52-39d5fb0a6c58/content>.
- [130] J. M. Ortolano, J. A. Hernández Ortega, and J. Oliver. *A comparative study on homogenization strategies for multi-scale analysis of materials*, vol. 135 of *Monograph CIMNE*. International Center for Numerical Methods in Engineering, Barcelona, 1 edition, 2013. ISBN 978-84-941004-6-8.
- [131] M. Pan, F. Chen, and W. Tong. Volumetric spline parameterization for isogeometric analysis. *Computer Methods in Applied Mechanics and Engineering*, 359:112769, 2020. DOI: 10.1016/j.cma.2019.112769.
- [132] J.-S. Park and S.-J. Oh. A new concave hull algorithm and concaveness measure for n-dimensional datasets. *Journal of Information science and engineering*, 28(3): 587–600, 2012.
- [133] D. K. Patel, A. M. Waas, and C.-F. Yen. Direct numerical simulation of 3D woven textile composites subjected to tensile loading: An experimentally validated multiscale approach. *Composites Part B: Engineering*, 152:102–115, 2018. DOI: 10.1016/j.compositesb.2018.06.012.
- [134] L. Piegl and W. Tiller. *The NURBS Book*. Springer, Berlin, Heidelberg, 1997. ISBN 978-3-540-61545-3.
- [135] L. Podshivalov, A. Fischer, and P. Z. Bar-Yoseph. On the road to personalized medicine: Multiscale computational modeling of bone tissue. *Archives of Computational Methods in Engineering*, 21(4):399–479, 2014. DOI: 10.1007/s11831-014-9120-1.
- [136] ProCon X-Ray GmbH. PXR PROCON X-RAY, 2021. URL <https://procon-x-ray.de/ct-xpress/>.
- [137] A. Qsymah, R. Sharma, Z. Yang, L. Margetts, and P. Mummery. Micro X-ray computed tomography image-based two-scale homogenisation of ultra high performance fibre reinforced concrete. *Construction and Building Materials*, 130:230–240, 2017. DOI: 10.1016/j.conbuildmat.2016.09.020.
- [138] K. Raju, T.-E. Tay, and V. B. C. Tan. A review of the FE2 method for composites. *Multiscale and Multidisciplinary Modeling, Experiments and Design*, 4(1):1–24, 2021. DOI: 10.1007/s41939-020-00087-x.

- [139] J. N. Reddy. *Mechanics of Laminated Composite Plates and Shells*. CRC Press, 2003. ISBN 978-042921069-3.
- [140] R. Reichel and S. Klinkel. A non-uniform rational B-splines enhanced finite element formulation based on the scaled boundary parameterization for the analysis of heterogeneous solids. *International Journal for Numerical Methods in Engineering*, 124(9):2068–2092, 2023. DOI: 10.1002/nme.7202.
- [141] E. Reissner. On the theory of bending of elastic plates. *Journal of Mathematics and Physics*, 23(1-4):184–191, 1944. DOI: 10.1002/sapm1944231184.
- [142] A. Reuss. Berechnung der Fließgrenze von Mischkristallen auf Grund der Plastizitätsbedingung für Einkristalle. *ZAMM - Journal of Applied Mathematics and Mechanics / Zeitschrift für Angewandte Mathematik und Mechanik*, 9(1):49–58, 1929. DOI: 10.1002/zamm.19290090104.
- [143] I. A. Rodrigues Lopes and F. M. Andrade Pires. Unlocking the potential of second-order computational homogenisation: An overview of distinct formulations and a guide for their implementation. *Archives of Computational Methods in Engineering*, 29(3):1339–1393, 2022. DOI: 10.1007/s11831-021-09611-9.
- [144] D. F. Rogers. *An introduction to NURBS: With historical perspective*. Morgan Kaufmann Publishers, San Francisco, Calif., 2001. ISBN 978-1-55860-669-2.
- [145] O. Ronneberger, P. Fischer, and T. Brox. U-net: Convolutional networks for biomedical image segmentation. In: *Medical Image Computing and Computer-Assisted Intervention – MICCAI 2015: 18th International Conference, Munich, Germany, October 5-9, 2015, proceedings, Part III 18*, pp. 234–241. Springer, 2015. URL <http://arxiv.org/pdf/1505.04597v1>.
- [146] G. Sachs. Zur Ableitung einer Fließbedingung. In: O. Bauer, M. Hansen, F. v. Göler, G. Sachs, E. Schmid, G. Wassermann, K. Sipp, H. Sieglerschmidt, R. Karnop, W. Kuntze, K. Laute, R. Eisenschitz, B. Rabinowitsch, K. Weissenberg, W. Boas, and M. Masima (eds.), *Mitteilungen der deutschen Materialprüfungsanstalten*, pp. 94–97. Springer Berlin Heidelberg, Berlin, Heidelberg, 1929. ISBN 978-3-642-90188-1.
- [147] S. Saeb, P. Steinmann, and A. Javili. Aspects of computational homogenization at finite deformations: A unifying review from Reuss’ to Voigt’s bound. *Applied Mechanics Reviews*, 68(5), 2016. DOI: 10.1115/1.4034024.
- [148] B. Sauren, S. Klarmann, L. Kobbelt, and S. Klinkel. A mixed polygonal finite element formulation for nearly-incompressible finite elasticity. *Computer Methods in Applied Mechanics and Engineering*, 403:115656, 2023. DOI: 10.1016/j.cma.2022.115656.

- [149] O. Schenk. *Scalable parallel sparse LU factorization methods on shared memory multiprocessors*. PhD thesis, ETH Zurich, 2000.
- [150] O. Schenk and K. Gärtner. Solving unsymmetric sparse systems of linear equations with PARDISO. *Future Generation Computer Systems*, 20(3):475–487, 2004. DOI: 10.1016/j.future.2003.07.011.
- [151] K. Schneider, M. Butler, and V. Mechtcherine. Carbon Concrete Composites C³ – Nachhaltige Bindemittel und Betone für die Zukunft. *Beton- und Stahlbetonbau*, 112(12):784–794, 2017. DOI: 10.1002/best.201700058.
- [152] R. M. Sencu, Z. Yang, Y. C. Wang, P. J. Withers, and C. Soutis. Multi-scale image-based modelling of damage and fracture in carbon fibre reinforced polymer composites. *Composites Science and Technology*, 198:108243, 2020. DOI: 10.1016/j.compscitech.2020.108243.
- [153] R. Sevilla, S. Fernández-Méndez, and A. Huerta. NURBS-Enhanced Finite Element Method (NEFEM). *Archives of Computational Methods in Engineering*, 18(4):441–484, 2011. DOI: 10.1007/s11831-011-9066-5.
- [154] J. C. Simo and T. J. R. Hughes. *Computational inelasticity*, vol. 7 of *Interdisciplinary applied mathematics Mechanics and materials*. Springer, New York, NY, corr. 2. print edition, 2000. ISBN 0-387-97520-9.
- [155] J. C. Simo and M. S. Rifai. A class of mixed assumed strain methods and the method of incompatible modes. *International Journal for Numerical Methods in Engineering*, 29(8):1595–1638, 1990. DOI: 10.1002/nme.1620290802.
- [156] R. Smit, W. A. M. Brekelmans, and H. Meijer. Prediction of the mechanical behavior of nonlinear heterogeneous systems by multi-level finite element modeling. *Computer Methods in Applied Mechanics and Engineering*, 155(1-2):181–192, 1998. DOI: 10.1016/S0045-7825(97)00139-4.
- [157] C. Song. *The Scaled Boundary Finite Element Method*. John Wiley & Sons, Ltd, Chichester, UK, 2018. ISBN 978-1-119-38848-7.
- [158] C. Song and J. P. Wolf. The scaled boundary finite-element method—alias consistent infinitesimal finite-element cell method—for elastodynamics. *Computer Methods in Applied Mechanics and Engineering*, 147(3-4):329–355, 1997. DOI: 10.1016/S0045-7825(97)00021-2.
- [159] C. Song and J. P. Wolf. The scaled boundary finite-element method – a primer: solution procedures. *Computers & Structures*, 78(1-3):211–225, 2000. DOI: 10.1016/S0045-7949(00)00100-0.

- [160] S. Sudarsono and K. Ogi. Fatigue Behavior of Open-Holed CFRP Laminates with Initially Cut Fibers. *Open Journal of Composite Materials*, 07(01):49–62, 2017. DOI: 10.4236/ojcm.2017.71003.
- [161] B. Sun, X. Wang, and Z. Li. Meso-scale image-based modeling of reinforced concrete and adaptive multi-scale analyses on damage evolution in concrete structures. *Computational Materials Science*, 110:39–53, 2015. DOI: 10.1016/j.commatsci.2015.07.050.
- [162] G. I. Taylor. Plastic Strain in Metals. *Journal of the Institute of Metals*, 62:307–324, 1938.
- [163] R. L. Taylor. FEAP—a finite element analysis program, 2003. URL <http://projects.ce.berkeley.edu/feap/>.
- [164] K. Terada, N. Hirayama, K. Yamamoto, M. Muramatsu, S. Matsubara, and S.-n. Nishi. Numerical plate testing for linear two-scale analyses of composite plates with in-plane periodicity. *International Journal for Numerical Methods in Engineering*, 105(2):111–137, 2016. DOI: 10.1002/nme.4970.
- [165] P. Thilakarathna, K. S. Kristombu Baduge, P. Mendis, V. Vimonsatit, and H. Lee. Mesoscale modelling of concrete – A review of geometry generation, placing algorithms, constitutive relations and applications. *Engineering Fracture Mechanics*, 231:106974, 2020. DOI: 10.1016/j.engfracmech.2020.106974.
- [166] S. Trautner, B. Jüttler, and M.-S. Kim. Representing planar domains by polar parameterizations with parabolic parameter lines. *Computer Aided Geometric Design*, 85:101966, 2021. DOI: 10.1016/j.cagd.2021.101966.
- [167] S. Vlachoutsis. Shear correction factors for plates and shells. *International Journal for Numerical Methods in Engineering*, 33(7):1537–1552, 1992. DOI: 10.1002/nme.1620330712.
- [168] W. Voigt. Ueber die Beziehung zwischen den beiden Elasticitätsconstanten isotroper Körper. *Annalen der Physik*, 274(12):573–587, 1889. DOI: 10.1002/andp.18892741206.
- [169] A. M. Vukicevic, S. Çimen, N. Jagic, G. Jovicic, A. F. Frangi, and N. Filipovic. Three-dimensional reconstruction and NURBS-based structured meshing of coronary arteries from the conventional X-ray angiography projection images. *Scientific reports*, 8(1):1711, 2018. DOI: 10.1038/s41598-018-19440-9.
- [170] F. Wagner. Carbon Rovings Segmentation Dataset, 2023. URL <https://www.kaggle.com/datasets/franzwagner/carbon-rovings>.
- [171] F. Wagner. Roving surface extractor, 2023. URL https://gitlab.com/fra-wa/roving_surface_extractor.

- [172] F. Wagner and H.-G. Maas. A comparative study of deep architectures for voxel segmentation in volume images. In: *Proceedings of the ISPRS Geospatial Week 2023*. 2023.
- [173] F. Wagner, L. Mester, S. Klinkel, and H.-G. Maas. Analysis of thin carbon reinforced concrete structures through microtomography and machine learning. *buildings*, 13(9):2399, 2023. DOI: 10.3390/buildings13092399.
- [174] W. Wagner and F. Gruttmann. A robust non-linear mixed hybrid quadrilateral shell element. *International Journal for Numerical Methods in Engineering*, 64(5):635–666, 2005. DOI: 10.1002/nme.1387.
- [175] W. Wagner and F. Gruttmann. A consistently linearized multi-scale model for shell structures. *Shell Structures: Theory and Applications*, 3:453–456, 2013.
- [176] Y. Wang, L. Gao, J. Qu, Z. Xia, and X. Deng. Isogeometric analysis based on geometric reconstruction models. *Frontiers of Mechanical Engineering*, 16(4):782–797, 2021. DOI: 10.1007/s11465-021-0648-0.
- [177] P. Wriggers. *Computational Contact Mechanics*. Wiley, Chichester, 2002. ISBN 0-471-49680-4.
- [178] P. Wriggers. *Nonlinear Finite Element Methods*. Springer, Berlin, Heidelberg, 2008. ISBN 978-3-540-71000-4.
- [179] T. Wu, İ. Temizer, and P. Wriggers. Computational thermal homogenization of concrete. *Cement and Concrete Composites*, 35(1):59–70, 2013. DOI: 10.1016/j.cemconcomp.2012.08.026.
- [180] J. Wüst and W. Wagner. Systematic prediction of yield-line configurations for arbitrary polygonal plates. *Engineering Structures*, 30(7):2081–2093, 2008. DOI: 10.1016/j.engstruct.2008.01.005.
- [181] L. Xu, G. Cheng, and S. Yi. A new method of shear stiffness prediction of periodic Timoshenko beams. *Mechanics of Advanced Materials and Structures*, 23(6):670–680, 2016. DOI: 10.1080/15376494.2015.1029156.
- [182] H. T. Y. Yang, S. Saigal, A. Masud, and R. K. Kapania. A survey of recent shell finite elements. *International Journal for Numerical Methods in Engineering*, 47(1-3):101–127, 2000. DOI: 10.1002/(SICI)1097-0207(20000110/30)47:1/3<101::AID-NME763>3.0.CO;2-C.
- [183] S. Yi, L. Xu, G. Cheng, and Y. Cai. FEM formulation of homogenization method for effective properties of periodic heterogeneous beam and size effect of basic cell in thickness direction. *Computers & Structures*, 156:1–11, 2015. DOI: 10.1016/j.compstruc.2015.04.010.

- [184] B. Zastrau, I. G. Lepeş, and M. Richter. On the multi scale modeling of textile reinforced concrete. *Technische Mechanik-European Journal of Engineering Mechanics*, 28(1):53–63, 2008.
- [185] O. C. Zienkiewicz, R. L. Taylor, and J. M. Too. Reduced integration technique in general analysis of plates and shells. *International Journal for Numerical Methods in Engineering*, 3(2):275–290, 1971. DOI: 10.1002/nme.1620030211.
- [186] O. C. Zienkiewicz, R. L. Taylor, and J. Z. Zhu. *The Finite Element Method: Its Basis and Fundamentals*. Elsevier, Butterworth-Heinemann, Amsterdam, seventh edition edition, 2013. ISBN 978-1-85617-633-0.
- [187] J. Zoller. *Entwicklung eines Mehrskalenmodells für Sandwichstrukturen mit dünnwandigen Kernen*. PhD thesis, Technische Universität Darmstadt, Darmstadt, 2022.

Schriftenreihe
des Lehrstuhls für Baustatik und Baudynamik
der RWTH Aachen

- 01 (2013): Okayay Altay, Flüssigkeitsdämpfer zur Reduktion periodischer und stochastischer Schwingungen turmartiger Bauwerke, 2013, ISBN: 978-3-946090-01-4.
- 02 (2015): Francesca Taddei, Numerical Investigation of Soil-Structure Interaction for On-shore Wind Turbines Grounded on a Layered Soil, 2015, ISBN: 978-3-946090-00-7.
- 03 (2015): Wolfgang Dornisch, Interpolation of Rotations and Coupling of Patches in Iso-geometric Reissner–Mindlin Shell Analysis, 2015, ISBN: 978-3-946090-02-1.
- 04 (2015): Konstantinos Mykoniou, Dynamic analysis of multiple liquid-storage tanks, 2015, ISBN: 978-3-946090-03-8.
- 05 (2015): Benedikt Kohlhaas, Ein Finite-Elemente-Modell zur Analyse des Verhaltens von Formgedächtnisfaserkompositen mit beliebiger Mikrostruktur, 2015, ISBN: 978-3-946090-04-5.
- 06 (2016): Lin Chen, Numerical Models for the Analysis of Soil, Structure and Their Interaction, 2016, ISBN: 978-3-946090-05-2.
- 07 (2016): Julia Rosin, Seismische Auslegung von Tankbauwerken, 2016, ISBN: 978-3-946090-06-9.
- 08 (2019): Sreelakshmy Rajan, Probabilistic Seismic Safety Analysis of Multicomponent Systems, 2019, ISBN: 978-3-946090-07-6.
- 09 (2020): Maximilian Praster, Entwicklung eines adaptiven FE² Ansatzes zur Simulation von thermomechanisch beanspruchten Faser-Matrix-Kompositen, 2020, ISBN: 978-3-9460901-08-3.
- 10 (2020): Margarita Chasapi, Nonlinear Formulations and Coupling of Patches for Iso-geometric Analysis of Solids in Boundary Representation, 2020, ISBN: 978-3-946090-09-0.
- 11 (2021): Philipp Michel, Boden-Bauwerk-Fluid-Interaktion flüssigkeitsgefüllter Tankbauwerke auf nachgiebigen, vielfach geschichteten Böden unter seismischer Einwirkung, 2021, ISBN: 978-3-946090-10-6.
- 12 (2021): Okayay Altay, Structural Vibration Control with Semi-Active and Shape Memory Alloy Based Systems, 2021, ISBN: 978-3-946090-11-3.

- 13 (2021): Niklas Boesen, Trag- und Verformungsverhalten von unbewehrten Mauerwerksscheiben unter Berücksichtigung der Interaktion mit der Gebäudestruktur, 2021, ISBN: 978-3-946090-12-0.
- 14 (2022): Simon Schleiter, Entwicklung einer numerischen Methode zur Identifikation von Bauwerk-Dämpfer-Systemparametern, 2022, ISBN: 978-3-946090-13-7.
- 15 (2022): Georgia Kikis, Locking and Brittle Fracture in Isogeometric Reissner-Mindlin Plate and Shell Analysis, 2022, ISBN: 978-3-946090-14-4.
- 16 (2022): Sven Klinkel, Simon Klarmann, Forschungskolloquium Baustatik-Baupraxis, 2022, ISBN: 978-3-946090-15-1.
- 17 (2022): Andreas Kaup, Constitutive Modeling of Superelastic Shape Memory Alloy Damping Considering Dynamic Effects, 2022, ISBN: 978-3-946090-16-8.
- 18 (2022): Thomas Kubalski, Modellierung von seismisch beanspruchten Mauerwerksausfachungen in Stahlbetonrahmentragwerken, 2022, ISBN: 978-3-946090-17-5.
- 19 (2023): Rainer Reichel, A polytope finite element formulation for the analysis of non-linear mechanical behavior of composite materials, 2023, ISBN: 978-3-946090-18-2.

Lebenslauf

Name	Leonie Charlotte Josfine Mester
Geburtsdatum	12.05.1994
Geburtsort	Bergisch Gladbach
2004 – 2013	Schulbildung Abtei-Gymnasium Brauweiler, Pulheim Abitur
2013 – 2017	Studium des Bauingenieurwesens Rheinisch-Westfälische Technische Hochschule Aachen Bachelor of Science
2015 – 2016	Auslandsstudium Imperial College London, Großbritannien
2017 – 2020	Studium des Bauingenieurwesens Rheinisch-Westfälische Technische Hochschule Aachen Master of Science
2019	Forschungspraktikum University of Alberta, Edmonton, Canada
2020 – 2024	Wissenschaftliche Mitarbeiterin Lehrstuhl für Baustatik und Baudynamik Rheinisch-Westfälische Technische Hochschule Aachen

